High-Speed Permanent Magnet Motor with Immersion Evaporative Cooling

vorgelegt von

M.Sc.
Liuxin Bi

an der Fakultät IV- Elektrotechnik und Informatik
der Technischen Universität Berlin
zur Erlangung des akademischen Grades

Doktor der Ingenieurwissenschaften
- Dr.-Ing. -

genehmigte Dissertation

Promotionsausschuss:
Vorsitzender: Prof. Dr.-Ing. Clemens Gühmann
Gutachter: Prof. Dr.-Ing. Uwe Schäfer
Gutachter: Prof. Dr.-Ing. Felix Ziegler
Gutachter: Prof. Dr.-Ing. Shanming Wang
Tag der wissenschaftlichen Aussprache: 30. Juli 2021

Berlin 2021

ACKNOWLEDGEMENTS

This dissertation is the fruit of my five years of hard work as a Ph.D. student at the Department of Electrical Drives (EA) in TU-Berlin.
First and foremost, I would like to thank my supervisor, Professor Dr.-Ing. Uwe Schaefer for his valuable guidance, inspiring advice, and firm support throughout my Ph.D. career. Moreover, thanks for his careful revising and reviewing of this dissertation.
I would also like to thank Professor Dr.-Ing Shanming Wang for his encouragement and help in starting my unforgettable Ph.D. journey.
During my study in Berlin, I would also like to express my sincere gratitude to Tao Wang, Shouhui Ni, Shan Zhu, and Dr.-Ing Rong Dong for their academic exchanges and warm help in life.
I would also like to thank Tianjin EMAGING Technology Co., Ltd for their help in the prototype manufacturing, testing, and permit to publish the relevant research results.
Finally, I would like to thank my wife, son, and parents for their endless support.

Abstract

High-speed permanent magnet synchronous machines (PMSM) feature their excellent electrical performance are the most competitive and widely used motor type for direct driving compressors. However, accurate calculation of the losses, efficient cooling method, and expanding the power limit have always been challenges. In this thesis, an immersion evaporative cooled high-speed PMSM prototype with HFE-7100 as the coolant has been designed, built, and load tested. The loss models and thermal models have been established and verified.

A new high-frequency iron loss model was used to calculate the iron losses, considering the punching and burrs' connection effects. The iron losses of a bonded stator core (silicon steel laminations are stacked by glue) with three different magnetized rotors (sinusoidal magnetization, radial magnetization with a full magnet pitch, and radial magnetization with a reduced magnet pitch of 0.85) have been measured to verify the calculation method of iron losses. Among the three magnetizations, the last one is the best choice for the high-speed surface-mounted PMSM from the point of view of iron losses and output power capacity. The measured additional iron losses caused by welding and radial pressure show that the manufacturing factors greatly influence iron losses. The welded stator core with ventilation ducts and end plates used in the prototype introduces too much additional iron losses and should be avoided for high-speed motors.

A new method for determining air friction losses of high-speed permanent magnet machines has been proposed to compensate for the systematic errors caused by temperature rise and effectively improve the accuracy. The air friction losses with different air gap lengths have been studied experimentally. The retardation method was used to separate losses and determine the stator iron losses, air friction losses, and the iron losses in the rotor of magnetic bearings. A series connection of windings has been proposed to minimize the influence of iron losses on AC resistance measurement. The calculated results of the AC to DC resistance ratio in random-wound windings agree with the experimental results.

A thermal network model for stator with immersion evaporative cooling method has been established and verified. The thermal loading limit of this cooling method has been deduced. The effects of non-condensable gas (air), finned tubes, and fixation bandage of end windings on heat transfer were studied experimentally. The axial extension of the magnet can increase the typically low air gap flux density of high-speed surface-mounted PMSM.

The final experimental results show that the immersion evaporative cooling method can significantly enhance the thermal loading and expand the high-speed motors' power limit. Calorimetry was used to determine the motor's efficiency, and the results prove the accuracy and effectiveness of the loss models presented in this thesis.

Kurzfassung

Hochgeschwindigkeits-Permanentmagnet-Synchronmaschinen (PMSM) zeichnen sich durch ihre hervorragende elektrische Leistung aus und sind die wettbewerbsfähigsten und am weitesten verbreiteten Motortypen für direkt angetriebene Kompressoren. Die genaue Berechnung der Verluste, eine effiziente Kühlmethode und die Erweiterung der Leistungsgrenze waren jedoch schon immer Herausforderungen. In dieser Arbeit wurde ein tauchverdunstungsgekühlter Hochgeschwindigkeits-PMSM-Prototyp mit HFE-7100 als Kühlmittel entworfen, gebaut und unter Last getestet. Die Verlustmodelle und thermischen Modelle sind erstellt und verifiziert.

Zur Berechnung der Eisenverluste unter Berücksichtigung der Stanz- und Gratverbindungseffekte wurde ein neues Hochfrequenz-Eisenverlustmodell verwendet. Die Eisenverluste eines geklebten Statorblechpackets (Siliziumstahlbleche werden durch Klebstoff gestapelt) mit drei unterschiedlich magnetisierten Rotoren (sinusförmige Magnetisierung, radiale Magnetisierung mit voller Magnetteilung und radiale Magnetisierung mit einer reduzierten Magnetteilung von 0,85) wurden gemessen, um die Berechnungsmethode der Eisenverluste zu überprüfen. Unter den drei Magnetisierungen ist die letzte die beste Wahl für das oberflächenmontierte Hochgeschwindigkeits-PMSM im Hinblick auf Eisenverluste und Ausgangsleistungskapazität. Die gemessenen zusätzlichen Eisenverluste, die durch das Schweißen und den Radialdruck verursacht werden, zeigen, dass die Fertigungsfaktoren die Eisenverluste stark beeinflussen. Der im Prototyp verwendete geschweißte Statorblechpacket mit Lüftungskanälen und Endplatten bringt zu viel zusätzliche Eisenverluste und sollte für schnelllaufende Motoren vermieden werden.

Es wurde ein neues Verfahren zur Bestimmung der Luftreibungsverluste von Hochgeschwindigkeits-Permanentmagnetmaschinen vorgeschlagen, um die durch Temperaturanstieg verursachten systematischen Abweichungen zu kompensieren und die Genauigkeit effektiv zu verbessern. Die Luftreibungsverluste bei unterschiedlichen Luftspaltlängen wurden experimentell untersucht. Die Retardationsmethode wurde verwendet, um die Verluste zu trennen und die Eisenverluste des Stators, die Luftreibungsverluste und die Eisenverluste im Rotor von Magnetlagern zu bestimmen. Um den Einfluss von Eisenverlusten auf die AC-Widerstandsmessung zu minimieren, wurde eine Reihenschaltung von Wicklungen vorgeschlagen. Die berechneten Ergebnisse des AC-DC-Widerstandsverhältnisses in wild gewickelten Wicklungen stimmen mit den experimentellen Ergebnissen überein.

Ein thermisches Netzwerkmodell für Statoren mit Tauchverdunstungskühlverfahren wurde erstellt und verifiziert. Die thermische Belastungsgrenze dieser Kühlmethode wurde abgeleitet. Die Auswirkungen von nicht kondensierbarem Gas (Luft), Rippenrohren und Fixierbandage von Wickelköpfen auf die Wärmeübertragung wurden experimentell untersucht. Die axiale Verlängerung des Magneten kann die typischerweise niedrige Luftspaltflussdichte von oberflächenmontierten Hochgeschwindigkeits-PMSM erhöhen.

Die abschließenden Versuchsergebnisse zeigen, dass das Tauchverdunstungskühlverfahren die thermische Belastung deutlich erhöhen und die Leistungsgrenze der

Hochdrehzahlmotoren erweitern kann. Kalorimetrie wurde verwendet, um den Wirkungsgrad des Motors zu bestimmen, und die Ergebnisse belegen die Genauigkeit und Wirksamkeit der in dieser Arbeit vorgestellten Verlustmodelle.

Contents

1 Introduction

1.1 Background

1.1.1 Applications of high-speed electrical machines

High-speed electrical machines characterized by high power density are very suitable for directly driving the high-speed impeller loads. By eliminating the gearbox, the transmission efficiency is improved. They are usually equipped with air foil bearings or magnetic bearings offering oil-free and wear-free features and can adjust the rotational speed by a drive [1]. In the last few decades, high-speed machines develop quickly. They have been widely used in oil and gas compressors, air compressors, refrigeration compressors, air blowers, microturbine, turbocharger, and turbo-molecular pump [2, 3].

1.1.2 Types of high-speed electrical machines

Switched reluctance machines feature a simple rotor structure and good fault tolerance but also suffer from poor electrical performance and high vibration and noise issues. They are mainly used in the aerospace field, where the reliability requirements are stringent [4].

Induction machines (IM), especially solid rotor induction machines, dominate in the MW power range due to their maximum circumferential speed (max. 550 m/s, rated 400 m/s reported in [5]), best rotor dynamics, easy assembly, and low-cost [1]. For example, MAN Diesel & Turbo Inc. launched a hermetically sealed integrated oil and gas compressor driven by a solid rotor induction motor rated at 14.8 MW and 9,175 rpm, supported by magnetic bearings. In 2016, more than 100 compressors were operating in gas storage and transport [6]. Sundyne Inc. developed an 8 bar, oil-free air compressor driven by a 300 kW, 60 krpm solid rotor induction motor supported by magnetic bearings [5]. However, the poor power factor of solid rotor induction motors (typically 0.7 [5]) and their low efficiency have hindered their applications in low power range such as blowers described below. Even if induction motors also feature easy field-weakening, which is essential for spindle and flywheel applications, this is not required for compressors.

Permanent magnet synchronous machines have an overall advantage in power density, efficiency, and power factor [1], and thus have dominated industrial applications below 400 kW. Surface-Mounted Permanent Magnet (SPM) machines with non-magnetic high-strength retaining sleeve (titanium, Inconel, or carbon fiber) are more attractive than Interior Permanent Magnet (IPM) machines because the magnetic bridges of the latter are always a bottleneck for overall rotor strength [7]. Almost all commercial applications adopted the SPM scheme as follows:

(1) High-speed single-stage centrifugal blowers (usually below 30 krpm) from Neuros Inc. (SPM, up to 250 kW), K-turbo Inc. (SPM, up to 400 kW), Suzler Inc. (IM for small power range, SPM for 400 kW), Piller Inc. (SPM, up to 300 kW) [2] or Esurging Inc. (SPM, up to 700 kW) [8].

(2) Oil-free multi-stage centrifugal air compressors (usually above 35 krpm) from Atlas Copco Inc. (two motors, total 350 kW) [9] or Tamturbo Inc. (SPM, up to 325 kW) [10]. These centrifugal air compressors can achieve 25% energy saving compared with dry screw compressors [10].

(3) Danfoss Turbocor Inc. launched a series of oil-free compressors (SPM, up to 400 kW) for the heating ventilation air conditioning industry. Up to now, over 70,000 units are running in the field around the world [11].

(4) Capstone Inc. launched a micro-turbine family named C30 (SPM, 30 kW, 96 krpm), C65 (SPM, 65 kW, 96 krpm) and C200 (SPM, 200 kW, 61 krpm), which are compact, ultra-low-emission turbo-generators providing combined heat and electric power [12].

The issue of the rotor assembly of SPM machines can be solved by post-magnetization, making large power SPM machines possible. Nidec Inc. has designed, manufactured, and tested a 640 kW, 10 krpm Halbach-array slotless SPM motor equipped with active magnetic bearings for gas industry[13, 14]. DDS Inc. has developed and tested an 8 MW, 15 krpm medium-voltage SPM motor for oil and gas compressors and is developing a 12 MW, 10 krpm prototype [15]. The research object of this dissertation is also a high-speed SPM motor supported by magnetic bearings.

1.1.3 Limits of high-speed electrical machines

For high-speed electrical machines, the limits of power and speed have always been a concern. When comparing the design challenge of high-speed motors with different speeds, the "$\mathrm{rpm} \cdot \sqrt{\mathrm{kW}}$" figure-of-merit was introduced as an appropriate indicator, the value of which is nowadays limited to 10^6 [3]. According to the classical formula of motor design:

$$S = \pi^2 \cdot A_\mathrm{s} \cdot B_\delta \cdot k_\mathrm{w} \cdot D_\mathrm{si}^2 \cdot l_\mathrm{Fe} \cdot n \tag{1.1}$$

where S is the apparent power, A_s the specific electric loading, B_δ the root mean square (RMS) value of the air gap flux density, k_w the winding factor, D_si the stator inner diameter, l_Fe the stator core length and n the rotational speed.

The power limit of the motor at a given speed n depends on the size and $A_\mathrm{s} \cdot B_\delta$, which are ultimately limited by mechanical strength and cooling effectiveness, respectively [16]. The maximum rotor stress is proportional to the square of rotor circumferential speed. As reported in [3, 5, 15], the maximum circumferential speed for solid rotors is 550 m/s, that of laminated rotors is 290 m/s, and SPM rotors with carbon fiber sleeve is 330 m/s. For a given speed of n, D_{si} is limited by the strength of the material. l_{Fe} is mainly limited by rotor dynamics because high-speed motors usually run below the first bending critical speed. B_δ is restricted by the remanence of the permanent magnet. Therefore, increasing A_{s} by enhancing cooling efficiency is a feasible way to increase the power limit further. Table 1.1 shows the thermal loading of turbo-generators under different cooling methods. By direct-cooling the hollow copper bar through hydrogen or water, the generator's thermal loading can be significantly increased, thus expanding its power limit.

Table 1.1: Thermal loading of turbo-generator [17, 18]

Cooling method	Air indirect-cooling	Hydrogen indirect-cooling	Hydrogen direct-cooling	Water direct-cooling
Current density ($\mathrm{A/mm^2}$)	2.5–3.5	3.5–4.5	6–8	8–12
Electric loading (A/cm)	500–600	600–800	1,000–1,300	1,800–2,400
Thermal loading $\mathrm{A^2/\,(mm^2 \cdot cm)}$	1,600–2,000	2,100–3,600	6,000–9,000	12,000–25,000
Power limit (MVA)	300		700	1,000 (2 poles) 1,700 (4 poles)

Unfortunately, due to the skin effect, high-speed motors usually adopt random-wound windings. Thus, they cannot use the water direct-cooling method. Since high-speed motors' power is usually limited to a few hundred kW, using hydrogen will cause cost, explosion-proof, and other complex problems. Therefore, high-speed motors usually adopt pure air cooling or stator water jacket cooling plus rotor air cooling methods. These inefficient cooling methods limit the electric loading of high-speed motors, so it is urgent to find an efficient cooling method suitable for them.

1.2 Motivation

One of this dissertation's purposes is to apply the immersion evaporative cooling method to high-speed electrical machines. This phase-change heat transfer can significantly enhance the cooling effect of the stator side, thus improve the electric loading and expand the limits of power. Therefore, it is necessary to establish a thermal network of a motor with an immersion evaporative cooling method and build a prototype to verify its feasibility. Besides, the accuracy of the thermal networks depends heavily on the accuracy of heat sources. Another goal is to calculate and verify losses in high-speed PM electrical machines, such as iron losses, air friction losses, and copper losses.

1.3 Outline

Chapter 1 presents an overview of high-speed electrical machines and the motivation and outline of this dissertation.

In Chapter 2, the iron losses of a high-speed PM motor, including the punching and burrs' connection effects, are calculated by the proposed iron loss model. The predicted results are validated by experiments. The impact of other manufacturing factors on iron losses are also studied.

In Chapter 3, the air friction losses of a high-speed PM motor supported by magnetic bearings are calculated and verified. The bearing losses are also determined.

In Chapter 4, the AC resistance ratio of high-speed electrical machines with random-wound windings is investigated, which is used to calculate copper losses.

In Chapter 5, a thermal network model for stator with immersion evaporative cooling method is built. An evaporative cooling test device has been designed and manufactured to verify it.

In Chapter 6, a high-speed PM motor prototype with immersion evaporative cooling method is designed, fabricated, and tested.

Chapter 7 gives a conclusion of the whole thesis and some suggestions for further work.

2 Iron Loss Calculation and Experimental Verification

2.1 Introduction

Accurate prediction and experimental verification of iron losses of high-speed motors have always been a challenge, mainly from the following aspects:

(1) The fundamental frequency of high-speed motors is usually hundreds of Hz, and there is a large number of low-order harmonic magnetic fields in a radially magnetized permanent magnet motor. In order to reduce the eddy current losses in the rotor as far as possible, the switching frequency of the drive is usually above 10 kHz [19]. Therefore, the frequency spectrum of the magnetic field in the high-speed motors is very wide, from hundreds of Hz to tens of kHz, thus causing a significant skin effect in the laminated stator core. The iron losses are calculated by iron loss models with fixed coefficients in [20, 21], which has been proven to be unsuitable for such wide spectrum applications [22]. In order to cover a wide spectrum range, iron loss models with variable coefficients have been used in [23, 24], where the whole frequency range has been divided up into several sub-ranges. However, the model fails when the effective frequency range of the fitted data is exceeded. This occurs typically in high-speed motors. In addition, the magnetic field inside the motor is rotating instead of alternating. The rotating magnetic field can be decomposed into two spatially orthogonal scalars and then treated separately [22, 25, 26]. The total eddy losses of the non-sinusoidal magnetic field are equal to the sum of all harmonic's eddy losses. However, the total hysteresis losses cannot be modeled using the superposition theorem. A minor loop coefficient associated with the waveform was used instead [27]. Furthermore, the temperature has a significant influence on iron losses [28].

(2) The manufacturing process of the stator core, such as punching, burrs' connection, welding, radial pressure, and so on, will lead to deterioration of magnetic properties and to an increase in iron losses [29]. These manufacturing factors often make the experimental iron losses value far larger than the calculated value [30]. In [31], the iron losses with aluminum casing (radial pressure 4 MPa) increased by about 10% compared with no casing. In [30], the test results showed that the permeability was reduced by about 50%, and the iron losses increased by about 10% due to shrinkage fit. In [32], the results showed that, compared with the loosed laminations, the specific losses of the bonded sample (bonded with glue) only increased by 2.5–5%, while they increased in welded samples by 5–8% for with 2 and 15–25% with 6 welding lines. In [33], a stator core was wound as a toroidal specimen to test the iron losses. The

test results showed that the iron losses of the welded stator increased by about 20% compared with loose lamination, and the punching effect resulted in a 15–20% increase in iron losses. However, in this case, the flux density in the core was alternating rather than rotating. In [34], the authors attempted to study the effect of annealing on iron losses of laminated cores experimentally. Although the calculation results showed that the iron losses could be reduced by 20% (the absolute value was only 0.6 W), the experimental accuracy could not verify the calculated results because the rated power of the motor was only 120 W. Besides, annealing usually requires high-temperature treatment, which damages the insulation coating and increases manufacturing costs [35]. In [36], the test results show that the axial pressure below an 8 MPa has a negligible effect on permeability and specific losses of the silicon steel with insulation coating.

(3) The iron losses of high-speed PM motors are difficult to separate from other losses experimentally. In [24], the laminated rotor of an interior PM motor was fixed, and the permanent magnets were removed. The iron losses (including the iron losses in the rotor) were equal to the total input power minus the calculated copper losses. Unfortunately, this method is not suitable for high-speed PM motors, whose magnets are usually surface-mounted on the solid rotor. Thus the stator's rotating magnetic field will generate a large amount of heat in the solid rotor. Besides, it is also difficult to calculate the copper losses in high-speed motors due to skin effect, proximity effect, and uneven currents between the parallel strands [37]. In [38] an induction motor under test is directly connected to the grid, and the rotor is driven by a synchronous motor with the same synchronous speed, thus running in a zero slip state. The windage losses and bearing losses are provided by the synchronous motor, so the induction motor's input power is the sum of copper losses and iron losses. However, this method cannot be applied to PM motors, and the problem of copper loss separation still exists. The retardation test is widely used for determining no-load losses of high-speed PM motors [39, 20, 40]. The total no-load losses consist of iron losses, windage losses, and bearing losses. In [39], an 8 MW, 15 krpm high-speed PM machine with form-wound windings was studied. The magnetic losses in the stator core and windings were obtained by subtracting the windage losses (calculated by an analytical method) and the magnetic bearing losses (determined by the calorimetric method) from the total no-load losses. In [20], the iron losses are separated from the total no-load losses by the mathematical fitting. However, all these methods belong to indirect methods with high uncertainty. In [40], the iron losses were not further separated from the bearing losses. In [31], the iron losses of a magnetized rotor minus those of a non-magnetized rotor yield the no-load iron losses. However, this method suffers from the expensive high-speed torque meter and difficult shaft alignment when applied to high-speed motors.

In order to solve the three problems mentioned above, this chapter makes the following suggestions:

(1) The high-frequency iron loss model proposed in [41], which can cover a wide frequency spectrum range and consider the punching and burrs' connection effects, is applied to iron loss calculation of a high-speed PM motor. The iron losses of a bonded stator core (silicon steel laminations are stacked by glue) with three different rotors are measured to verify the calculation method.

(2) The stator iron losses are directly separated by means of the retardation method and a non-magnetized rotor. Based on this method, the additional iron losses caused by welding and radial pressure are measured, respectively, as well as the temperature influence on iron losses. These are useful for high-speed motor engineers.

In this dissertation, the calculated iron losses using the loss coefficients obtained from the wire-electrode cutting sample are called basic iron losses. The increased iron losses caused by manufacturing factors are called additional iron losses.

2.2 Basic iron loss models for motors

The magnetic flux density vector $\vec{B}(t)$ at the centroid of any element within a fundamental period can be obtained by solving the two-dimensional motor model with the transient time-stepping finite element method. The non-sinusoidal rotational flux density $\vec{B}(t)$ can be decomposed into two spatially orthogonal scalars, and then each non-sinusoidal time-varying scalar can be further resolved into a Fourier series [42]. This section introduces the basic iron loss model for the non-sinusoidal rotational flux density, whose product with the mass of the element renders the basic iron losses of the element. The sum of the basic iron losses of all elements gives the total basic iron losses.

2.2.1 Orthogonal decomposition of rotational magnetic field

There are three commonly used two-dimensional coordinate systems, namely Cartesian [25], polar [42], and major-minor system [26]. They can be transformed into each other [26]. The polar system was chosen because of the cylindrical structure of the stator core. Then the rotational flux density can be expressed as [42]:

$$\vec{B}(t) = B_{\mathrm{r}}(t) \cdot \overrightarrow{e_{\mathrm{r}}} + B_{\theta}(t) \cdot \overrightarrow{e_{\theta}} \tag{2.1}$$

where $\vec{B}(t)$ is a rotational flux density vector, $\overrightarrow{e_{\mathrm{r}}}$ and $\overrightarrow{e_{\theta}}$ are unit vectors in the r-axis and θ-axis directions, respectively, $B_{\mathrm{r}}(t)$ and $B_{\theta}(t)$ are the non-sinusoidal alternating components in the r-axis and θ-axis directions, respectively.

2.2.2 Iron loss model for non-sinusoidal flux density

$B_{\mathrm{r}}(t)$ and $B_{\theta}(t)$ can be further resolved into the following Fourier forms [42]:

$$\begin{aligned} B_{\mathrm{r}}(t) &= \textstyle\sum_{k=1}^{\infty} B_{\mathrm{krm}} \cdot \sin\left(2\pi \cdot k \cdot f \cdot t + \theta_{\mathrm{kr}}\right) \\ B_{\theta}(t) &= \textstyle\sum_{k=1}^{\infty} B_{\mathrm{k\theta m}} \cdot \sin\left(2\pi \cdot k \cdot f \cdot t + \theta_{\mathrm{k\theta}}\right) \end{aligned} \tag{2.2}$$

where k is the harmonic order, f the fundamental frequency, B_{krm} and $B_{\mathrm{k\theta m}}$ are the amplitude of k-th order harmonic in the r-axis and θ-axis directions, respectively, and θ_{kr} and $\theta_{\mathrm{k\theta}}$ are the phase of k-th order harmonic in the r-axis and θ-axis directions, respectively.

2.2.2.1 Eddy current losses

The eddy current losses for the non-sinusoidal magnetic field are equal to the sum of all harmonic eddy current losses [27]. For example, the eddy current loss model for $B_{\mathrm{r}}(t)$ can be written as:

$$p_{\mathrm{c,r}} = \sum_{k=1}^{\infty} p_{\mathrm{c,sin}}\left(T, k \cdot f, B_{\mathrm{krm}}\right) \tag{2.3}$$

where $p_{\mathrm{c,r}}$ are the specific total eddy current losses for $B_{\mathrm{r}}(t)$, and $p_{\mathrm{c,sin}}\left(T, k \cdot f, B_{\mathrm{krm}}\right)$ are the specific eddy current losses of k-th order harmonic in the radial direction at temperature T [41].

2.2.2.2 Hysteresis losses

The superposition theorem of harmonics cannot be applied to hysteresis losses. The extra hysteresis losses only depend on whether the waveform contains reversals [27], as shown in Fig. 2.1. If it contains a reversal, it will produce a corresponding small hysteresis loop thus increasing the hysteresis losses.

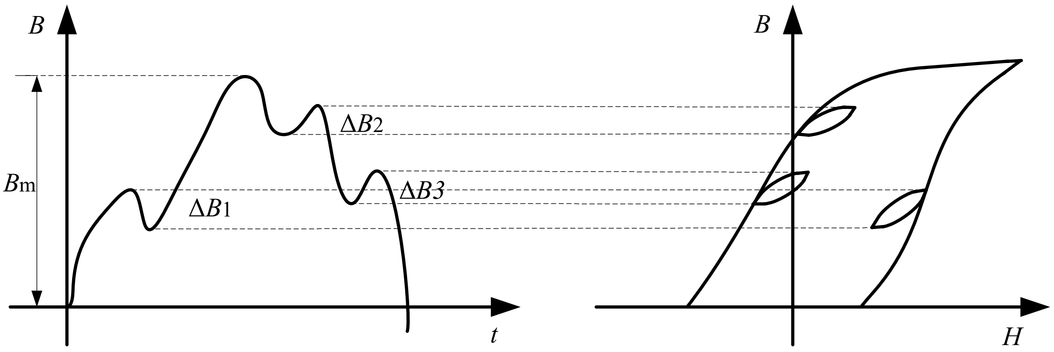

Fig. 2.1: Flux density waveform with reversals and corresponding minor loops [27]

A simple and practical method of correcting the hysteresis losses for the effects of minor loops was established in [27] and has been widely used [22, 24, 42]. Taking the radial component as an example, the hysteresis loss model for $B_{\mathrm{r}}(t)$ can be expressed as:

$$\begin{aligned} p_{\mathrm{h,r}} &= k_{\mathrm{total,r}} \cdot p_{\mathrm{h,sin}}\left(f, B_{\mathrm{rm}}\right) \\ k_{\mathrm{total,r}} &= 1 + k_{\mathrm{h}} \cdot \frac{1}{B_{\mathrm{rm}}} \cdot \sum_{j=1}^{N} \Delta B_{\mathrm{jr}} \end{aligned} \tag{2.4}$$

where $p_{\mathrm{h,r}}$ is the specific total hysteresis losses for $B_{\mathrm{r}}(t)$, B_{rm} the amplitude of $B_{\mathrm{r}}(t)$, ΔB_{jr} the flux reversal, N the number of reversals in the positive half cycle, $p_{\mathrm{h,sin}}\left(f, B_{\mathrm{rm}}\right)$ the specific hysteresis losses for sinusoidal flux density with amplitude of B_{rm} at frequency f [41], $k_{\mathrm{total,r}}$ a correction factor of harmonic distortion for $B_{\mathrm{r}}(t)$, k_{h} a coefficient depending on properties of silicon steel sheet, which is a value in the range of 0.6–0.7 [27]. The average value 0.65 was recommended in [42].

2.2.3 Iron loss model for rotational flux density

Finally, the total iron loss model for a rotational flux density $\vec{B}(t)$ is:

$$p_{\text{fe,rot}} = p_{\text{fe,r}} + p_{\text{fe},\theta} = p_{\text{c,r}} + p_{\text{h,r}} + p_{\text{c},\theta} + p_{\text{h},\theta} \tag{2.5}$$

where $p_{\text{fe,r}}$ and $p_{\text{fe},\theta}$ are the specific iron losses corresponding to $B_{\text{r}}(t)$ and $B_{\theta}(t)$, respectively.

2.3 Additional iron losses due to punching and burrs' connection

In [41], two types of punching edges have been identified, and the corresponding additional iron loss models have been obtained, as shown in Table 2.1. This chapter will describe how to apply them to a motor. In this dissertation, a pear-shaped slot with parallel teeth was adopted, as shown in Fig. 2.2. Due to the periodic symmetric structure, only one tooth pitch needs to be calculated.

Table 2.1: Definition of specific additional iron losses [41]

	Deterioration	Burrs' connection	Total
Punching edge type I	p_{Id}	p_{Ib}	$p_{\text{I}} = p_{\text{Id}} + p_{\text{Ib}}$
Punching edge type II	p_{IId}	p_{IIb}	$p_{\text{II}} = p_{\text{IId}} + p_{\text{IIb}}$

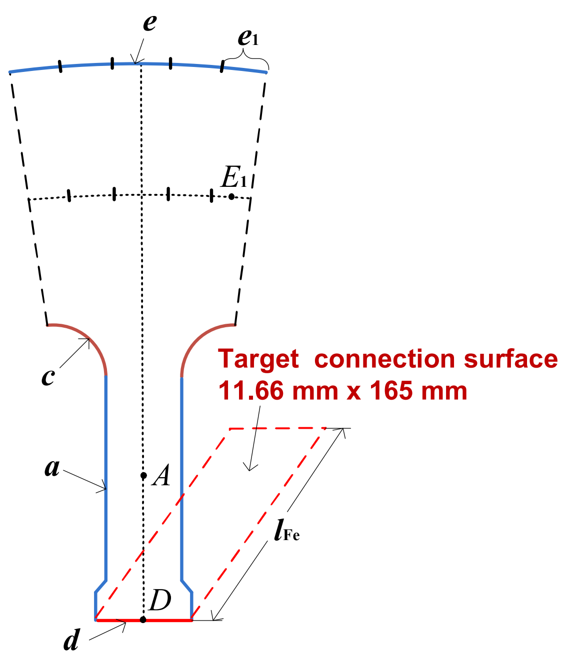

Fig. 2.2: Schematic diagram of one tooth pitch

2.3.1 Additional iron losses of punching edge type I

As definition in [41], both sides of the tooth (lines a) and the outer circle (lines e) belong to punching edge type I.

2.3.1.1 Line segment a

As found in [41], the average flux density in the parallel direction between two parallel punching edges must be used in the additional loss model. As it is a parallel tooth structure, the radial flux density $B_{\mathrm{r}}(t)$ of point A is taken, then the additional iron losses corresponding to line segment a are:

$$P_{\mathrm{I}} = (p_{\mathrm{I,h}} + p_{\mathrm{I,c}}) \cdot l_{\mathrm{a}} \cdot l_{\mathrm{Fe}} \tag{2.6}$$

where l_{a} is the length of line segment a, l_{Fe} the stator core length, and $p_{\mathrm{I,h}}$ and $p_{\mathrm{I,c}}$ are the additional hysteresis losses and eddy current losses per unit punching area, respectively. Considering the harmonics, according to (2.4), $p_{\mathrm{I,h}}$ can be written as:

$$p_{\mathrm{I,h}} = k_{\mathrm{total,I}} \cdot p_{\mathrm{I,h,sin}}\left(f, B_{\mathrm{rm}}\right) \tag{2.7}$$

where $k_{\mathrm{total,I}}$ is the corresponding correction factor of harmonic distortion, $p_{\mathrm{I,h,sin}}\left(f, B_{\mathrm{rm}}\right)$ the additional hysteresis losses per unit punching area for sinusoidal magnetic flux density with amplitude of B_{rm} at frequency f [41].

According to (2.3), $p_{\mathrm{I,c}}$ can be expressed as:

$$p_{\mathrm{I,c}} = \sum_{k=1}^{\infty} p_{\mathrm{I,c,sin}}\left(k \cdot f, B_{\mathrm{krm}}, T\right) \tag{2.8}$$

where $p_{\mathrm{I,c,sin}}\left(k \cdot f, B_{\mathrm{krm}}, T\right)$ are the additional eddy current losses per unit punching area of k-th order harmonic of $B_{\mathrm{r}}(t)$ at temperature T [41].

2.3.1.2 Arc segment e_1

Because the loci of magnetic density are mainly tangential components (see Fig. 2.13(b)) and slightly different at different locations of the yoke, the outer arc e is divided into five small arcs. Their losses are calculated separately and then added together. Taking the arc of e_1 as an example, the tangential component flux density of point E_1, as shown in Fig. 2.2, is taken, and the subsequent calculation process is the same as line a.

2.3.1.3 Arc segment c

As shown in Fig. 2.2, part of the arc c belongs to the tooth, and the other part to the yoke. The locus of flux density approximates an ellipse, as shown in Fig. 2.12(b). Therefore, the calculation of its additional iron losses is simplified in the following way. First, the additional iron losses are calculated with the radial flux density at the tooth point A and the tangential flux density at the yoke point E_1, respectively. Then the arithmetic average value is taken as the result.

2.3.2 Additional iron losses of punching edge type II

Fig. 2.2 shows that the burrs connecting the punching edge type II (represented by line segment d) form a target connection surface, where the varying flux density is perpendicular to. In [41], the surface-related specific additional iron losses due to the performance deterioration p_{IId} and the surface-related specific additional iron losses caused by burrs' connection p_{IIb} have been obtained experimentally.

Assuming that the additional iron losses due to deterioration P_{IId} are proportional to the punching area, then the calculation method is the same as P_{I} in Section 2.3.1.1.

In addition, it is assumed that additional iron losses caused by burrs' connection P_{IIb} are pure eddy current losses, which are both surface shape and area dependent. They are difficult to solve analytically, because of the skin effect and the uncertain state of the real connection surface. In this work, P_{IIb} have been obtained by using the 3-D eddy current magnetic field FEM combined with the experimental data.

2.3.2.1 Experimental p_{IIb}

The experimental surface-related specific additional iron losses p_{IIb} for a 12.5 mm × 6 mm burrs' connection surface of the sample are represented by circles in Fig. 2.3.

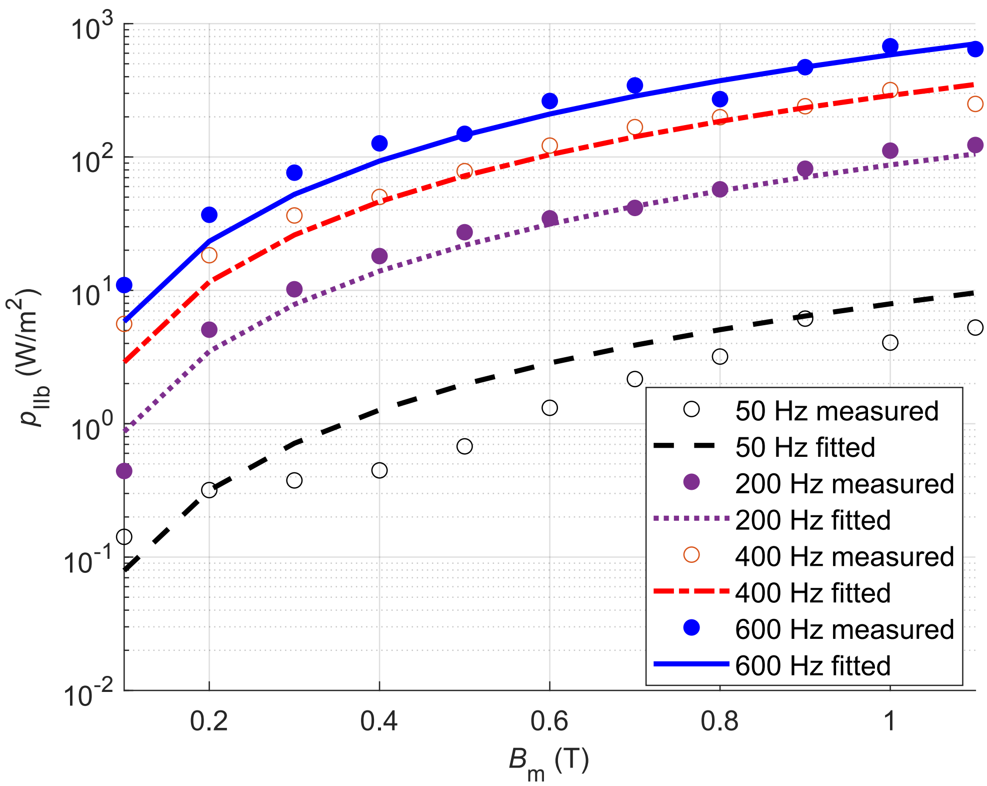

Fig. 2.3: Experimental and prediction data of p_{IIb} [41]

Considering the skin effect in the burrs' connection surface, a simple fixed coefficients formula was used to fit the experimental data by means of the least square deviation method:

$$p_{\mathrm{IIb}} = k_{\mathrm{c}} \cdot f^{\alpha} \cdot B_{\mathrm{m}}^{2} \tag{2.9}$$

The fitting results are shown in Fig. 2.3, with $\alpha = 1.73$, $k_{\mathrm{c}} = 9.12 \cdot 10^{-3}\ \mathrm{W}/\left(\mathrm{kg} \cdot \mathrm{T}^{2} \cdot \mathrm{Hz}^{\alpha}\right)$, and a total fitting error 16%. The big total error mainly comes from the poor smoothness of the measured data [41].

2.3.2.2 Simulated specific eddy-current loss ratio

As the punching die's clearance is 0.035–0.004 mm, the thickness of burrs' connection surface was assumed to be 0.035 mm. The resistivity is $4 \cdot 10^{-7}\ \Omega \cdot \mathrm{m}$ [41], and the $B - H$ curve of the 10 mm width in Fig. 2.10(a) was used. A uniform AC magnetic field strength H with a frequency of f perpendicular to the surface was applied. The solution results using the 3-D eddy current magnetic field solver of Ansys Maxwell are shown in Fig. 2.4. Due to the skin effect, the current density in the connection surface is concentrated on the edges.

Next, the eddy current losses of the target connection surface (11.66 mm $\times$ 165 mm) under the same condition were also determined. Then, (2.9) was used to fit the simulated loss data of the sample surface and the target surface, respectively. After that, a simulated specific eddy-current loss ratio k_{IIb} was defined as:

$$k_{\mathrm{IIb}} = \frac{k_{\mathrm{c2}}}{k_{\mathrm{c1}}} \cdot f^{(\alpha_2 - \alpha_1)} \tag{2.10}$$

where k_{c2}, α_2 are the fitting results of simulated eddy current losses for the target surface, and k_{c1}, α_1 are the fitting results of simulated eddy current losses for the sample surface.

According to the fitting results, $\frac{k_{\mathrm{c2}}}{k_{\mathrm{c1}}} = 4.08$ and $\alpha_2 \approx \alpha_1$ gives $k_{\mathrm{IIb}} \approx 4.08$.

2.3.2.3 Calculation of P_{IIb}

Finally, the additional iron losses caused by burrs' connection P_{IIb} for arc segment d in Fig. 2.2 can be calculated as:

$$P_{\mathrm{IIb}} = k_{\mathrm{IIb}} \cdot l_{\mathrm{d}} \cdot l_{\mathrm{Fe}} \cdot \sum_{k=1}^{\infty} p_{\mathrm{IIb}} = k_{\mathrm{IIb}} \cdot l_{\mathrm{d}} \cdot l_{\mathrm{Fe}} \cdot \sum_{k=1}^{\infty} k_{\mathrm{c}} \cdot (k \cdot f)^{\alpha} \cdot B_{\mathrm{krm}}^{2} \tag{2.11}$$

where l_{d} is the length of line segment d, l_{Fe} the stator core length, α and k_{c} have been determined in Section 2.3.2.1, and B_{krm} is the amplitude of k-th order harmonic of radial flux density at point D.

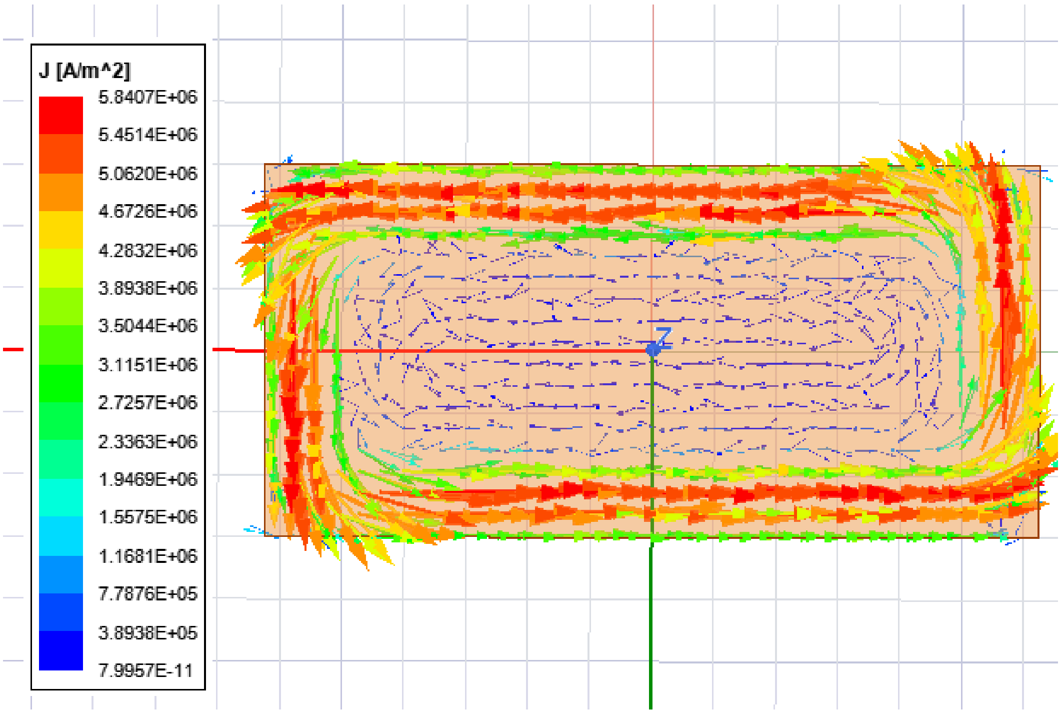

(a) Vector plot of induced current density

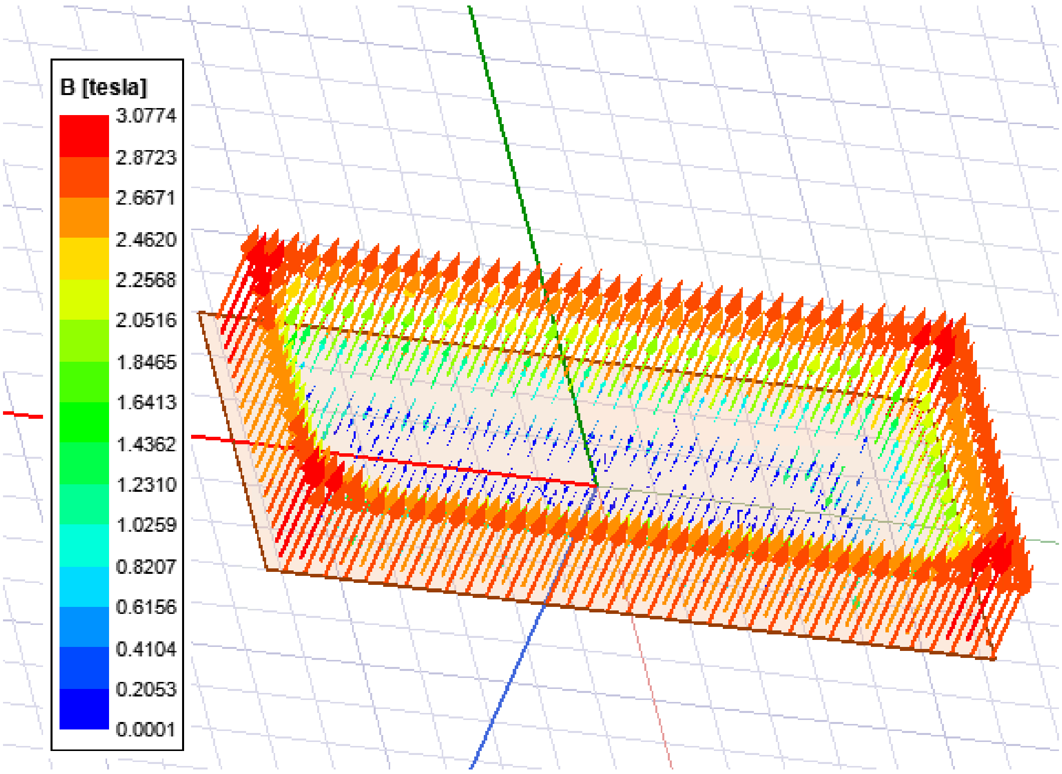

(b) Vector plot of flux density

Fig. 2.4: Simulation results in the burrs' connection surface of the sample at 400 Hz

2.4 Experimental scheme

2.4.1 Experimental setup

The tested motor is an air-water cooled 100 kW, 24 krpm high-speed permanent magnet motor supported by active magnetic bearings, as shown in Fig. 2.5, whose specifications are listed in Table A1 in the Appendix. In order to study the iron losses produced by harmonics, 3 rotors with different magnetization patterns have been manufactured (see Fig. 2.6). They have the same radial size. The first one is a parallel or sinusoidal magnetization rotor, the air gap radial flux density waveform of which is purely sinusoidal. Each pole consists of 2 identical pieces of magnet blocks, the magnetic direction of which is shown in Fig. 2.6(a). The second one is a full pitch magnet rotor with $\alpha = 1$, the air gap radial flux density waveform of which is approximately flat-topped. Each pole consists of 4 identical pieces of parallel magnetization magnet blocks, as shown in Fig. 2.6(b). The third one is a rotor with a reduced magnet pitch of α=0.85, the slots of which were filled by stainless steel blocks, as shown in Fig. 2.6(c). Besides, a non-magnetized rotor (the structure is identical to the $\alpha = 1$ one but not magnetized) is needed to separate the no-load iron losses. The surface-mounted magnets on the rotor are all protected by a 4 mm thick titanium alloy retaining sleeve, as shown in Fig. 2.6(d). So all the rotors have the same surface roughness.

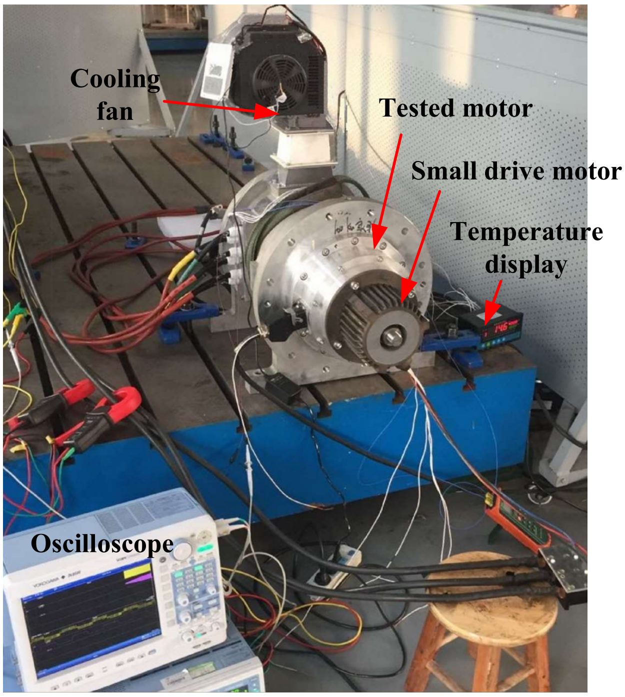

Fig. 2.5: Experimental setup for iron loss separation

The influence of radial pressure and welding on additional iron losses is studied experimentally. Three housings with different interference fits were manufactured. Their inner diameter and concentricity were measured at the same temperature. The same stator core was shrunk into these housings in turn. The maximum Von Mises stresses of the stator yokes were analyzed by FEM at the test temperature, and the corresponding stresses were 0 MPa (0 MPa means that there was a loose fit between the stator core and the housing; fixing was obtained by glue), 10 MPa, and 30 MPa, respectively.

The no-load iron losses of a bonded core and a welded core made with the same type of silicon steel sheet will be directly compared (see Fig. 2.7) to reflect the effect of welding on the iron losses caused by the rotating magnetic field.

The instruments are listed in Table A5 in the Appendix.

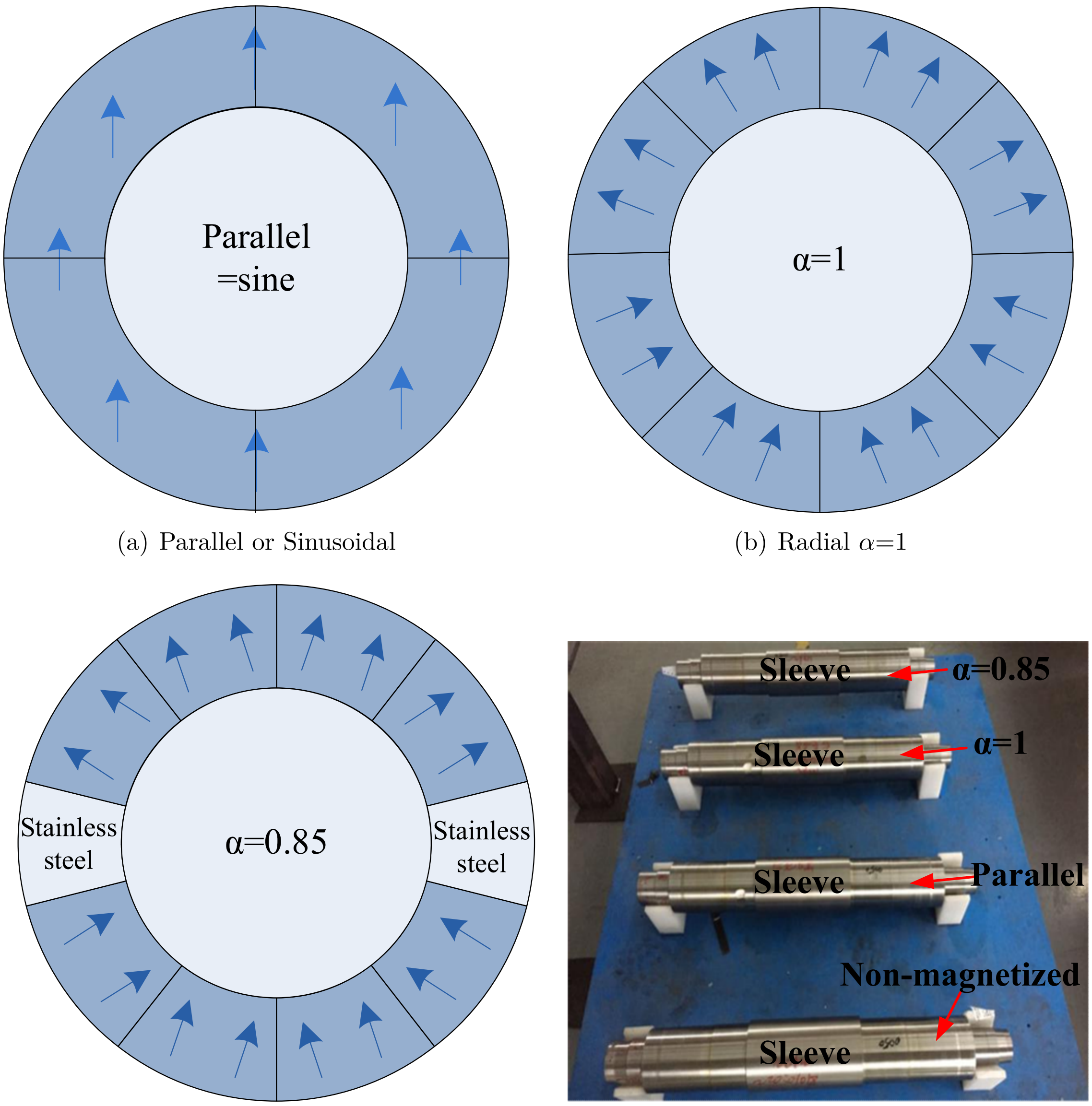

(a) Parallel or Sinusoidal

(b) Radial α=1

(c) Radial α=0.85

(d) Assembled rotors

Fig. 2.6: Four different magnetized rotors

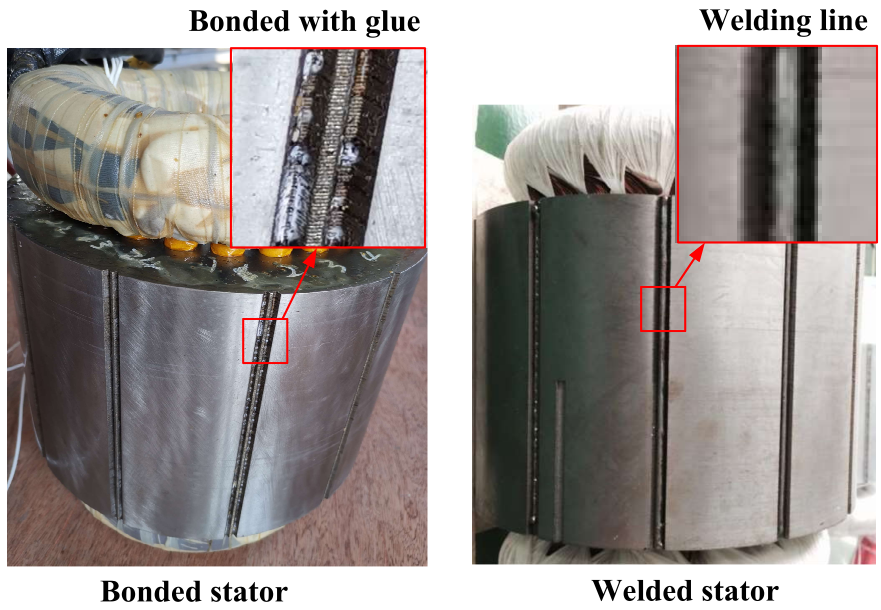

Fig. 2.7: Bonded and welded stator

2.4.2 Methods for determining the no-load iron losses

For high-speed PM motors, the retardation method is an efficient method to measure the no-load losses. The total no-load losses P_t can be determined by using the following equations [43]:

$$P_\mathrm{t} = -\frac{\mathrm{d}E(t)}{\mathrm{d}t}, \quad E(t) = \frac{1}{2} \cdot J \cdot \omega^2(t) \tag{2.12}$$

where $E(t)$ is the rotor kinetic energy, J the moment of inertia, and $\omega(t)$ the mechanical angular rotational speed of the rotor.

The rotors were modeled by 3-D modeling software. The density of each component on the rotor was given. Finally, the theoretical moment of inertia of the rotors could be obtained. The calculated moments of inertia of the rotors are listed in Table 2.2.

Table 2.2: Calculated moments of inertia of the rotors ($\mathrm{kg} \cdot \mathrm{m}^2$)

Non-magnetized	Parallel	α=1	α=0.85	Small motor
$4.757 \cdot 10^{-2}$			$4.751 \cdot 10^{-2}$	$9.820 \cdot 10^{-4}$

Because most encoders cannot withstand such a high rotational speed, and more importantly, the rotor supported by magnetic bearings will have a probable displacement of 0.4 mm in both axial and radial directions, encoders are usually not available on high-speed motors. Instead, a simple and practical method for determining the rotational speed by means of measurement of the back EMF waveform. Firstly, the back EMF waveform is recorded by an oscilloscope during coast-down, then $\omega(t)$ can be measured through zero-crossing point detection of the waveform described below.

If t_n and t_{n+1} are zero-crossing points of the back EMF waveform, the angular rotational speed ω at $\frac{t_n+t_{n+1}}{2}$ can be assumed as the average speed between t_n to the t_{n+1}:

$$\omega\left(\frac{t_n+t_{n+1}}{2}\right)=\frac{\pi}{(t_{n+1}-t_n)\cdot p} \tag{2.13}$$

where p is the number of pole pairs.

In order to drive the rotor (the non-magnetized rotor cannot drive itself), a 10 kW, 26 krpm small PM motor was manufactured. The rotor of the small motor is directly fixed on the driving end of the large motor via a pull rod, as shown in Fig. 2.8. The stator mounted on the large motor frame via a flange. The small drive motor was used to drive the four different rotors to the desired speed for the retardation test. Since the four rotors' external dimensions are identical, the air friction losses are assumed the same. The same magnetic bearing stator and controller have been used, so the magnetic bearing losses are assumed equal. Therefore, the total no-load losses of a magnetized rotor minus that of the non-magnetized rotor equal the stator iron losses corresponding to the magnetized rotor. The back EMF waveform of the non-magnetized rotor can be measured from the small PM motor terminals.

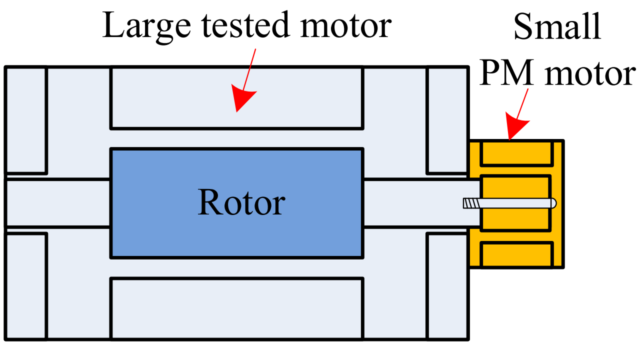

Fig. 2.8: Experimental scheme for separation of iron losses

2.4.3 Random error analysis

2.4.3.1 Rotation speed error

The accuracy of the rotational speed calculated by (2.13) depends on the ratio of the sampling frequency to the fundamental frequency of the back EMF. Since there are two zero-crossing points per cycle, the sampling frequency is 500 kHz, and the fundamental frequency is 400 Hz, the relative error of the rotational speed is:

$$\frac{\Delta\omega}{\omega}=\frac{2}{500\,\mathrm{kHz}/400\,\mathrm{Hz}}=0.16\% \tag{2.14}$$

2.4.3.2 Moment of inertia error

The rotor is simplified into a cylinder to analyze the moment of inertia error. The moment of inertia of the cylinder can be expressed as:

$$J = \frac{1}{2} \cdot M \cdot r^2 \tag{2.15}$$

where M is the mass of the cylinder, and r the outer radius.

As long as the density of each component is uniform, the error of moment of inertia depends on the precision of dimension and density. An electronic scale was used to measure the mass of rotor components for checking the density. The accuracy of the mass is $\pm 0.03\%$ and the accuracy of the radius is $\pm 0.01\%$. According to the propagation of uncertainty, the relative error of moment of inertia is:

$$\frac{\Delta J}{J} = \sqrt{\left(\frac{\Delta M}{M}\right)^2 + \left(2 \cdot \frac{\Delta r}{r}\right)^2} = \sqrt{(0.03\%)^2 + (2 \cdot 0.01\%)^2} = 0.036\% \tag{2.16}$$

2.4.3.3 Kinetic energy error

According to (2.12) the relative error of the kinetic energy error is

$$\frac{\Delta E}{E} = \sqrt{\left(\frac{\Delta J}{J}\right)^2 + \left(2 \cdot \frac{\Delta \omega}{\omega}\right)^2} = \sqrt{(0.036\%)^2 + (2 \cdot 0.16\%)^2} = 0.32\% \tag{2.17}$$

In practice, $\omega(t)$ curve was first fitted to a polynomial by the least square deviation method, then the no-load losses P_{t} can be solved analytically by (2.12).

2.5 Field calculation results and verification

2.5.1 Locus plots of rotational flux density

As shown in Fig. 2.9, a 2-D FEM model of one pole pitch of the motor was established according to the dimensions in Table A1 and the material properties in Table A2, and the drawings of Table A3 in the Appendix. The points A, B, and C show the loci of flux density. A full-pitch probe winding was added to measure the air gap flux density waveform, and the number of turns is 2.

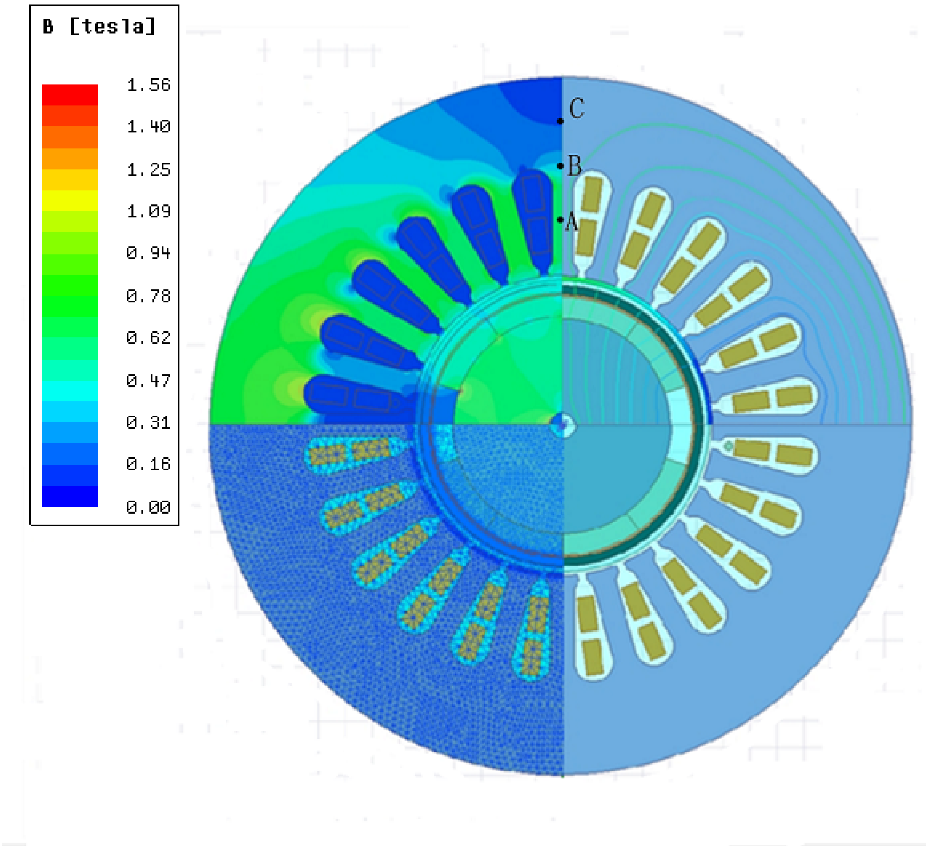

Fig. 2.9: FEM model of the motor with α=0.85

The punching process will lead to the deterioration of the magnetic characteristic of the silicon steel sheet, and the narrower the sample, the more apparent [44]. Fig. 2.10 shows that the magnetic permeability decreases significantly with the decrease of the width. Nonetheless, because the equivalent air gap of this motor is more than 15 mm (PM thickness 8 mm, sleeve thickness 4 mm, and air gap length 3.5 mm), the deterioration of the permeability of the silicon steel sheet has little effect on the air-gap flux density of the motor. The teeth were given the $B-H$ curve of the 7.5 mm width (at 400 Hz), while the yoke was given the $B-H$ curve of the 30 mm width. The model was simulated by the magnetic transient time-stepping solver. The rotational speed n is 24 krpm. The total number of steps for a fundamental cycle is 360, and the maximum harmonic order is 99th when the iron losses are calculated.

Fig. 2.11–2.13 show the radial and tangential components as well as locus plots of the rotational flux density at different locations, as defined in Fig. 2.9. The direction of flux density is mainly radial at the tooth part and mainly tangential at the yoke part. Only a few parts, such as tooth tip and tooth root, look more ellipsoidally. With α=1 and α=0.85 magnetizations, the flux density waveforms in the stators contain a large number of 3rd, 5th, 7th, and 9th order harmonics. The corresponding frequencies are 1,200 Hz, 2,000 Hz, 2,800 Hz, and 3,600 Hz, all exceeding 1,000 Hz. These harmonics will cause obvious skin effect in the eddy current iron losses. In contrast, the harmonic content of the parallel magnetization is very small.

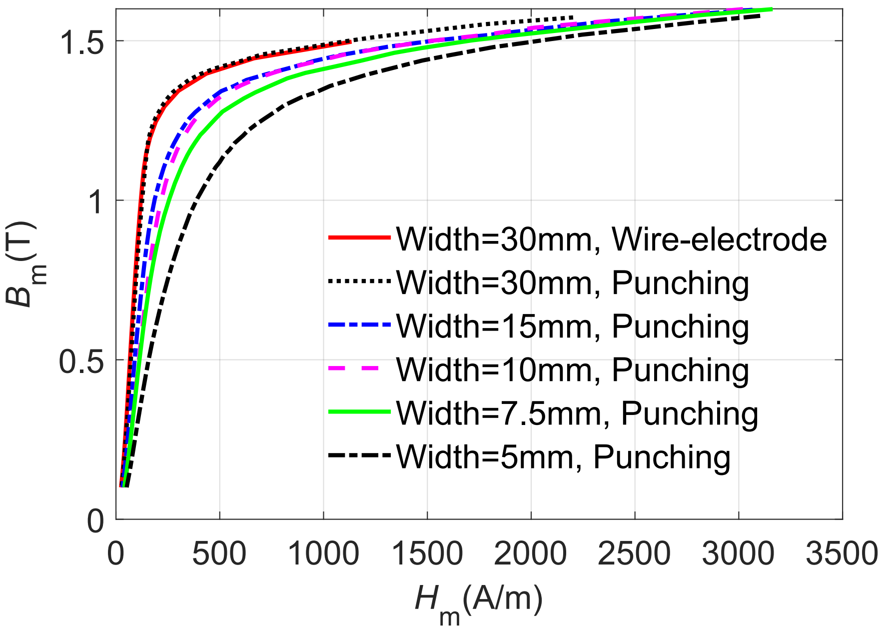

(a) $B-H$ curves

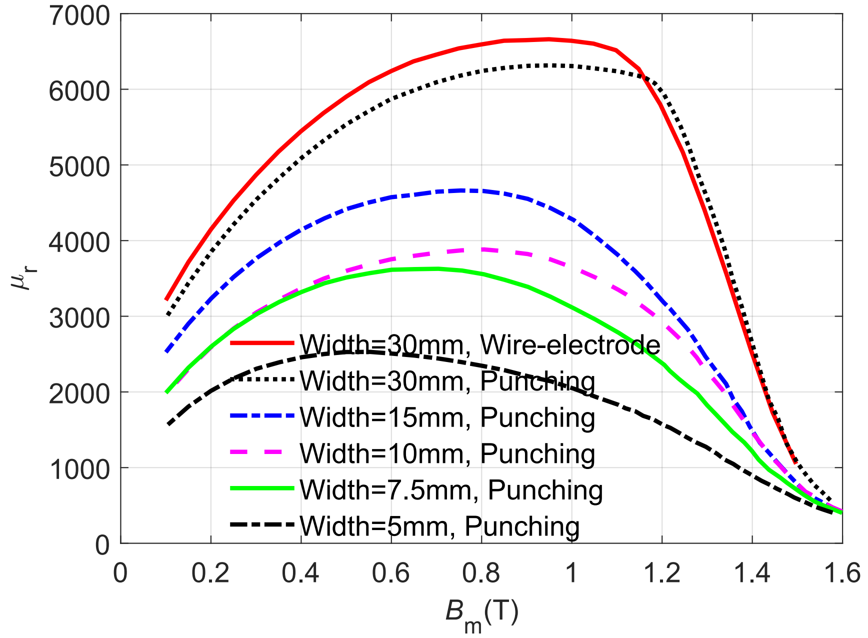

(b) $B-\mu_r$ curves

Fig. 2.10: Experimental magnetic characteristic of punched samples at 400 Hz

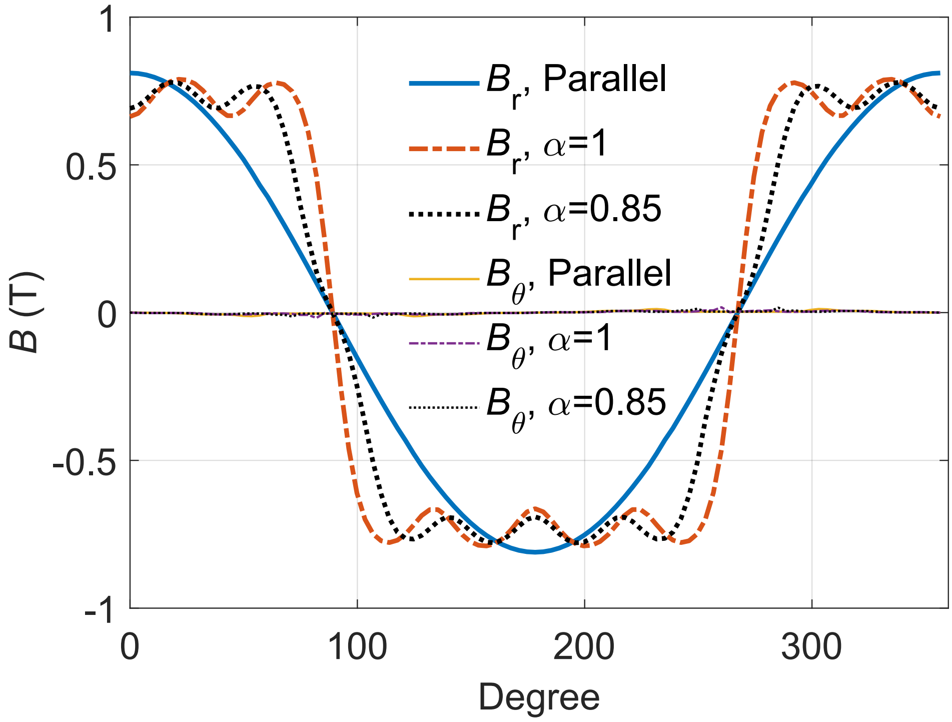

(a) Components

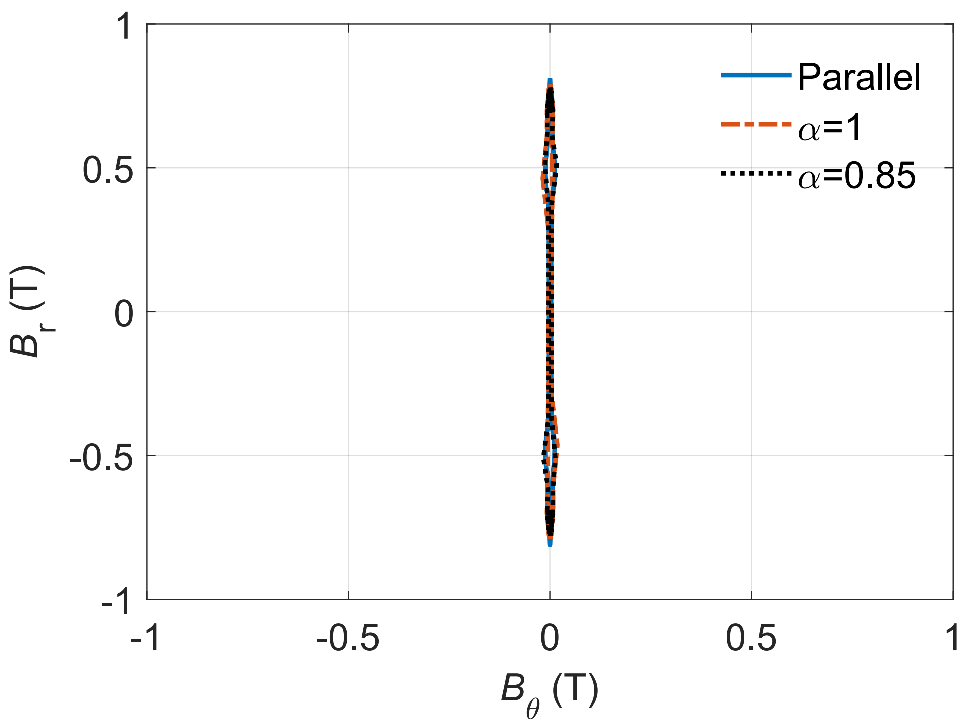

(b) Locus plots

Fig. 2.11: Flux density components at point A

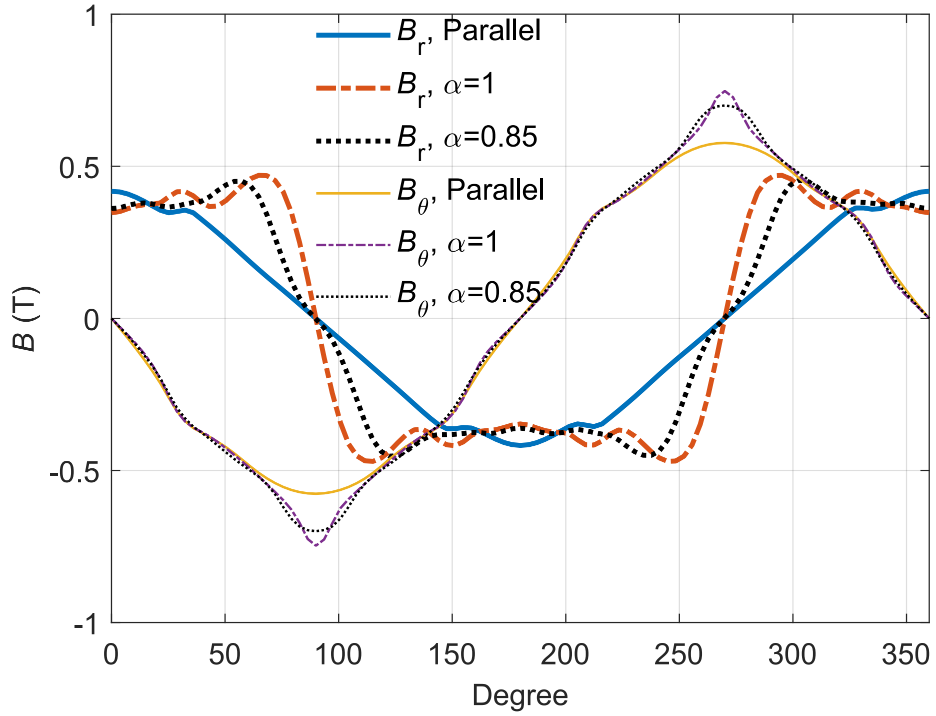

(a) Components

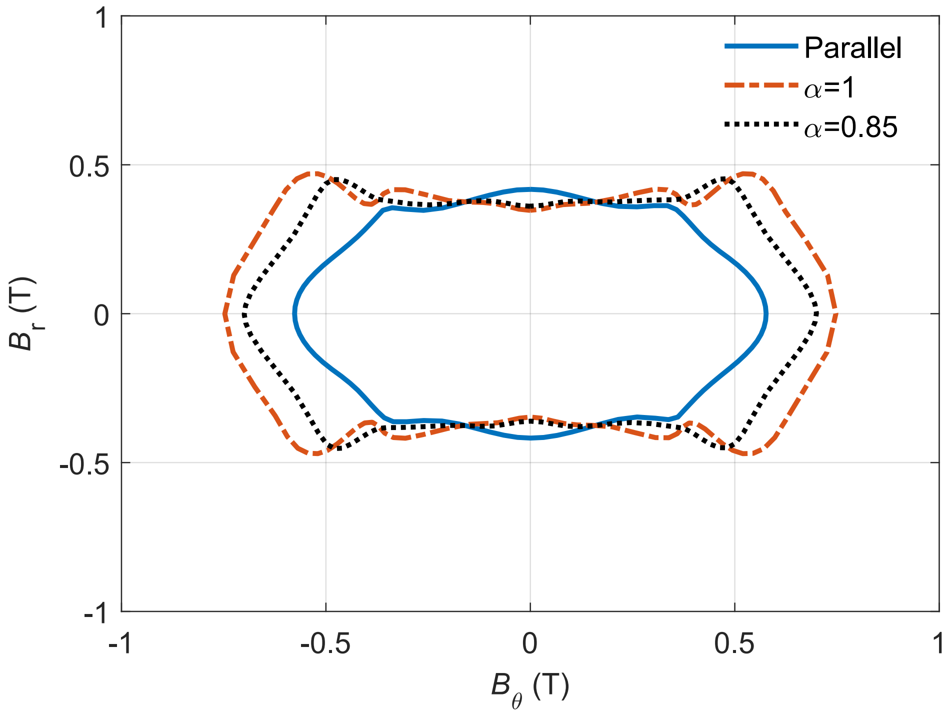

(b) Locus plots

Fig. 2.12: Flux density components at point B

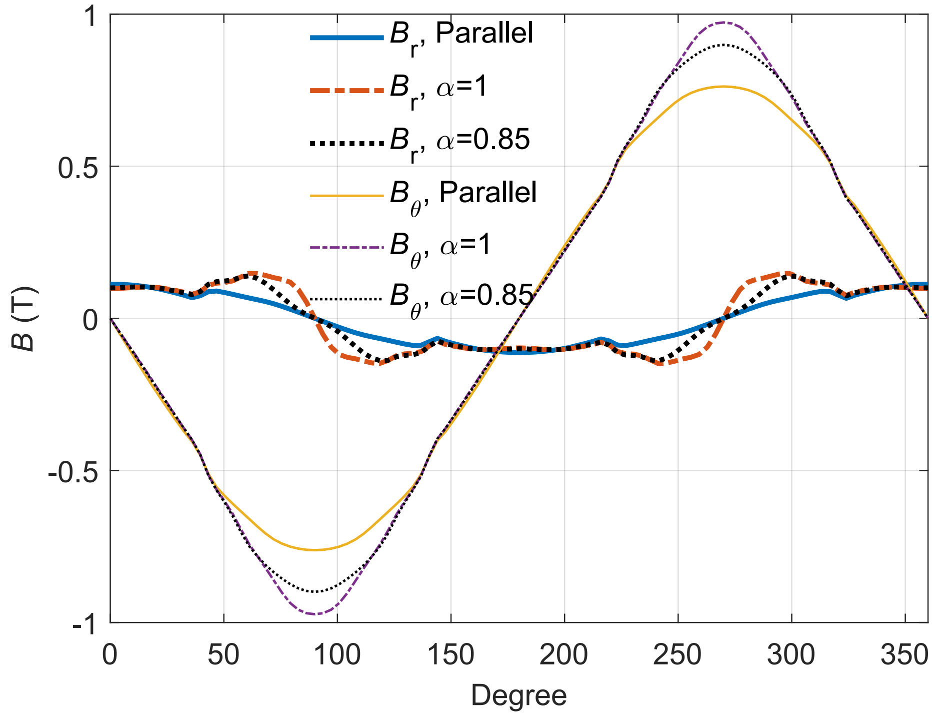

(a) Components

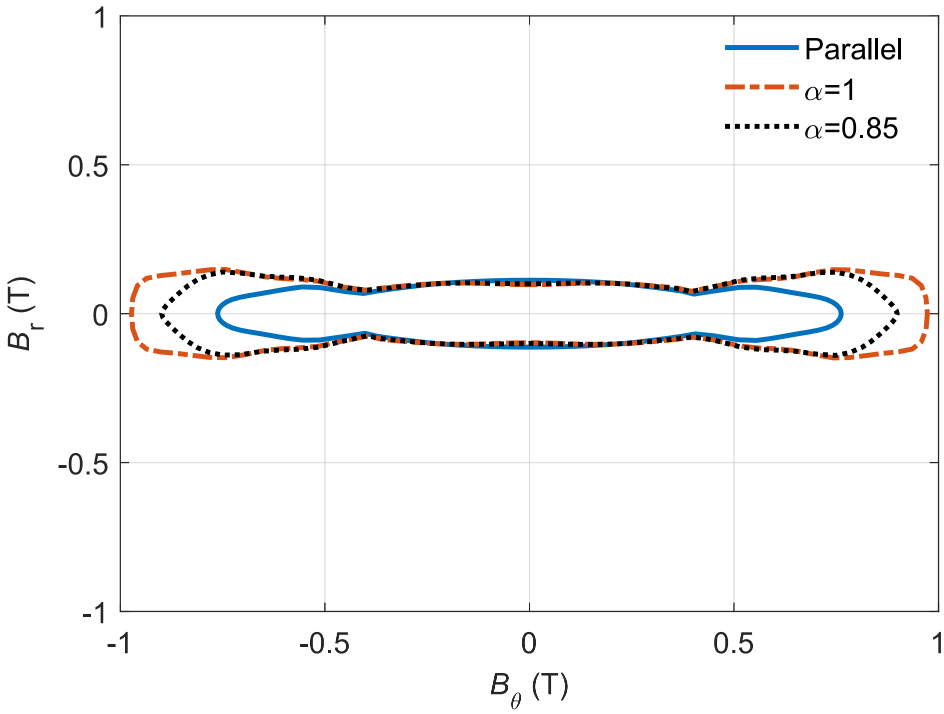

(b) Locus plots

Fig. 2.13: Flux density components at point C

2.5.2 Back EMF verification

Fig. 2.14 shows that the calculated and measured voltage waveforms at 24 krpm are in good agreement. Since the probe winding is a full-pitch winding, its voltage waveform is the same as that of air-gap radial flux density. As shown in Fig. 2.14(a), the waveforms of air-gap radial flux density of the Parallel rotor is almost sine. The waveforms of air-gap radial flux density of the rotor α=1 and α=0.85 are close to a square wave but with several small fluctuations. The reason is that each magnetic pole consists of multiple magnet blocks, and each block is parallel magnetized instead of radial magnetized. Since the stator windings adopt 5/6 short-pitch, the no-load line voltage waveforms of all three rotors are close to sine, as shown in Fig. 2.14(b).

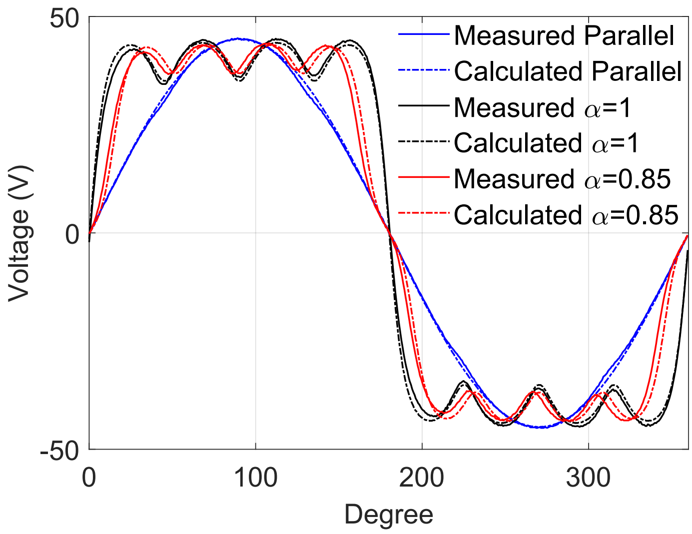

(a) Voltage of probe winding

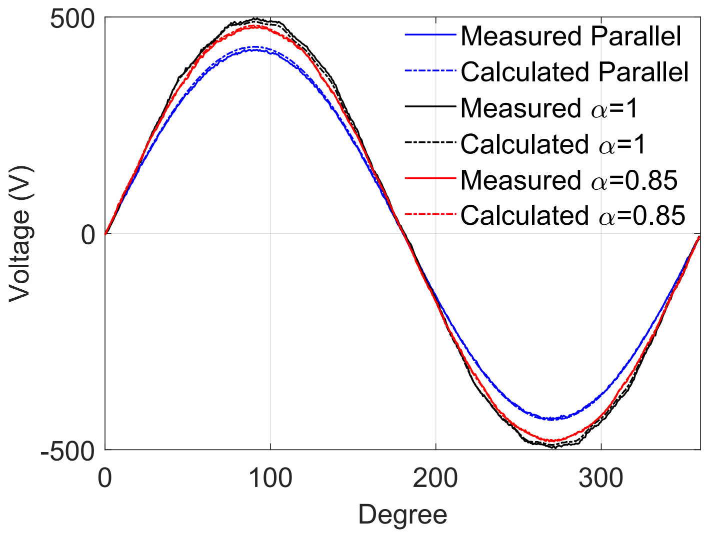

(b) Line voltage of distributed winding

Fig. 2.14: Experimental verification of voltage waveforms

Fig. 2.15 shows the back EMF values of different magnetization patterns with the same thickness of the magnets. The back EMF of α=0.85 is almost equal to that of α=1, while the values of the parallel magnetization and the classic α=2/3 magnetization are significantly reduced by 14%. Since the stress of rotor retaining sleeve is a real challenge in high-speed SPM motors, with the same thickness of permanent magnet, the scheme with higher back EMF and larger output power capacity is preferred. That is also the purpose of this thesis—to extend the power limit.

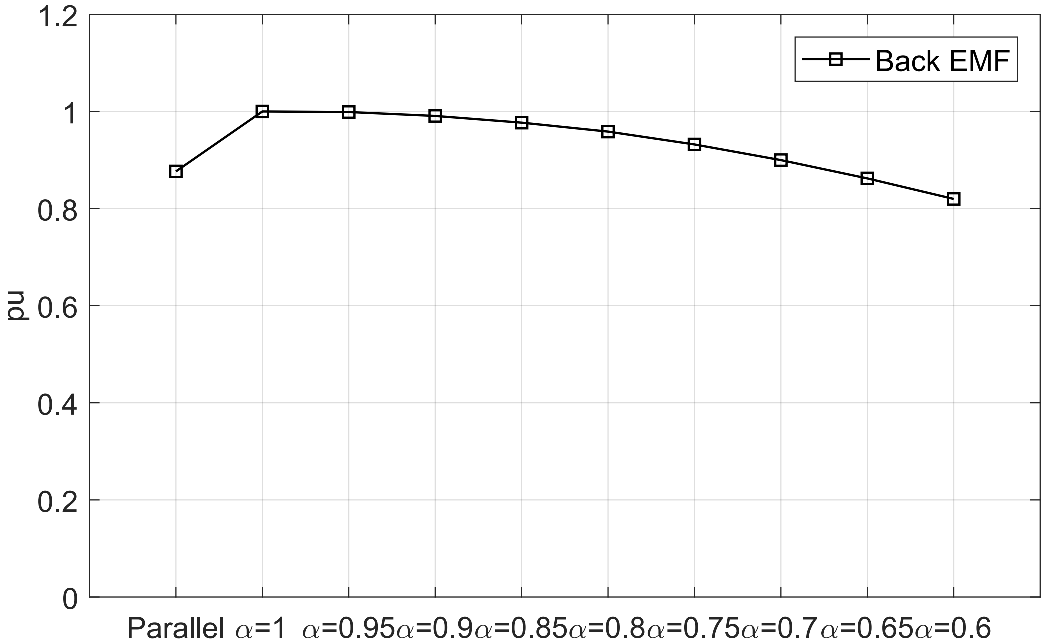

Fig. 2.15: Normalized back EMF of different magnetization patterns

2.6 Validation of iron loss model

2.6.1 Calculated basic iron losses

Table 2.3 shows the calculated basic iron losses (defined in Section 2.1) for different rotors at 24 krpm, 25°C. Where E_0 represents the RMS value of the fundamental component of line voltage of back EMF, P_{fe} are the total basic iron losses. E_0 of the Parallel rotor is the lowest, and the corresponding total iron losses are also the lowest. In order to compare the iron losses of different rotors more fairly, the total iron losses are normalized to the same E_0 = 347.5 V. Considering that the iron losses are proportional to the square of the flux density, and the flux density is proportional to E_0, the following formula can be obtained:

$$P'_{\mathrm{fe}} = P_{\mathrm{fe}} \cdot \left(\frac{347.5\ \mathrm{V}}{E_0} \right)^2 \tag{2.18}$$

where P'_{fe} are the total basic iron losses corresponding to 347.5 V.

Since the air gap flux density harmonics do not contribute to the effective torque, only additional iron losses are generated. Therefore, the lower the harmonics content is, the smaller P'_{fe} will be. From this point of view, parallel magnetization is the best choice, and α=1 is the worst choice. However, considering the significantly reduced E_0 of the same thickness of magnet, parallel magnetization is not economical. The iron losses of α=0.85 are reduced by 20% compared with α=1, while the back EMF is almost the same, so α=0.85 is the optimal choice among the three rotors.

Table 2.3: Calculated basic iron losses for different rotors

Rotor type	E_0	P_{fe}	P'_{fe}	Harmonics iron losses	Proportion of Harmonics iron losses
Parallel	304.6 V	435.0 W	566.0 W	6.0 W	1%
α=0.85	339.5 V	633.8 W	664.0 W	95.9 W	15%
α=1	347.5 V	815.8 W	815.8 W	225.8 W	28%

Table 2.4 further shows the composition of basic iron losses for α=0.85, where eddy current losses dominate.

Table 2.4: Composition of basic iron losses for α=0.85

Hysteresis	Eddy current	Teeth	Yoke	Total
195.4 W	438.4 W	168.8 W	465.0 W	633.8 W

2.6.2 Calculated additional iron losses due to punching and burrs' connection

Table 2.5 shows the calculated additional iron losses of the three rotors. The ratio of the additional losses to basic losses is larger than the results reported in [33], where only the punching effect was considered, and the increased proportion was only 15%–20%.

Table 2.5: Calculated additional iron losses for different rotors

Rotor type	Additional iron losses	Ratio of additional iron losses to basic iron losses	Total iron losses
Parallel	107.3 W	24.7%	542.3 W
α=0.85	172.6 W	27.2%	806.4 W
α=1	259.1 W	31.8%	1,074.9 W

Table 2.6 further gives the additional losses of the two punching edges respectively. Although the specific additional losses of punching edges I are small, the additional losses still dominate due to the larger area.

Table 2.6: Composition of additional iron losses for α=0.85

Punching edges I	Punching edges II	Total additional iron losses
129.4 W	43.2 W	172.6 W

2.6.3 No-load eddy current losses in the rotor

Due to the existence of harmonic magnetic field components caused by slot openings, eddy current losses will also occur in the rotor. The no-load eddy current losses in the rotor for α=1 is only 18 W at 24 krpm calculated by FEM, which is negligible.

2.6.4 Measured total no-load losses

Fig. 2.16 shows the coast-down rotational speed curves of the four different rotors. According to (2.12), the total no-load losses of each rotor can be determined as shown in Fig. 2.17. Then the iron losses of the three magnetized rotors can be obtained by loss separation.

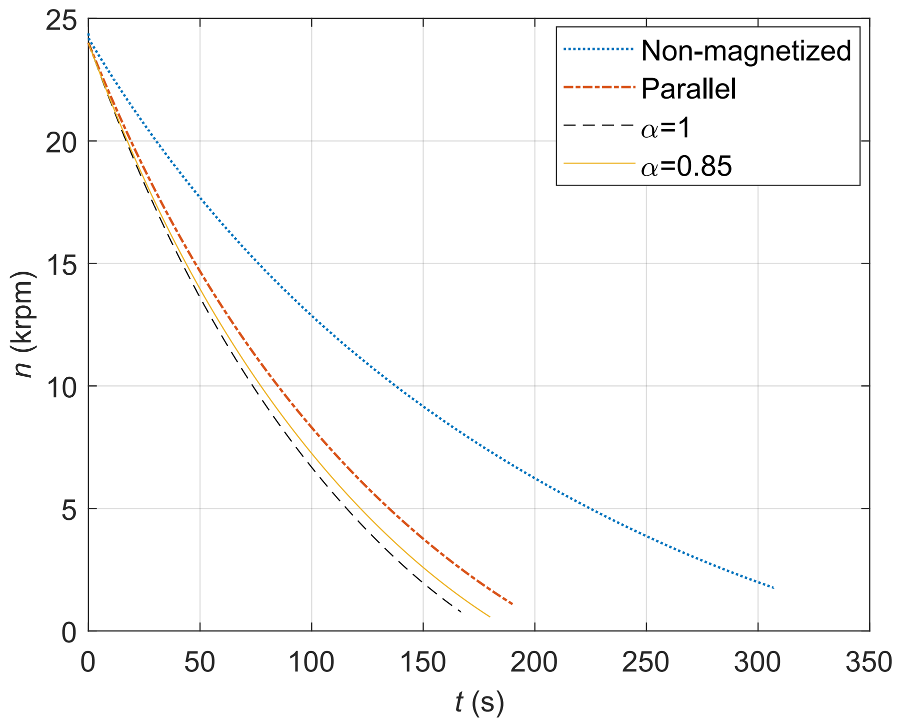

Fig. 2.16: Measured coast-down rotational speed curves of different rotors (welded stator, 0 MPa)

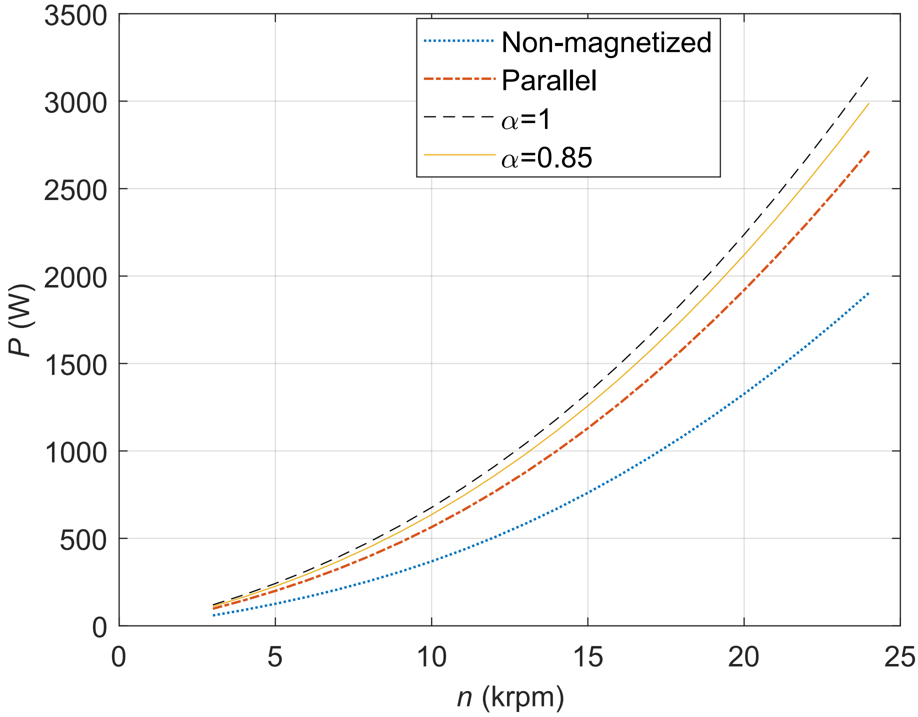

Fig. 2.17: Total no-load losses of different rotors (welded stator, 0 MPa)

2.6.5 Temperature effect on test accuracy

The total no-load losses measured by the retardation method include: stator iron losses, iron losses in the magnetic bearing rotor, and air friction losses. Temperature will affect these losses in the following ways: (a) the eddy current losses coefficient depends on temperature; (b) B_r decreases with temperature increase; (c) both density and viscosity of air vary with temperature. In this chapter, a number of controlled experiments have been carried out to obtain the effects of several manufacturing factors on stator iron losses. The assumption is that the total no-load loss difference between controlled experiments equals the stator iron loss difference. This assumption is only true when the temperature of the motor is the same in all tests.

In order to study the influence of temperature on the test accuracy, the no-load losses at three different temperatures were tested, and each temperature was repeated three times. At each time, the motor was driven to 24 krpm and maintained the speed until the winding temperature reaches the expected value, then coast-down. In this set of tests, the housing and stator are loose fit, so the iron losses will not be affected by radial pressure variation due to thermal expansion.

The test results in Fig. 2.18 show that temperature rise can significantly reduce the total no-load losses. At 24 krpm, the no-load loss difference between at 90°C and 20°C is 228 W, accounting for 18% of the stator iron losses of 1,243 W at 20°C. Taking the winding temperature rise as a reference, each K corresponds to 0.26% iron losses. In the following test, the winding temperature was kept within 26°C ± 3°C, so the error caused by temperature variation can be controlled within ± 1%.

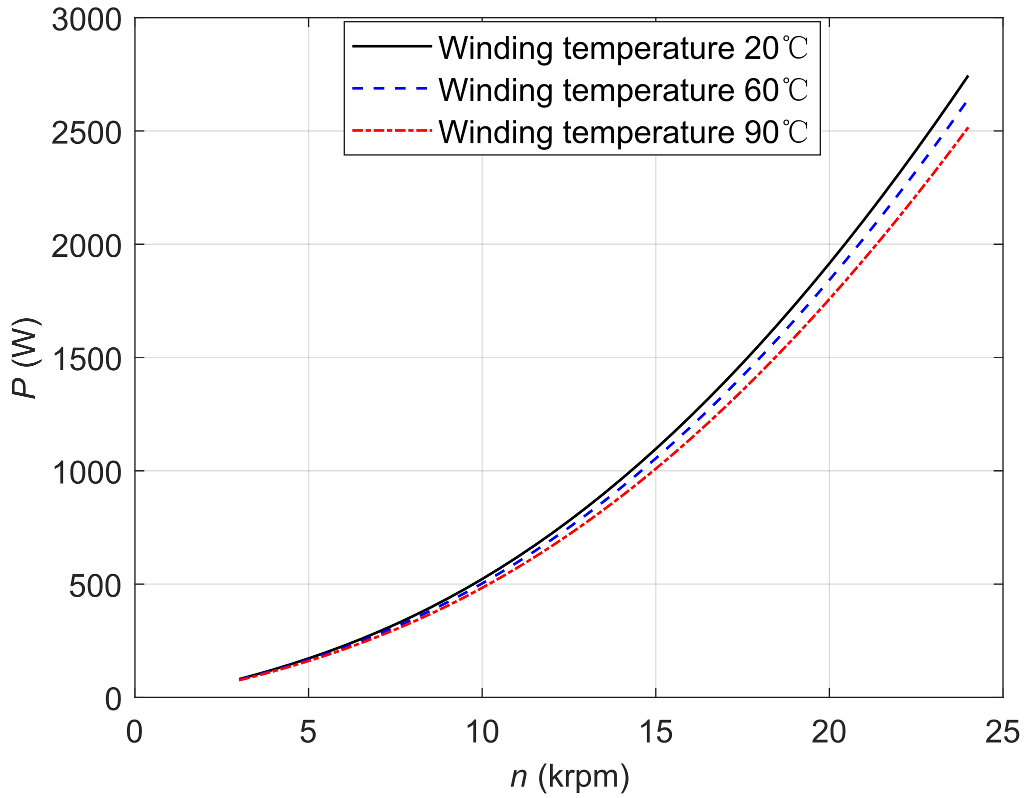

Fig. 2.18: Tested total no-load losses at different temperatures (α=1, welded stator, 0 MPa, without the small motor)

2.6.6 Effects of radial pressure and welding

The test results of Table 2.7 show that welding the stator with 12 lines increases the iron losses by 15% compared with the bonded stator, which is similar to the results reported in [32, 33].

Radial pressure significantly increases the iron losses by about 12% for 10 MPa and 24% for 30 MPa. So it is necessary to reduce the allowance of interference fit between the housing and stator when the torque transfer is satisfied. To study whether the influence of stress on iron losses is recoverable, the test sequence is 0 MPa, 10 MPa, 30 MPa, and 0 MPa. The results show that the influence of radial pressure below 30 MPa on the iron loss characteristics of the silicon steel sheet is recoverable.

It is worth noting that for α=0.85, if all manufacturing factors are ignored, the experimental iron losses of the welded stator (30 MPa) will be near twice the calculated basic iron losses.

Table 2.7: Effects of radial pressure and welding (α=0.85)

Stator type	Iron losses	Stator type	Iron losses
Bonded, 0 MPa	827.6 W	Welded, 10 MPa	1,111 W
Welded, 0 MPa	990.8 W	Welded, 30 MPa	1,225 W

2.6.7 Verification of iron losses including the punching and burrs' connection effects

Fig. 2.19 shows that for the three different magnetized rotors, the measured and the calculated iron losses are in good agreement from 3 krpm to 24 krpm, which proves that the calculation method of iron losses can cover a wide frequency band and is effective for both sinusoidal and non-sinusoidal magnetic fields. There is no further separation of the basic iron losses and the additional iron losses because the additional iron losses due to burrs' connection still remain even though annealing can relieve the additional iron losses caused by punching deterioration.

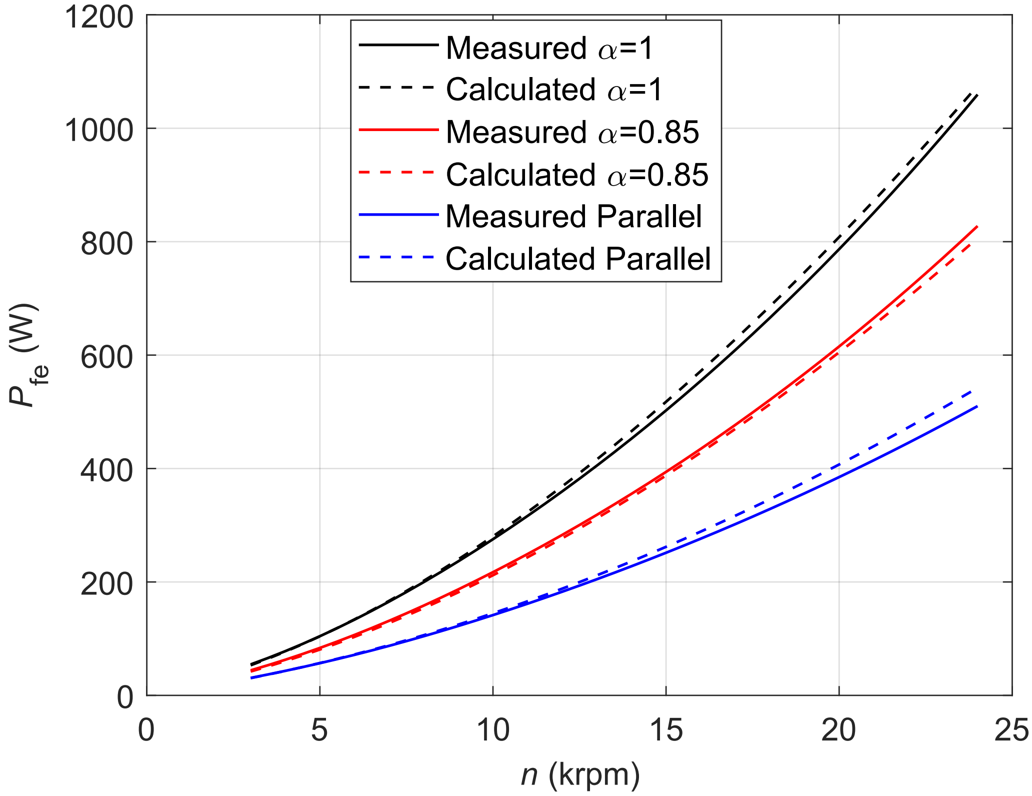

Fig. 2.19: Comparison of calculated and measured iron losses including the punching and burrs' connection effects (bonded stator, 0 MPa)

2.7 Summary

(1) The high-frequency iron loss model proposed in [41] was used to calculate the iron losses of a high-speed permanent magnet motor, considering the rotational and harmonic effects as well as the punching and burrs' connection effects. The calculated iron losses agree well with the measured results, which verifies the proposed method.

(2) Temperature rise obviously influences the total no-load losses, so temperature stability is crucial for iron loss separation.

(3) The radial magnetization of α=0.85 is the best choice of the three magnetizations for the high-speed SPM motor from the point of view of iron losses and output power capacity.

(4) In this work, the punching and burrs' connections, welding, and radial pressure significantly increase the iron losses by about 27%, 15%, and 24%, respectively. Ignoring the influence of machining factors, the real iron losses will be much higher than the predicted values. It is useful to reduce iron losses by optimizing the manufacturing process.

3 Air Friction Losses Calculation and Experimental Verification

3.1 Introduction

Air friction losses, which increase approximately proportional to n^3 [45], become significant and should not be neglected in high-speed motors [1, 20]. Accurate calculation of air friction losses is essential for high-speed motors design. Compared with the CFD, the analytical calculation method is time-saving while giving a satisfactory accuracy [45]. In [45], the air friction losses of a high-speed induction motor were calculated by an analytical calculation method, which was verified by the friction loss difference between R134a and air. However, the method needs non-air media, which is complex, and the induction motor has no stator iron losses after power off. On the other hand, the temperature rise has a noticeable influence on the permanent magnet motors' iron losses, introducing an obvious error when friction losses shall be identified by loss separation. In [20], it was assumed that the iron losses are proportional to $n^{1.531}$, and the air friction losses are proportional to $n^{2.576}$ according to the calculated results, then the iron losses and air friction losses were separated by fitting the total no-load losses determined by retardation test, and finally the calculated results were verified by the separated air friction losses. This method is based on a circular argument and is not logically rigorous.

In this chapter, the air friction losses of a high-speed permanent magnet motor supported by active magnetic bearings were first calculated using the analytical method. Next, the air friction loss differences under different air pressure values were tested by the retardation method in a vacuum chamber. Finally, the air friction coefficient was obtained. Due to the poor heat dissipation in the vacuum chamber, the temperature rise of the stator core results in a significant reduction of iron losses, affecting the accuracy of air friction losses determination. To solve this problem, a new test method for permanent magnet motors is proposed, which effectively compensates for the influence of temperature rise on the iron losses and improves the accuracy of air friction loss determination. The air friction losses with different air gap lengths were studied by experimental methods.

3.2 Calculation of air friction losses

3.2.1 Nature of the gas flow

3.2.1.1 Reynolds number

The Reynolds number, the ratio of inertial and viscous forces, determines the flow patterns. The nature of circumferential gas flow in the air gap can be described by the Reynolds number for Taylor Couette flow [46]:

$$Re_\delta = \rho \cdot u_1 \cdot \delta / \mu \tag{3.1}$$

where ρ is the fluid density, u_1 the circumferential speed of the rotor, δ the air gap length, and μ the dynamic viscosity of the fluid.

When a cylinder rotates in free space, the Reynolds number for rotating flow is:

$$Re_\mathrm{r} = \rho \cdot u_1 \cdot r / \mu \tag{3.2}$$

where r is the radius of the cylinder.

3.2.1.2 Gas properties

The dynamic viscosity of the gas is significantly related to temperature, but it is almost irrelevant to the pressure. When the temperature is below 1673 K, the dynamic viscosity of the gas can be calculated by Sutherland's law [47]:

$$\mu = \mu_0 \cdot \left(\frac{T}{T_0}\right)^{1.5} \cdot \frac{T_0 + S}{T + S} \tag{3.3}$$

and the gas density can be calculated according to the ideal gas state equation:

$$\rho = \rho_0 \cdot \frac{p}{p_0} \cdot \frac{T_0}{T} \tag{3.4}$$

where T is the static temperature of the gas in K, p the absolute pressure of the gas in Pa, S is called as Sutherland constant with S=113 K for air. The reference values for air at T_0=273.15 K are as follows [48]: p_0=101.32 kPa, $\mu_0 = 1.72 \cdot 10^{-5}$ Pa · s, $\rho_0 = 1.293$ kg/m^3.

Now the dynamic viscosity and density of the air at a given temperature and pressure can be determined according to (3.3) and (3.4).

3.2.2 Cylinders rotating

The air friction losses P_f for a rotating cylinder follow the equation [49]:

$$P_\mathrm{f} = k_\mathrm{f} \cdot C_\mathrm{f} \cdot \pi \cdot \rho \cdot \omega^3 \cdot r^4 \cdot l \tag{3.5}$$

where C_f is the air friction coefficient depending on the dimensions and the Reynolds number, ω the angular speed of rotor, l the length of cylinder, r the rotor radius, and k_f the roughness coefficient, which is expected to be constant at different rotation speeds [45]. It is 1 for smooth surfaces and 2–4 for rough surface [50].

Depending on the flow conditions and the proximity of local geometry, there are three distinguished flow configurations for the rotating rotor in an internal rotor motor:

(1) Rotating cylinder in free space, such as the drive end.

(2) Concentric cylinders with inner cylinder rotation, such as the rotor rotating in the air gap.

(3) Concentric cylinders with inner cylinder rotation and axial throughflow.

3.2.2.1 Rotating cylinder in free space

For cylinder rotating in free space, the friction coefficients are [50]:

$$C_\mathrm{f} = 4 \cdot Re_\mathrm{r}^{-1}, \quad Re_\mathrm{r} \leq 170 \tag{3.6}$$

$$\frac{1}{\sqrt{C_\mathrm{f}}} = -0.6 + 4.07 \cdot \log_{10}\left(Re_\mathrm{r} \cdot \sqrt{C_\mathrm{f}}\right), \quad Re_\mathrm{r} > 170 \tag{3.7}$$

3.2.2.2 Concentric cylinders with inner cylinder rotation

Depending on the Reynolds number and dimensionless gap length, three regimes can be distinguished as in Table 3.1.

Table 3.1: C_f for concentric cylinders with inner cylinder rotation [46]

	Laminar	Transition		Turbulent	
Re_δ	<64	64–500		500–10^4	>10^4
δ/r	-	<0.07	>0.07	-	-
C_f	$5 \cdot \frac{\left(\frac{\delta}{r}\right)^{0.3}}{Re_\delta}$	$\frac{\left(2+\frac{\delta}{r}\right)\cdot\left[1+D_1\cdot\left(1-\frac{Ta_c^2}{Ta^2}\right)\right]}{Re_\delta}$	$\frac{\left(\frac{\delta}{r}\right)^{0.3}}{Re_\delta^{0.6}}$	$0.515 \cdot \frac{\left(\frac{\delta}{r}\right)^{0.3}}{Re_\delta^{0.5}}$	$0.0325 \cdot \frac{\left(\frac{\delta}{r}\right)^{0.3}}{Re_\delta^{0.2}}$

where $D_1 = 1.4472$ is a constant. Taylor number is defined as:

$$Ta = Re_\delta \cdot \sqrt{\delta/r} \tag{3.8}$$

where Ta_{c} is the critical Taylor number, and viscous instabilities start from $Ta > Ta_{\mathrm{c}} = 41.3$ [46].

Because the high-speed machines mostly run in $Re_{\delta} > 10^4$, substituting C_{f} into (3.5), the following practical equation can be obtained:

$$P_{\mathrm{f}} = 0.0325 \cdot \pi \cdot k_{\mathrm{f}} \cdot \mu^{0.2} \rho^{0.8} \cdot \delta^{0.1} \cdot \omega^{2.8} \cdot r^{3.5} \cdot l, \quad Re_{\delta} > 10^4 \tag{3.9}$$

However, in some vacuum applications, such as the flywheel energy storage, the Reynolds number will fall into the non-turbulent regimes.

3.2.2.3 Concentric cylinders with axial flow

When an axial cooling gas passes through the air gap, additional torque is needed to accelerate the gas circumferentially. The additional air friction losses caused by axial flow are [51]:

$$P_{\mathrm{axial}} = \frac{2}{3} \cdot \pi \cdot \rho \cdot \left[(r + \delta)^3 - r^3 \right] \cdot v_{\mathrm{a}} \cdot u_{\mathrm{c}} \cdot \omega \tag{3.10}$$

$$u_{\mathrm{c}} = k_2 \cdot \omega \cdot r \tag{3.11}$$

where v_{a} and u_{c} are the average axial and circumferential fluid velocities, respectively.

In [51], k_2 is assumed to be 0.48. However, in [45], k_2 is determined experimentally. It is 0.15 when slots are open and 0.18 when the slots are filled. Both values are quite different from the value of 0.48.

3.2.3 Disk rotating

For a rotating disk, the air friction losses of both sides are calculated as [49]:

$$P_{\mathrm{f}} = 0.5 \cdot C_{\mathrm{f}} \cdot \rho \cdot \omega^3 \cdot \left(r_2^5 - r_1^5 \right) \tag{3.12}$$

where r_1 and r_2 are the inner and outer radii of the disk, respectively.

3.2.3.1 Rotating disk in free space

The air friction coefficients for a free disk are [50]:

$$C_{\mathrm{f}} = 3.87 \cdot Re_{\mathrm{r}}^{-0.5}, \quad \mathrm{Re}_{\mathrm{r}} \leq 3 \cdot 10^5 \tag{3.13}$$

$$C_{\mathrm{f}} = 0.146 \cdot Re_{r}^{-0.2}, \quad \mathrm{Re}_{\mathrm{r}} > 3 \cdot 10^5 \tag{3.14}$$

3.2.3.2 Rotating disk in an enclosure

When a disk rotates in an enclosure (see Fig. 3.1), the friction coefficient depends on the Reynolds number and space ratio s/r_2 [52]. Four flow regimes are classified and the friction coefficients are listed in Table 3.2:

Table 3.2: C_f for enclosed rotating disks [52]

Regime	I	II	III	IV
Flow mode	Laminar, merged boundary layers	Laminar, separate boundary layers	Turbulent, merged boundary layers	Turbulent, separate boundary layers
C_f	$\frac{2\pi}{(s/r_2)\cdot Re_\mathrm{r}}$	$\frac{3.7\cdot(s/r_2)^{0.1}}{Re_\mathrm{r}^{0.5}}$	$\frac{0.08}{(s/r_2)^{0.167}\cdot Re_\mathrm{r}^{0.25}}$	$\frac{0.0102\cdot(s/r_2)^{0.1}}{Re_\mathrm{r}^{0.2}}$

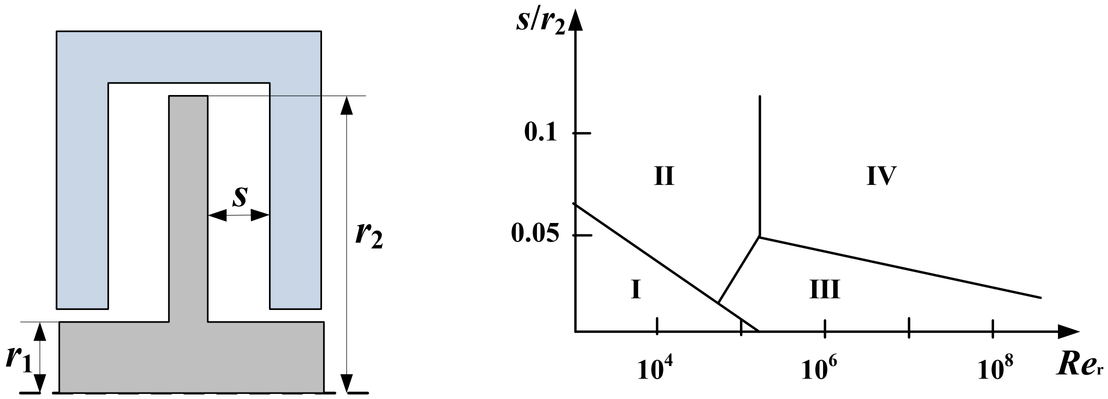

(a) Geometric sketch (b) Regimes approximate classification

Fig. 3.1: Rotating disk in an enclosure [45]

For axial magnetic bearings typically with a very small space ratio and large Reynolds number, it mainly runs in the regime III.

3.3 Experimental scheme

3.3.1 Experimental method

3.3.1.1 Air friction losses without axial flow

Due to the performance limitation of vacuum pumps, an absolute vacuum cannot be obtained. So the air friction loss differences under different pressure are used to verify the calculation results.

The motor under test is the air-water cooled high-speed permanent magnet motor (welded stator, radial pressure=0 MPa, α=1) from Chapter 2. As shown in Fig. 3.2, the motor is placed in a closed chamber. A vacuum was created by a vacuum pump.

Alternatively, an overpressure was produced by compressed air. The absolute pressure range in the chamber is 0.4–376 kPa. The minimum pressure is limited by the vacuum pump's performance, and the maximum pressure is limited by the deformation of the chamber. A vacuum gauge is used to measure the underpressure, while a positive pressure gauge is used to measure the overpressure. They will be switched, depending on the inner pressure. The absolute environmental pressure is measured by a barometer.

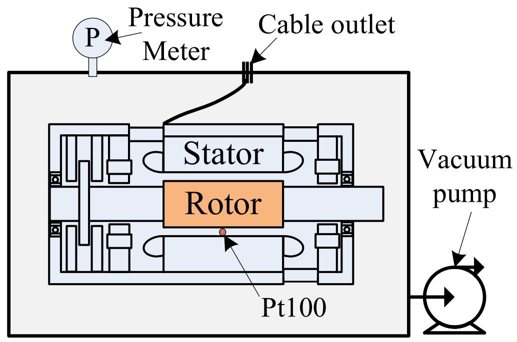

(a) Diagram

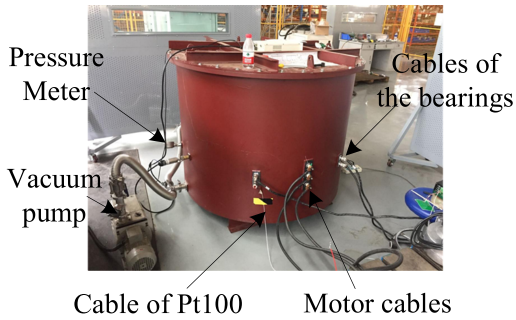

(b) Experimental setup

Fig. 3.2: Experiment of air friction losses without axial flow

Two glass fiber sleeves were produced, 1 mm thick and 2 mm thick, respectively, to study the influence of slot openings and different air gap lengths on air friction losses. The slot opening dimensions and the air gap length are shown in Fig. 3.3(a). For ease of installation and removal, the total length of the sleeves is 200 mm, slightly longer than the stator with 165 mm. The sleeves were divided into two parts, and two Pt100 elements were placed in the axial and radial centers of the air gap supported by plastic brackets, as shown in Fig. 3.3(b), to measure the air temperature in the air gap. The plastic brackets can effectively isolate the heat transfer between the sensors and the stator core.

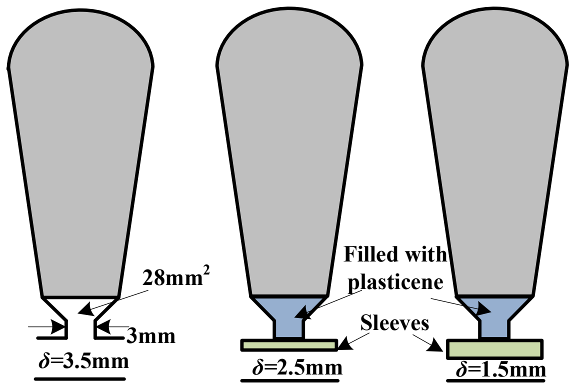

(a) Slot opening dimensions

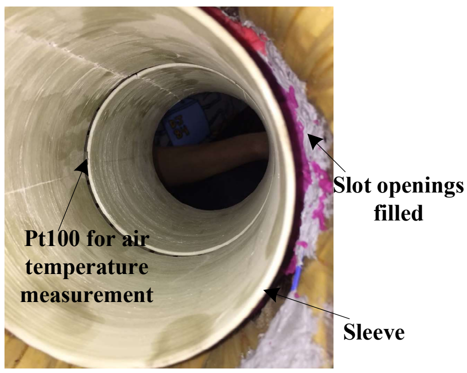

(b) Sleeve assembly

Fig. 3.3: Sleeves used to adjust the air gap length

Under different absolute pressure, retardation tests were carried out to get the total no-load losses vs. speed curves. Assuming the iron losses and the bearing losses remaining constant for all tests, the total no-load loss difference between tests is the air friction loss difference. However, due to the poor heat dissipation in the vacuum chamber, the temperature rise will reduce iron and bearing losses, resulting in systematic errors. How to compensate for these errors will be discussed later.

3.3.1.2 Air friction losses with axial flow

As shown in Fig. 3.4, all other motor outlets are blocked by tapes, leaving only one inlet and two outlets to ensure that all air passes only through the motor air gap. The flow rate of the inlet was measured and divided by the cross-section area of the air gap to get the axial velocity of flow in the air gap. A speed adjustable blower was used to adjust the airflow rate. After installing the sleeve, as shown in Fig. 3.3(b), the slot openings are blocked by the plasticine to ensure that all flow passes through the air gap. As this test is carried out outside the chamber, it is easy to cool the motor and control the temperature of the stator winding at 40°C before each retardation to relieve the effect of temperature rise on iron losses. When the inverter drives the motor to 24 krpm, the motor's input power is measured by a power analyzer with a sampling period of 1 s. Then an average value of 20 points is taken, which is used to compare it with the results of the retardation method. Last, the retardation test is carried out, and the starting and ending air gap temperature are recorded. Each test has been repeated three times to take the average to reduce the random error.

Table A6 in the Appendix lists the range, accuracy, and function of the instruments.

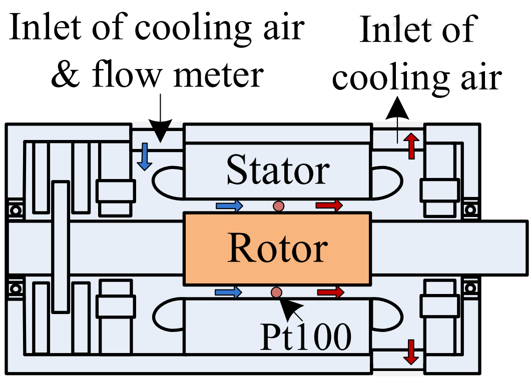

(a) Diagram

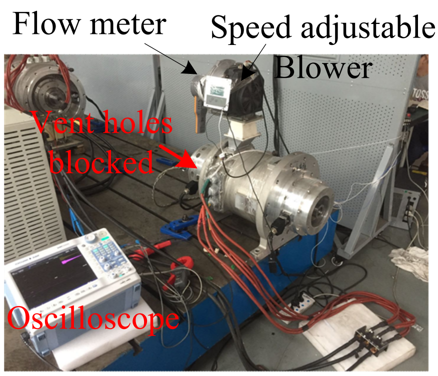

(b) Experimental setup

Fig. 3.4: Experiment of air friction losses with axial flow

3.3.2 Compensation method for systematic errors

3.3.2.1 Systematic errors analysis

As shown in Table 3.3, the calculated friction losses at 0.4 kPa are still 1/10 of the calculated value at 100 kPa. The reason is that the rotor will fall into the non-turbulent regime at 0.4 kPa (see Table 3.3) and the corresponding friction coefficient is very large, according to Table 3.1. So in this dissertation, the air friction loss difference under different pressure is used to verify the calculated results.

Table 3.3: Experimental conditions of without axial flow (Meas.: Measured, Calc.: Calculated)

No	p (kPa)	T_δ (°C)	μ (Pa·s)	ρ (kg/m^3)	Re_δ	Re_r (disk)	P'_f (kW)
	Meas.	Meas.	Calc.	Calc.	Calc.	Calc.	Calc.
1	100.2	40.2	$1.91{\cdot}10^{-5}$	1.115	$2.70{\cdot}10^{4}$	$7.72{\cdot}10^{5}$	0.625
2	0.4	40.8	$1.91{\cdot}10^{-5}$	0.004	$1.00{\cdot}10^{2}$	$3.10{\cdot}10^{3}$	0.060
3	19.7	53.6	$1.97{\cdot}10^{-5}$	0.210	$0.49{\cdot}10^{4}$	$1.41{\cdot}10^{5}$	0.200
4	49.6	65.2	$2.02{\cdot}10^{-5}$	0.511	$1.16{\cdot}10^{4}$	$3.34{\cdot}10^{5}$	0.358
5	79.5	75.4	$2.07{\cdot}10^{-5}$	0.795	$1.78{\cdot}10^{4}$	$5.08{\cdot}10^{5}$	0.499
6	100.2	79.7	$2.09{\cdot}10^{-5}$	0.989	$2.19{\cdot}10^{4}$	$6.26{\cdot}10^{5}$	0.587
7	205.2	89.0	$2.13{\cdot}10^{-5}$	1.974	$4.29{\cdot}10^{4}$	$1.23{\cdot}10^{6}$	0.980
8	376.2	81.1	$2.09{\cdot}10^{-5}$	3.700	$8.17{\cdot}10^{4}$	$2.34{\cdot}10^{6}$	1.559

The total no-load losses determined by the retardation method include air friction losses, stator iron losses P_fe, and the iron losses in the rotor of the magnetic bearings $P_\mathrm{bearing,r}$:

$$P_\mathrm{t}(p) = P_\mathrm{f}(p) + P_\mathrm{fe} + P_\mathrm{bearing,r} \tag{3.15}$$

where $P_\mathrm{t}(p)$ and $P_\mathrm{f}(p)$ are the total no-load losses and air friction losses at absolute pressure p, respectively. The schematic diagram of the radial magnetic bearing is shown in Fig. 3.5. The rotor steel laminations rotate in the spatial static magnetic field created by the stator of the magnetic bearing, thus producing iron losses.

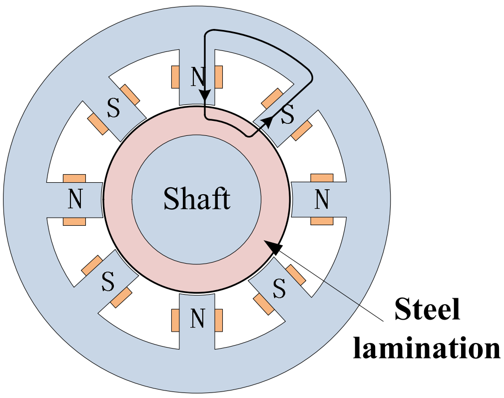

Fig. 3.5: Diagram of a radial magnetic bearing

The total loss difference between tests under an arbitrary pressure p and 0.4 kPa is:

$$\Delta P_\mathrm{t} = P_\mathrm{t}(p) - P_\mathrm{t}(0.4\,\mathrm{kPa}) = P_\mathrm{f}(p) - P_\mathrm{f}(0.4\,\mathrm{kPa}) = \Delta P_\mathrm{f} \tag{3.16}$$

Fig. 3.6 shows the measured air friction loss difference ΔP_f varying approximately linearly with the pressure difference Δp, which can be explained by (3.5) and (3.4).

According to (3.5), the following formula can be obtained:

$$P_\mathrm{f}(p) = k_\mathrm{f} \cdot P'_\mathrm{f}(p) \tag{3.17}$$

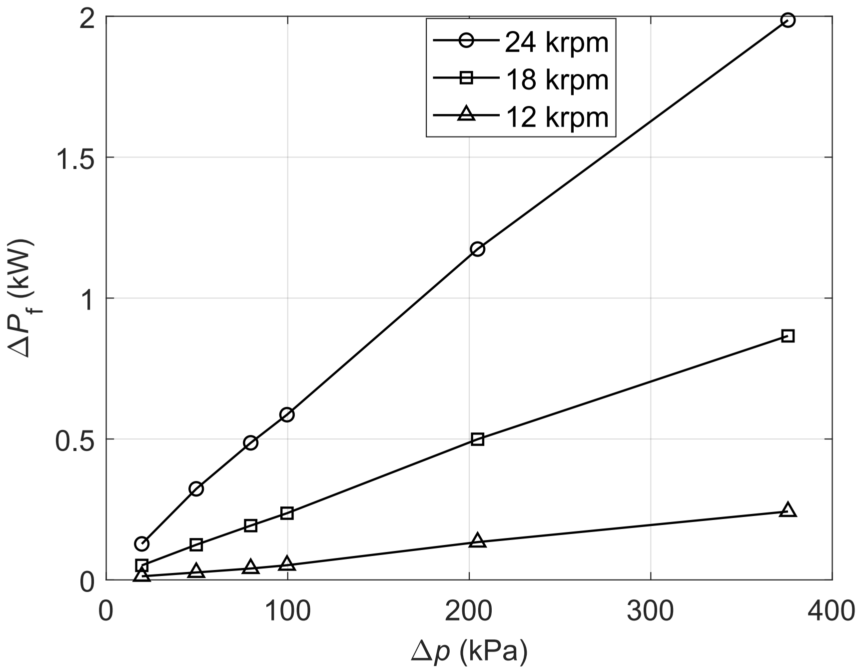

Fig. 3.6: Measured ΔP_{f} vs. Δp

where $P'_{\mathrm{f}}(p)$ are the calculated air friction losses with $k_{\mathrm{f}} = 1$.

Combining (3.16) and (3.17), the actual roughness coefficient can be derived:

$$k_{\mathrm{f}} = \frac{P_{\mathrm{t}}(p) - P_{\mathrm{t}}(0.4\,\mathrm{kPa})}{P'_{\mathrm{f}}(p) - P'_{\mathrm{f}}(0.4\,\mathrm{kPa})} \tag{3.18}$$

Since the vacuum chamber hardly dissipates heat, the stator and rotor temperatures will increase during each retardation test. Equation (3.16) has been established on the premise that P_{fe} and $P_{\mathrm{bearing,r}}$ are constant. However, Fig. 3.7 shows the measured total loss difference in the cold (see case no.1 in Table 3.3) and hot state (see case no.6 in Table 3.3) at 100.2 kPa, 24 krpm is 132 W, about 20% of the calculated air friction losses. The measured total loss difference is far larger than the calculated air friction loss difference, so an apparent systematic error will occur if the temperature rise effect is ignored.

The effect of temperature rise on losses is as follows:

(1) Temperature affects the air viscosity and density, thus air friction losses. Since there are Pt100 sensors in the air gap, this effect can be considered in the calculation of air friction losses, as shown in Fig. 3.7.

(2) The temperature rise will cause the magnetic remanence of the magnets to decrease and reduce the iron losses. These iron losses' variation can be corrected by the back EMF coefficient.

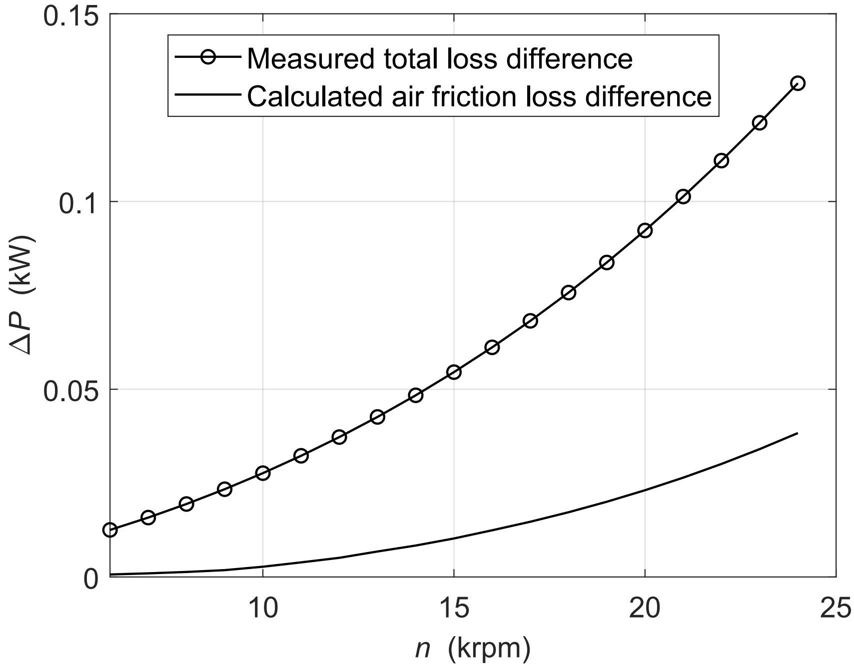

Fig. 3.7: Loss differences due to temperature rise vs. rotational speed

(3) The temperature rise causes the silicon steel's conductivity to decrease, thereby significantly reducing the eddy current losses. Although it can be compensated by measuring the temperatures of the stator and the magnetic bearing rotor, the exact temperatures of the stator core and the magnetic bearing rotor are not easily obtained. Moreover, even if the exact temperatures were obtained, the surface of silicon steel laminations in the rotor is connected due to machining. The accurate eddy current losses are difficult to calculate [53].

3.3.2.2 Compensation method

When the pressure in the vacuum chamber rises, the heat dissipation capability becomes better. It can be seen from Table 3.3 that after the air gap temperature reaches 80°C, the temperature rise saturates, implying the heat dissipation and losses tend to be balanced. Therefore, the loss difference between the cold state and the hot state under normal pressure can be used to compensate for the systematic errors.

For the convenience of description, P_{fe} and $P_{\text{bearing,r}}$ are combined into P_{feb}:

$$P_{\text{feb}} = P_{\text{fe}} + P_{\text{bearing,r}} \tag{3.19}$$

$P_{\text{feb}}\,(\text{C})$ and $P_{\text{feb}}\,(\text{H})$ are defined as the losses at around 40°C and 80°C, respectively.

For the 1st case in Table 3.3, the total losses can be expressed as:

$$P_{\text{t}}(100.2\,\text{kPa}, 40°\text{C}) = P_{\text{f}}(100.2\,\text{kPa}, 40°\text{C}) + P_{\text{feb}}\,(\text{C}) \tag{3.20}$$

For the 6th case in Table 3.3, the total losses can be expressed as:

$$P_{\mathrm{t}}(100.2\,\mathrm{kPa}, 80°\mathrm{C}) = P_{\mathrm{f}}(100.2\,\mathrm{kPa}, 80°\mathrm{C}) + P_{\mathrm{feb}}\,(\mathrm{H}) \tag{3.21}$$

The difference between (3.20) and (3.21) renders:

$$\begin{gathered}[P_{\mathrm{feb}}\,(\mathrm{H}) - P_{\mathrm{feb}}\,(\mathrm{C})] \\ = [P_{\mathrm{t}}(100.2\,\mathrm{kPa}, 80°\mathrm{C}) - P_{\mathrm{t}}(100.2\,\mathrm{kPa}, 40°\mathrm{C})] - [P_{\mathrm{f}}(100.2\,\mathrm{kPa}, 80°\mathrm{C}) - P_{\mathrm{f}}(100.2\,\mathrm{kPa}, 40°\mathrm{C})]\end{gathered} \tag{3.22}$$

The larger the air friction losses are, the smaller the relative error caused by the variation of iron losses is. Therefore 80 kPa, 100 kPa, 205 kPa, and 376 kPa in Table 3.3 were selected as the analysis objects. So the total losses at air gap temperature T_δ and pressure p minus the total losses at temperature 40°C and pressure 0.4 kPa is:

$$[P_{\mathrm{t}}(p, T_\delta) - P_{\mathrm{t}}(0.4\,\mathrm{kPa}, 40°\mathrm{C})] = [P_{\mathrm{f}}(p, T_\delta) - P_{\mathrm{f}}(0.4\,\mathrm{kPa}, 40°\mathrm{C})] + [P_{\mathrm{feb}}\,(\mathrm{H}) - P_{\mathrm{feb}}\,(\mathrm{C})] \tag{3.23}$$

substitute $[P_{\mathrm{feb}}\,(\mathrm{H}) - P_{\mathrm{feb}}\,(\mathrm{C})]$ with (3.22) gives:

$$\begin{aligned}&[P_{\mathrm{t}}(p, T_\delta) - P_{\mathrm{t}}(0.4\,\mathrm{kPa}, 40°\mathrm{C})] + [P_{\mathrm{t}}(100.2\,\mathrm{kPa}, 40°\mathrm{C}) - P_{\mathrm{t}}(100.2\,\mathrm{kPa}, 80°\mathrm{C})] \\ &= [P_{\mathrm{f}}(p, T_\delta) - P_{\mathrm{f}}(0.4\,\mathrm{kPa}, 40°\mathrm{C})] + [P_{\mathrm{f}}(100.2\,\mathrm{kPa}, 40°\mathrm{C}) - P_{\mathrm{f}}(100.2\,\mathrm{kPa}, 80°\mathrm{C})]\end{aligned} \tag{3.24}$$

substitute P_{f} with (3.17), the roughness coefficient expression after systematic errors' compensation can be obtained:

$$k_{\mathrm{f}} = \frac{[P_{\mathrm{t}}(p, T_\delta) - P_{\mathrm{t}}(0.4\,\mathrm{kPa}, 40°\mathrm{C})] + [P_{\mathrm{t}}(100.2\,\mathrm{kPa}, 40°\mathrm{C}) - P_{\mathrm{t}}(100.2\,\mathrm{kPa}, 80°\mathrm{C})]}{[P'_{\mathrm{f}}(p, T_\delta) - P'_{\mathrm{f}}(0.4\,\mathrm{kPa}, 40°\mathrm{C})] + [P'_{\mathrm{f}}(100.2\,\mathrm{kPa}, 40°\mathrm{C}) - P'_{\mathrm{f}}(100.2\,\mathrm{kPa}, 80°\mathrm{C})]} \tag{3.25}$$

3.4 Evaluation of the experimental method

3.4.1 Air friction losses without axial flow

Table 3.3 lists the experimental conditions of air friction losses without axial flow. Test no.1 was carried out outside the chamber in a cold state. The rest of the tests ran in the chamber, and the air gap temperature T_δ went up gradually. Up from the no.6, T_δ began to stabilize around 80°C, which was defined as a hot state.

Fig. 3.8(a) shows the measured and calculated air friction loss differences varying with speed at different pressures. Fig. 3.9(a) shows the roughness coefficients calculated by (3.25) with compensation of temperature. The average roughness coefficient k_{f} for all pressures is 1.34, while the average roughness coefficient for 100 kPa alone is 1.28. As shown in Fig. 3.10(a), the measured values and the calculated values with the roughness coefficient agree well.

By comparison, Fig. 3.8(b), 3.9(b) and 3.10(b) show the results calculated by (3.18) without compensation of temperature. It can be seen that the results with systematic errors' compensation are more reasonable.

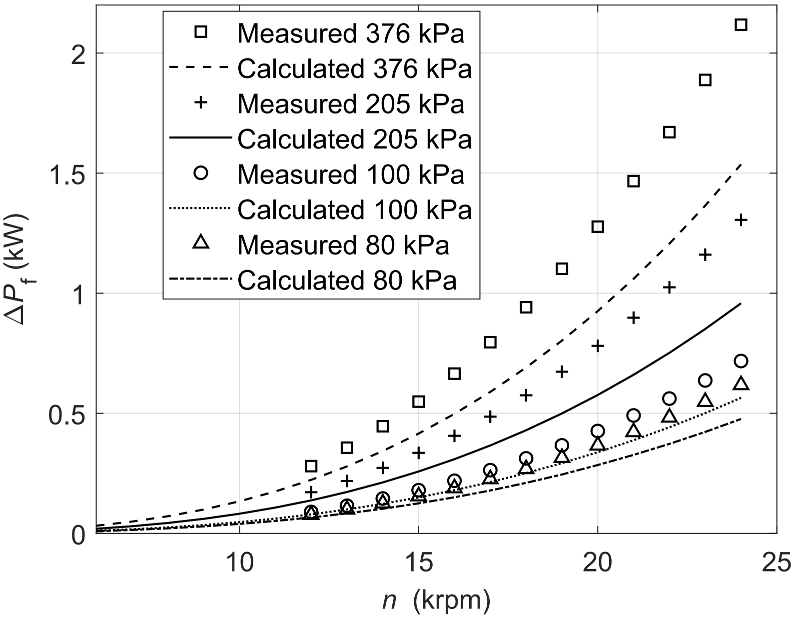

(a) With compensation of temperature

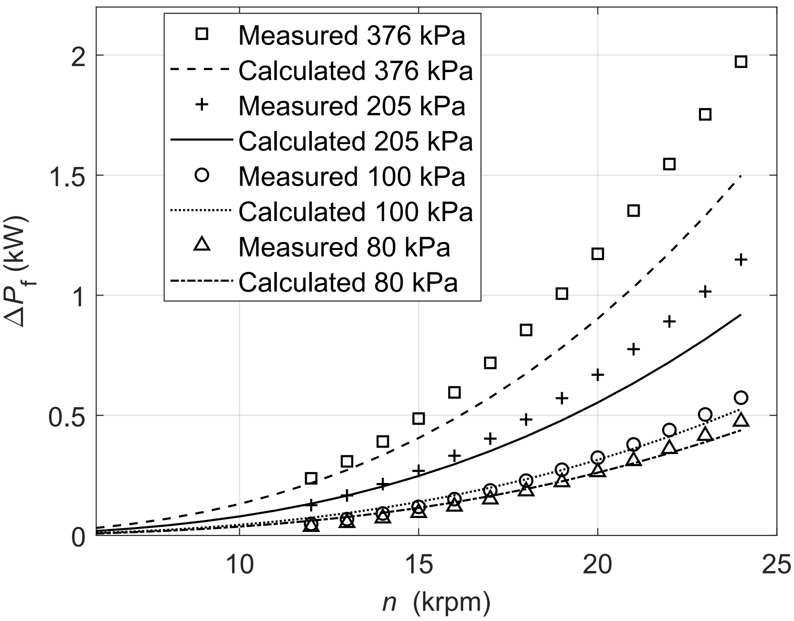

(b) Without compensation of temperature

Fig. 3.8: Measured and calculated ($k_\mathrm{f} = 1$) air friction loss differences

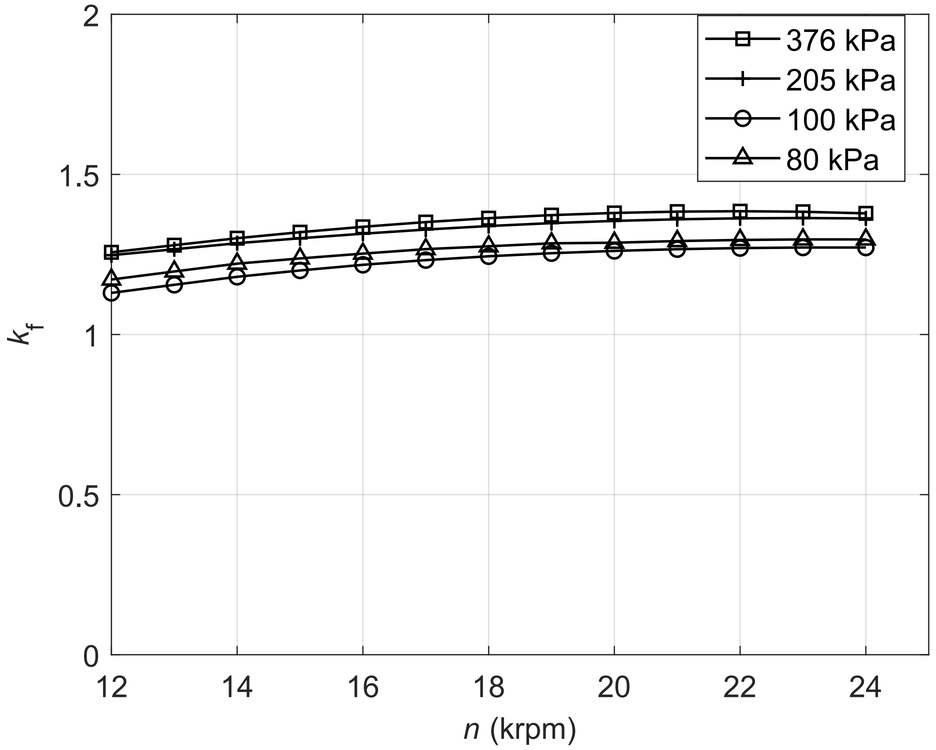

(a) With compensation of temperature

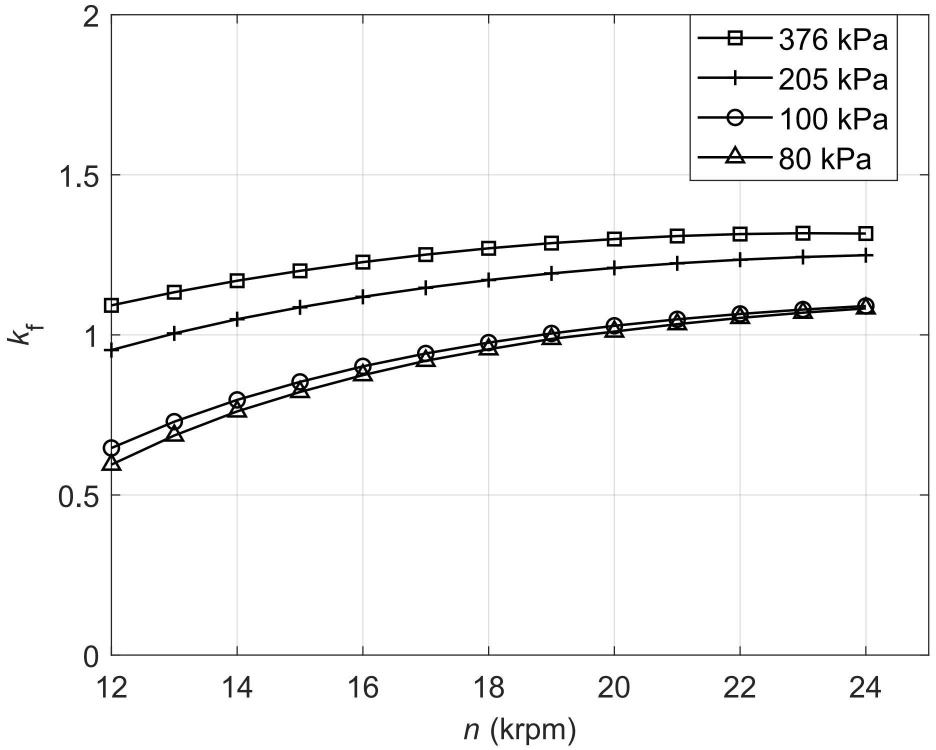

(b) Without compensation of temperature

Fig. 3.9: k_f identified from Fig. 3.8

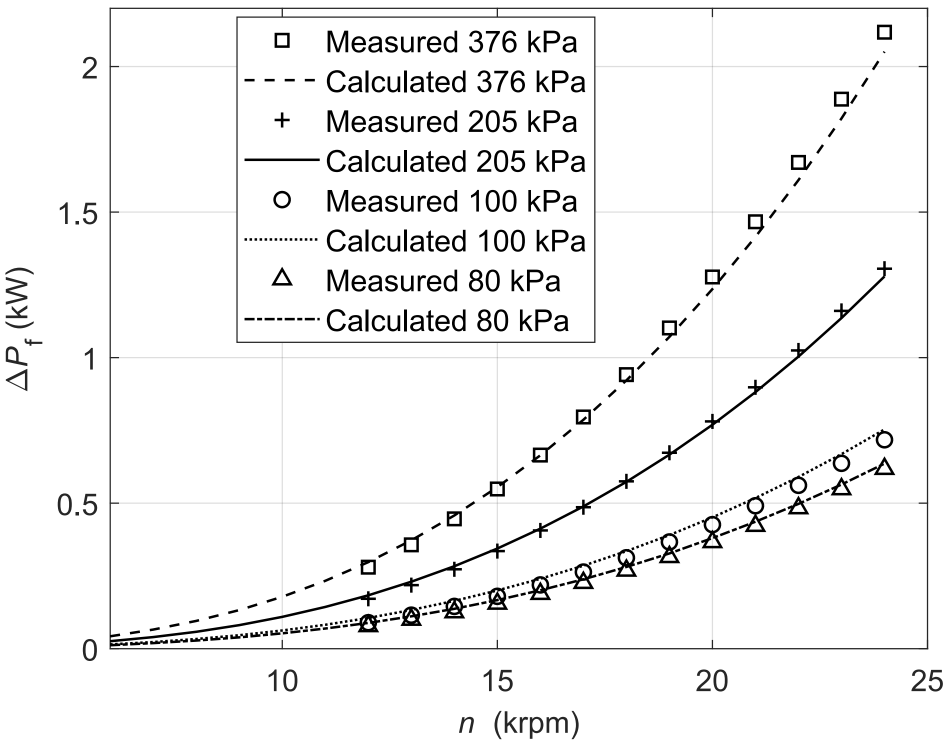

(a) With compensation of temperature

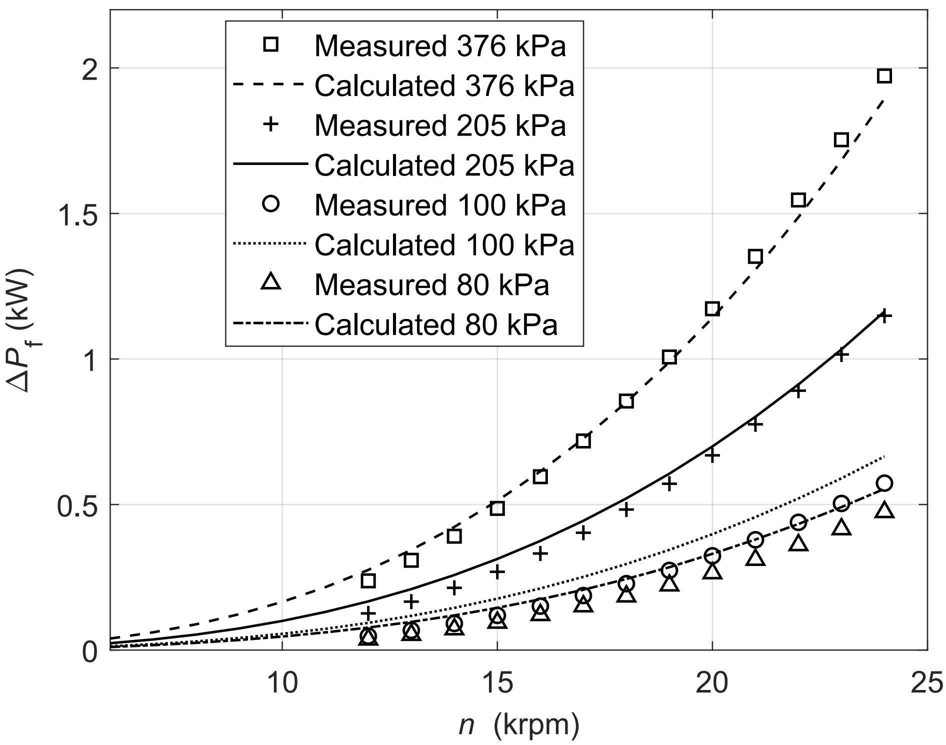

(b) Without compensation of temperature

Fig. 3.10: Measured and calculated (with the fitted k_f) air friction loss differences

Table 3.4 gives the calculated air friction losses of different parts in the rotor, as shown in Fig. A1 in the Appendix. It is worth noting that the air friction losses of the thrust disk, due to its larger diameter, account for a large portion of the total air friction losses.

Table 3.4: Calculated air friction losses of different parts at 24 krpm, 100 kPa, with $k_f = 1.28$

Air gap	End windings	Thrust disk	Radial bearings	The others	Total
168 W	101 W	206 W	94 W	229 W	798 W

* The others represent the axial space from end windings to radial magnetic bearings, and shaft ends.

Two sleeves with different thicknesses were installed and tested. Fig. 3.11 shows that the measured air friction losses decrease slightly as the air gap decreases, which is consistent with (3.9)—the air friction losses are proportional to $\delta^{0.1}$.

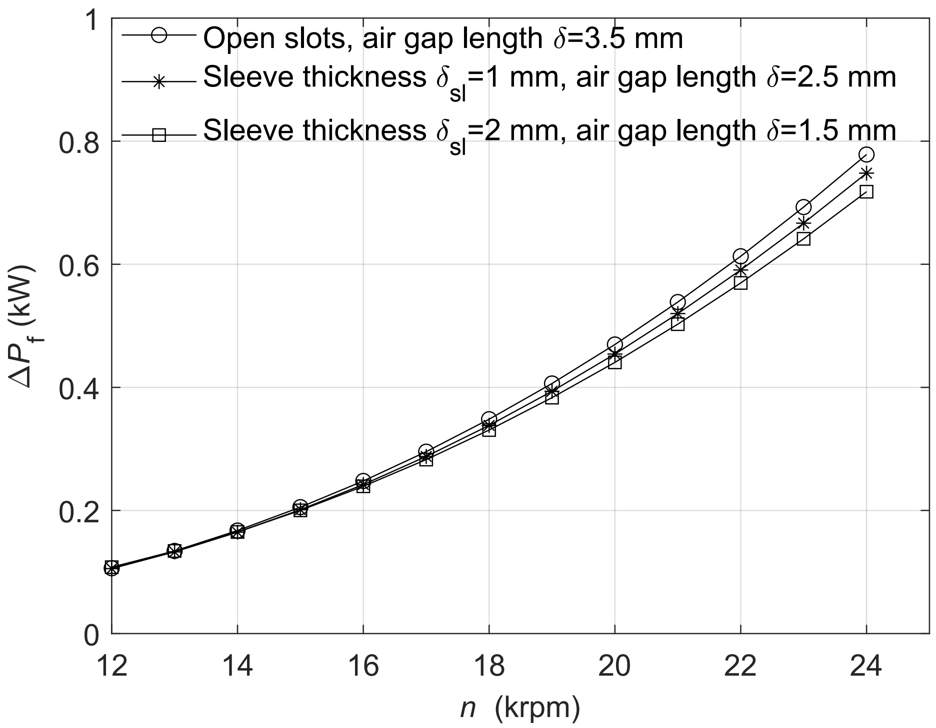

Fig. 3.11: Measured air friction losses with different air gap conditions (at 100 kPa)

Fig. 3.12 shows that for open slots $k_f = 1.28$, which is 4% larger than 1.23 for closed slots (with sleeve). As can be seen from Table 3.4, the friction losses of the air gap only account for 21% of the total friction losses, so it can be concluded that the friction coefficient with open slots would increase by 19% compared with closed slots. In [45], k_f is 1.25 for open slots while it is 1.13 for closed slots. Fig. 3.12 also shows that the air gap length has little effect on the roughness coefficient.

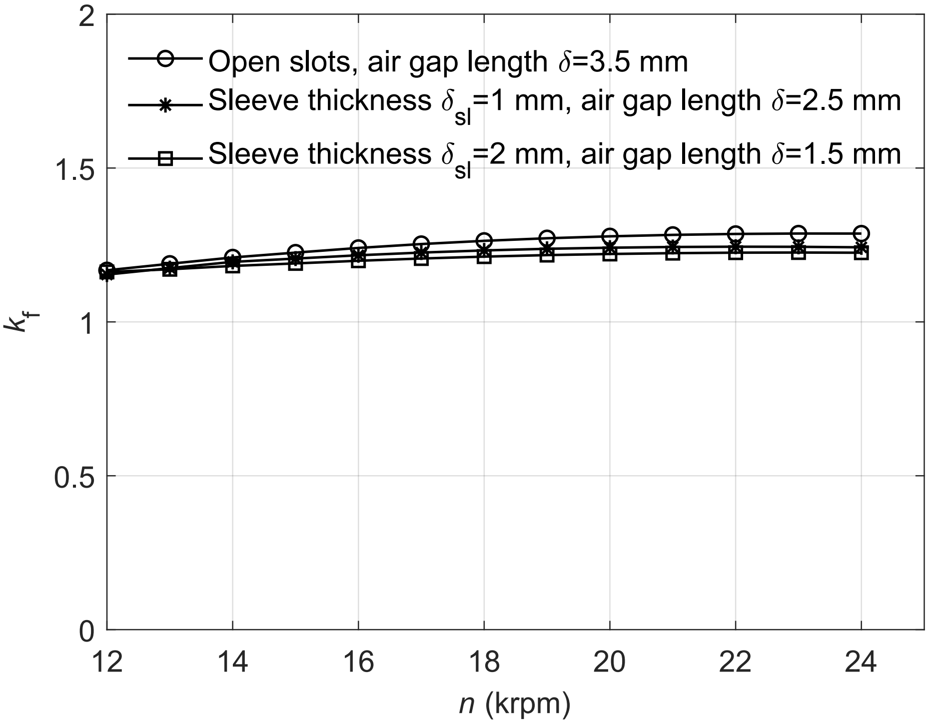

Fig. 3.12: k_{f} with different air gap conditions (at 100 kPa)

3.4.2 Separation of the no-load losses

In Chapter 2, the stator iron losses P_{fe} have been separated from the total no-load losses. In this chapter, the air friction losses P_{f} are separated from the remaining losses, so the rest of the losses are the iron losses in the rotor of magnetic bearings $P_{\mathrm{bearing,r}}$. Fig. 3.13 shows the separated three loss components (shown in markers) respectively.

Engineers need to know how these three losses vary with the rotation speed. The following power function of n is used to fit these three loss components through the least square deviation method:

$$P = C_1 \cdot n^D \tag{3.26}$$

where C_1 is a constant coefficient, D the exponent, P in kW, and n in krpm.

The fitted power coefficients are shown in Table 3.5.

Table 3.5: Fitted results of the power coefficients

	P_{fe}	P_{f}	$P_{\mathrm{bearing,r}}$
C_1	$1.25 \cdot 10^{-2}$	$9.16 \cdot 10^{-5}$	$2.26 \cdot 10^{-3}$
D	1.47	2.85	1.79

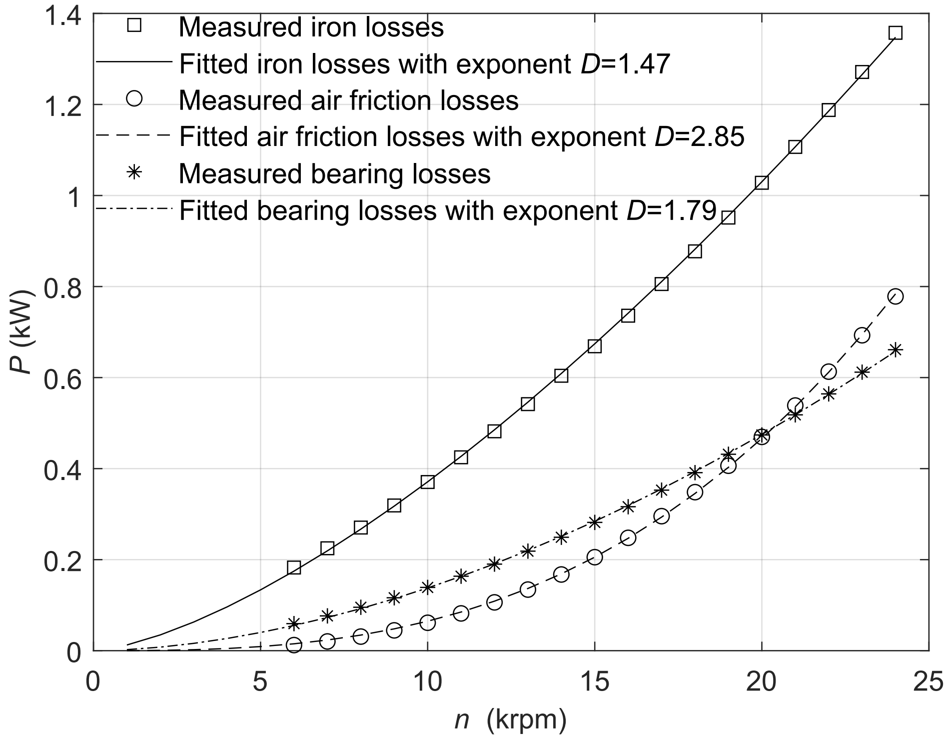

Fig. 3.13: Separation results of no-load losses

Fig. 3.13 shows the fitted curves (shown in lines). The exponent D of P_{f} is 2.85, which is slightly larger than the theoretical value 2.8 from (3.9). The air friction losses are approximately proportional to the cube of rotation speed, which means special attention should be paid to designing an ultra-high-speed motor. The exponent D of $P_{\mathrm{bearing,r}}$ is larger than that of P_{fe}, because the surface of the laminations in the magnetic bearing rotor is connected together after turning, which significantly increases the eddy current losses [53].

3.4.3 Air friction losses with axial flow

Combining (3.10) and (3.11) , the additional air friction losses caused by axial cooling gas can be expressed as:

$$P_{\mathrm{axial}} = \frac{2}{3} \cdot \pi \cdot \rho \cdot \left[(r+\delta)^3 - r^3\right] \cdot v_{\mathrm{a}} \cdot k_2 \cdot \omega^2 \cdot r \tag{3.27}$$

So the total air friction losses with axial flow can be written as:

$$P_{\mathrm{f}} = P_{\mathrm{f0}} + P_{\mathrm{axial}} \tag{3.28}$$

where P_{f0} is the air friction losses without axial flow.

Table 3.6, 3.7 and 3.8 show the experimental air friction losses with different axial fluid velocities v_{a} for open slots, sleeve thickness δ_{sl}=1 mm and sleeve thickness δ_{sl}=2 mm, respectively. P_{t1} represents the total no-load losses determined by retardation method. P_{t2} represents the measured total no-load input power of the motor driven by an inverter.

Table 3.6: Experimental air friction losses with axial flow (open slots)

v_{a} (m/s)	T_{δ} (°C)	12 krpm P_{f} (kW)	18 krpm P_{f} (kW)	24 krpm P_{f} (kW)	24 krpm P_{t1} (kW)	24 krpm P_{t2} (kW)
0	60	0.106	0.348	0.778	2.743	3.450
10.2	56	0.120	0.374	0.817	2.782	3.477
24.4	45	0.121	0.376	0.820	2.785	3.470
33.0	40	0.128	0.392	0.851	2.816	3.491

Table 3.7: Experimental air friction losses with axial flow (δ_{sl}=1 mm)

v_{a} (m/s)	T_{δ} (°C)	12 krpm P_{f} (kW)	18 krpm P_{f} (kW)	24 krpm P_{f} (kW)	24 krpm P_{t1} (kW)	24 krpm P_{t2} (kW)
0	66	0.105	0.338	0.748	2.713	3.422
14.6	63	0.115	0.355	0.771	2.736	3.440
27.3	55	0.125	0.377	0.806	2.771	3.477
43.2	50	0.136	0.401	0.853	2.818	3.528

Table 3.8: Experimental air friction losses with axial flow (δ_{sl}=2 mm)

v_{a} (m/s)	T_{δ} (°C)	12 krpm P_{f} (kW)	18 krpm P_{f} (kW)	24 krpm P_{f} (kW)	24 krpm P_{t1} (kW)	24 krpm P_{t2} (kW)
0	73	0.108	0.331	0.718	2.683	3.356
19.9	70	0.112	0.339	0.73	2.695	3.357
35.2	66	0.125	0.366	0.775	2.74	3.387
53.8	60	0.138	0.395	0.823	2.788	3.449

Fig. 3.14–3.16 show the experimental results on air friction losses (shown in markers) varying with the axial fluid velocity v_{a}, and the fitted results of k_2 for open slots, δ_{sl}=1 mm and δ_{sl}=2 mm, respectively. The fitted results are in good agreement with the experimental results. The experimental results show that k_2 increases with the decrease of the air gap length, but it is still much lower than the theoretical value 0.48. Essentially, k_2 is the ratio of the average circumferential fluid velocity in the air gap to the rotor's circumferential speed. Thus, the reduction of the air gap length probably increases the average circumferential velocity of the fluid. In [45], k_2 is 0.15 with open slots and 0.18 with closed slots, which are also much smaller than the theoretical value.

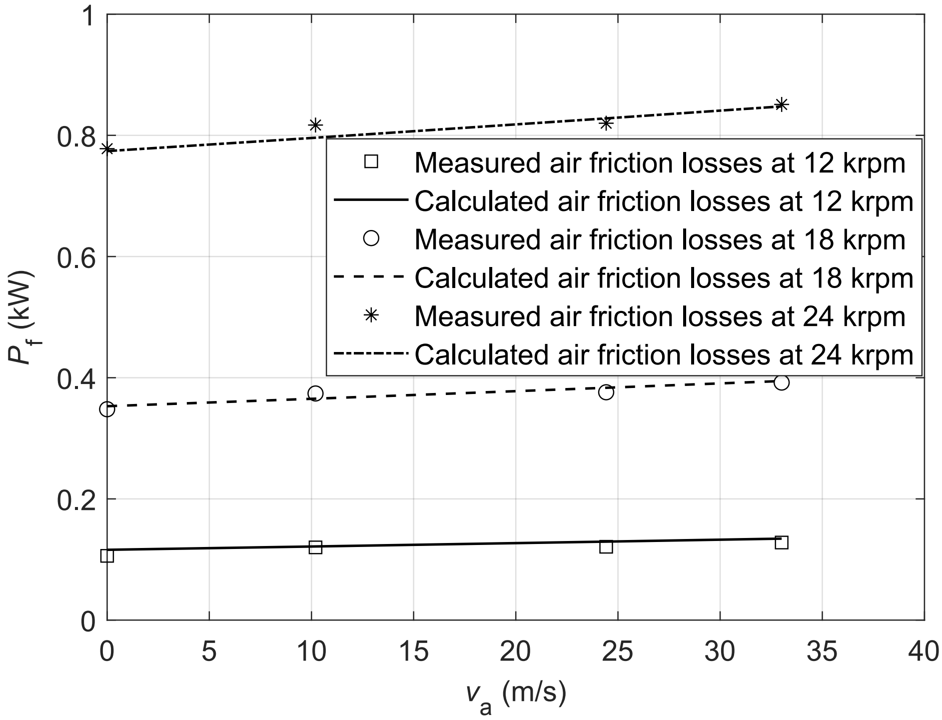

Fig. 3.14: Air friction losses varying with the axial fluid velocity, open slots, fitted k_2=0.095

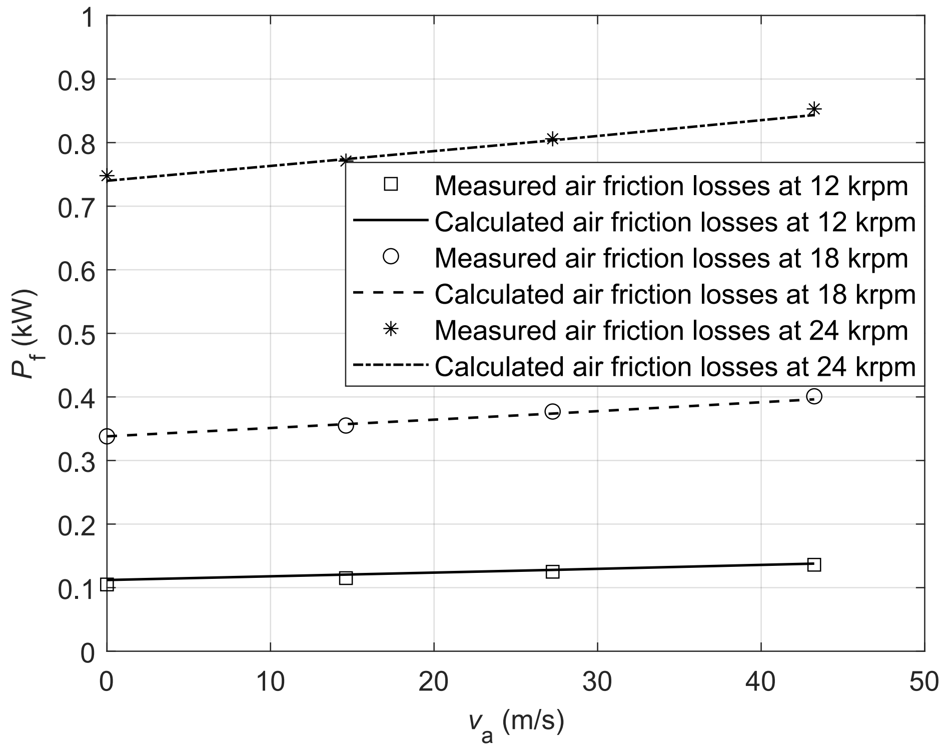

Fig. 3.15: Air friction losses varying with the axial fluid velocity, δ_{sl}=1 mm, fitted k_2=0.147

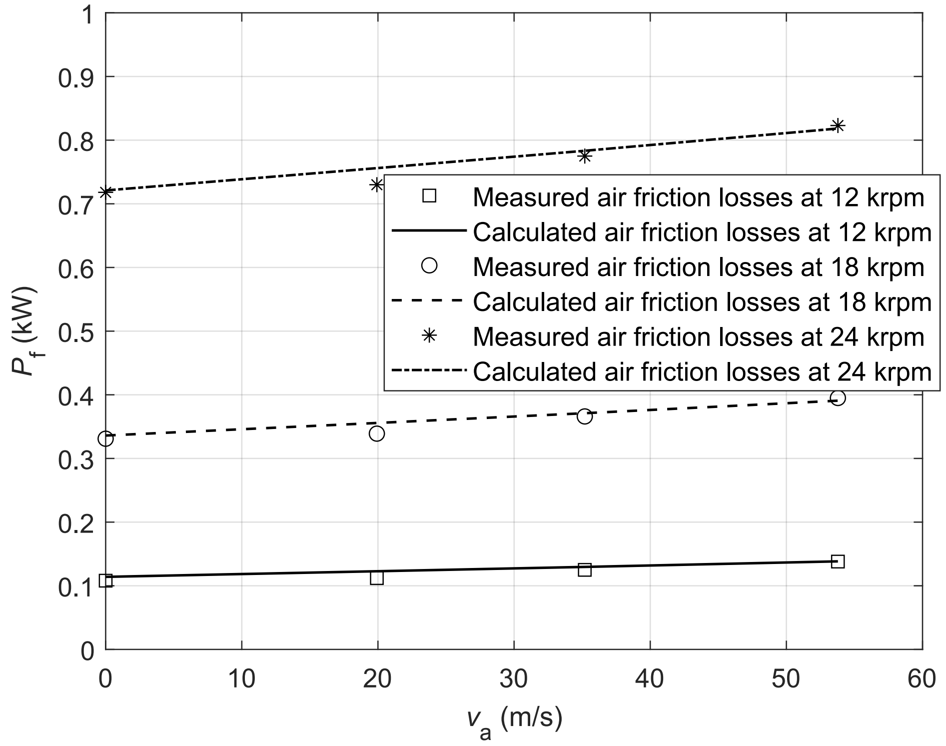

Fig. 3.16: Air friction losses varying with the axial fluid velocity, δ_{sl}=2 mm, fitted k_2=0.195

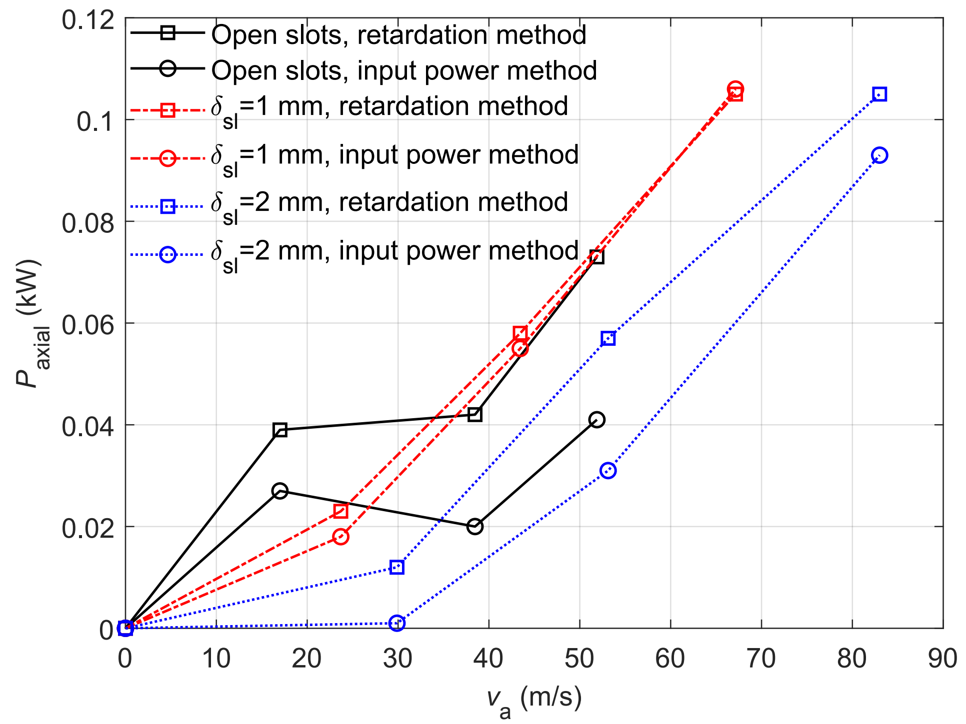

Fig. 3.17: P_{axial} varying with v_{a}, by two different methods (at 24 krpm)

Since the cooling is adequate with axial flow, the motor temperature can be kept constant during each test. Thus P_{fe} and $P_{\mathrm{bearing,r}}$ can be assumed constant. The additional air friction losses caused by axial flow P_{axial} are equal to the difference between the total losses with axial flow and the total losses without axial flow. Fig. 3.17 shows that P_{axial} obtained by the retardation method and the measured input power method are approximately equal, which supports the credibility of the experimental results.

3.5 Summary

(1) The air friction losses of a high-speed permanent magnet motor supported by active magnetic bearings have been calculated by the analytical method and verified by the experiment.

(2) A new experimental method has been proposed to separate the air friction losses without axial flow. This method can effectively compensate for the systematic errors caused by temperature rise and improve the accuracy of loss separation .

(3) Combined with Chapter 2, stator iron losses, iron losses in the magnetic bearing rotor, and air friction losses have been separated based on tested results.

(4) The air friction losses with different air gap lengths have been studied by the experimental method. The air friction losses without axial flow decrease slightly as the air gap decreases, but the roughness coefficient k_{f} is substantially constant. Axial flow does not significantly increase the air friction losses. The ratio of the average circumferential fluid velocity in the air gap to the rotor's circumferential speed k_2 will increase with the decrease of air gap length. However, it is still much smaller than the theoretical value.

4 AC Resistance Ratio Calculation and Experimental Verification

4.1 Introduction

In high-speed motors, copper losses increase significantly with frequency, mainly due to skin effect, proximity effect, and eddy currents generated by rotor magnetic flux [37]. The eddy current generated by the rotor magnetic flux mainly appears in the case of large slot openings, and it is concentrated in the wires near the slot openings. This component exists even when the winding current is 0, so it does not belong to the AC resistance and is out of this thesis's scope. To reduce the skin effect, low-voltage high-speed motors mostly use random-wound windings, where characteristically dozens or hundreds of magnet wires are connected in parallel. However, the uneven current distribution between strands will also lead to extra copper losses [37, 54]. Accurate calculation of the AC copper losses is an essential task in the design of high-speed motors. Analytical methods have been developed to evaluate eddy-current losses of windings in slots. The classic method is to simplify the real slot to a rectangular form. The round conductors are transformed into rectangular ones or stripes to calculate an analytical solution [55, 56]. Some authors [57, 58] have deduced analytical solutions for the round wires, but the calculation formulas are complicated. The finite element method can be used to considerate the circulating currents [59], but it still suffers from the problem caused by the uncertain wire position of random-wound windings.

In the experimental investigation, iron losses in the stator core cannot be easily separated from copper losses caused by skin and proximity effects. Some authors used ferrite cores, and the calculated results were very close to the experimental values [60]. Most motors require a core made of laminated silicon steel sheets, where the iron-resistance accounts for a large portion of the measured AC resistance [61]. Therefore, the elimination or reduction of the influence of iron losses when testing the AC resistance of motors is a practical and essential problem. This thesis proposes a new AC resistance test method, which can minimize the iron losses and improve the verification accuracy of the AC resistance.

4.2 Calculation of AC to DC resistance ratio in random-wound windings

4.2.1 Skin effect

The skin effect causes the current to concentrate on the surface of the conductor when an AC current passes through the conductor, resulting in higher copper losses than in the DC case. Skin depth δ_s is used to indicate the strength of the skin effect and defined as:

$$\delta_s = \frac{1}{\sqrt{\pi \cdot f \cdot \mu \cdot \sigma}} \tag{4.1}$$

where f is the frequency of a sinusoidal current, μ and σ are the permeability and conductivity of the conductor, respectively.

The ratio of AC effective resistance R_{AC} to DC resistance R_{DC} due to skin effect in the round wire is known as [37]:

$$k_{ACR1} = \frac{R_{AC}}{R_{DC}} = 1 + \frac{1}{48}\left(\frac{r}{\delta_s}\right)^4 \tag{4.2}$$

where r is radius of the wire. For the magnet wire used in the machine described in this thesis, the diameter excluding insulation is 0.7 mm and the variation of k_{ACR1} with frequency is shown in Fig. 4.1. Obviously, the skin effect can be ignored here.

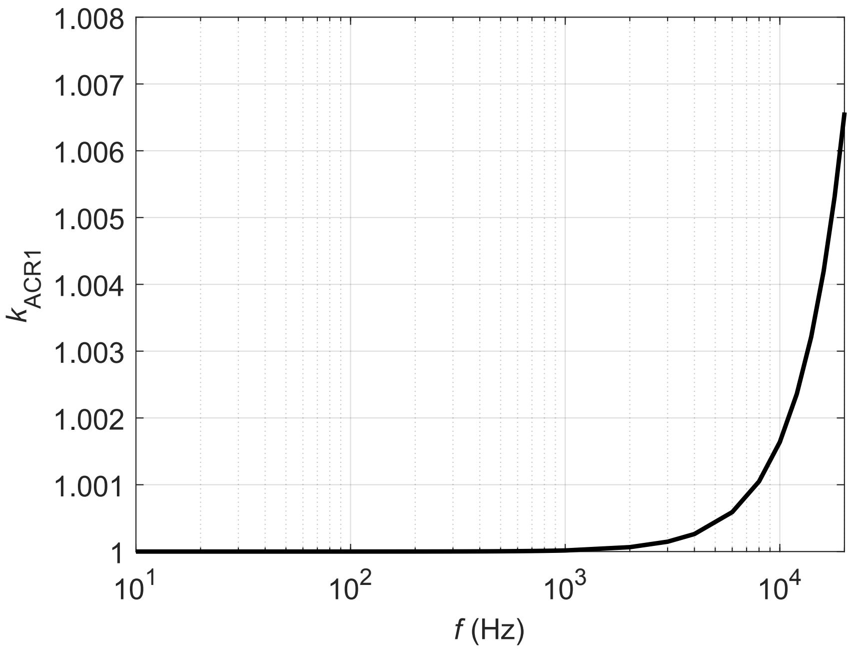

Fig. 4.1: k_{ACR1} vs. f

4.2.2 Proximity effect in slots

Fig. 4.2(a) shows that the pear-shaped slot is simplified into a rectangular slot of the same height and the same area. As shown in Fig. 4.2(b), double-layer windings are applied, where the upper layer is in red, and the lower layer is in blue. $m \times n$ strands are distributed in the slot. According to Ampere's law applied for an ideal iron core, all magnetic flux lines are parallel to the slot ground. When the current phase of the upper and the lower winding is the same, the absolute value of the flux density depends on the distance from the slot ground as shown in the solid line of 0–1–2. The closer the conductor is to the slot opening, the larger magnetic flux density it suffers, and the larger the eddy current losses. When the current of the upper and the lower winding is opposite (this case will be used later), the absolute value of magnetic flux density is shown in the solid line of 0–1–3.

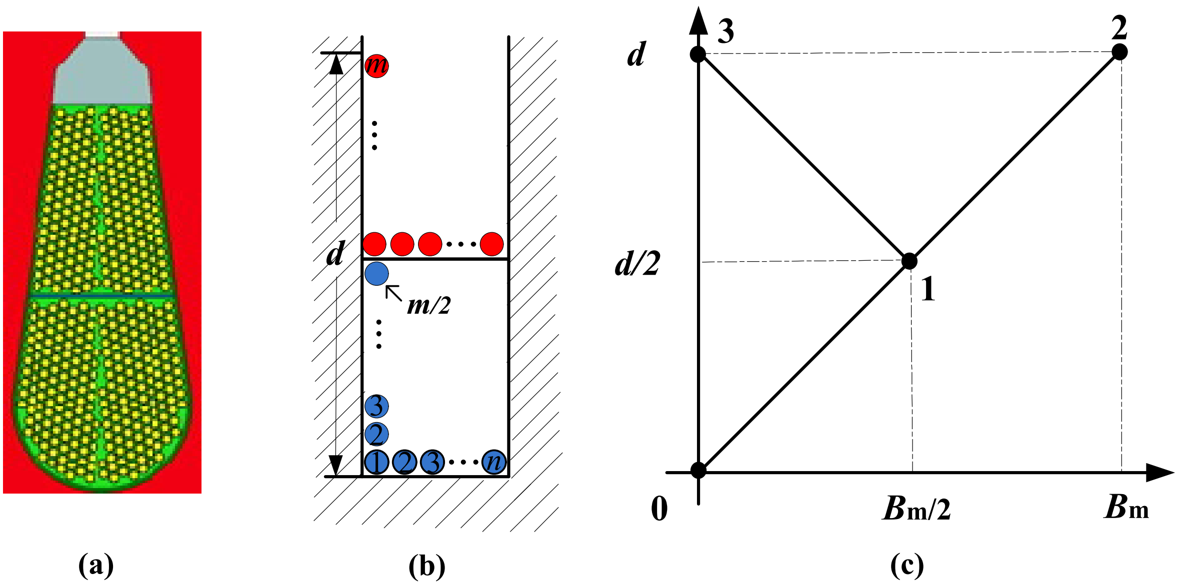

Fig. 4.2: Double-layer windings: (a) pear-shaped slot, (b) equivalent rectangular slot, (c) absolute value of magnetic flux density in the slot

Then, according to the classical calculation method [55, 62], the average AC resistance ratio k_{ACR2} due to proximity effect in slots is:

$$k_{\mathrm{ACR2}} = \frac{R_{\mathrm{AC}}}{R_{\mathrm{DC}}} = \varphi(\xi) + \left[\frac{m^2-1}{3} - \left(\frac{m}{2}\cdot\sin\left(\frac{\gamma}{2}\right)\right)^2\right]\cdot\psi(\xi) \tag{4.3}$$

with

$$\varphi(\xi) = \xi\cdot\frac{\sinh(2\xi)+\sin(2\xi)}{\cosh(2\xi)-\cos(2\xi)}, \quad \psi(\xi) = (2\xi)\cdot\frac{\sinh(\xi)-\sin(\xi)}{\cosh(\xi)+\cos(\xi)} \qquad \xi = r/\delta_{\mathrm{s}} \tag{4.4}$$

where γ is the phase angle between the currents of upper and lower layer.

4.2.3 Proximity effect in end windings

Because the coils are bound together in end windings , the coils will affect each other by their leakage magnetic fields and produce extra AC losses, which are difficult to calculate by analytical methods. In this chapter, the AC resistance ratio of a coil placed in air, as shown in Fig. 4.4, is directly measured and taken as the AC resistance ratio of the end windings k_{ACR3}. The specifications of the coil are the same as those of the tested stator 1.

4.2.4 Circulating currents

The slot-leakage inductance of each strand paralleled in one coil is different because of their different locations in the slots. When AC voltage is applied, uneven currents between the strands will occur, which will increase the copper losses. This uneven current distribution is also called circulating currents. It is impossible to calculate the circulating currents exactly because of the unpredictable positions of strands in random-wound windings. In some papers, FEM and loop current equation methods have been used to calculate circulating currents [37, 54]. These methods were just qualitative analysis and could not be applied practically. Although Litz wires can realize a transposition between strands to eliminate circulating currents, they cannot be placed into slots due to the small slot opening of high-speed motors required to reduce rotor eddy current losses. Therefore, for low-voltage high-speed motor windings, multiple magnet wires in parallel without transposition are used. In this chapter, two stators with different numbers of parallel strands have been tested, and the difference of AC to DC resistance ratios is tiny, which proves that the circulating currents in the final prototype stator are small and can be neglected.

4.2.5 Total AC to DC resistance ratio

When the skin effect and circulating current are ignored, the average AC to DC resistance ratio of the whole winding can be expressed as [63]:

$$
\begin{aligned}
k_{\mathrm{ACR}} =& k_{\mathrm{ACR2}} \cdot k_{\mathrm{s}} + k_{\mathrm{ACR3}} \cdot (1 - k_{\mathrm{s}}) \,, \\
k_{\mathrm{s}} =& l_{\mathrm{Fe}} / l_{\mathrm{av}}
\end{aligned}
\tag{4.5}
$$

where k_{s} is the ratio of windings in slots, l_{Fe} the stator core length, and l_{av} the average half turn length.

4.3 Experimental Verification

4.3.1 Experimental setup

Two stators have been designed and manufactured. Stator 1 has been designed for the final evaporative prototype as shown in Fig. 4.3(a), and detailed parameters are listed in Table A1 in the Appendix. Stator 2 has been designed for the evaporative cooling device as shown in Fig. 4.3(b). To study the influence of circulating currents on the AC to DC resistance ratio, the two stators are almost identical except for the parameters shown in Table 4.1.

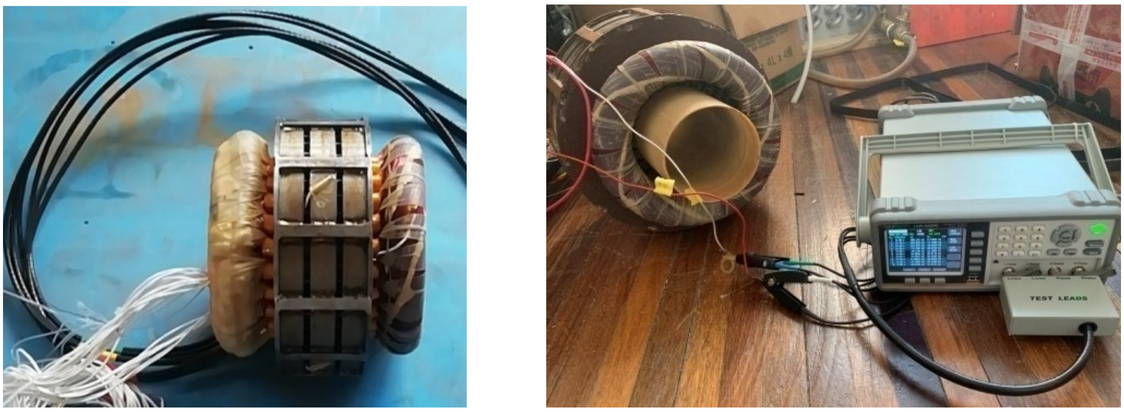

(a) Stator 1

(b) Stator 2 and LCR Meter

Fig. 4.3: Tested stators

Table 4.1: Differences between the 2 tested stators

	Number of parallel branches	Number of parallel strands
Stator 1	2	36
Stator 2	1	4

Fig. 4.4 shows a coil of stator 1 used to test the AC to DC resistance ratio in air.

Table A7 in the Appendix lists the instruments. The volt and ampere meter method was used to test AC resistance and inductance to validate the LCR test results. An adjustable AC power source provided variable frequency AC power, and a power analyzer was used to measure the output voltage, current, active and reactive power.

4.3.2 Validation of LCR test method

The tested AC resistance contains the iron-resistance R_{fe} corresponding to iron losses. When using the LCR test method, the excitation current is very small, corresponding to the starting point of the $B-H$ curve. Due to the typical nonlinearity of the silicon steel sheet's permeability, it is necessary to validate the LCR test results by the volt

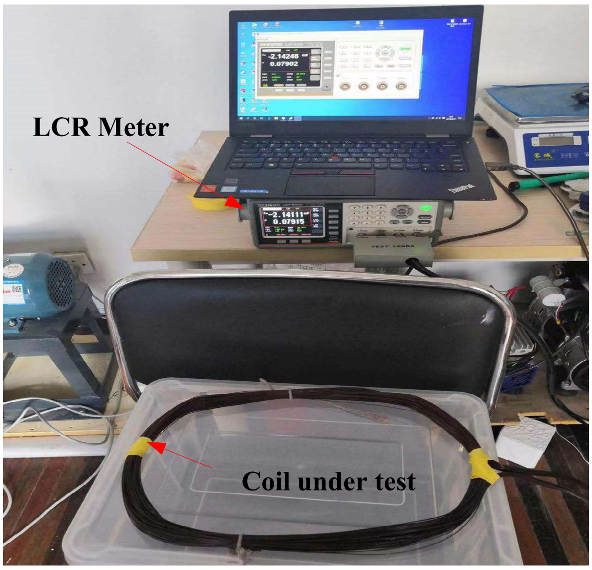

Fig. 4.4: Coil tested in air

and ampere meter method. As the AC power source's maximum current is limited, stator 2 was chosen to be the test object. The maximum phase current in this test is 4.7 A, corresponding to a slot current of 423 A, a current density of 3 A/mm^2, and a specific electric loading of 289 A/cm. The LCR test method and volt and ampere meter method were used to test the AC resistance and inductance of a phase winding, respectively. The results are shown in Table 4.2. The AC resistance and inductance are stable with the variation of excitation current. The volt and ampere meter method test results are consistent with the ones of the LCR (in bold type), indicating that the test results of the LCR meter are plausible.

Table 4.2: Test results of stator 2

	100 Hz				400 Hz			
	LCR	1.0 A	2.0 A	4.7 A	**LCR**	0.33 A	0.72 A	1.44 A
R_{phase} (Ω)	**3.24**	3.29	3.33	3.32	**4.50**	4.68	4.77	5.02
L_{phase} (mH)	**58.71**	61.21	61.38	61.56	**58.40**	60.91	60.88	61.20

4.3.3 AC resistance ratio of the coil in air

The test results of AC to DC resistance ratio of a coil in air are shown in Fig. 4.5. The results are taken as the AC resistance ratio of the end windings k_{ACR3}.

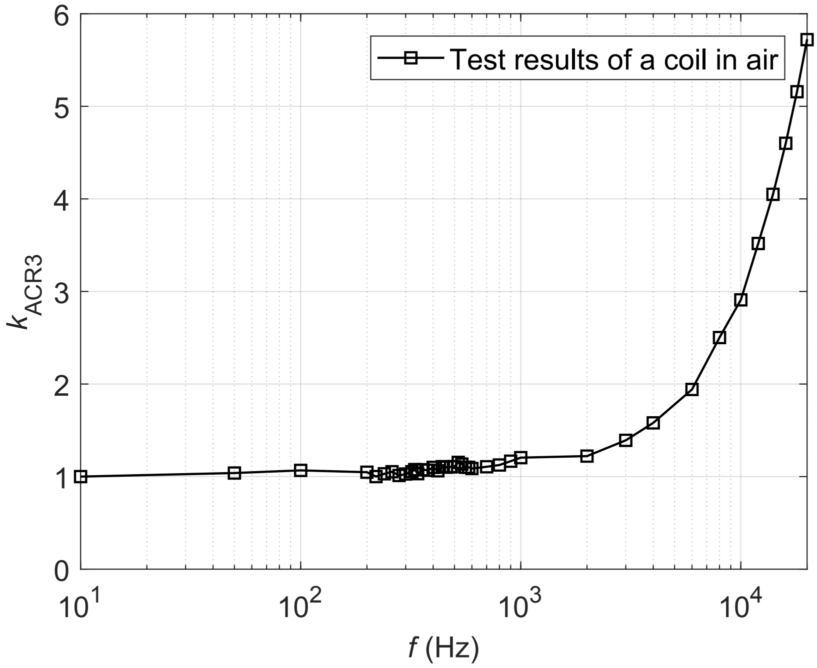

Fig. 4.5: Test results of the coil in air

4.3.4 A proposed series connection of windings for minimum iron losses

In the AC resistance test, iron losses are inevitably included. It is difficult to separate iron losses from total losses, which is a challenge to the effective verification of AC resistance. One method is to use a ferrite core to minimize iron losses [60], but this can hardly be applied to larger motors. Another common method is to subtract the calculated iron losses from the tested total losses, which introduces calculation errors and reduces the reliability of the test results. For example, the calculated iron losses in [61] were almost equal to the copper losses. Such a large iron loss contribution obviously reduces the precision of AC resistance measurement. In this chapter, a series connection of windings for minimum iron losses is presented, which can improve the precision of AC resistance measurement. As shown in Fig. 4.6, the three-phase windings are connected in series resulting in $I_{\mathrm{A}} = I_{\mathrm{B}} = I_{\mathrm{C}}$. The three-phase windings with a shift of 120 degrees in space result in a 0 synthetic MMF, minimizing the iron losses. When three-phase windings are connected in series, and the rotor material is set as air, the flux density distribution of stator 2 is shown in Fig. 4.7. There is only a local leakage magnetic field. The iron losses calculated by FEM are 0.913 W, and the corresponding iron-resistance R_{fe} is 0.44 Ω for a series connected model. The AC resistance of the series connected three-phase windings R_{ABC} was measured as 10.59 Ω and the inductance L_{ABC} was measured as 65.02 mH tested by LCR meter at 400 Hz. Compared with the results in Table 4.2, R_{ABC} is significantly lower than $3 \cdot R_{\mathrm{phase}}$, which proves that this connection can effectively minimize iron losses. The ratio of the calculated iron-resistance R_{fe} to the total measured AC resistance R_{ABC} is only 4.2%.

It is worth noting that although the parallel connection of three-phase windings can theoretically achieve the same effect, it will lead to a new problem of uneven currents.

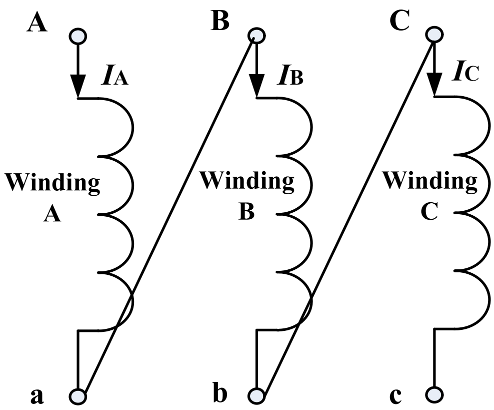

Fig. 4.6: The proposed series connection

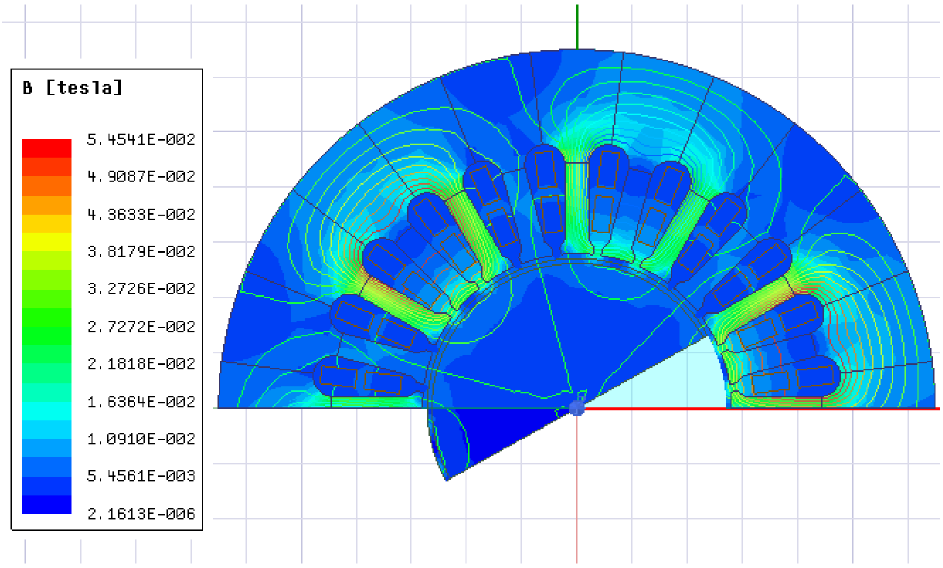

Fig. 4.7: Flux density of stator 2 in series connection, $I = 1.439\,\mathrm{A}$, $f = 400\,\mathrm{Hz}$

4.3.5 Comparison of AC resistance ratio between two stators

The DC resistances have been measured by the DC resistance meter and the AC resistances and inductances from 10 Hz–100 kHz by the LCR meter. The test results at typical frequencies are listed in Table 4.3 and Table 4.4.

The test results at different frequencies are normalized by the following equation:

$$k_{\mathrm{ACR}}(f) = \frac{R_{\mathrm{AC}}(f)}{R_{\mathrm{DC}}}, \quad k_{\mathrm{ACL}}(f) = \frac{L_{\mathrm{AC}}(f)}{L_{10\,\mathrm{Hz}}} \tag{4.6}$$

where k_{ACL} is the AC inductance ratio, and $L_{10\,\mathrm{Hz}}$ the AC inductance at 10 Hz.

Table 4.3: Test results of stator 1 at 27.5°C

	DC	100 Hz	400 Hz	1 kHz	10 kHz
R_{Aa} (mΩ)	10.11	10.67	15.22	31.81	665.90
R_{Bb} (mΩ)	10.14	10.97	16.05	34.40	653.00
R_{Cc} (mΩ)	10.33	10.57	15.52	33.30	663.50
R_{ABC} (mΩ)	30.59	31.01	35.62	53.30	1,003.70
L_{ABC} (uH)	199.40 (10 Hz)	198.37	196.55	188.26	151.12

Table 4.4: Test results of stator 2 at 26.4°C

	DC	100 Hz	400 Hz	1 kHz	10 kHz
R_{Aa}(Ω)	3.05	3.21	4.54	9.33	310.6
R_{Bb}(Ω)	3.06	3.21	4.56	9.43	320.5
R_{Cc}(Ω)	3.05	3.19	4.36	8.51	312.9
R_{ABC}(Ω)	9.05	9.27	10.59	15.53	1,209.3
L_{ABC}(mH)	65.75 (10 Hz)	65.71	65.32	65.02	114.7

Fig. 4.8 shows the comparison of k_{ACR} and k_{ACL} between two stators, which remain almost equal up to 2 kHz. At about 12 kHz, the first winding resonance appears for stator 2. Therefore, Fig. 4.9 only shows k_{ACR} below 2 kHz to reduce the influence of resonance.

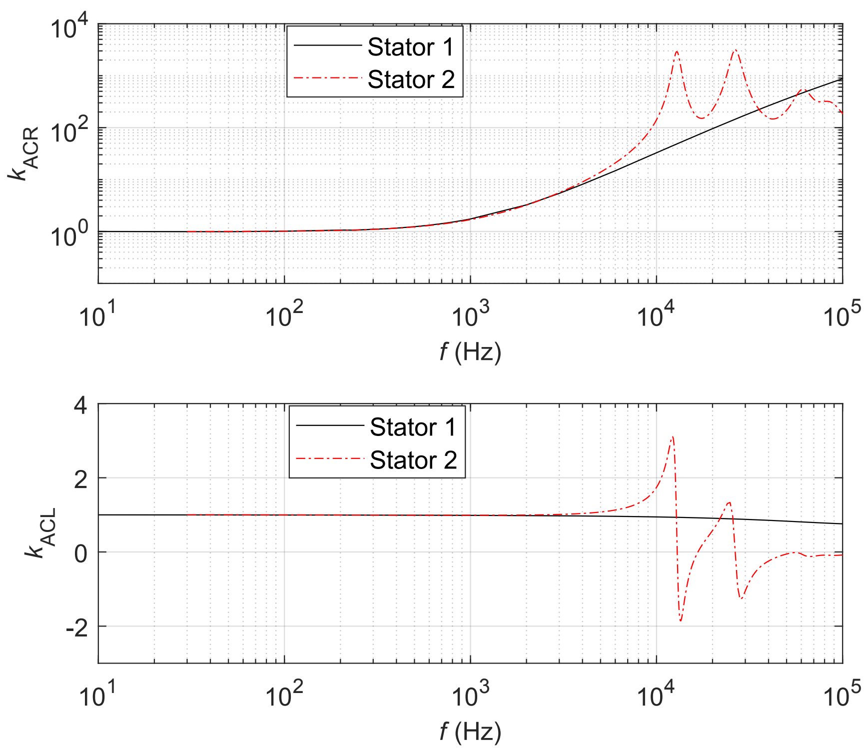

Fig. 4.8: Measured k_{ACR} and k_{ACL} of both stators

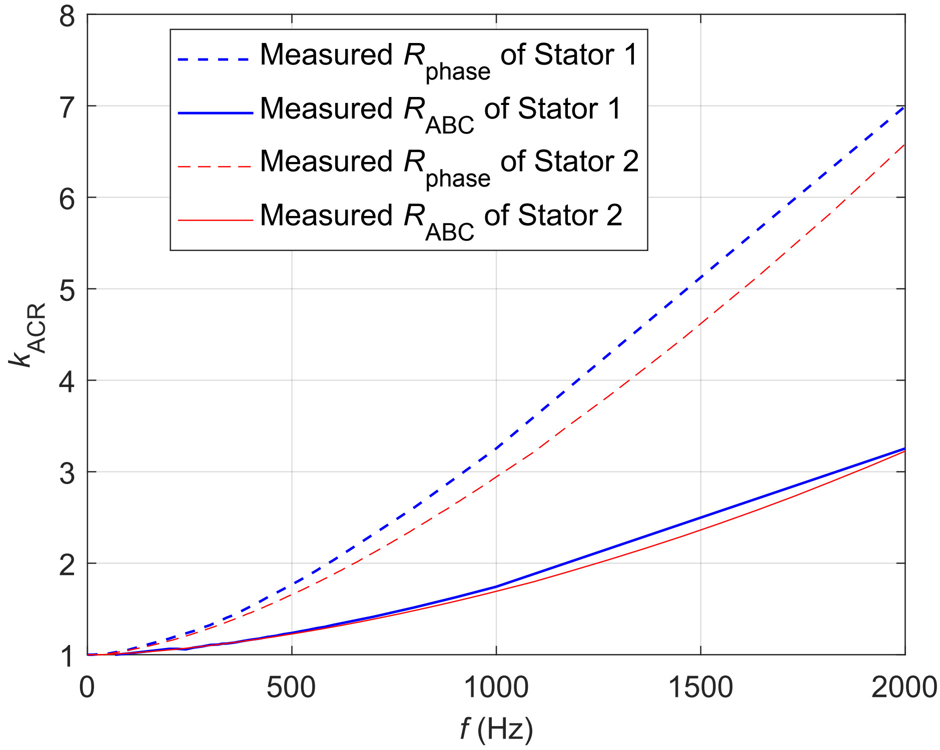

Fig. 4.9: AC resistance ratio of two stators

Since the number of strands of stator 2 is only 4, it is reasonable to assume that there are no circulating currents. According to the theoretical analysis above, if there are no circulating currents, and the number of wires per slot and wire gauge are identical, then k_{ACR} of both stators should be the same. The test results show that k_{ACR} of stator 1 is only slightly larger than that of stator 2, indicating that the losses due to circulating currents caused by the increase of parallel strands are low.

Since iron losses are included in the measured AC resistance, the AC to DC resistance ratio of R_{phase} (R_{phase} is the average value of R_{Aa}, R_{Bb} and R_{Cc}) is much higher than that of R_{ABC}. This is consistent with the test results in [63] that the AC resistance ratio containing iron losses is more than twice the calculated value, where the iron losses were ignored.

4.3.6 Experimental verification of AC to DC resistance ratio

The phase distribution diagram of the windings in Y connection is shown in Table 4.5. When the stator is powered by a three-phase power supply, the phase shift between upper and lower layer of the winding is 60°. Then the average AC resistance ratio $k_{\mathrm{ACR2,Y}}$ in Y connection can be calculated by:

$$k_{\mathrm{ACR2,Y}} = 0.5 \cdot k_{\mathrm{ACR2}}\left(\gamma = 0°\right) + 0.5 \cdot k_{\mathrm{ACR2}}\left(\gamma = 60°\right) \tag{4.7}$$

Table 4.5: Phase distribution diagram in Y connection (one pole)

B-	B-	B-	B-	A	A	A	A	C-	C-	C-	C-
C	C	B-	B-	B-	B-	A	A	A	A	C-	C-

When the three phases of the winding are connected in series as shown in Table 4.6, the average AC resistance ratio $k_{\mathrm{ACR2,ABC}}$ can be calculated by:

$$k_{\mathrm{ACR2,ABC}} = 0.5 \cdot k_{\mathrm{ACR2}}\left(\gamma = 0^{\circ}\right) + 0.5 \cdot k_{\mathrm{ACR2}}\left(\gamma = 180^{\circ}\right) \tag{4.8}$$

Table 4.6: Phase distribution diagram in series connection (one pole)

A-	A-	A-	A-	A	A	A	A	A-	A-	A-	A-
A	A	A-	A-	A-	A-	A	A	A	A	A-	A-

Fig. 4.10 shows the calculated k_{ACR2} with different γ. Since the upper layer is exposed to the synthetic magnetic field of both layers, k_{ACR2} reaches the maximum with $\gamma = 0°$, and k_{ACR2} gets the minimum with $\gamma = 180°$.

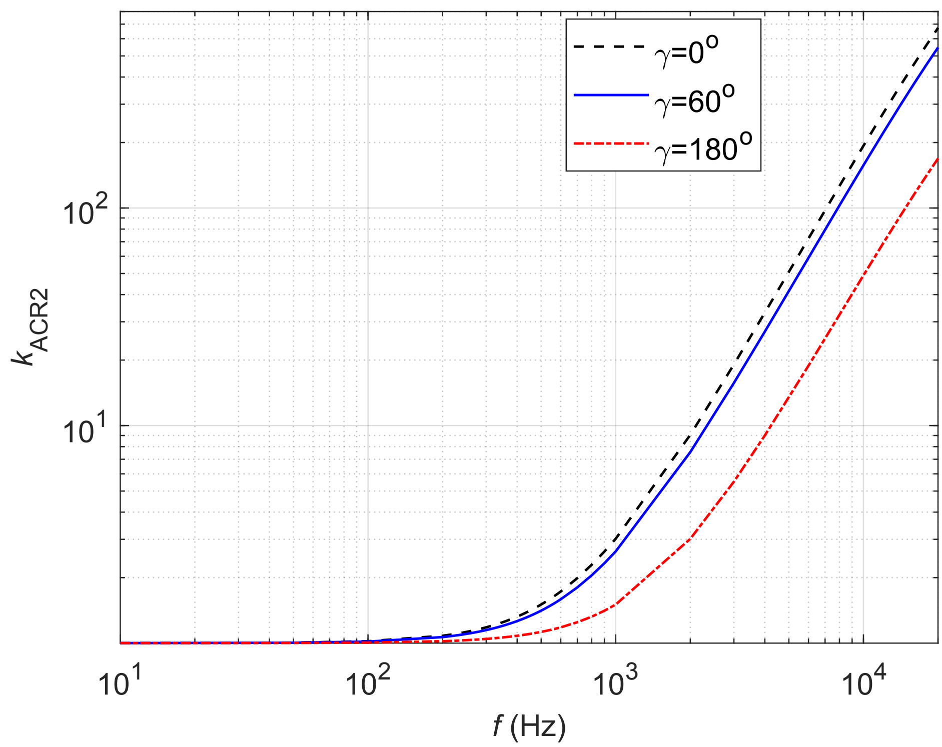

Fig. 4.10: Calculated k_{ACR2} with different γ

The eddy current losses of the wires in slots are proportional to the square of the flux density. Therefore, according to the distribution of the flux density in the slots (see

Fig. 4.2 (c)), the following equation can be deduced:

$$\frac{k_{\mathrm{ACR2}}\left(\gamma = 0°\right) - 1}{k_{\mathrm{ACR2}}\left(\gamma = 180°\right) - 1} = 4 \tag{4.9}$$

that is valid for f approaching infinity

$$\lim_{f \to \infty} \frac{k_{\mathrm{ACR2}}\left(\gamma = 0°\right)}{k_{\mathrm{ACR2}}\left(\gamma = 180°\right)} = 4 \tag{4.10}$$

The iron losses of stator 1 have been calculated for all windings connected in series at different freqencies by FEM. Then the iron-resistance R_{fe} has been extracted and normalized as shown in Fig. 4.11.

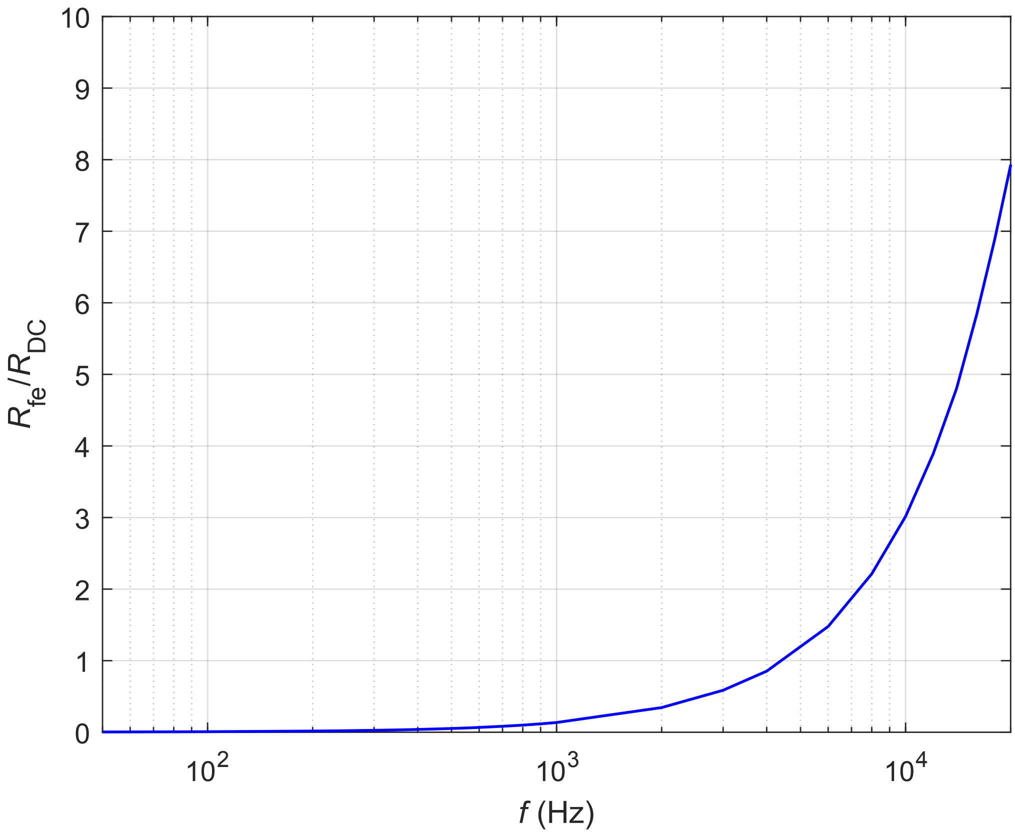

Fig. 4.11: Calculated R_{fe} of stator 1 in series connection

Fig. 4.12 shows the comparison between calculated and measured results of the AC to DC resistance ratio. Below 5 kHz, the experimental value after subtracting iron-resistance agrees well with the calculated value. The experimental value is slightly larger than the calculated value because the calculated value ignores the circulating current. However, the calculated value beyond 5 kHz is larger than the measured value, which will affect the accuracy of AC copper losses of the harmonic currents. Fortunately, the harmonic content of the current is usually less than 10% of the rated current, limiting its influence on the overall copper losses. The dotted red line is the calculated AC to DC resistance ratio in Y connection supplied by a three-phase power source. It will be used to calculate the copper losses in Chapter 6.

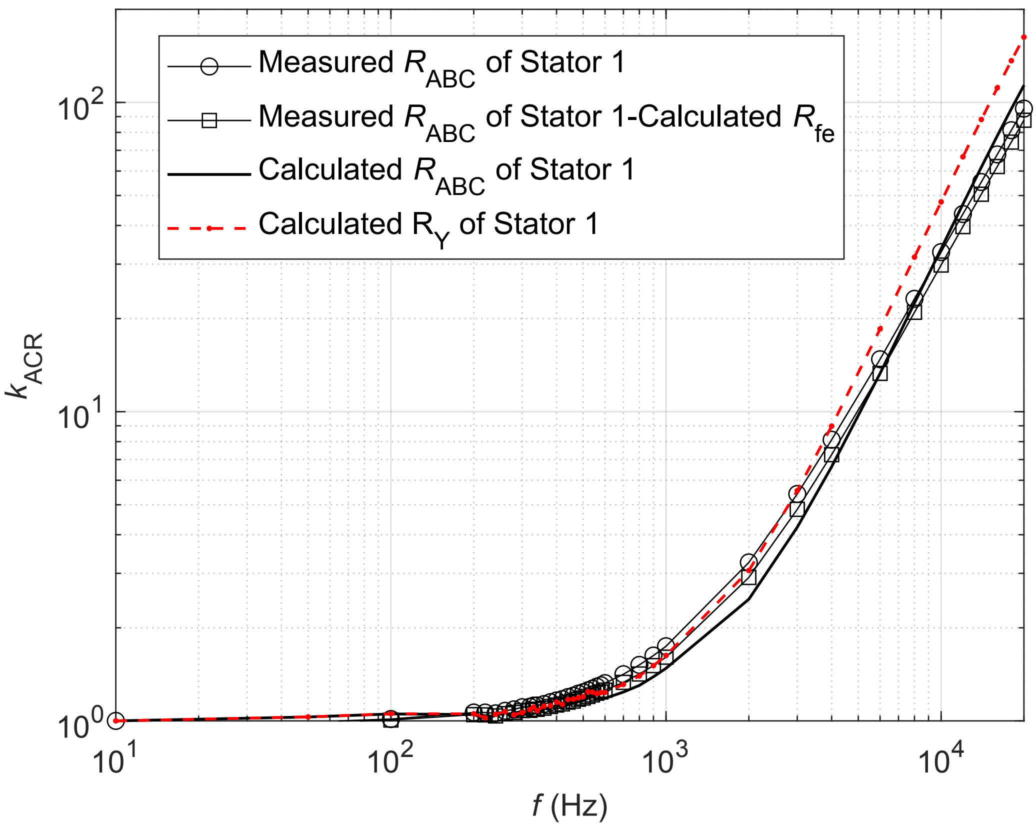

Fig. 4.12: Comparison between calculated and test results

4.4 Summary

In this chapter, the AC to DC resistance ratio of random-wound windings has been studied by an analytical method and verified by experiments. The main results are as follows:

(1) A series connection of three-phase windings was proposed to minimize the influence of iron losses on the AC resistance test. The calculated results of the AC to DC resistance ratio agree with the experimental results.

(2) The experimental results show that circulating currents of random-wound windings in the prototype can be ignored.

(3) The LCR test method was confirmed by the volt and ampere meter method, which indicates that the LCR test results are reliable when the AC resistance including iron loss effects is measured.

5 Thermal Network Model Establishment and Experimental Verification

5.1 Introduction

Efficient cooling methods should have the following characteristics: high heat transfer coefficient, low contact thermal resistance, and large heat transfer area. Table 5.1 compares the heat transfer coefficients of different heat transfer types.

Table 5.1: Range of heat transfer coefficients in $\mathrm{W}/\left(\mathrm{m}^2 \cdot \mathrm{K}\right)$ [48]

Heat transfer type	Media	Heat transfer coefficient
Natural convection	Air	1–10
	Water	200–1,000
Forced convection	Air	20–100
	Water	1,000–15,000
Boiling (evaporation)	Water	2,500–35,000
Condensation	Water	5,000–25,000

Obviously, the cooling efficiency of air cooling is poor. Although the heat transfer effect of forced water cooling is excellent, the thermal resistance between the water jacket and the windings is too large. Therefore, traditional air cooling or water jacket cooling methods for high-speed motors are not efficient. Boiling and condensation have the highest heat transfer coefficients due to phase transitions. However, water is not suitable as an evaporative cooling medium for windings due to its high boiling point and bad insulation properties. Therefore, an organic engineered fluid HFE-7100 ($C_4F_9OCH_3$), which offers good dielectric properties to contact the stator core and windings directly, is selected as the coolant.

In a traditional semi-enclosed refrigeration compressor motor, liquid refrigerant is usually sprayed directly to windings and rotor for cooling. The liquid refrigerant vaporizes and takes heat away. However, for a high-speed motor, liquid sprayed directly on the rotor will produce huge friction losses. Danfoss Turbocor developed the first magnetic suspension oil-free centrifugal refrigeration compressor driven by high-speed motors, as shown in Fig. 5.1(a). The cooling path is shown in Fig. 5.1(b). A solenoid valve is used to adjust the flow rate to ensure that the coolant passing through the air gap is a pure gas, avoiding the huge friction losses caused by liquid contact with the high-speed rotor. Since the compressor and motor are in the same cavity, the compressor side is allowed to leak a certain amount of refrigerant into the motor through the labyrinth seal. Therefore, this cooling method is limited to the refrigeration compressor. When the motor drives other loads, refrigerant leakage through the dynamic seal will be a problem.

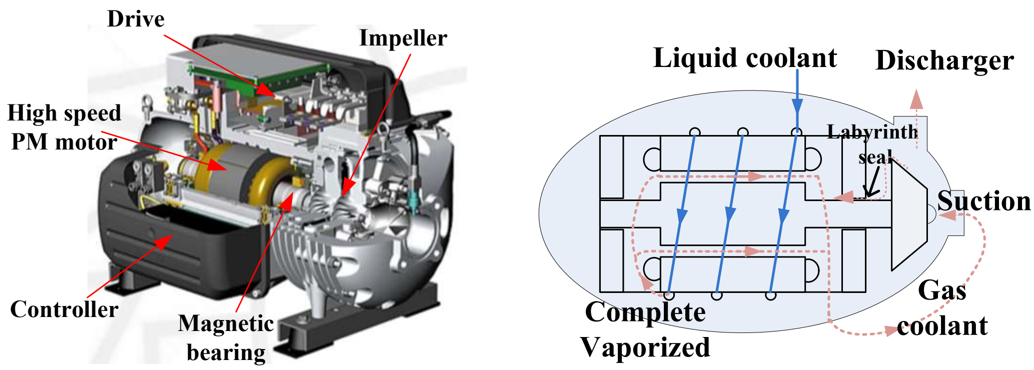

(a) Structure (b) Cooling path

Fig. 5.1: Turbocor refrigeration compressor [64]

The institute of Electrical Engineering in Chinese Academy of Sciences (IEECAS) has launched the research on evaporative cooling in 1958. Between 1974–1975, G. Gu first applied the immersion evaporative cooling method to a 1,200 kVA, 400 V, 3,000 rpm turbo-generator with form-wound windings [17]. As shown in Fig. 5.2, there is a glass fiber sleeve attached to the stator's inner cylinder barrel, which forms a sealed enclosure including the condenser and stator. Coolant CFC-113 is then injected to immerse the stator completely. The coolant absorbs heat from the stator and vaporizes. Then the vapor rises and meets the condenser, exothermically liquefies, and falls back to the liquid surface to form a natural circulation. The electrically excited rotor is also cooled by the evaporative cooling method. This cooling method was also applied to an induction generator rated at 1,600 kW, 1,000 V, 6,521 rpm, which also adopted form-wound windings [17].

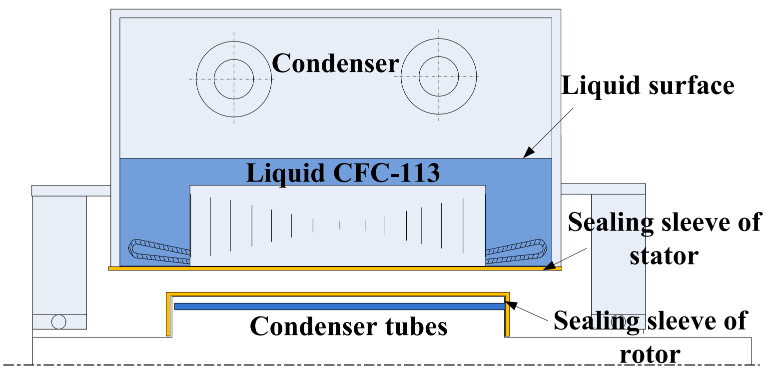

Fig. 5.2: Structural diagram of immersion evaporative cooled motor [17]

For protecting the ozonosphere, IEECAS began to use HFC-4310mee to replace CFC-113 [65]. The research objects of IEECAS are mostly large generators with form-wound windings. The temperature rise of the motor is calculated by the three-dimensional finite element method (3-D FEM) , and the calculation of the heat transfer coefficient of the condenser is not studied in detail [17]. The evaporative heat transfer coefficient is obtained by experiments and only applicable to CFC-113, banned. HFC-4310mee, the alternative, however, is highly toxic and has an extensive global warming potential [66].

The low-voltage high-speed PM motor studied in this dissertation has the following characteristics:

- Random-wound windings with thin insulation.
- High copper loss density due to high thermal loading selected and high AC resistance ratio.
- High iron loss density.
- Low rotor eddy-current losses due to electromagnetic optimization, high switch frequency and with a choke.

According to the characteristics mentioned above, the stator is immersion evaporative cooled with a sealing sleeve while the rotor is air-cooled. HFE-7100 is used as the coolant. This cooling scheme makes full use of the advantages of the immersion evaporative cooling method, which can fully cool the high losses of the stator.

This chapter aims to establish a thermal network model for a stator with immersion evaporative cooling. In order to verify it, an evaporative cooling test device was designed and manufactured. Compared with the final prototype motor, this device is more convenient to adjust test conditions.

5.2 Design of evaporative cooling test device

5.2.1 Introduction of HFE-7100

HFE-7100 is an environment-friendly and regulations permitted engineered fluid [66]. It also offers additional advantages like non-flammability, high dielectric strength, inertness, non-corrosiveness, low viscosity, and suitable boiling point. These characteristics make it ideal as immersion evaporative cooling fluid, which is now widely used in power electronics, data centers and supercomputers for cooling [67]. Its physical properties at 25°C are shown in Table 5.2. The physical properties varying with temperature can be found in [68, 69].

The variation of saturated vapor pressure with temperature can be calculated as [66]:

$$\ln\left(p_{\mathrm{s}}/\mathrm{Pa}\right) = 22.415 - 3641.9/(T_{\mathrm{s}}/\mathrm{K}) \tag{5.1}$$

where p_s is the saturated vapor pressure in Pa and T_s the temperature of saturated vapor in K.

Table 5.2: Typical physical properties of HFE-7100 at 25°C [66, 70]

Property	Symbol	Unit	Value
Formula			$C_4F_9OCH_3$
Relative Molar Mass	M_r	dimensionless	250
Specific Heat Capacity	c_f	$J/(kg \cdot K)$	$1.172 \cdot 10^3$
Liquid Thermal Conductivity	λ_L	$W/(m \cdot K)$	$6.9 \cdot 10^{-2}$
Boiling Point		°C	61
Freeze Point		°C	-135
Surface Tension	σ	N/m	$1.36 \cdot 10^{-2}$
Latent Heat	H_{fg}	J/kg	$1.26 \cdot 10^5$
Liquid Density	ρ_L	kg/m^3	$1.52 \cdot 10^3$
Liquid Dynamic Viscosity	μ_L	Pa·s	$5.8 \cdot 10^{-4}$
Liquid Electrical Conductivity	σ	S/m	$5 \cdot 10^{-10}$
Liquid Dielectric Strength	E_d	kV/m	$1.1 \cdot 10^4$
Saturated vapor pressure	p_s	kPa	28
Critical Pressure	p_{crit}	MPa	2.325

5.2.2 Description of the test device

As shown in Fig. 5.3, the evaporative cooling test device is a cuboid-shaped box with insulation foam covered outside to reduce surface heat dissipation. A stator under test and three heaters are placed inside, and the leads are connected out from the power terminals. After sealing and vacuuming, HFE-7100 liquid was injected until the stator was fully immersed. The liquid surface can be observed through a liquid level observation window.

There are 18 stainless tubes with smooth inner and outer surfaces divided into 3 rows, located on the top, functioning as a condenser. There is a water collection cover at each end of the tubes. Branching plates in the collection cover are used to change the number of tubes in parallel. In order to avoid residual air inside the tubes, the water inlet is located at the bottom of the water collection cover, and the outlet at the top. The water outlet has a flow meter. The HFE-7100 can be recycled through the drain outlet at the bottom. The exhaust outlet at the top is used to drain the non-condensable air. Both of them have valves.

The input power of the stator is adjusted by a voltage regulator. In some cases, additional heaters are used to increase the total power. The input power is measured

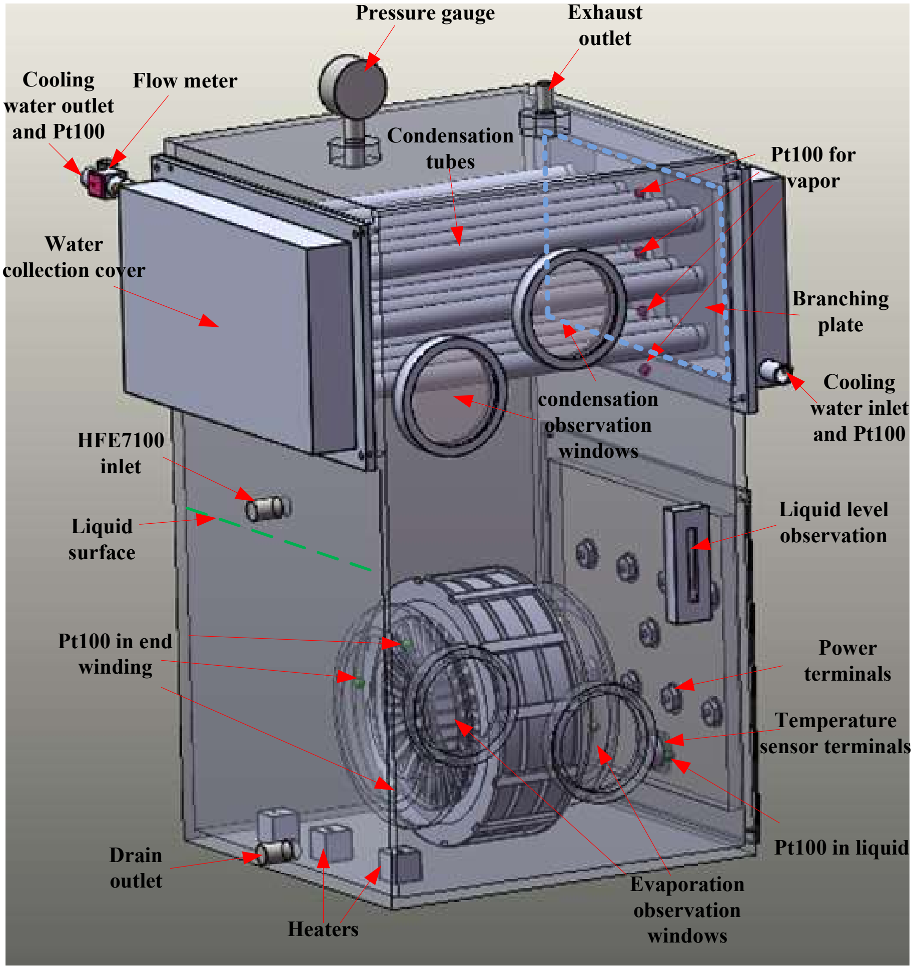

Fig. 5.3: Structural schematic of the immersion evaporative cooling test device

by a power analyzer. The energized stator and heaters raise the liquid's temperature, which evaporates and takes heat away when the boiling point is reached. Hot vapor rises up, comes into contact with the cold tubes to transfer heat to them and liquefies, and drips back. The entire box is like a large heat pipe, with a hot end at the bottom and a cold end at the top. The internal cycle of the system eventually stabilizes to a balanced temperature and pressure. The evaporation and condensation phenomenon can be observed through the observation windows.

The cooling water temperature is regulated by an external cooling fan. The flow rate is regulated by a pump. The relative internal pressure is measured by a pressure gauge. There are 14 Pt100 elements in the winding, 4 sensors for liquid temperature measurement, and 4 sensors for vapor temperature measurement distributed at different heights. The inlet and outlet of cooling water are also equipped with temperature sensors. All Pt100 sensors use three-wire technology. They are connected to one common inspection instrument that displays the temperature values.

Without power input, the device cools to room temperature, and the relative internal pressure will be negative. Air may leak into the vessel, affecting the test results.

Therefore, all the tests in this chapter have been run in a positive pressure state. When the test was interrupted, the flow of cooling water was turned off, and a continuous 300 W input power was still provided to maintain positive pressure inside.

5.2.3 Simplified thermal network model of the evaporative cooling device

Fig. 5.4 is a simplified thermal network model of the evaporative cooling device, which is used to explain the calculation process of stator temperature rise. There are three heat sources in the entire model: copper losses P_{cu}, iron losses P_{fe}, and heater losses P_{heater}. There are two cooling paths in the model, P_2 represents the surface heat dissipation, and P_1 represents the losses taken away by the cooling water. Based on the law of conservation of energy, the following equation can be obtained:

$$P_{\text{all}} = P_1 + P_2 = P_{\text{cu}} + P_{\text{fe}} + P_{\text{heater}} \tag{5.2}$$

where P_{all} is the total losses.

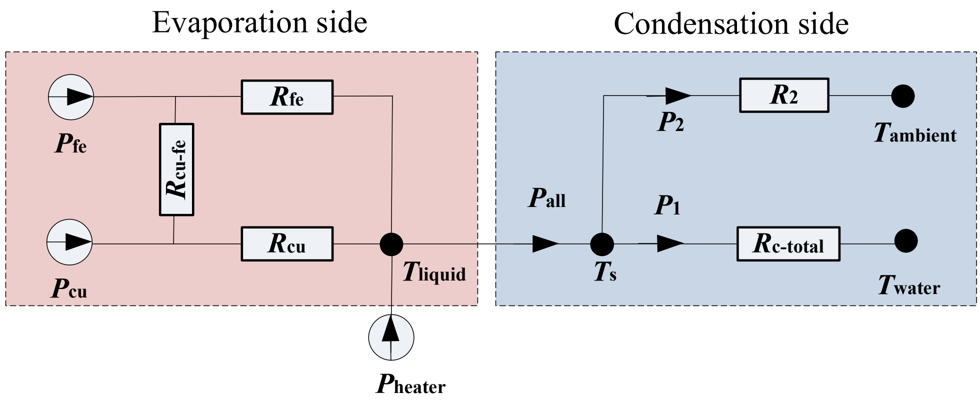

Fig. 5.4: Simplified thermal network model of evaporative cooling device

R_{cu} and R_{fe} are the thermal resistances from winding to liquid and core to liquid, respectively. $R_{\text{cu-fe}}$ represents the thermal resistance between the windings and core. R_2 represents the thermal resistance of surface heat dissipation. $R_{\text{c-total}}$ represents the thermal resistance between saturated vapor and water.

According to the boiling rule, the liquid temperature T_{liquid} is equal to the saturated vapor temperature T_{s} when the liquid boils. Therefore, the entire thermal network model can be divided into two parts, as shown in Fig. 5.4. The box on the right contains the condensation side thermal network, and the box on the left contains the evaporation side thermal network. They are connected via T_{liquid} and T_{s}. When the total losses P_{all} are known, the condensation side thermal network model can be solved first to obtain T_{s}. The evaporation side thermal network model is then solved to get the temperature of the stator windings and core. Detailed thermal network models of the condensation and evaporation sides will be presented and verified later.

5.3 Thermal network model of condensation side

Fig. 5.5 is a detailed thermal network model of the condensation side, where R_2 is the thermal resistance of surface heat dissipation including the effects of conduction through both casing and insulation foam as well as natural convection. $R_\mathrm{c}\,(T_\mathrm{s}, T_\mathrm{wo})$ is a condensation thermal resistance between the vapor to the outer wall of the cooling tubes. It is a variable thermal resistance associated with the vapor temperature T_s and the tube outer wall temperature T_wo. R_w is the conduction thermal resistance of the wall of the tubes. R_f is the convection thermal resistance of water in the tubes. R_3 corresponds to the vapor-to-water cooling path caused by the water collection covers and consists of two main paths: (1) the wall inside the blue dashed box covered by the water collection cover (see Fig. 5.3) is cooler than the vapor, the vapor will condense on this area, and transfer heat to the water; (2) if the cooling water is running only through a part of the tubes while the others contain air, the latter will conduct heat from surrounding vapor mainly by conduction through its solid wall. Since there will not be water collection covers in the final prototype, R_3 has not been studied in this dissertation. Its value has been obtained by the test.

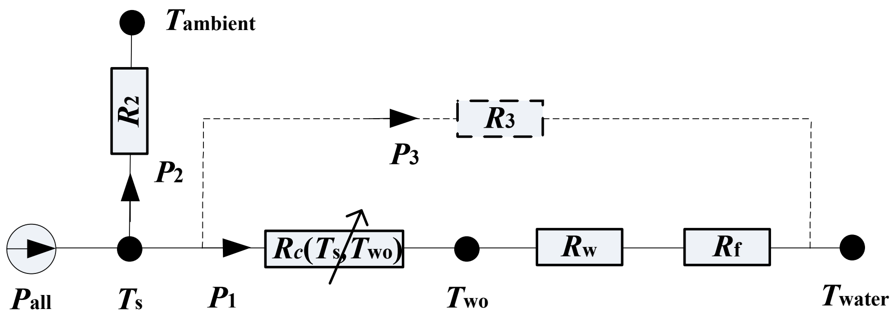

Fig. 5.5: Detailed thermal network model of condensation side

5.3.1 Thermal resistance of surface heat dissipation

Since the insulation foam cannot cover the observation windows and some auxiliary instruments, the actual thermal resistance of surface heat dissipation is difficult to calculate accurately. So R_2 is also determined by the test.

5.3.2 Turbulent flow in tubes

Because the cooling water in the tubes is turbulent in this work, the Gnielinski's simplified heat transfer correlation including entrance effect correction factor and temperature difference correction factor is adopted [71]:

$$Nu = 0.012 \cdot (Re^{0.87} - 280) \cdot Pr^{0.4} \cdot \left[1 + \left(\frac{d_i}{l_\mathrm{tu}}\right)^{\frac{2}{3}}\right] \cdot \left(\frac{Pr}{Pr_\mathrm{w}}\right)^{0.11} \quad \text{for} \quad 1.5 \leq Pr \leq 500, \quad 3 \cdot 10^3 \leq Re \leq 10^6 \tag{5.3}$$

with

$$Re = \frac{u \cdot d_\mathrm{i}}{\nu}, \quad \nu = \frac{\mu}{\rho}, \quad Pr = \frac{\mu \cdot c_\mathrm{f}}{\lambda_\mathrm{f}} \tag{5.4}$$

where Nu is the Nusselt number, Re the Reynolds number, u the velocity of the fluid in the tube, d_i the inner diameter of the tube, l_tu the tube length, ν the fluid kinematic viscosity, ρ the fluid density, μ the fluid dynamic viscosity, λ_f the fluid thermal conductivity, c_f the fluid specific heat at constant pressure, Pr the Prandtl number and Pr_w the Prandtl number at the wall temperature.

Then the convection heat transfer coefficient can be expressed as:

$$h_\mathrm{f} = Nu \cdot \lambda_\mathrm{f}/d_i \tag{5.5}$$

Thus the convection thermal resistance of water in the tubes R_f can be obtained.

5.3.3 Thermal resistance of the tube wall

The thermal resistance of one tube wall can be modeled as:

$$R_\mathrm{w1} = \frac{\ln\left(\frac{d_\mathrm{o}}{d_\mathrm{i}}\right)}{2\pi \cdot \lambda_\mathrm{w} \cdot l_\mathrm{tu}} \tag{5.6}$$

where d_o is the outer diameter of the tube, λ_w is the thermal conductivity of the tube wall.

5.3.4 Condensation heat transfer and enhancement

5.3.4.1 Condensation heat transfer coefficient for horizontal tube

Fig. 5.6(a) shows that the vapor condenses at its saturation temperature T_s due to a cooler wall temperature T_w of a tube.

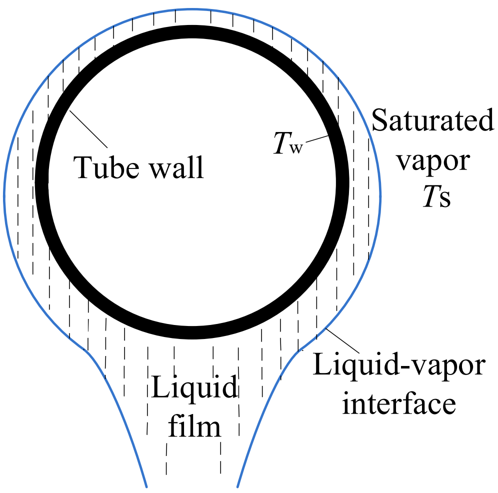

(a) Outside horizontal tube

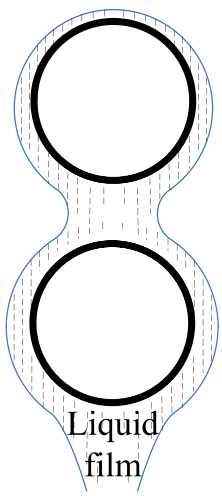

(b) On tube bundle

Fig. 5.6: Film condensation [72]

The average condensation heat transfer coefficient h_c for a tube of outer diameter d_o is [73]:

$$h_c = 0.729 \cdot \left[\frac{\lambda_L^3 \cdot \rho_L \cdot (\rho_L - \rho_s) \cdot g \cdot H_{fg}}{\mu_L \cdot (T_s - T_{wo}) \cdot d_o} \right]^{0.25} \tag{5.7}$$

where λ_L is the thermal conductivity of the liquid, ρ_L the liquid density, ρ_s the density of the saturated vapor, g the gravitational acceleration, H_{fg} the latent heat of the liquid, μ_L the dynamic viscosity of the liquid, T_s the temperature of the saturated vapor, T_{wo} the temperature of the outer surface of tube wall.

For λ_L, ρ_L and μ_L, the values at the average temperature of the liquid film $(T_s + T_{wo})/2$ are taken.

5.3.4.2 Condensation heat transfer coefficient for horizontal tube bundle

When there are multiple tubes arranged vertically, the upper tube's drainage causes the liquid film of the lower tube to thicken, thus weakening the heat transfer of the lower tube, as shown in Fig. 5.6(b). Assuming N_r is the number of rows in the vertical direction, the average heat transfer coefficient for the horizontal tube bundle is [72]:

$$h_{cN} = N_r^{-0.25} \cdot h_c \tag{5.8}$$

Then the condensation thermal resistance R_c of smooth tubes can be calculated.

5.3.4.3 Condensation enhancement

Table 5.3 shows the comparison of the physical properties of HFE-7100 and water at standard atmosphere pressure, where h_c is the condensation heat transfer coefficient calculated by (5.7) when d_o is 27 mm and $(T_s - T_{wo})$ is 5 K.

Table 5.3: Physical properties of HFE-7100 and water

	λ_L	ρ_L	ρ_s	H_{fg}	μ_L	T_s	h_c
	W/(m · K)	kg/m^3	kg/m^3	kJ/kg	Pa·s	°C	W/(m^2 · K)
HFE-7100	$5.9 \cdot 10^{-2}$	$1.426 \cdot 10^3$	9.5	126	$4.41 \cdot 10^{-4}$	61	$1.244 \cdot 10^3$
Water	0.683	958	0.6	$2.26 \cdot 10^3$	$2.83 \cdot 10^{-4}$	100	$1.471 \cdot 10^4$

The heat transfer coefficient h_c of HFE-7100 is only 1/12 that of water, so in the water-cooled organic vapor condensation heat exchanger, the condensation thermal resistance R_c is probably 2–3 times the water side convection thermal resistance R_f. To improve the heat exchange efficiency, the reinforcement of condensation transfer is necessary [72]. Condensation thermal resistance mainly depends on the film's thickness, so thinning the liquid film is the primary means of condensation enhancement. As shown in Fig. A3 in the Appendix, the trapezoidal finned tube is a relatively inexpensive and straightforward fin geometry that can reduce the thickness of the liquid film at the tip of the fin by surface tension and significantly improve the condensation heat transfer coefficient [73]. The condensation effect of the smooth tubes and the finned tubes is compared through experiments in Chapter 6.

5.4 Thermal network model of evaporation side

Iron and copper loss densities of stators in high-speed motors are very high. This makes heat dissipation difficult. So a high accuracy of temperature rise calculation is essential. The calculation methods of temperature rise mainly include the thermal network method based on lumped parameters, FEM, and CFD [74]. The latter two methods are accurate but time-consuming. The thermal network method offers short solution times and satisfactory accuracy, which makes it a valuable tool. N. Simpson et al. [74] proposed a general arc segment element for 3-D thermal modeling, which can accurately consider internal heat generation. The arc segment is particularly suited for modeling stator.

5.4.1 T-network representation of an arc segment

Fig. 5.7 illustrates an arc segment, where α is the arc-angle in rad, r_1 the inner radius, r_2 the outer radius, l_a the axial length, λ_a, λ_r and λ_c the thermal conductivity in axial, radial, and circumferential direction, respectively. The heat flow in the three directions are assumed to be independent and each axis is represented by a 1-D T-network [74]. Negative thermal resistances R_{a3}, R_{c3} and R_{r3} are added to consider the temperature profile with heat generation. The 3-D T-networks are connected at a central node, which gives the average temperature of the volume, T. A current source P denotes the internal heat generation. A capacitance C represents the thermal storage [74]. Because only the steady-state temperature rise is considered in this dissertation, the capacitance C can be removed. The 3-D T-networks are masked like a building block.

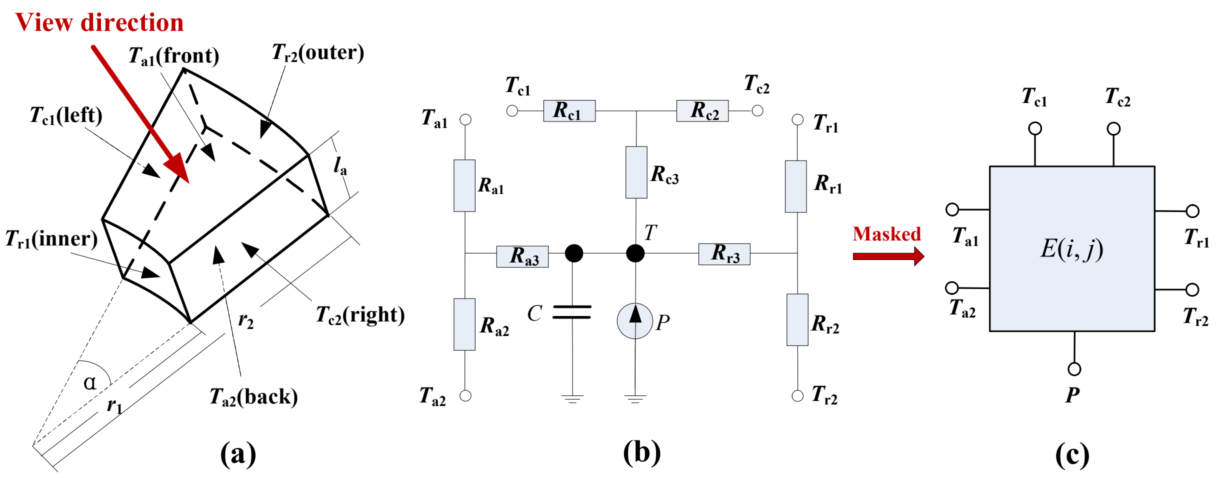

Fig. 5.7: An arc segment element: (a) geometry [74], (b) 3-D T-networks [74], (c) masked block

5.4.1.1 Axial heat flow

The thermal resistances of axial heat flow are modeled as [74]:

$$R_{\mathrm{a}1} = R_{\mathrm{a}2} = \frac{l_{\mathrm{a}}}{\alpha \cdot \lambda_{\mathrm{a}} \cdot (r_2^2 - r_1^2)}, \quad R_{a3} = -\frac{1}{3} \cdot R_{\mathrm{a}1} \tag{5.9}$$

5.4.1.2 Circumferential heat flow

The thermal resistances of circumferential heat flow are modeled as [74]:

$$R_{\mathrm{c}1} = R_{\mathrm{c}2} = \frac{\alpha \cdot (r_1 + r_2)}{4 \cdot \lambda_{\mathrm{c}} \cdot l_{\mathrm{a}} \cdot (r_2 - r_1)}, \quad R_{\mathrm{c}3} = -\frac{1}{3} \cdot R_{\mathrm{c}1} \tag{5.10}$$

5.4.1.3 Radial heat flow

The thermal resistances of radial heat flow are modeled as [74]:

$$\begin{aligned}
R_{\mathrm{r}1} &= \frac{1}{2 \cdot \alpha \cdot \lambda_{\mathrm{r}} \cdot l_{\mathrm{a}}} \cdot \left[\frac{2 \cdot r_2^2 \cdot \ln\left(\frac{r_2}{r_1}\right)}{(r_2^2 - r_1^2)} - 1 \right] \\
R_{\mathrm{r}2} &= \frac{1}{2 \cdot \alpha \cdot \lambda_{\mathrm{r}} \cdot l_{\mathrm{a}}} \cdot \left[1 - \frac{2 \cdot r_1^2 \cdot \ln\left(\frac{r_2}{r_1}\right)}{(r_2^2 - r_1^2)} \right] \\
R_{\mathrm{r}3} &= \frac{-1}{4 \cdot \alpha \cdot \lambda_{\mathrm{r}} \cdot l_{\mathrm{a}} \cdot (r_2^2 - r_1^2)} \cdot \left[r_2^2 + r_1^2 - \frac{4 \cdot r_1^2 \cdot r_2^2 \cdot \ln\left(\frac{r_2}{r_1}\right)}{(r_2^2 - r_1^2)} \right]
\end{aligned} \tag{5.11}$$

5.4.1.4 Treatment of adiabatic boundaries

Because the stator is periodically symmetrical in the circumferential direction, the central planes of the teeth or slots are adiabatic boundaries. By definition, the terminal corresponding to the adiabatic surface is set to open circuit as shown in Fig. 5.8.

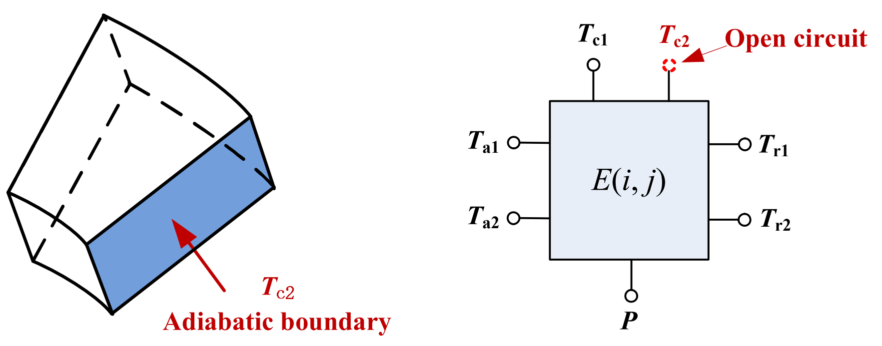

Fig. 5.8: Treatment of adiabatic boundary

5.4.2 Thermal conductivity of material

5.4.2.1 Slot liner insulation

As shown in Fig. 5.9, the slot liner insulation includes two layers of corona-resistant (CR) polyimide film and a layer of NHN composite insulation. The latter is a sandwich structure with a layer of polyimide film between two layers of Nomex.

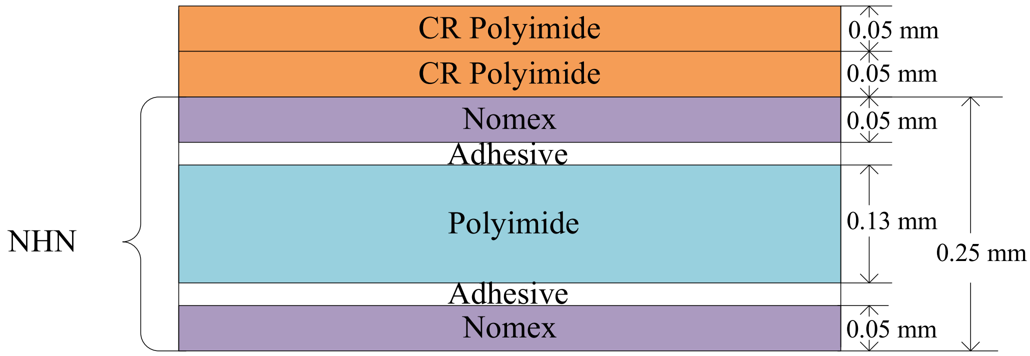

Fig. 5.9: Composition of slot liner insulation

According to DuPont's product manuals, the thermal conductivity of the insulation materials are listed in Table 5.4.

Table 5.4: Thermal conductivity of insulation materials

CR Polyimide	Nomex	Polyimide	Adhesive
$0.385\ \mathrm{W/(m \cdot K)}$	$0.094\ \mathrm{W/(m \cdot K)}$	$0.2\ \mathrm{W/(m \cdot K)}$	$0.2\ \mathrm{W/(m \cdot K)}$

According to the series connection, the equivalent thermal conductivity of the slot liner λ_{liner} can be obtained:

$$\lambda_{\mathrm{liner}} = \frac{\delta_{\mathrm{liner}}}{\sum_1^n \frac{\delta_{\mathrm{i}}}{\lambda_{\mathrm{i}}}}, \quad \text{with} \quad \delta_{\mathrm{liner}} = \sum_1^n \delta_{\mathrm{i}} \tag{5.12}$$

where λ_{i} is the thermal conductivity of material i, δ_{i} the thickness of material i, δ_{liner} the equivalent thickness of the slot liner.

5.4.2.2 Random-wound windings

The random-wound windings of high-speed motors are made of magnet wires and impregnated with resin. Because fill factor, impregnation and curing process differ from coil to coil, the equivalent thermal conductivity of winding varies strongly. In this section, FEM was used to calculate the equivalent thermal conductivity. The ideal distribution of magnet wire in an orthocyclic winding is shown in Fig. 5.10(a), where r is the radius of the copper, and R is the half distance between the centers of the adjacent magnet wires.

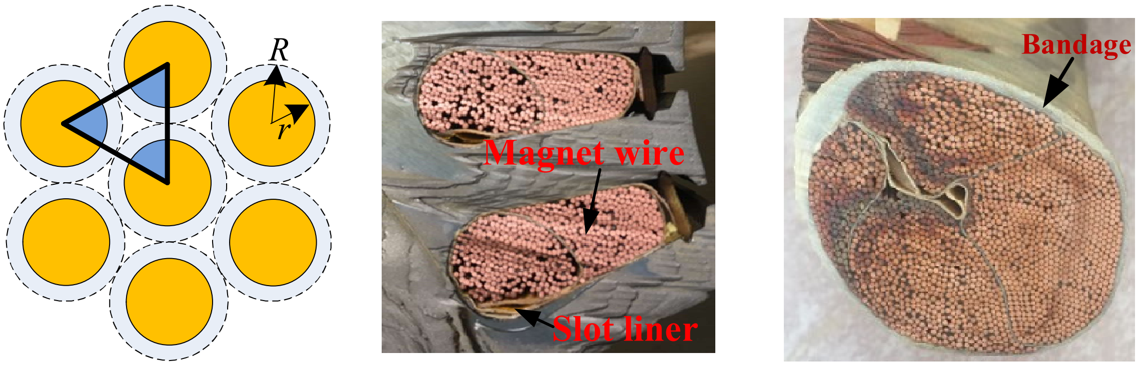

(a) (b) (c)

Fig. 5.10: Random-wound windings: (a) ideal distribution of magnet wires, (b) cross-section of coil sides in slots, (c) cross-section of a coil in and end winding

The copper fill factor S_f of an orthocylic winding as in Fig. 5.10(a) is defined as the ratio of the blue area to the total triangular area:

$$S_\mathrm{f} = \frac{0.5 \cdot \pi \cdot r^2}{\sqrt{3} \cdot R^2} \tag{5.13}$$

The diameter of the magnet wire used is 0.77 mm with an internal copper diameter of 0.7 mm. Thus the maximum fill factor can be calculated as $S_\mathrm{fmax} = 0.75$, if the wires are closely attached to each other. According to the actual cross-section of windings in Fig. 5.10(b) and 5.10(c), the S_f in slots is 44%, and in end windings is 72.5%.

Fig. 5.11(a) is a schematic of thermal conductivity calculation in x direction, where the thermal conductivity of copper wire λ_cu is known as 380 W/(m · K), and the space filled with resin is assumed as 0.2 W/(m · K). The left and right boundaries are set to constant temperatures T_1 and T_2 each, and then the heat flux q can be obtained using a FEM software as shown in Fig. 5.11(b).

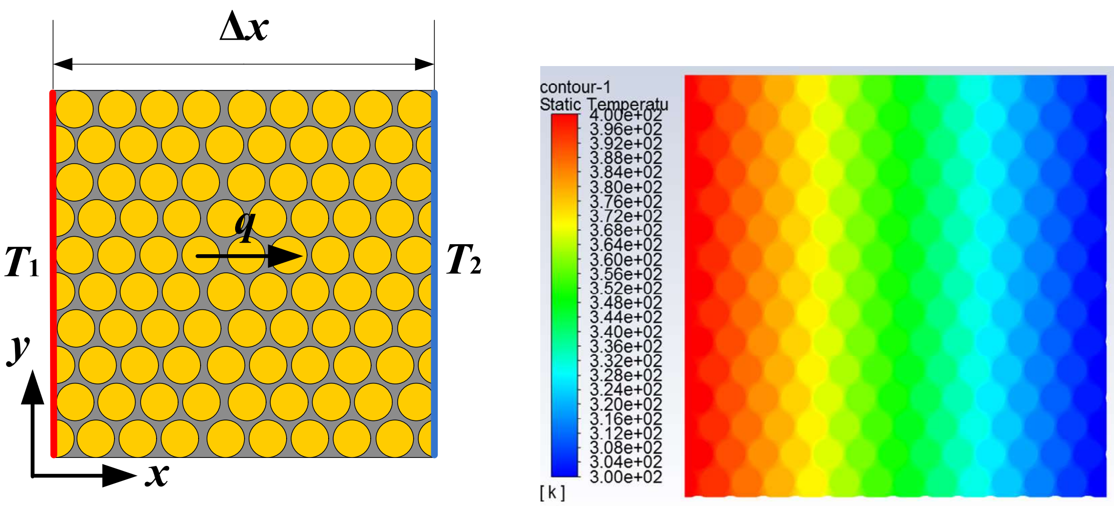

(a) Schematic diagram in the xy plane (b) Simulation results in x direction

Fig. 5.11: Thermal conductivity calculation of random-wound windings

By definition, the equivalent thermal conductivity λ_x in x direction can be expressed as:

$$\lambda_x = \frac{q \cdot \Delta x}{T_1 - T_2} \tag{5.14}$$

where Δx is the distance in x direction.

While r is kept constant, R is changed to get the thermal conductivities at different fill factors. Table 5.5 shows that increasing the fill factor can effectively improve the thermal conductivity in the xy plane.

Table 5.5: Thermal conductivity of random-wound windings in $\mathrm{W/(m \cdot K)}$

S_f	λ_x	λ_y	λ_{av}	S_f	λ_x	λ_y	λ_{av}
40%	0.458	0.452	0.455	50%	0.575	0.567	0.571
42%	0.474	0.480	0.477	70%	1.054	1.037	1.046
44% (in slots)	0.492	0.481	0.487	72.5% (end winding)	1.164	1.166	1.165
46%	0.522	0.509	0.515	75%	1.292	1.346	1.319

* λ_{av} is the average thermal conductivity in the xy plane.

The thermal conductivity along the direction of the wire can be obtained by ignoring the thermal conductivity of resin:

$$\lambda_a \approx \lambda_{cu} \cdot S_f \tag{5.15}$$

5.4.2.3 Laminated stator core

The actual stacking factor k_{Fe} of the laminated core is 98%. The laminates' gap is filled with resin and air, but the ratio is difficult to determine. In this dissertation, it is assumed that the gap is air-filled for safety. Thus, the equivalent thermal conductivity of the laminated core can be derived as:

$$\begin{aligned} \lambda_a &= \frac{1}{\frac{k_{Fe}}{\lambda_1} + \frac{1-k_{Fe}}{\lambda_2}} \\ \lambda_c &= \lambda_r = k_{Fe} \cdot \lambda_1 + (1 - k_{Fe}) \cdot \lambda_2 \end{aligned} \tag{5.16}$$

where λ_2 is the thermal conductivity of static air. The value is known as $0.025\ \mathrm{W/(m \cdot K)}$. λ_1 is the thermal conductivity of the silicon steel, which varies with the silicon content, as shown in Table 5.6. The silicon content of silicon steel used for the stator is about 3%, thus the thermal conductivity is $23\ \mathrm{W/(m \cdot K)}$.

Table 5.6: λ_1 varying with the silicon content [75]

Silicon content	1%	2%	3%	4%
λ_1	$40\ \mathrm{W/(m \cdot K)}$	$29\ \mathrm{W/(m \cdot K)}$	$23\ \mathrm{W/(m \cdot K)}$	$20\ \mathrm{W/(m \cdot K)}$

The calculated thermal conductivities of the laminated core are listed in Table 5.7.

Table 5.7: Thermal conductivity of laminated core

	λ_a	λ_c	λ_r
Laminated core	1.19 W/(m · K)	22.54 W/(m · K)	22.54 W/(m · K)

5.4.3 Evaporative heat transfer

5.4.3.1 Introduction to pool boiling

"When heat is applied to a surface in contact with a liquid, if the wall temperature is sufficiently above the saturation temperature, boiling occurs on the wall. Boiling may occur under quiescent fluid condition, which is referred to as pool boiling, or under forced-flow conditions, which is referred to as forced convective boiling" ([73], p. 636). Obviously, the immersion evaporative cooling is pool boiling. First tested by Nukiyama (1934), the saturated pool boiling curve and phenomena of water are depicted in Fig. 5.12, where four distinct heat transfer regimes can be divided: natural convection (A–B), nucleate boiling (B–C), transition boiling (C–D) and film boiling (above D).

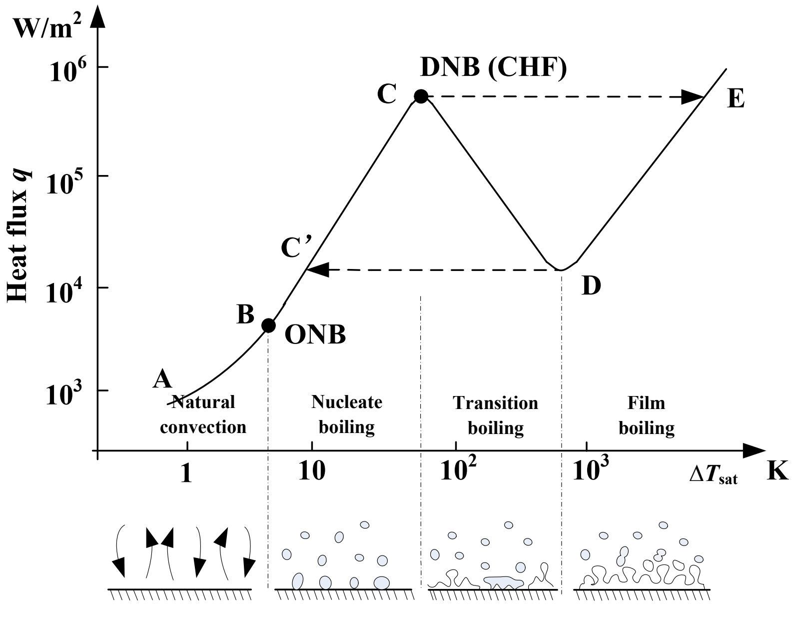

Fig. 5.12: Saturated pool boiling curve of water. ΔT_{sat} is the temperature difference between the surface and the saturation temperature of water [73].

The nucleate boiling is the most common and useful boiling condition, characterized by low overtemperature [72, 48]. It starts from the Onset of Nucleate Boiling (ONB) and ends at the Departure from Nucleate Boiling (DNB) or the Critical Heat Flux (CHF). Following the point DNB, if the heated surface is externally temperature controlled, the boiling curve runs along the solid line of C-D-E. Else if the heated surface is flux controlled, such as electrical-resistance elements, the boiling curve will jump directly from C to E along the dashed line, where the temperature of the heated surface will rise sharply. Therefore, in engineering applications, the heat flux exceeding the CHF of the liquid should be avoided [73].

5.4.3.2 Onset of Nucleate Boiling and Critical Heat Flux

L. Tadrist assumed that when the heat transfer coefficient of nucleate pool boiling is larger than that of natural convection, the corresponding heat flux is q_{ONB}, thus derived the expression [76]. For a smooth copper surface facing upward at $T_{\mathrm{s}} = 56°\mathrm{C}$, the measured q_{ONB} of HFE-7100 is $5,000\ \mathrm{W/m^2}$ [77].

The CHF q_{DNB} determines the maximum cooling limit of the immersion evaporative cooling. The expression for flat infinite heaters facing upward is [78]:

$$q_{\mathrm{DNB}} = 0.149 \cdot \rho_s^{0.5} \cdot H_{\mathrm{fg}} \cdot [g \cdot (\rho_{\mathrm{L}} - \rho_{\mathrm{s}}) \cdot \sigma]^{0.25} \tag{5.17}$$

where σ is the surface tension of the liquid in N/m, the other symbols are the same as those in (5.7).

Because of vapor accumulation near the surface, the inclination angle θ of the surface has an obvious effect on the CHF. For a smooth copper surface immersed in HFE-7100 at $T_{\mathrm{s}} = 56°\mathrm{C}$, the CHF achieves its maximum value $2.45 \cdot 10^5\ \mathrm{W/m^2}$ at 0° (upward-facing), next decreases slowly with θ from 0° to 90° (vertical), then decreases sharply when θ exceeds 90°, finally reaches the lowest value $4.3 \cdot 10^4\ \mathrm{W/m^2}$ at 180° (downward-facing) [77]. The calculated value according to (5.17) is $1.89 \cdot 10^5\ \mathrm{W/m^2}$, which gives a safe estimation for 0°–90°, but an overestimation for 90°–180°.

5.4.3.3 Nucleate Pool Boiling Correlations

Nucleate pool boiling is a complex two-phase fluid dynamics, which makes pure analytical analysis impossible. Therefore, the boiling correlations are usually determined empirically [73]. There are many correlations that generally fall into two categories:

- Correlations with empirical constants related to liquid-surface combination, e.g. bubble agitation correlation according to Rohsenow [79].
- General correlations without empirical constant, e.g. reduced pressure correlation according to Cooper, which is highly recommended for general use and has been widely used for the calculation of heat transfer of refrigerant [73, 48].

For new fluids, such as HFE-7100, the empirical constant is difficult to obtain, so the correlation of Cooper is adopted [80]:

$$\begin{aligned} h_{\mathrm{evp}} &= 55 \cdot \frac{\mathrm{W}^{0.33}}{\mathrm{m}^{0.66} \cdot \mathrm{K}} \cdot q^{0.67} \cdot M_{\mathrm{r}}^{-0.5} \cdot p_{\mathrm{r}}^{m} \cdot (-\log_{10} p_{\mathrm{r}})^{-0.55} \\ \text{with} \quad m &= 0.12 - 0.2 \cdot \log_{10}(R_{\mathrm{p}}/\mu\mathrm{m}) \end{aligned} \tag{5.18}$$

where h_{evp} is the nucleate pool boiling heat transfer coefficient, p_{r} the reduced pressure, defined as $p_{\mathrm{r}} = p_{\mathrm{s}}/p_{\mathrm{crit}}$, p_{crit} the critical pressure, M_{r} the relative molar mass, dimensionless, and R_{p} the mean surface roughness in μm ($R_{\mathrm{p}} = 1$ μm for unspecified surfaces [80], also for this dissertation). Higher roughness can enhance the heat transfer coefficient and the CHF [81], but also easily lose its effect due to fouled surface [73].

5.4.3.4 Evaporation thermal resistance

By definition, evaporation thermal resistance R_{evp} can be expressed as:

$$R_{\mathrm{evp}} = \frac{1}{h_{\mathrm{evp}} \cdot A} \tag{5.19}$$

where A is the area of the evaporation surface.

Because (5.19) implicitly contains heat flux $q = P/A$, R_{evp} is essentially a power controlled temperature rise source, similar to the current controlled voltage source in the circuit principle. Therefore, the circuit model and simplified symbol are shown in Fig. 5.13.

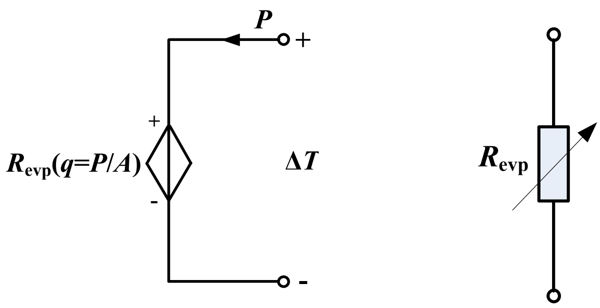

(a) Circuit model (b) Symbol

Fig. 5.13: Evaporation thermal resistance

5.4.3.5 Nucleate Pool Boiling curve of HFE-7100

According to Fourier's law of heat transfer, the wall overtemperature ΔT_{sat} can be expressed as:

$$\Delta T_{\mathrm{sat}} = R_{\mathrm{evp}} \cdot P = \frac{q}{h_{\mathrm{evp}}} \propto q^{0.33} \tag{5.20}$$

As shown in Fig. 5.14, the dashed line is the calculated boiling curve according to (5.20), while the solid line is the measured curve (upward-facing) cited from [77]. The calculated curve is overestimated in the low overtemperature range, while it is underestimated in the high overtemperature range. The diamond markers denote the heat flux of the end windings and stator core in the final prototype (see Table 5.8). The heat flux of the stator core is larger than q_{ONB} but far less than q_{DNB} (even for downward-facing case), whereas the average heat flux of the end windings is less than q_{ONB}. Thus, nucleate boiling occurs at the stator core, while natural convection occurs at the end windings. The theoretical analysis is consistent with the experimental phenomenon of the final prototype. Intense nucleate boiling occurs at the stator core's outer surfaces and ventilating ducts, while mild nucleate boiling occurs at the end windings, as shown in Fig. 6.10.

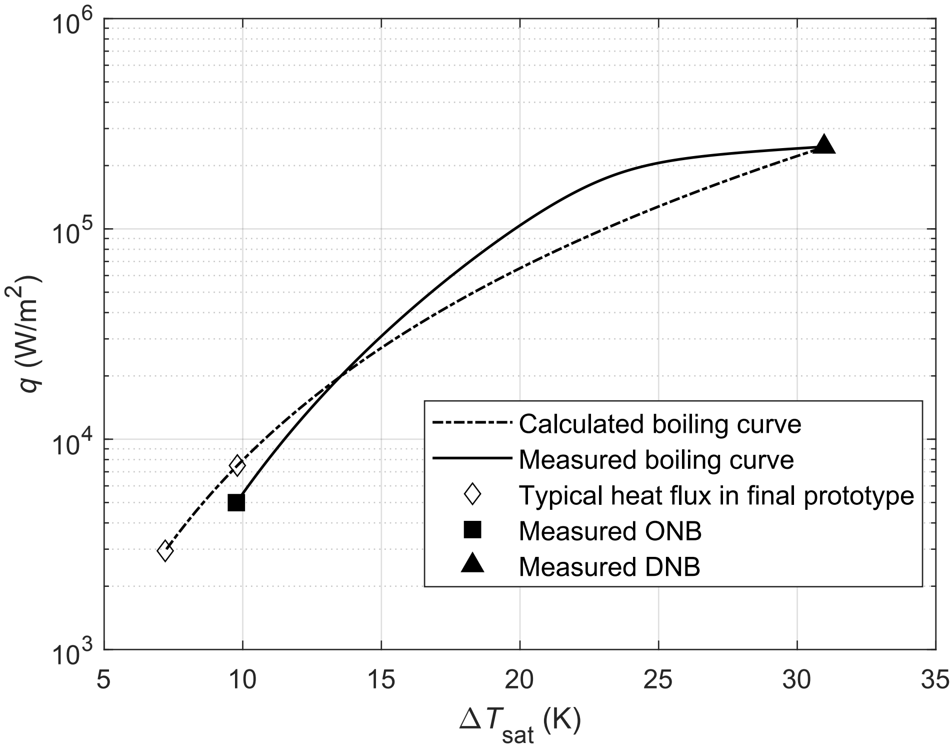

Fig. 5.14: Nucleate pool boiling curve of HFE-7100 at $T_s = 56°C$ (measured data cited from [77])

The inclination angle has a weak effect on the nucleate boiling curve in the low overtemperature range ($\Delta T_{sat} < 13$ K) [77], where the final prototype runs. Therefore, all evaporation surfaces in the machine are assumed to be upward-facing.

In this dissertation, all wet surfaces are assumed to be evaporation surfaces for the following reasons:

- The nucleate boiling and natural convection coexist on the stator surface of the final prototype. Bubbles generated will enhance the convective disturbance, making it difficult to accurately calculate the heat transfer coefficient of natural convection.

- In the natural convection regime, the heat transfer coefficient calculated by the Cooper correlation is underestimated [76] and thus gives a safe result.

Due to the high heat transfer coefficient of evaporative cooling (see Table 5.8), the overtemperature in the final prototype is less than 10 K, as shown in Fig. 5.14. Therefore, it will not bring too much error to the total temperature rise of the windings despite the above-mentioned assumptions.

Table 5.8: Approximate heat flux and heat transfer coefficient of the final prototype

	Losses	Surface area	Heat flux	Heat transfer coefficient
	W	m^2	W/m^2	$W/(m^2 \cdot K)$
End windings	548	0.186	$2.946{\cdot}10^3$	440
Stator core	$2.189 \cdot 10^3$	0.292	$7.497{\cdot}10^3$	821

* The stator core losses contain copper losses in slots and iron losses.

5.4.4 Thermal network of stator

5.4.4.1 Description of the stator under test

Fig. 5.15(a) shows a photo of the tested stator. The end winding on supply side is continuously wrapped by 1.6 mm thick glass tape, while the passive end winding is discontinuously wrapped. The purpose is to compare the effect of bandage layout on temperature rise. The stator core is axially divided into three segments by "H" beams forming two ventilating ducts. This layout can significantly increase the evaporation area. The end plates and ribs are used to press them together. The stator's inner circle has a glass fiber sleeve to simulate the actual design of the final prototype. Fig 5.15(b) are excerpts of the stator core drawings. For simulation, only 1/2 slot and 1/2 tooth in the red box, namely one 48th of the stator, was modeled. The teeth and slots are simplified into arc segments according to the principle of area equivalence. A ray (the blue dotted line) passing through the red point from the center is used as the boundary between the tooth and slot. The red point is the intersection of one parallel edge of the tooth and the average radius of the slot.

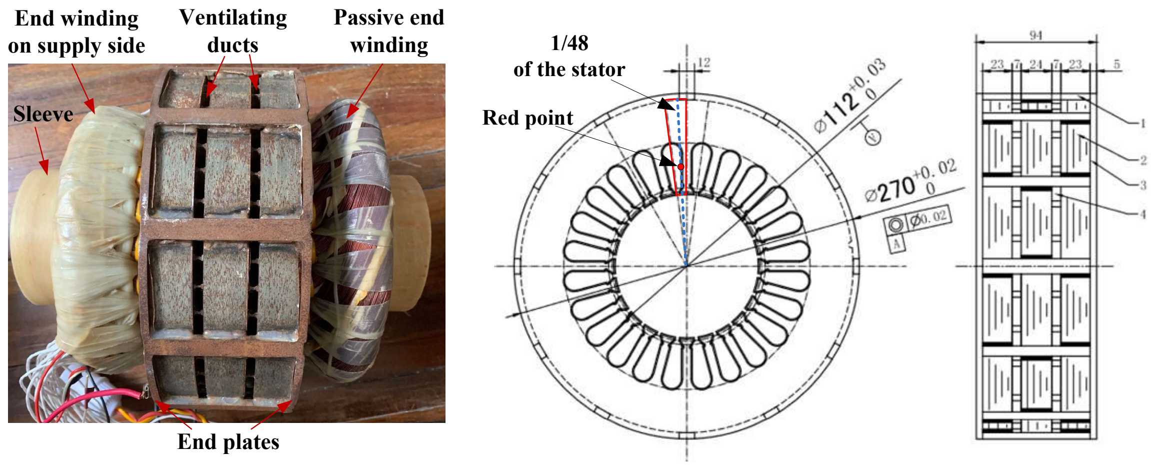

(a) Photo (b) Core drawings

Fig. 5.15: The tested stator

Fig. 5.16 shows an axial schematic of the stator, where the layers 1, 2, and 3 correspond to core segments, the layers 4, 5, 6, and 7 to the ventilating ducts and the straight parts of the end windings. The end 1 and end 2 correspond to the passive end winding and end winding on supply side, respectively.

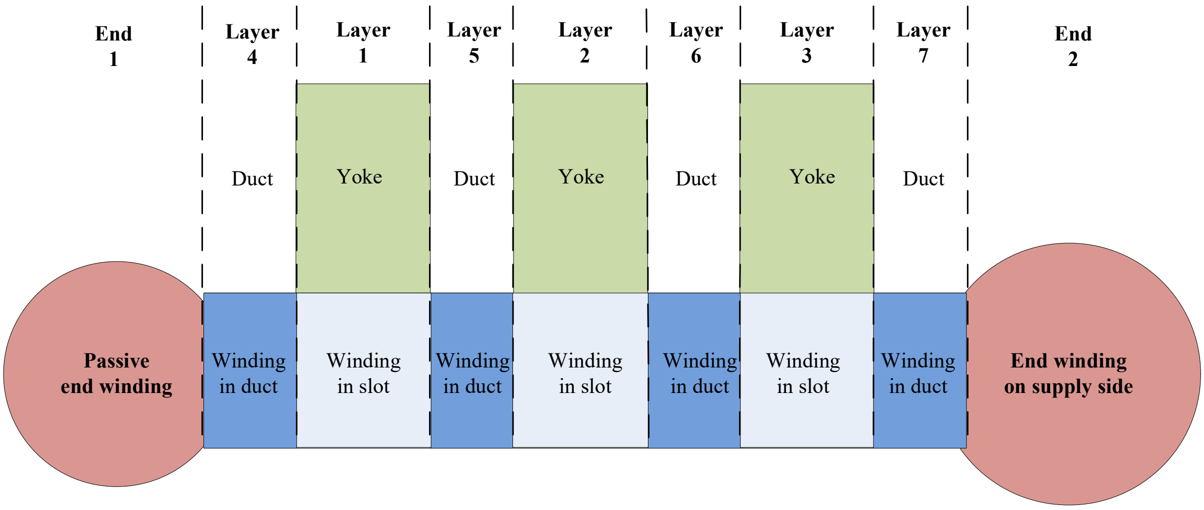

Fig. 5.16: Axial schematic of the stator

5.4.4.2 Thermal network of layers 1, 2, and 3

Layers 1, 2, and 3 have the same cross-section. In the following, layer 1 is taken as representative for these similar layers. Fig. 5.17 shows 1/48 of the cross-section of this layer seen from the passive side, where 1 represents the winding in slot, 2 denotes the tooth, 3 and 4 represent the yoke parts. The central planes of the teeth and slots are adiabatic boundaries. The front and rear faces of element 1 are layer interfaces. The other faces in contact with liquid are evaporative boundaries. The red lines indicate the position of the slot liner and the blue line indicates the position of the slot wedge.

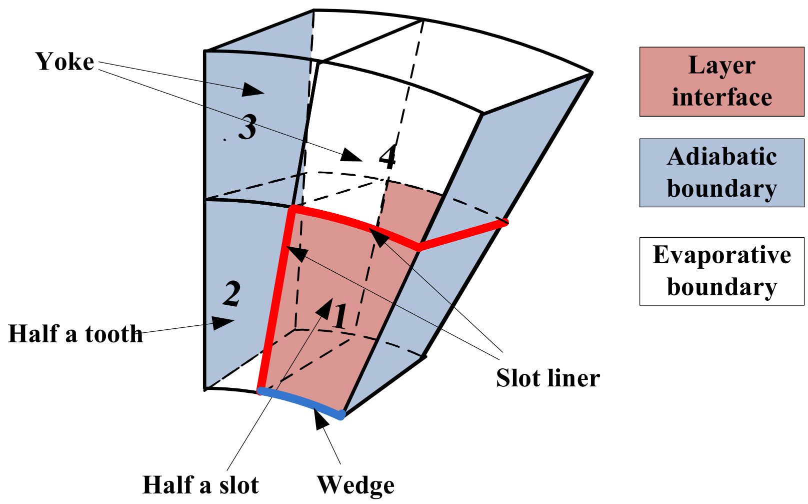

Fig. 5.17: Geometric sketch of layer 1

Fig. 5.18 shows the thermal network of layer 1, where the masked blocks incorporate the T-network of arc segments (see Section 5.4.1). The terminals are connected according to the contact relationship of the elements. The terminals corresponding to

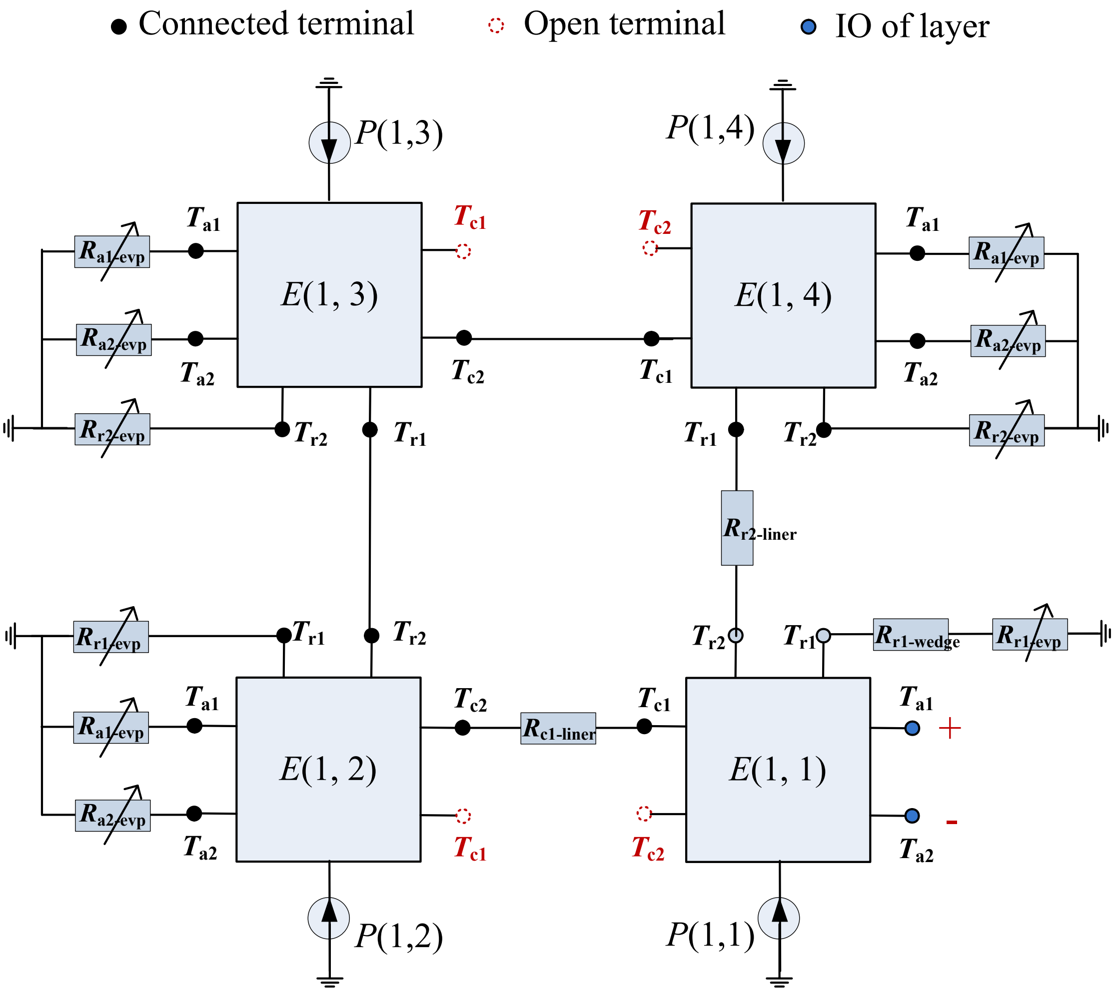

Fig. 5.18: Thermal network of layer 1

the adiabatic surfaces are set open, and the evaporative surfaces are represented by connecting the evaporation thermal resistance. The ground represents the temperature of the surrounding liquid. The thermal resistances of the slot-liner and wedge are placed between the corresponding terminals. The thermal conductivity of the wedge is 0.2 W/(m · K). $E(1{,}2)$ is taken as an example: $E(1{,}2)$ represents the T-network of the second element of layer 1; P (1,2) is its internal losses; the terminals T_{r1}, T_{a1} and T_{a2} are connected to the corresponding evaporation thermal resistance; $R_{\mathrm{c1-liner}}$ represents the slot-liner; T_{c1} terminal is set open; T_{r2} is directly connected to the T_{r1} of $E(1{,}3)$. In addition, T_{a1} and T_{a2} of E (1,1) are the external interfaces of this layer.

5.4.4.3 Thermal network of layer 4–7

As layers 4–7 have the same cross-section, layer 4 is taken as an example. Fig. 5.19(a) shows 1/48 cross-section of layer 4. This layer only contains windings, so it can be represented by a single element. The thermal network of layer 4 is shown in Fig. 5.19(b).

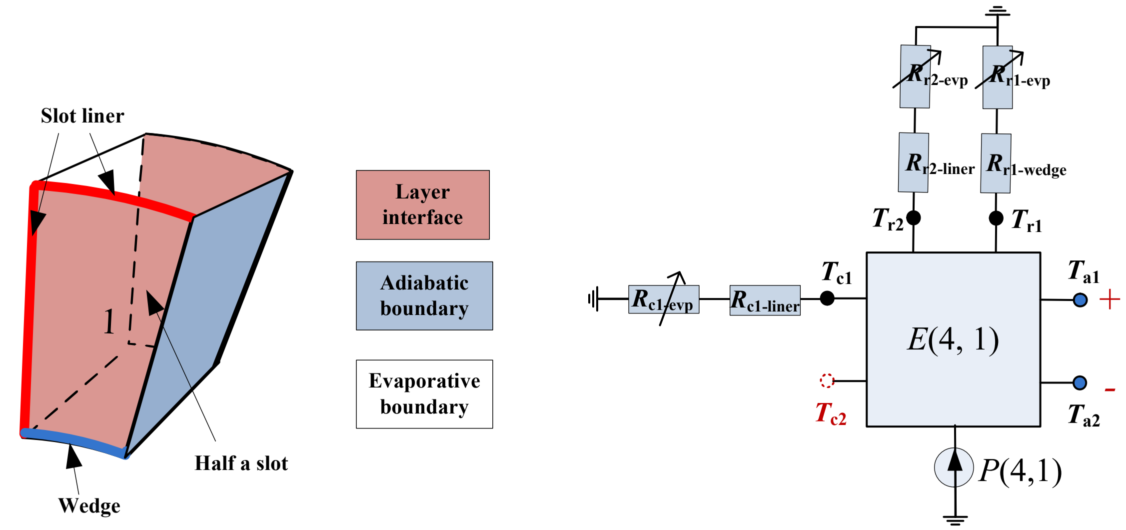

(a) Geometric sketch (b) Thermal network

Fig. 5.19: Layer 4

5.4.4.4 Thermal network of end-winding

The complex end winding is simplified into a toroid, the cross-section of which is shown in Fig. 5.10(c). 1/48 of the toroid can be further simplified as a cylinder ignoring its curvature, as shown in Fig. 5.20(a). The z-axis of the cylinder is along the magnet wires in the end windings.

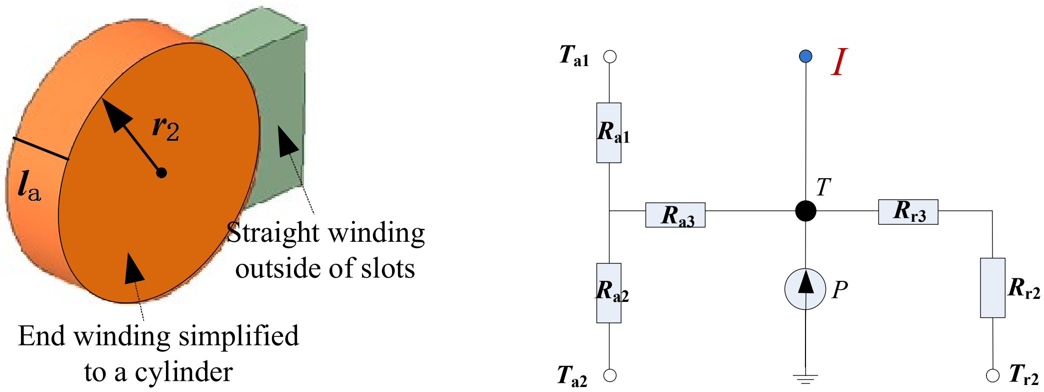

(a) Geometric sketch (b) Thermal network

Fig. 5.20: End winding equivalent to a cylinder

A cylinder is a special arc segment, where $r_1 \to 0, \alpha = 2\pi$. Then the thermal resistances for radial heat flow of the cylinder can be deduced from (5.11):

$$R_{r1} = \infty, \quad R_{r2} = \frac{1}{4\pi \cdot \lambda_r \cdot l_a}, \quad R_{r3} = \frac{-1}{8\pi \cdot \lambda_r \cdot l_a} \tag{5.21}$$

Since a cylinder does not have circumferential heat flow, there are no circumferential terminals either. However, an interface between the end winding and the adjacent layer is necessary. Fig. 5.20(a) shows the connection of the end winding and axially straight part of the winding. Because each magnet wire in the slots extends directly into the end winding and the magnet wire's thermal conductivity is excellent, the heat conveyed from the slots into the end winding can be considered as a uniform internal heat source. Thus the T-network of the cylinder is shown in Fig. 5.20(b) with an external interface I connected directly to the T point. Both axial faces of the end winding are periodically adiabatic boundaries. Fig. 5.21(a) shows that a bandage covers the outer ring of the end winding. Fig. 5.21(b) shows the thermal network of the passive end winding.

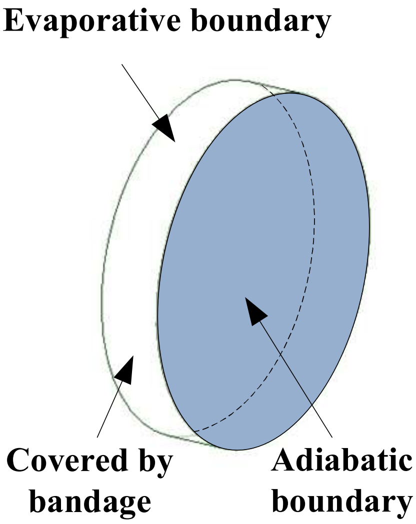

(a) Geometric sketch

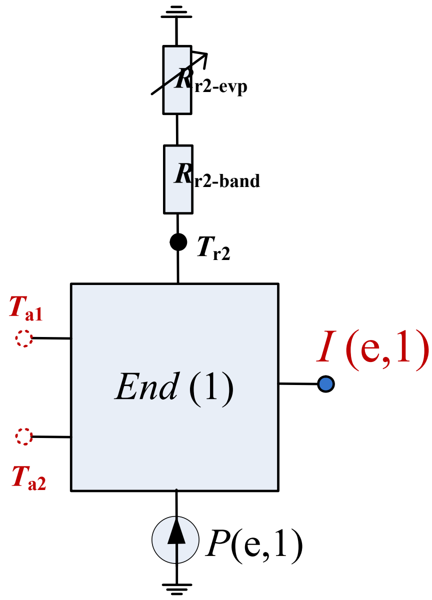

(b) Thermal network

Fig. 5.21: End 1

5.4.5 Total thermal network model of evaporation side

Fig. 5.22 gives the total thermal network model of the evaporation side, where the boxes represent the thermal network of the corresponding layers. They are connected according to Fig. 5.16. The nodal analysis method can be used to determine the temperature rise.

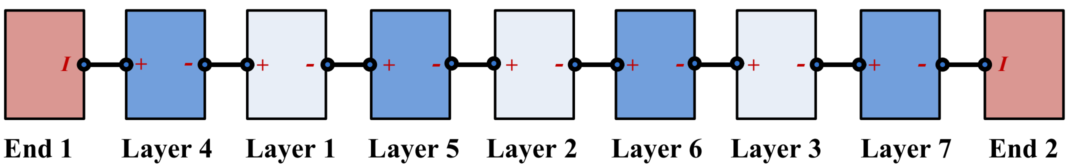

Fig. 5.22: Total thermal network model of evaporation side

5.5 Experimental verification

5.5.1 Experimental setup

Fig. 5.23 shows a photo of the evaporative cooling experimental device, the operating principle of which has been described in Section 5.2.2. Table A8 in the Appendix lists the instruments for the experimental setup.

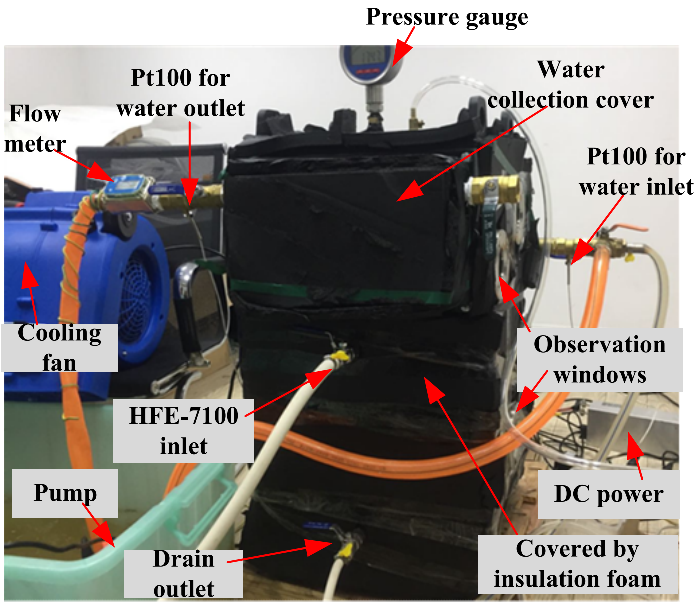

Fig. 5.23: Evaporative cooling experimental device

5.5.2 Withstand voltage tests

Withstand voltage tests, according to IEC 60034-1:2010, have been carried out to verify the insulation characteristics of HFE-7100. The leakage currents are listed in Table 5.9.

Table 5.9: Withstand voltage test results

Before immersion	1.92 mA	After immersion	2.00 mA

5.5.3 Condensation experiment

The heat exchange capacity of all condensation tubes exceeds the power limit of the laboratory. Therefore, only one row of tubes has been used while the others were blocked by plugs. Since the liquid condensed from the upper row will drip onto the lower tubes to affect observation, the bottom row is used by default, as shown in

Fig. 5.24(b). The top row ran water only when the influence of non-condensable gas was studied.

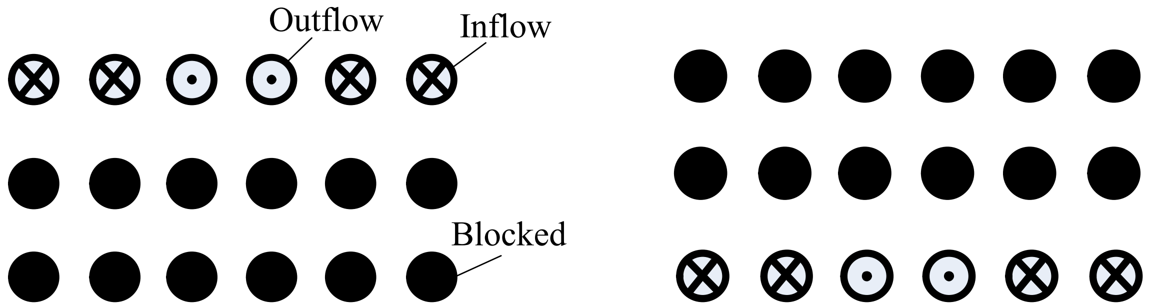

(a) Water flows through the top row (b) Water flows through the bottom row

Fig. 5.24: Diagram of the condensation tubes

In one row, 3 sets of 2 parallel smooth tubes are connected in series. The specifications of the smooth tubes are listed in Table 5.10.

Table 5.10: Specifications of the smooth tubes

Inner diameter	Outer diameter	Length	Material
23 mm	27 mm	450 mm	SAE 304 stainless steel

5.5.3.1 Surface heat dissipation test

This test aims to determine the thermal resistance of surface heat dissipation R_2, as described in Section 5.3. The input power of the stator was measured as the total losses P_{all}. There is no cooling water. Most of the heat passes through the casing wall and the insulation foam and then dissipates by natural convection. The rest of the heat passes through the observation windows. Table 5.11 records the surface heat dissipation test results, where T_{s} is the measured temperature of the saturated vapor, T_{ambient} the measured ambient temperature.

Table 5.11: Surface heat dissipation test results

No.	P_{all} (W)	T_{ambient} (°C)	T_{s} (°C)	R_2 (K/W)
1	316	17.5	67.9	0.160
2	338	16.7	71.5	0.162
3	391	16.6	77.6	0.156
4	396	12.5	75.4	0.159

Then R_2 can be calculated as:

$$R_2 = \frac{T_{\text{s}} - T_{\text{ambient}}}{P_{\text{all}}} \tag{5.22}$$

The average value of R_2 =0.159 K/W serves for further considerations.

5.5.3.2 Influence of water velocity on heat transfer coefficient

The water temperature T_{water} (average temperature of inlet and outlet) was kept around 40°C by adjusting the cooling fan, while the saturated vapor temperature of HFE-7100 T_{s} was kept around 68°C by adjusting the input electric power P_{all}. Three different water flow rates Q were tested, as shown in Table 5.12. The experimental results indicate that the heat transfer capacity of the condenser increase with the flow rate.

Table 5.12: Test results at different flow rates

No.	Q (L/min)	P_{all} (W)	T_{water} (°C)	T_{s} (°C)	T_{ambient} (°C)
1	3.2	2,679	40.3	68.0	21.5
2	8.0	3,312	40.2	67.6	22.0
3	15.0	3,909	40.8	67.8	18.0

As shown in Fig. 5.29(a), strong condensation occurs outside the bottom tubes when water flows through the bottom tubes. However, some dew on the outside of the middle and top tubes indicates that slight condensation occurs there too. The upper two rows of tubes transfer heat to water by heat conduction of the tube walls. This cooling channel is represented by R_3 in the thermal network model of the condensation side (see Fig. 5.5). When R_3 branch is ignored, the calculated value T_{sc1} is obviously higher than the test results, and the smaller the water flow rate, the greater the error, as shown in Fig. 5.25. Assuming R_3 is a fixed value, then $R_3 = 0.052$ K/W can be determined by trial-and-error method until the calculated value T_{sc2} is consistent with the test results. Table 5.13 gives the calculated results at different flow rates.

Table 5.13: Calculated results at different flow rates (two tubes in parallel)

No.	Q	u	Re	T_{sc1}	T_{sc2}	h_{c}	h_{f}
	L/min	m/s		°C	°C	$\mathrm{W/(m^2 \cdot K)}$	$\mathrm{W/(m^2 \cdot K)}$
1	3.2	0.064	2,249	83.4	72.0	1,008	392
2	8.0	0.16	5,613	73.3	67.0	920	1,083
3	15.0	0.30	10,633	73.3	67.8	867	1,999

* T_{sc1} is the calculated saturated vapor temperature ignoring the R_3 branch; T_{sc2} is the calculated saturated vapor temperature considering the R_3 branch.

Fig. 5.26 shows that the convection heat transfer coefficient from the tube inside to water h_{f} increases with the flow rate. In contrast, condensation heat transfer coefficient from vapor to the outside of the tube h_{c} decreases slightly with the increase of flow rate, because the increase of the heat transfer capacity thickens the liquid film outside the tubes. It is worth noting that when the water flow in the tubes is intense turbulence ($Re > 10,000$), h_{f} is more than twice h_{c}. It is necessary to use finned tubes to strengthen condensation heat transfer to achieve comparable figures.

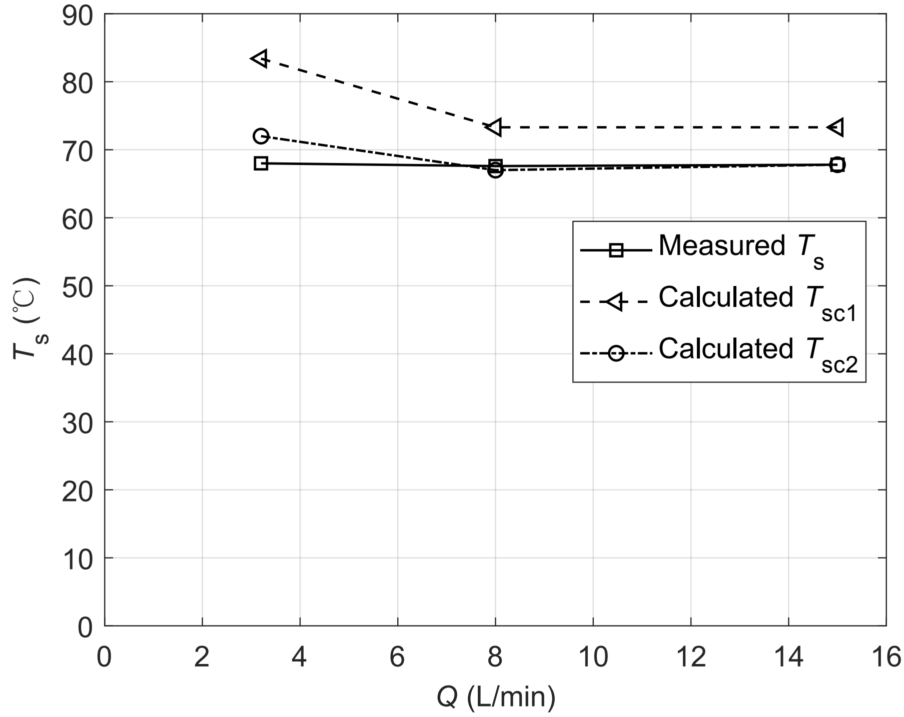

Fig. 5.25: Measured and calculated T_s

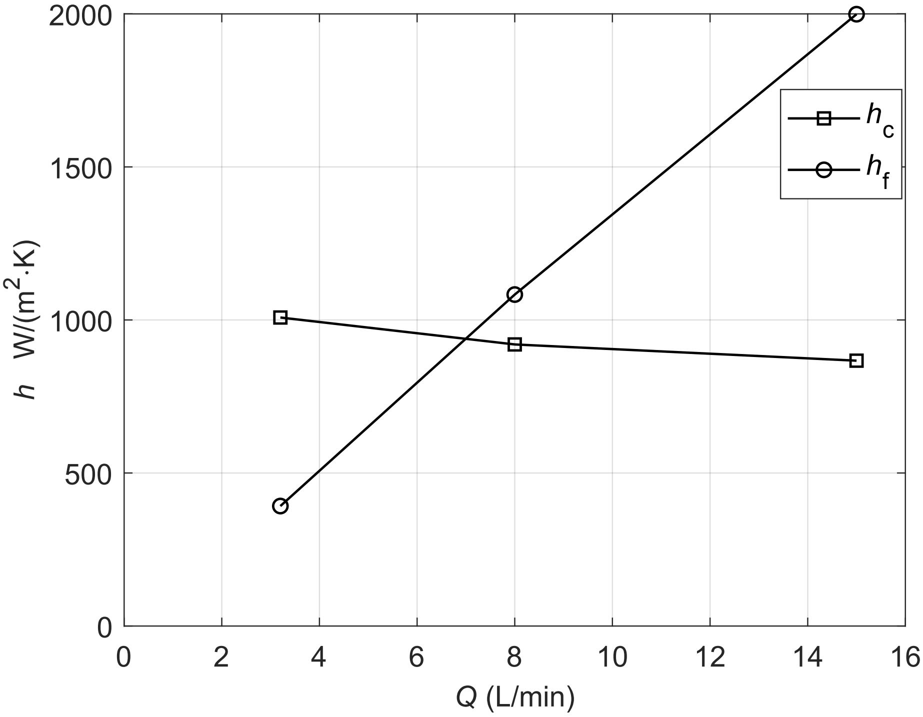

Fig. 5.26: Heat transfer coefficient vs. flow rate

5.5.3.3 Influence of non-condensable gas on condensation heat transfer

Even a small amount of non-condensable gas will significantly reduce the condensation heat transfer coefficient [82, 72]. Fig. 5.27 shows that when a mixture of vapor and non-condensable gas encounters a cold tube wall, the vapor condenses into a liquid. In contrast, the non-condensable gas accumulates around the tube, forming a gas layer, hindering the condensation and heat exchange process. The above references study a forced circulation system, where its vapor and the non-condensable gas mix uniformly. However, the device used in this work is based on a slow natural circulation process. When air (non-condensable gas) penetrates into the vessel, it tends to concentrate in the upper part of the vessel (the air density is about 1/8 of the one of HFE-7100), not mix uniformly with the vapor of HFE-7100.

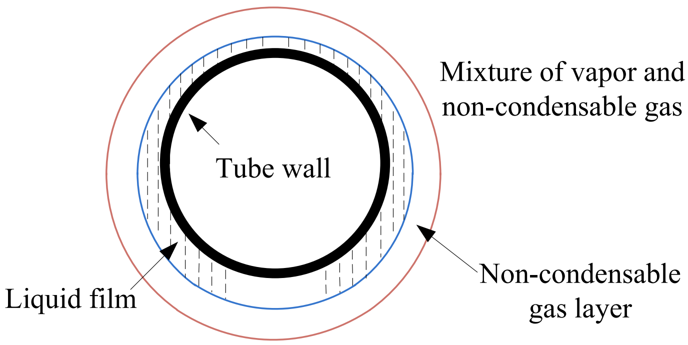

Fig. 5.27: Non-condensable gas accumulation around the condenser tube

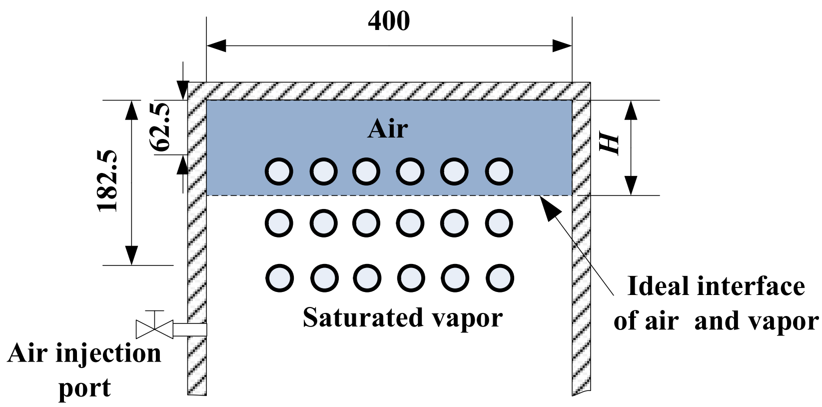

Fig. 5.28: Schematic diagram of the ideal state of air in the device (the depth is 400 mm)

The internal pressure of the vessel was adjusted to the normal atmospheric pressure first, and then the air gas was injected into the vessel by a scaled syringe from the HFE-7100 inlet. Fig. 5.28 shows an ideal state where the injected air is located in the upper part of the vessel and entirely separated from the heavier vapor. H is the distance from the interface to the top plate. It is an intuitive indicator of non-condensable gas quantity used to establish a position relationship with the tubes. In fact, due to internal circulation disturbances and gas diffusion, there will be a transition zone where the air can reach farther down than H.

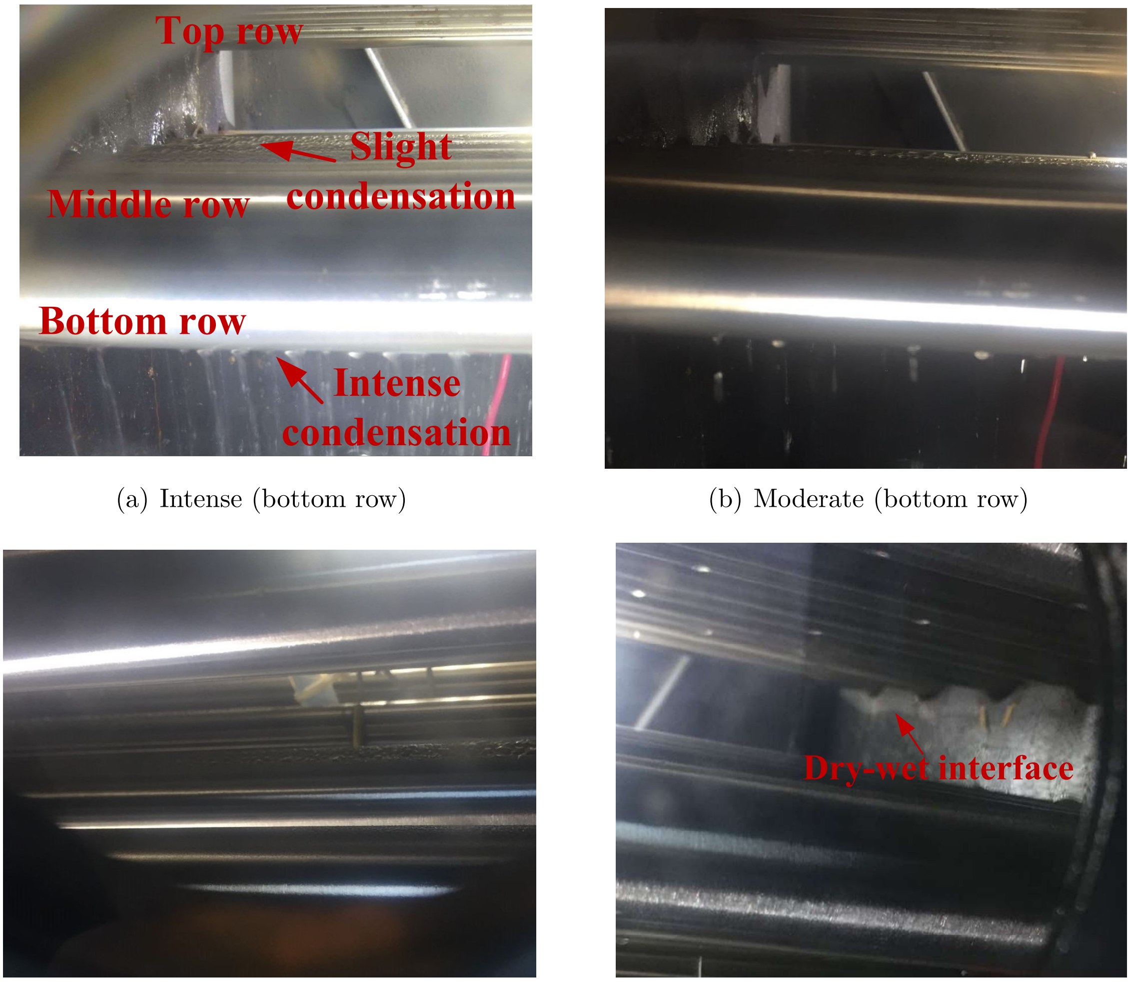

(a) Intense (bottom row)

(b) Moderate (bottom row)

(c) Stop (bottom row)

(d) Nearly stop (top row)

Fig. 5.29: Condensation phenomena

Flow rate and both temperatures of the cooling water and saturated vapor inside the vessel were kept approximately constant during the quantitative injection of air into the vessel in order to study the influence of non-condensable gas on the condensation heat transfer. After a certain amount of air was injected each time, the data was recorded when the internal state had been stable. When the condensation had stopped (see Fig. 5.29(c) and Fig. 5.29(d)), indicating that the non-condensable gas has completely surrounded the condensation tubes and prevented the condensation process, the further air injection was stopped.

The bottom row was chosen as the primary research object for easier observation of the condensation phenomenon. The influence of the content of non-condensable gases on the condensation heat transfer of the bottom row is shown in Table A10 in the

Appendix. In contrast, the results of the top row are shown in Table A11 in the Appendix.

In the thermal network model of the condensation side, as shown in Fig. 5.5, non-condensable gas mainly affects the condensation heat transfer power P_1, which is difficult to calculate accurately due to non-condensable gas. Therefore, assuming that non-condensable gas does not affect R_2 and R_3, P_1 can be indirectly calculated by the following formula:

$$\begin{aligned} P_1 &= P_{\text{all}} - P_2 - P_3 \\ &= P_{\text{all}} - \frac{T_{\text{s}} - T_{\text{ambient}}}{R_2} - \frac{T_{\text{s}} - T_{\text{water}}}{R_3} \end{aligned} \tag{5.23}$$

where R_2 and R_3 have been determined by experiment before and the other variables are measured quantities.

As shown in Table A10 and Table A11 in the Appendix, the results of P_1 in the last line are all nearly 0, which is consistent with the observed disappearance of condensation outside the tubes, and further proves the accuracy of the thermal network model.

Fig. 5.30 reflects that, with the same volume of non-condensable gas, the effect on the top tubes is stronger than that on the bottom tubes because the air is concentrated in the upper part. For the bottom tubes, the test results show that when the volume of non-condensable gas accounts for less than 1/3 of the total space from the tubes to the top plate ($H < 60$ mm), the effect of non-condensable gas on condensation is negligible. When it is more than 1/3, the effect is obvious, and when it is more than 2/3 ($H > 120$ mm), condensation almost stops. The phenomenon indicates that air and vapor are not strictly separated in space. There is a mixed transitional zone where the air content is gradually reduced from top to bottom. The air can actually reach a larger distance than H from the top plate of the vessel. This inference can be directly proved by another phenomenon. As shown in Fig. 5.29(d), after a certain amount of air has been injected, an obvious dry-wet interface appears on the inner wall of the vessel. The wall above the interface is dry without any condensation, while the wall below the interface is wet (the condensation on the inner wall of the vessel corresponding to the surface heat dissipation). The interface position is not fixed but presents a low-frequency fluctuation that reflects internal disturbance.

Fig. 5.31 shows the variation of saturated vapor pressure with temperature, which still follows (5.1) unaffected by the non-condensable gas. The reason is that the non-condensable gas is concentrated in the upper part, which has no influence on the boiling of the liquid.

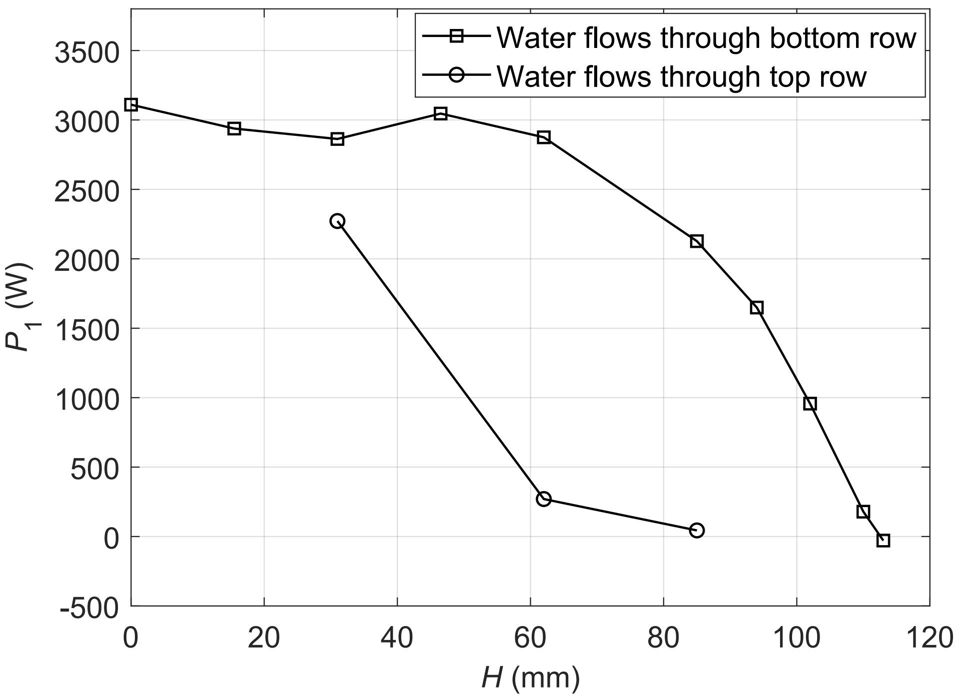

Fig. 5.30: P_1 vs. H

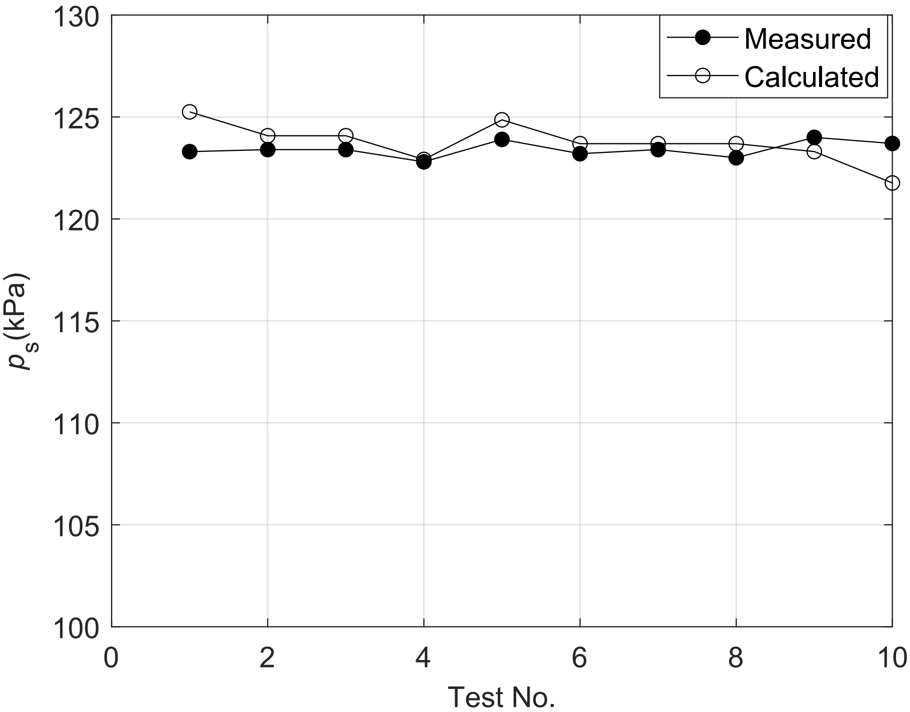

Fig. 5.31: Experimental verification of p_{s}

5.5.4 Evaporation experiment

Since the evaporative heat transfer coefficient depends on pressure p_s and heat flux q according to Cooper correlation, two groups of experiments were designed: (1) variable heat flux q at constant pressure p_s; (2) variable pressure p_s at constant heat flux q.

5.5.4.1 Variable heat flux q at constant pressure p_s

The stator input power was adjusted from 500 W to 1,000 W by an AC voltage regulator (the maximum voltage limits the maximum power). The step length was 100 W. To further increase the power, a 48 VDC power source (voltage non-adjustable) was used to supply the stator with a total power of 1,736 W. The heaters were not working. The internal pressure p_s was kept at 110 kPa by adjusting the cooling water temperature. As shown in Table 5.14, when the total input power is measured 1,000 W, the copper losses of the winding are dominant. Therefore, the total input power is assumed as copper losses in this experiment.

Table 5.14: Composition of losses of the stator fed by the 50 Hz AC voltage regulator

Input power	Phase current	Phase resistance	Copper losses	Other losses
1,000 W	9.4 A	3.66 Ω (at 86.6°C)	971 W	29 W

Fig. 5.32 shows a large number of bubbles coming out of the ventilating ducts, which corresponds to the copper losses in slots. Because the end winding on the supply side was continuously wrapped by glass tape, the boiling is relatively mild. Fig. 5.33 shows that the boiling on the passive end winding is intense and concentrated on the unwrapped areas.

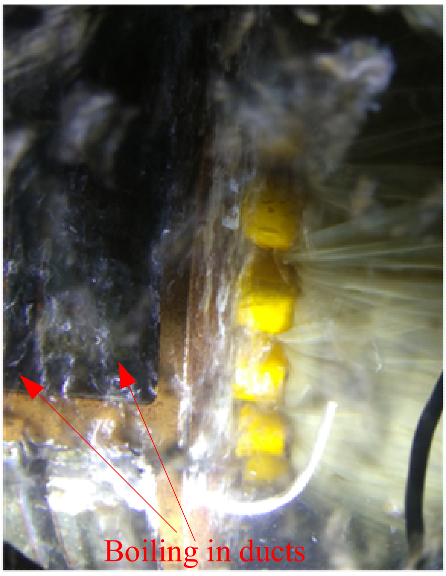

Fig. 5.32: Boiling of the end winding on supply side and stator core

Fig. 5.33: Boiling of the passive end winding

There are 14 Pt100 elements in the winding: 4 sensors for each end winding, evenly distributed circumferentially; 6 sensors located in the slots, evenly distributed circumferentially, radially located between the upper and lower conductors, and axially located at the center of the layer 3. There are also 4 Pt100 elements for liquid temperature measurement: two of them are located near the end windings, and the others in the ventilating ducts. Since the core temperature is difficult to measure accurately by Pt100, only the temperature rise of the windings was measured. Table A12 in the Appendix lists the detailed tested results of all Pt100 elements at different copper losses.

Because the resin in the windings of the layers 4 and 7 (see Fig. 5.16) is easily drained during the curing process, the liquid can directly contact the magnet wires. Thus the thickness of the slot liner of these two layers is set to 0. Table 5.15 compares the measured and calculated temperature rise at different copper losses, where the measured temperature rise of each part is the average value of all sensors in this part.

Table 5.15: Experimental verification of calculated temperature rise (K)

Copper losses (W)		1,736	1,000	900	800	700	610	500
Passive end winding	Measured	26.3	16.0	14.5	13.2	11.5	9.8	7.6
	Calculated	28.1	17.2	15.7	14.1	12.5	11.1	9.4
End winding on supply side	Measured	49.3	30.4	27.3	23.6	20.6	17.5	15.1
	Calculated	46.6	28.7	26.2	23.6	21.1	18.8	16.1
Windings in slots	Measured	32.0	20.0	18.0	16.0	14.0	12.0	9.7
	Calculated	34.8	22.3	20.5	18.8	16.9	15.3	13.5

Fig. 5.34 shows that the temperature rise increases linearly with the copper losses, and the calculated value is in good agreement with the measured value. The temperature rise of the continuously wrapped end winding on the supply side is significantly higher than the discontinuously wrapped passive end winding. The measured results in the slots are lower than the calculated values. The reason is that the gaps in the slots are not completely filled with resin, as shown in Fig. 5.10 (b), and liquid will enter the gaps, thus enhancing the evaporative heat transfer effect.

In order to further reveal the relationship between evaporative heat transfer coefficient and heat flux, a generalized thermal resistance was defined as the ratio of temperature rise to copper losses, as shown in Fig. 5.35. When the copper losses exceed 900 W, the thermal resistance slightly decreases with the increase of losses, which is consistent with the Cooper correlation that the evaporative heat transfer coefficient increases with the heat flux. However, when the losses are below 900 W, the measured thermal resistances are apparently lower than the calculated values. The reason may be that in the low heat flux range, there is not sufficient overtemperature to make the fluid boil, and heat is dissipated by natural convection, the heat transfer coefficient of which is larger than the value calculated by the Cooper correlation [76]. This inference is consistent with the weak boiling phenomenon observed at low copper losses.

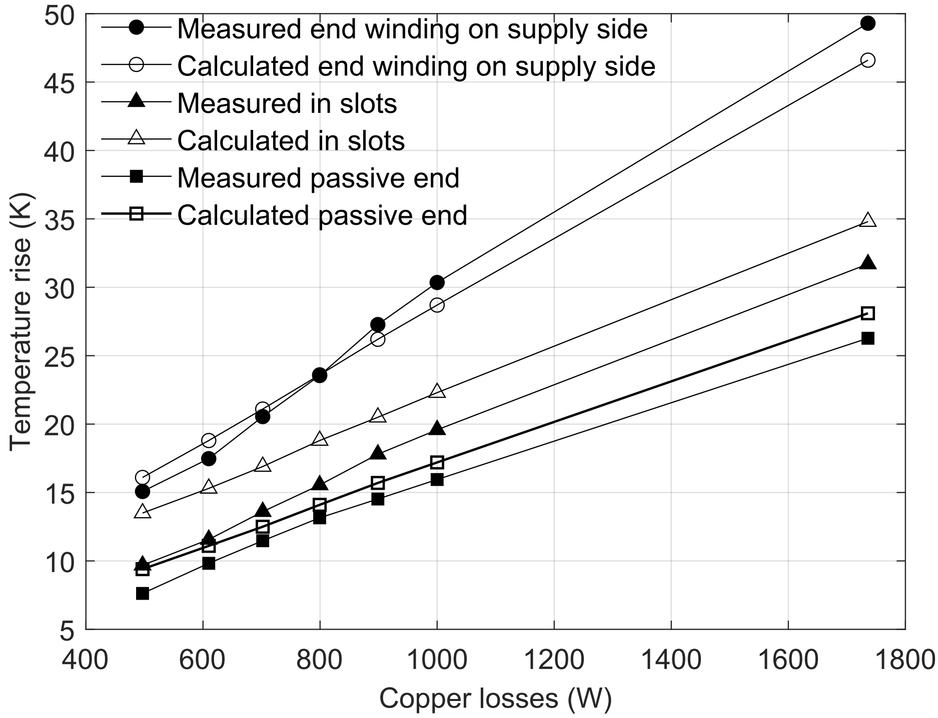

Fig. 5.34: Experimental verification of temperature rise

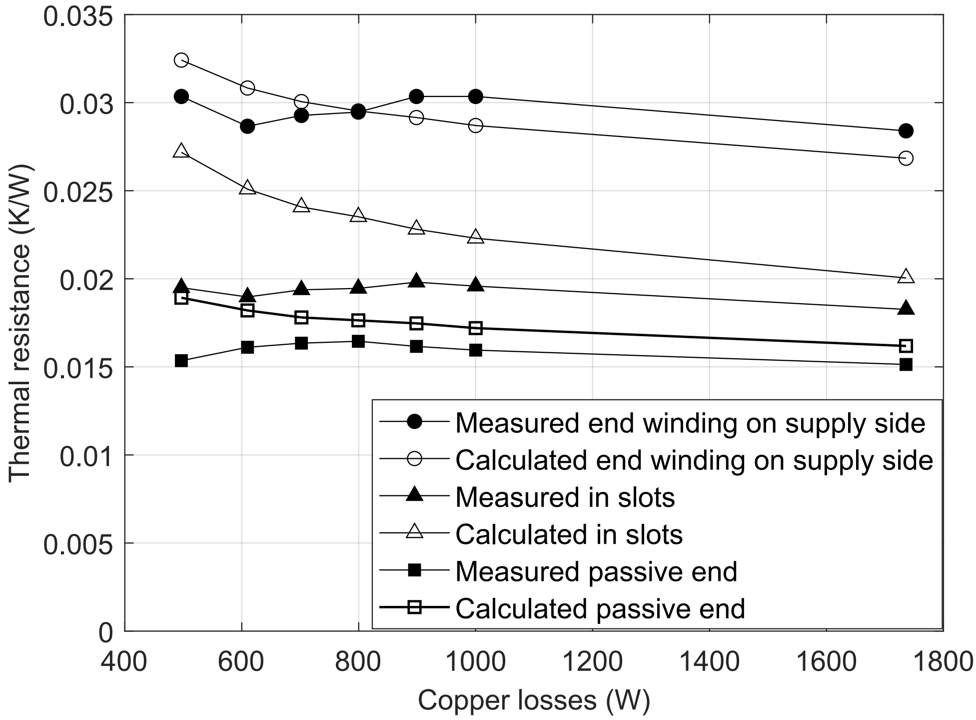

Fig. 5.35: Experimental verification of the generalized thermal resistance

5.5.4.2 Variable pressure p_s at constant heat flux q

To study the influence of p_s on the evaporative heat transfer coefficient, the internal pressures were adjusted to 110 kPa, 120 kPa, 130 kPa, 140 kPa, and 150 kPa, respectively, by changing the cooling water temperature. Table A13 in the Appendix shows the tested results of Pt100 elements at different pressure. The input power decreased slightly with the increase of p_s while the input DC voltage was kept constant. The reason is that T_s will increase with p_s, which leads to an increasing winding temperature and phase resistance.

Table 5.16 and Fig. 5.36 compare the measured and calculated temperature rise at different pressures. As shown in Fig. 5.37, the thermal resistance slightly decreases with the increase of pressure, which is consistent with the Cooper correlation that the evaporative heat transfer coefficient increases with the pressure. The passive end winding was taken as an example. From 110 kPa to 150 kPa, the calculated evaporation thermal resistance decreases by 11.4%, and the calculated evaporative temperature rise accounts for 34% of the total temperature rise. Therefore, the calculated total thermal resistance decreases by 11.4% $\cdot$ 34%=4%, which is consistent with the measured value 5%. Overall, however, the pressure within the available range has little effect on temperature rise.

Table 5.16: Experimental verification of calculated temperature rise (K)

Pressure		113 kPa	123 kPa	132 kPa	143 kPa	152 kPa
Input power		1,736 W	1,725 W	1,714 W	1,704 W	1,698 W
Passive end winding	Measured	26.0	25.6	25.1	24.8	24.1
	Calculated	28.1	27.8	27.4	27.1	26.9
End winding on supply side	Measured	49.0	48.9	48.2	47.8	47.1
	Calculated	46.6	46.3	45.9	45.4	45.1
Windings in slots	Measured	31.4	31.1	30.7	30.4	29.3
	Calculated	34.8	34.5	34.1	33.8	33.6

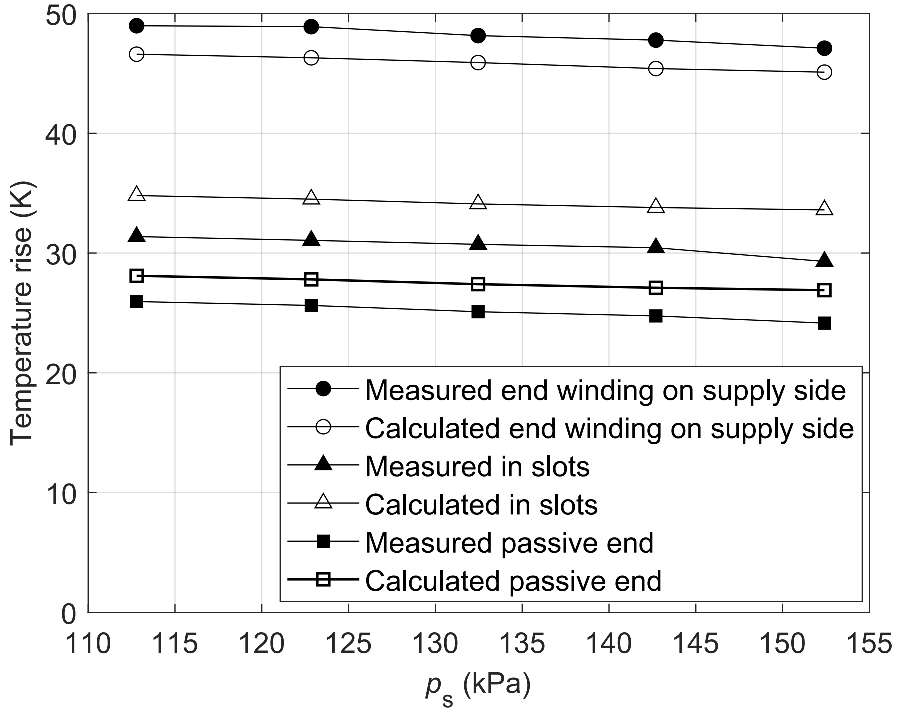

Fig. 5.36: Experimental verification of temperature rise

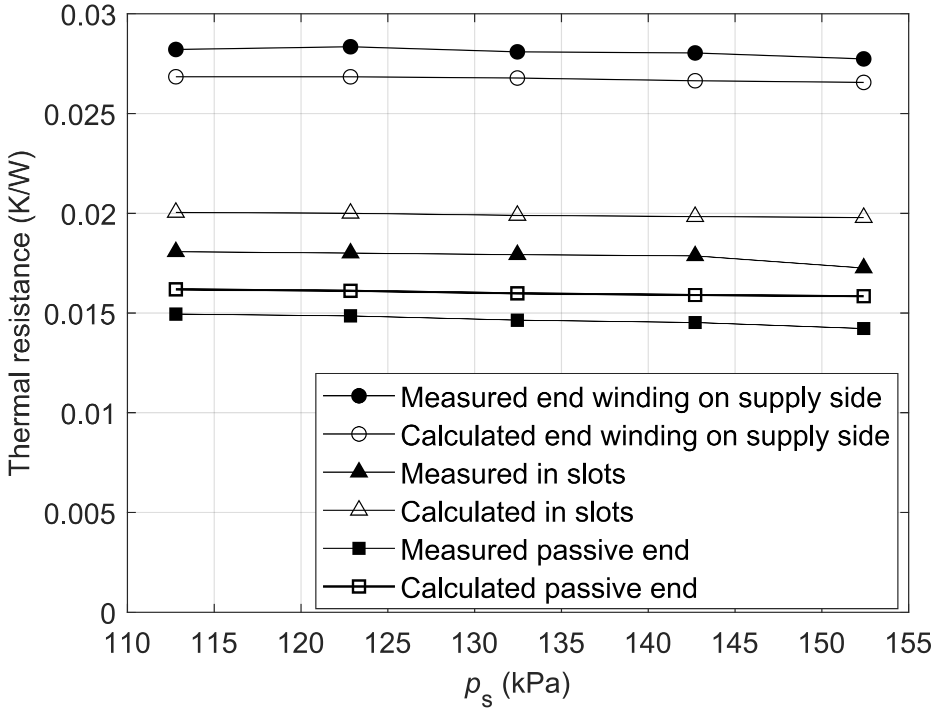

Fig. 5.37: Experimental verification of the generalized thermal resistance

5.6 Summary

(1) An experimental device was designed and built to verify the immersion evaporative cooling method. A complete thermal network model was set up, and experimental results show its satisfactory accuracy.

(2) It is necessary to use finned tubes instead of smooth tubes to enhance condensation because the condensation thermal resistance dominates when the water flow in the tubes is turbulent.

(3) The influence of non-condensable gas (air) on the upper tubes is stronger than that on the lower tubes because the air is concentrated in the upper part of the vessel. The experiment shows that when there is non-condensable gas inside the device, the variation of saturated vapor pressure with the temperature still meets (5.1).

(4) The evaporative heat transfer coefficient will increase with heat flux and pressure. However, as the evaporation thermal resistance accounts for only about 1/3 of the total thermal resistance, it has little influence on the total thermal resistance of the windings.

(5) A discontinuous fiber glass bandage of the end windings can effectively reduce the overtemperature compared to a closed version.

6 Prototype Design and Final Test

This chapter first describes the prototype's design scheme and then introduces the final test scheme and results.

6.1 Prototype design

6.1.1 Description of design

For manufacturing and testing convenience, the evaporative cooling prototype in this work borrows the magnetic bearings, rotor ($\alpha = 0.85$), and blower load of an existing air-water cooled high-speed motor. Therefore, rotor dynamics and rotor strength are both mature designs and will not be discussed here. Only the motor housing, the condenser, and the stator need to be redesigned. The punching die of the existing motor has not been changed, resulting in the same stator section. In order to demonstrate the cooling effect of immersion evaporative cooling on the stator, the effective length of the stator was halved and the thermal loading under the same power was four times in comparison with the existing motor. As shown in Fig. 6.1, the condenser has three rows of smooth tubes in the upper part, whereas the lowest row uses finned tubes. Stator cables and temperature sensor cables are lead out through a sealed terminal box.

Since samarium cobalt permanent magnets and titanium alloy are used in the rotor and both of them are heat-resistant, thermal calculation of the rotor is not required. Two calibrated infrared temperature sensors are used to monitor the rotor temperature. The tested surface is coated with black paint (see Fig. A2 in the Appendix). A cooling fan is used to cool the rotor. The cooling air passes through the air gap and then exits through the outlet.

As shown in Fig. A2 in the Appendix, the sealing sleeve, the end covers on both sides, and the condenser on the top form a closed chamber that surrounds the stator and separates it from the rotor. The sealing sleeve is made of glass fiber reinforced plastics with a thickness of 2 mm.

Assuming that the stator losses are dissipated by cooling water, and the other losses (eddy current losses in the rotor, air friction losses and magnetic bearing losses) are carried away by cooling air, so the stator and rotor thermal networks are independent of each other.

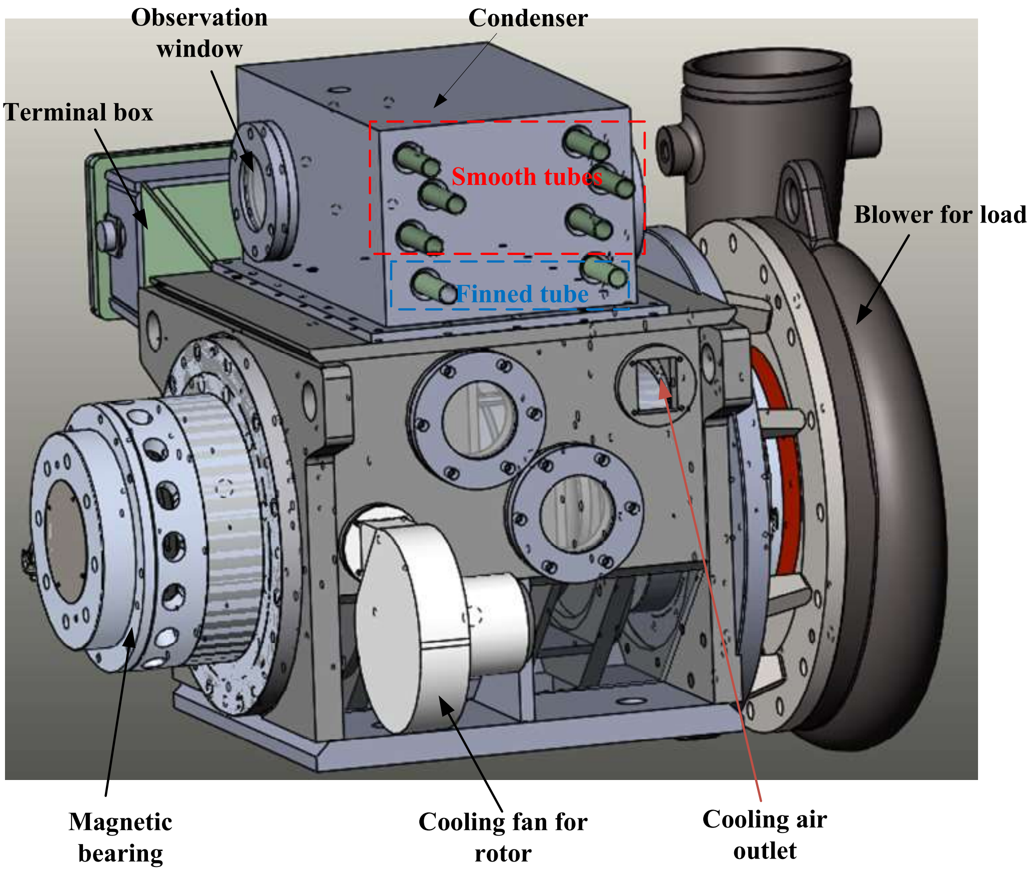

Fig. 6.1: 3-D model of the high-speed PM motor with evaporative cooling

6.1.2 Simulation model

In this dissertation, a time-stepping transient magnetic field 2-D finite element model coupled to an external voltage-fed PWM circuit has been used for simulation. This method is a common solution that provides both satisfactory accuracy and computational speed. Temperature affects the magnetic properties of the permanent magnet, the stator resistance, and the conductivity of the rotor material, which in turn influences the simulation results. The accurate calculation method is to modify the properties of each material according to the latest temperature calculation results and then simulate iteratively. However, samarium cobalt permanent magnets are used here, and their magnetic property has good temperature stability. Besides, the resistance of the winding of a high-speed motor is much lower than its reactance, so the influence of temperature on the results for current and magnetic field is ignored. The effect of temperature is taken into account only in the calculation of iron and copper losses.

6.1.2.1 The fringing effect

Since this stator core has radial ventilation ducts and the permanent magnet length of the borrowed rotor is much longer than the stack length, fringing magnetic fields will be generated at the ducts and end faces of the stator core as shown in Fig. 6.2. The related structure parameters are listed in Table 6.1. Because of the existence of the low permeability magnet in PM machines, their fringing field distribution near the air gap can not be solved by the classical conformal transformation [83]. The fringing effect of the ventilation ducts is similar to the slotting effect and can be considered by the Carter coefficient [84]. In [83], the analytical solution of the fringing flux distribution due to the axial extension of the magnet was obtained by solving Laplace's equation. Taking $(\delta_{\mathrm{ef}} + h_{\mathrm{m}})$ as the base value, a family curve of the normalized increment of core stack length varying with the normalized axial extension of the magnet length was given. Unfortunately, the normalized axial extension of the magnet length in this work is far beyond the range of the given curve. Considering that such a long extension is just a special case and not practical, the effective core stack length has been calculated by the 2-D magnetostatic field FEM as shown in Fig. 6.3.

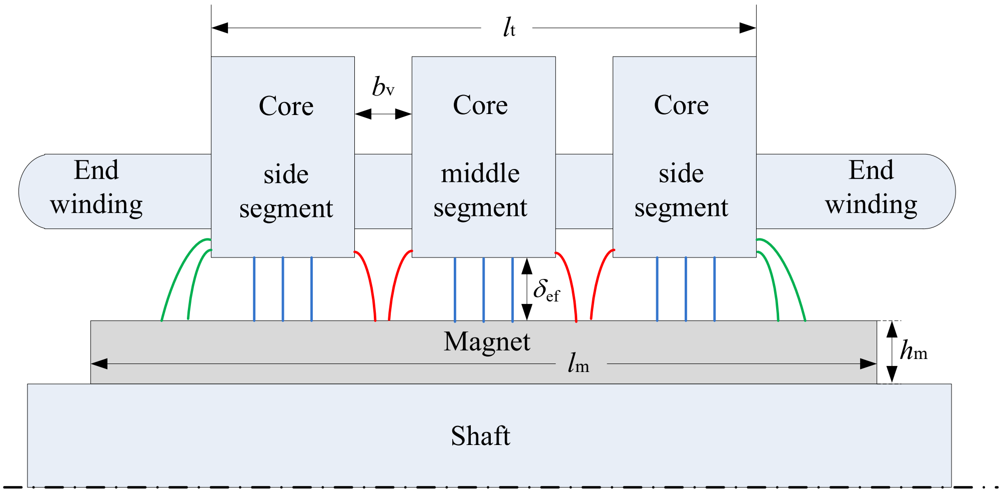

Fig. 6.2: Schematic diagram of air gap magnetic field distribution with radial ventilation ducts

Table 6.1: Related parameters of the prototype motor

l_{t}	N_{v}	b_{v}	δ_{ef}	l_{m}	h_{m}
84 mm	2	7 mm	7.5 mm	171 mm	8 mm

* N_{v} is the number of the ventilation ducts. δ_{ef} is the effective air gap length, whose value is the sum of air gap length and retaining sleeve thickness.

Because of mirror symmetry, only half the model needs to be built. The zero-flux boundaries are marked in orange solid lines. The magnetization direction of the permanent magnet is radial. The core stack and the magnetic paths are set to iron. When l_{m} changed from 84 mm to 171 mm, the flux passing through the line segment AB is extracted as Ψ_{AB}, as shown in Fig. 6.3(a). In Fig. 6.3(b), the ventilation ducts are filled with iron and $l_{\mathrm{m}} = l_{\mathrm{t}}$. The inside and outside boundaries are all set to zero-flux boundaries. The flux passing through the line segment AB is extracted as Ψ_{b}. The ratio of Ψ_{AB} to Ψ_{b} is defined as k_{m}. Then the effective core stack length l_{ef} can expressed as:

$$l_{\mathrm{ef}} = k_{\mathrm{m}} \cdot l_{\mathrm{t}} \tag{6.1}$$

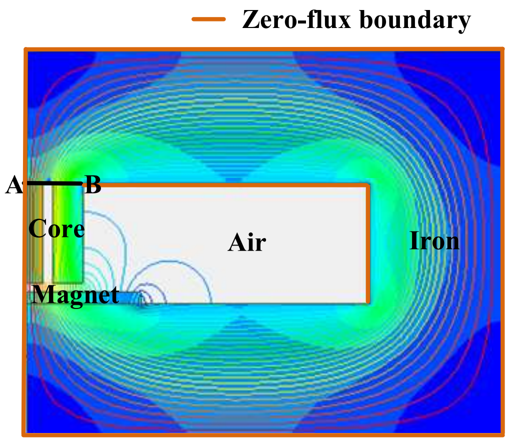

(a) With axial magnet extension and ducts

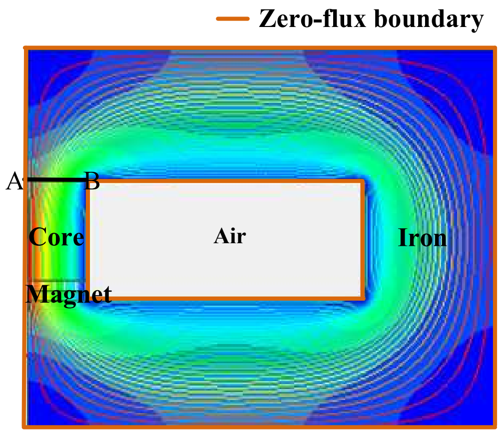

(b) Without axial magnet extension and ducts

Fig. 6.3: Simulation models of axial magnetic field distribution of air gap

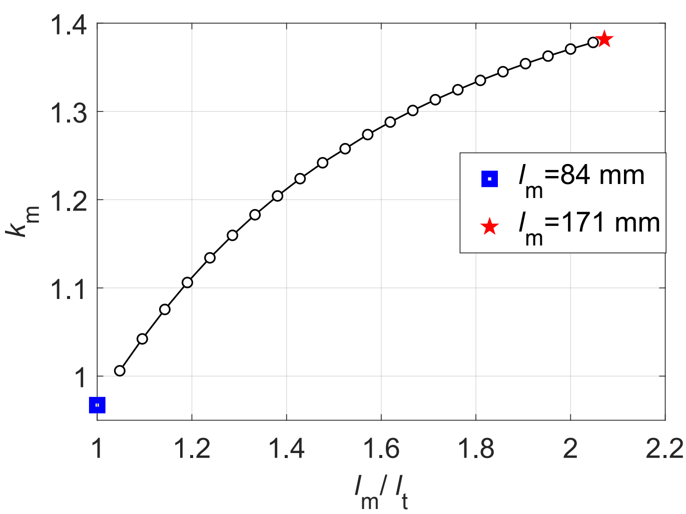

Fig. 6.4: k_m varying with l_m/l_t

Fig. 6.4 shows that k_{m} increases with l_{m}. The square marker indicates that with no axial magnet extension, the effective core stack length l_{ef} is shortened to $0.967l_{\mathrm{t}}$ due to the ventilation ducts and magnetic leakage at both ends of the magnet. The pentagram marker represents that under the actual extension of the permanent magnet, the effective core stack length l_{ef} is $1.38l_t$. It is well known that the effective air gap of high-speed SPM machines is large due to the retaining sleeve, resulting in a low air gap flux density. Fig. 6.4 indicates that high-speed SPM machines with an axial magnet extension can significantly increase their air gap flux density, thus extending their power limits.

It should be noted that this effective length will overestimate the slot leakage inductance since the slot leakage inductance should correspond to l_{t}. Therefore, when adding the end-winding leakage inductance L_{end} to the external circuit, the excessive part of the slot leakage L_{se} inductance was subtracted from it.

6.1.2.2 External electric circuit

Fig. 6.5 shows the schematic diagram of the system simulation. The 2-D FEM model is externally connected to the AC phase resistances, the difference between the end-winding leakage inductance and the excess slot leakage inductance, the choke, and finally connected to the inverter. The IGBTs are modeled as ideal switches without respecting interlock time. The switching signals are generated according to the reference currents i_q^* and i_d^* and the appropriate feedback values.

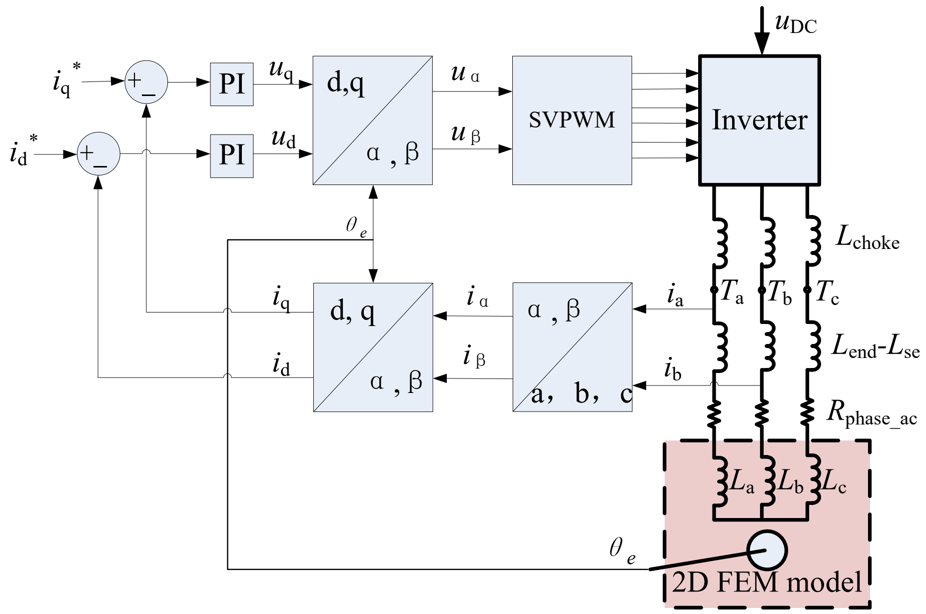

Fig. 6.5: Schematic diagram of 2-D FEM model coupled to external electric circuit

Since the resistance of the high-speed motor is much smaller than the reactance, the resistance has little influence on the current. The AC phase resistance $R_\mathrm{phase,AC}$ at 370 Hz and 75°C is adopted, assuming that the AC resistance of each harmonic is the same. The slot leakage inductance and end-winding leakage inductance has been calculated according to the classical formula [85]. To reduce the eddy current losses in the rotor, a choke is added between the motor and the inverter.

According to the final experiment, the speed was set to 22.2 krpm, the measured input power of the motor P_in was 84 kW, and the measured phase current I_N was 142 A. The experimental back EMF E_0 was 379.3 V at 22.2 krpm. So the q axis component of the phase current I_Nq can be calculated as:

$$I_\mathrm{Nq} = \frac{P_\mathrm{in} - 3 \cdot I_\mathrm{N}^2 \cdot R_\mathrm{phase,AC}}{\sqrt{3} \cdot E_0} = 126.7\,\mathrm{A} \tag{6.2}$$

and the d axis component is:

$$I_\mathrm{Nd} = \sqrt{I_N^2 - I_\mathrm{Nq}^2} = 64.1\,\mathrm{A} \tag{6.3}$$

With a power invariant dq transformation, the q axis current i_q and the d axis current i_d are:

$$i_\mathrm{q} = \sqrt{3} \cdot I_\mathrm{Nq} = 219.5\,\mathrm{A}, \quad i_\mathrm{d} = -\sqrt{3} \cdot I_\mathrm{Nd} = -111.0\,\mathrm{A} \tag{6.4}$$

where the minus sign means that i_d has a field weakening effect. This is why the motor terminal voltage (356.4 V) is lower than the back EMF (379.3 V), and the basic iron losses under load (585.6 W) are lower than the no-load value (653 W), which is described later.

So the simulation parameters are shown in Table 6.2, in which the DC bus voltage u_DC is a value read from the inverter panel, and the switching frequency f_s is the actual set value. The simulation step size is set to 5 μs, so there are 20 calculation points in each PWM switching cycle.

Table 6.2: Simulation parameter settings

u_DC	f	f_s	i_q^*	i_d^*	$R_\mathrm{phase,AC}$	L_end	L_se	L_choke
504 V	370 Hz	10 kHz	219.5 A	-111.0 A	12.94 mΩ	67 μH	22 μH	10.5 μH

6.1.3 Simulation results and verification

6.1.3.1 Back EMF

The experimental back EMF E_0 was determined by the retardation test. The average value of the two infrared sensors measuring the rotor temperature is 20°C. Table 6.3 compares the experimental and the calculated E_0.

Table 6.3: Back EMF E_0 at 370 Hz, 20°C

Experimental E_0	379.3 V	Calculated E_0	371.3 V	Relative error	-2%

6.1.3.2 Current

Fig. 6.6(a) shows that the simulated current waveform agrees well with the measured one. The FFT analysis results are shown in Fig. 6.6(b). Because the ratio of switching frequency to fundamental frequency is 27, the main harmonic orders are concentrated near 27th and 54th. The THD of the simulated current waveform is 7.86% compared with the 5.86% of the measured one.

6.1.3.3 Terminal voltage

Fig. 6.7(a) shows that the simulated terminal voltage waveform agrees well with the measured one. The RMS of the fundamental component of the simulated terminal voltage is 350.0 V, whereas the measured counterpart is 356.4 V. The error mainly comes from the error of the back EMF as described above.

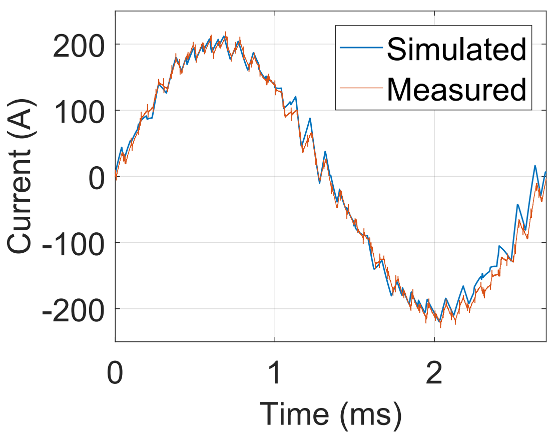

(a) Waveform

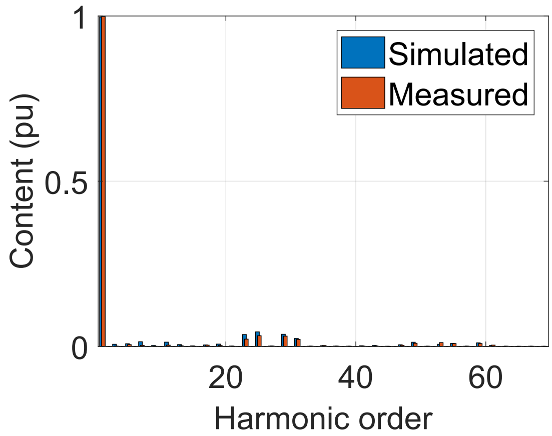

(b) FFT analysis

Fig. 6.6: Experimental verification of current results

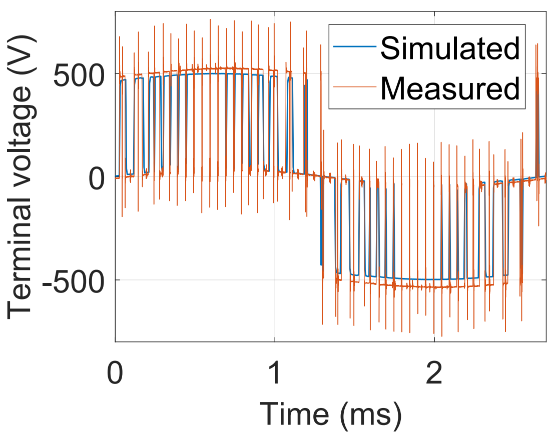

(a) Waveform

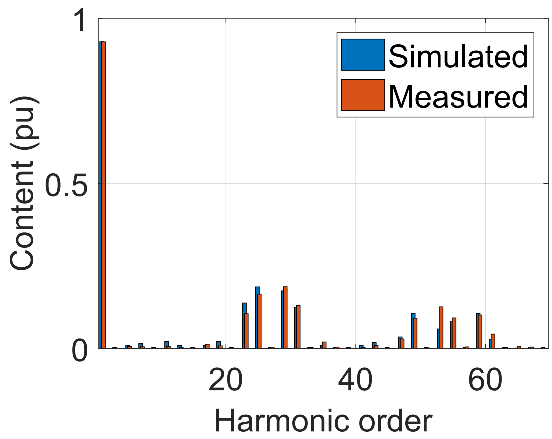

(b) FFT analysis

Fig. 6.7: Experimental verification of terminal voltage results

6.1.4 Calculation of losses under load

6.1.4.1 Iron losses

Because of the axial magnet extension, the average flux density in the side segments is larger than that of the middle segment as shown in Fig. 6.2. One side segment is taken as an example, the flux density $B^{'}$ extracted from the 2-D model needs to be converted into the actual flux density B_{side} according to the following formula:

$$B_{\text{side}} = \frac{B' \cdot l_{\text{ef}} \cdot \Psi_{\text{side}}}{k_{\text{Fe}} \cdot l_{\text{side}} \cdot \Psi_{\text{AB}}} \tag{6.5}$$

where k_{Fe} is the stacking factor of the laminated core, l_{side} the length of the side segment, Ψ_{side} the flux passing through the side segment in Fig. 6.3(a).

Fig. 6.8 compares flux density B_{side} at point C in Fig. 2.9 when the load current (see Fig. 6.6(a)) applied to the winding. Obviously, according to Lenz's law, the rotor eddy current will weaken the asynchronously rotating harmonic field components, especially high-order harmonics, making the flux density distribution in the stator core smoother, which reduces the iron losses. It is worth noting that this comparison is made under the same given current.

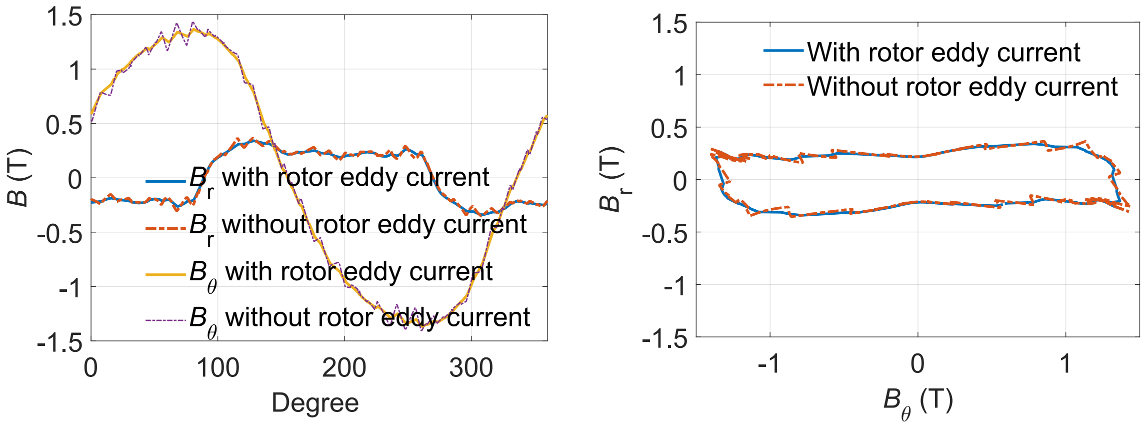

(a) Components (b) Locus plot

Fig. 6.8: Flux density components at point C under load

The calculation method of iron losses under load in each segment is similar to that of no-load iron losses in Chapter 2. Table 6.4 lists the calculated iron losses under load at 75°C. Where the additional iron losses due to other manufacturing effects are estimated values according to the retardation test results in Section 6.2.2. It is assumed that the values under no-load and load are the same, and all of them are considered to belong to the yoke part and uniformly distributed axially. Total iron losses in yoke and teeth act as heat sources in the thermal network. The calculation of iron losses requires an iterative solution with the result of temperature rise. The average calculated temperature of the core in the subsequent stator thermal model is 75°C.

Table 6.4: Iron losses under load at 75°C

Segment	Basic iron losses	Additional iron losses 1	Additional iron losses 2	In yoke	In teeth
Both sides	464.6 W	156.6 W	680.0 W	1,029.8 W	271.4 W
Middle	121.0 W	40.8 W	340.0 W	431.1 W	70.7 W
Total	585.6 W	197.4 W	1,020.0 W	1,460.9 W	342.1 W

* Additional iron losses 1 mean additional iron losses due to punching and burrs' connection.

* Additional iron losses 2 mean additional iron losses due to welding and radial pressure.

6.1.4.2 Eddy current losses in the rotor

Due to slotting, non-sinusoidal MMF distribution, and PWM effect, there will be many asynchronous rotating field harmonics in the air gap, producing eddy current losses in the titanium alloy retaining sleeve, permanent magnets, and rotor back iron [86, 87]. [88, 89] proposed a simultaneous solution of the magnetic field and the armature currents for voltage-fed PM machines. The harmonic model is directly coupled with the armature electric circuit equation to consider the PWM effect on rotor eddy-current losses without a priori knowledge of the armature currents. However, this method is complicated, and the losses caused by slots are not easy to calculate accurately. The common method is still the magnetic transient time-stepping 2-D FEM directly coupling the external electric circuit, which can accurately consider the PWM current harmonics, winding space harmonics, and slots harmonics. The Gibbs coefficient k_{e} [90] is used to consider the tangential eddy current losses at the rotor end circuit:

$$k_{\mathrm{e}} = 1 + \frac{2 \cdot \tau}{\pi \cdot l_{\mathrm{ef}}} \tag{6.6}$$

where τ is the pitch of the rotor. The calculated value of k_{e} is 1.905.

It is worth noting that the formula above overestimates the actual eddy-current losses because the pitch corresponding to the spatial high-order harmonics is much smaller than that of the fundamental wave. This actually gives a certain amount of safety for the estimation of rotor temperature rise.

Table 6.5 compares the impact of supply conditions on eddy current losses in the rotor. The rotor losses under no-load condition can be ignored, and the rotor eddy current losses with inverter feeding are nearly doubled compared with the sinusoidal current fed. Therefore, increasing the switching frequency, using the tri-level inverter, adding a choke or sine filter can effectively reduce the current harmonics, thus reducing the eddy current losses in the rotor.

Table 6.5: Calculated eddy current losses in the rotor with k_{e}

	Sleeve	Magnet	Interpole block	Back iron	Total
No-load	18.9 W	0.6 W	0 W	0 W	19.5 W
Sinusoidal current fed	214.0 W	19.8 W	2.9 W	0.8 W	237.5 W
Inverter-fed	375.3 W	76.2 W	13.3 W	5.7 W	470.5 W

6.1.4.3 Copper losses

The simulated current waveform can be resolved into Fourier series:

$$i(t) = \sum_{k=1}^{\infty} \sqrt{2} \cdot I_{\mathrm{k}} \cdot \sin\left(2 \cdot \pi \cdot k \cdot f \cdot t + \theta_{\mathrm{k}}\right) \tag{6.7}$$

where k is the harmonics order, f the fundamental frequency, I_{k} the RMS of k-th order harmonic, and θ_{k} the phase of k-th order harmonic.

Then considering the temperature effect on the electrical resistivity, the total copper losses at temperature T can be calculated as:

$$P_{\text{cu}} = \sum_{k=1}^{\infty} 3 \cdot I_{\text{k}}^2 \cdot R_{\text{phase,DC}}(T) \cdot k_{\text{ACR,Y}}(k \cdot f, T) \tag{6.8}$$

where $R_{\text{phase,DC}}(T)$ is the phase DC resistance at temperature T, and $k_{\text{ACR,Y}}(k\cdot f, T)$ the AC to DC resistance ratio when the windings are supplied by a three-phase symmetrical power source at frequency $k \cdot f$ and temperature T.

The calculated copper losses in different parts of the winding caused by different harmonic order ranges are listed in Table 6.6. For copper losses in slots, $k_{\text{ACR,Y}}$ in (6.8) should be replaced by $k_{\text{ACR2,Y}}$, which can be calculated by (4.7). For copper losses in end windings and ducts, k_{ACR3} in Section 4.2.3 is used instead.

Copper losses in different parts are used as heat sources for the subsequent thermal model. From the calculation results, the AC copper losses caused by harmonics are mainly concentrated in the slots because the leakage magnetic field suffered by the conductors in the slots is much higher than that of the outside. The largest amount of copper losses consists of components below twice the switching frequency. The copper losses in the slots increase by 80% due to harmonics compared to only 2% outside.

Table 6.6: Calculated copper losses under load at 75°C

	k=1	k=2–69	k=70–199	Total
Passive end winding	246.1 W	4.2 W	0.3 W	250.6 W
End winding on supply side	292.3 W	5.0 W	0.4 W	297.7 W
In slots	182.9 W	117.2 W	23.3 W	323.4 W
In ducts	61.5 W	1.0 W	0.1 W	62.6 W
Total	782.8 W	127.4 W	24.1 W	934.3 W

6.1.4.4 Air friction losses

As shown in Fig. A2 in the Appendix, all air friction losses related dimensions of the evaporative cooling prototype are the same as that of the air-water cooled motor (used in Chapter 3) except the air gap size. The calculation conditions are as follows: atmospheric pressure is 103 kPa; measured axial velocity v_{a} in the air gap is 65.5 m/s (total air volume rate is 2,000 L/min) and measured average air gap temperature is 45.2°C; friction coefficient $k_{\text{f}} = 1.28$ and k_2=0.195 for 2 mm sealing sleeve, which have been determined in Section 3.4. According to (3.28), the calculated air friction losses $P_{\text{f}} = 684.5$ W without axial flow, and $P_{\text{f}} = 789.5$ W with axial flow $v_{\text{a}} = 65.5$ m/s.

6.1.5 Condenser design and validation

6.1.5.1 Condenser design

The input data for the condenser design are: the heat exchange capacity is 3,000 W; the inlet temperature of the cooling water is 30°C; the temperature rise of the cooling water is 5 K; the water flowing inside the tube is turbulent.

Based on the thermal network model of the condensation side established in Section 5.3, the design results are as follows: for smooth tubes, the outer diameter is 20 mm, the inner diameter is 17.6 mm, and the effective length of a smooth tube is 1,624 mm, S shape. There are 3 layers of smooth tubes arranged vertically and connected in series. For the finned tube, the specifications are shown in Table A4 in the Appendix. There is only one layer of the finned tube, and the effective length of a finned tube is 1,600 mm. Fig. A4 in the Appendix shows a photo of one smooth and one finned tube. The smooth tubes and the finned tube will be tested separately.

6.1.5.2 Condenser validation

In order to compare the heat exchange capacity of the three layers of smooth tubes and the single layer of finned tubes, a comparative test was conducted under almost the same load conditions, water flow rates, and saturated vapor temperatures.

Table 6.7 shows the comparison between the experimental results and the calculated values by the thermal model established in Section 5.3. Detailed test records are listed in Table A14 in the Appendix. The total heat exchange power P_1 has been obtained by the calorimetric method. The calculated vapor temperature T_s of the smooth tubes agree well with the experimental value. However, the calculated T_s of the finned tube is much lower than the measured value. Part of the reason may be that the fins are pressed to the tube, so the contact thermal resistance cannot be ignored. The main reason should be that the enhancement ratio formula (A1 in the Appendix) for low-finned tubes (fin hight $e \leq 2$ mm) in [91] is exaggerated for high-finned tubes ($e = 5$ mm). However, the heat exchange capacity of a single layer finned tube is approximately equal to that of three layers of smooth tubes.

Table 6.7: Measured and calculated results of the condenser test

	Measured P_1	Measured T_s	Calculated T_s	Calculated h_c
Three layers smooth tubes	2,990 W	54°C	52°C	777 $W/(m^2 \cdot K)$
Single layer finned tube	2,914 W	56°C	46°C	13,000 $W/(m^2 \cdot K)$

Fig. 6.9 show the condensation of smooth tubes and finned tubes observed from the observation windows.

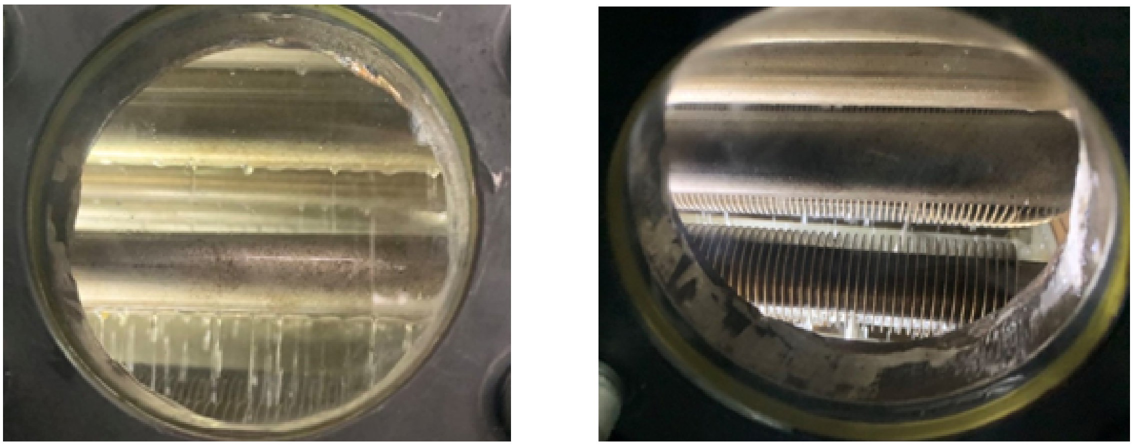

(a) Smooth tubes (b) Finned tubes

Fig. 6.9: Condensation photos

6.1.6 Stator temperature rise

6.1.6.1 Calculation and verification

The stator temperature rise has been calculated by the thermal network model established in Chapter 3. The end plates have not been included in the temperature rise model because they directly contact the liquid. The end winding on supply side was wrapped by glass tapes with an average thickness of 0.2 mm. The average thickness of the passive end bandage is 0.1 mm. Table 6.8 compares the measured and calculated results of stator temperature rise. The temperature of saturated vapor inside the chamber is 60°C. The measured overtemperatures are lower than the calculated values, especially in the slots. The main reason is that some insulation varnish drains away in the process of curing, resulting in air voids between magnet wires so that the liquid coolant can directly contact the wires for heat dissipation. The fill factor in the slots is lower than that of the end windings, so this phenomenon is more obvious there.

Table 6.8: Measured and calculated stator temperature rise

	Passive end winding	End winding on supply side	Winding in slots	Yoke	Teeth
Calculated	18 K	21 K	21 K	15 K	18 K
Measured	15 K	19 K	14 K	-	-

Fig. 6.10 show the boiling phenomena observed from the observation windows.

6.1.6.2 Thermal loading limit analysis

It is necessary to know the typical thermal loading limit of any new cooling method. Assuming the saturated vapor temperature is 60°C, the average temperature rise of

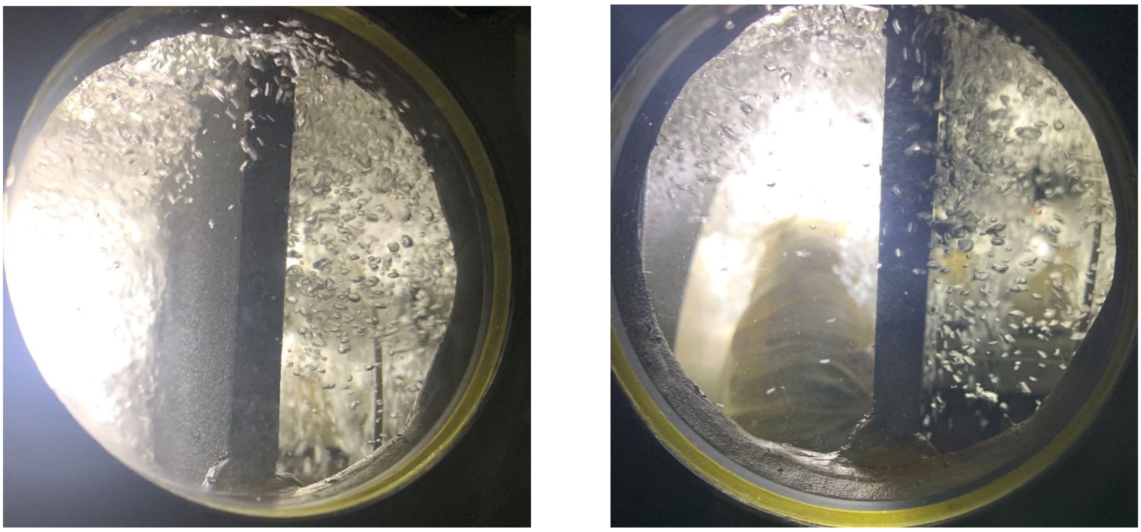

(a) Stator core (b) End windings

Fig. 6.10: Boiling photos

both the winding and stator core does not exceed 60°C. Based on the thermal model, the allowable percentage increases for copper and iron losses are +300% and +600%, respectively.

It is further assumed that the copper losses are proportional to the square of the current, and the iron losses are proportional to $n^{1.47}$ (see Chapter 3). From the thermal perspective, when the iron losses are the rated value, the maximum allowable current is 284 A, the corresponding specific electric loading is 968 A/cm, and the current density is 10.3 A/mm^2. When the copper losses are the rated value, the maximum allowable rotational speed is 83 krpm. It can be seen that the immersion evaporative cooling method has an excellent cooling effect and can significantly increase the thermal loading of high-speed motors, thus expanding their power limit.

6.2 Final test

6.2.1 Experimental setup

6.2.1.1 Description

The final experimental setup is shown in Fig. 6.11. A centrifugal blower has been used as load. The tested motor was fed by an inverter. The input power of the motor was measured by a power analyzer. Voltage and current waveforms were recorded by an oscilloscope. The cooling water temperature was adjusted by a chiller. Both the water inlet and outlet were equipped with temperature sensors. A valve was used to regulate the water flow rate, which was measured by a turbine flow meter. There was an exhaust port at the top of the condenser for vacuuming and exhausting the air. A container with desiccant was used to dehydrate the HFE-7100 in the chamber. A pressure transducer was used to measure the relative pressure inside the chamber; thus, the absolute pressure inside can be obtained by combining it with a barometer. A large number of Pt100 sensors were used to measure the temperatures of the motor winding at different locations, the temperature of the liquid, and the temperatures of the vapor at different heights. A high-pressure cooling fan was mounted on the frame to cool the rotor. For the calorimetry test, the cooling air inlet and outlet were also equipped with temperature sensors, and a flow meter was used to measure the flow rate. A data acquisition card was used to collect the sensor data at a sampling rate of once per second. Most of the instruments have been described in previous chapters, and additional instruments are listed in Table A9 in the Appendix.

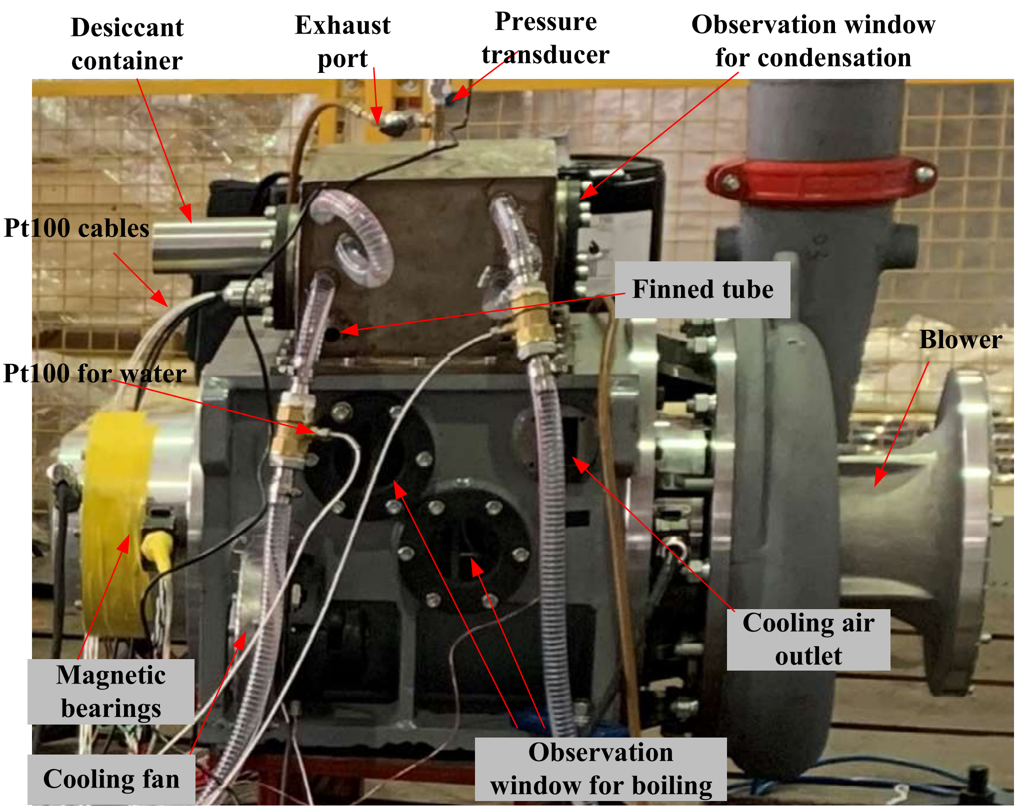

Fig. 6.11: Final experimental setup

6.2.1.2 Preparation for experiment

A vacuum pump has been used for reducing the vessel pressure from its atmospheric value of 103 kPa to 5 kPa. According to the standard [92], the seal has been qualified for maintaining pressure for 24 h with less than 2% change. Then the vessel was injected with HFE-7100 until the stator was fully immersed. The motor's external surface was wholly covered with heat insulation foam for calorimetric determination of total losses. The motor feet were also cushioned with rubber pads. When the motor started to run with cooling water, the internal temperature and pressure rose gradually. Since the residual air inside was concentrated in the top space, the internal vapor temperature decreased with height. When the relative pressure inside the vessel became positive, the exhaust valve at the top was opened, and a long transparent plastic pipe was connected to the exhaust port. First, the residual air at the top space came out, then a mixture of gases containing HFE-7100 vapor followed. The HFE-7100 vapor condenses on the plastic tube wall when cooled. The valve was kept open until the internal vapor temperature at different heights tended to be the same and equal to the liquid temperature.

6.2.2 No-load retardation test

Before the blower was mounted, the retardation test was carried out to get the motor's total no-load losses. The cooling fan was switched off during the coast down, so there was no air flowing through the air gap. The values of the two infrared sensors measuring the rotor temperature were 18°C and 22°C, respectively. The average temperature of the windings in the slots was 22°C.

Fig. 6.12 shows the total experimental no-load losses curve determined by the retardation method. The total experimental no-load losses P_{t} at 22.2 krpm are 3,735 W. As the same rotor and bearings are used, the bearing losses $P_{\mathrm{bearing,r}}$ of this motor are the same as those of the air-water cooled motor, which are 573 W at 22.2 krpm as shown in Fig. 3.13. Assuming that the air gap temperature is the average of the rotor temperature and the winding temperature in the slots, the calculated air friction losses P_{f} are 711 W. Therefore the rest losses are the no-load iron losses of 2,451 W. The calculated basic iron losses $P_{\mathrm{fe,b}}$ under no-load condition are 653 W, and the additional iron losses due to punching and burrs' connection $P_{\mathrm{fe,adp}}$ are 176 W. The stator core used in the prototype has 2 ventilation ducts, end plates, and 12 ribs with 24 welding lines, as shown in Fig. 4.3(a). Because the inner diameter of the end plates is only 1 mm larger than that of the stator core, the eddy current losses produced in the end plates $P_{\mathrm{edd,ep}}$ are about 600 W calculated by 3-D FEM as shown in Fig. 6.13. Finally, the additional iron losses due to welding and radial pressure $P_{\mathrm{fe,adw}}$ are 1,020 W by subtracting the above losses from the total no-load losses. The detailed components of no-load loss are shown in Table 6.9. By comparison, the additional losses due to 12 welding lines and radial forces are 400 W in Chapter 2. From the efficiency point of view, the stator core with ventilation ducts, end plates, and external 24 welding lines will bring large additional losses, although this structure is suitable for heat dissipation. Therefore, bonded stator cores would be preferred for high-speed motors.

Table 6.9: Composition of no-load losses (Meas.: Measured, Calc.: Calculated)

P_{t}	$P_{\mathrm{bearing,r}}$	P_{f}	$P_{\mathrm{edd,ep}}$	$P_{\mathrm{fe,b}}$	$P_{\mathrm{fe,adp}}$	$P_{\mathrm{fe,adw}}$
Meas.	Meas.	Calc.	Calc.	Calc.	Calc.	Estimated
3,735 W	573 W	711 W	600 W	653 W	176 W	1,020 W

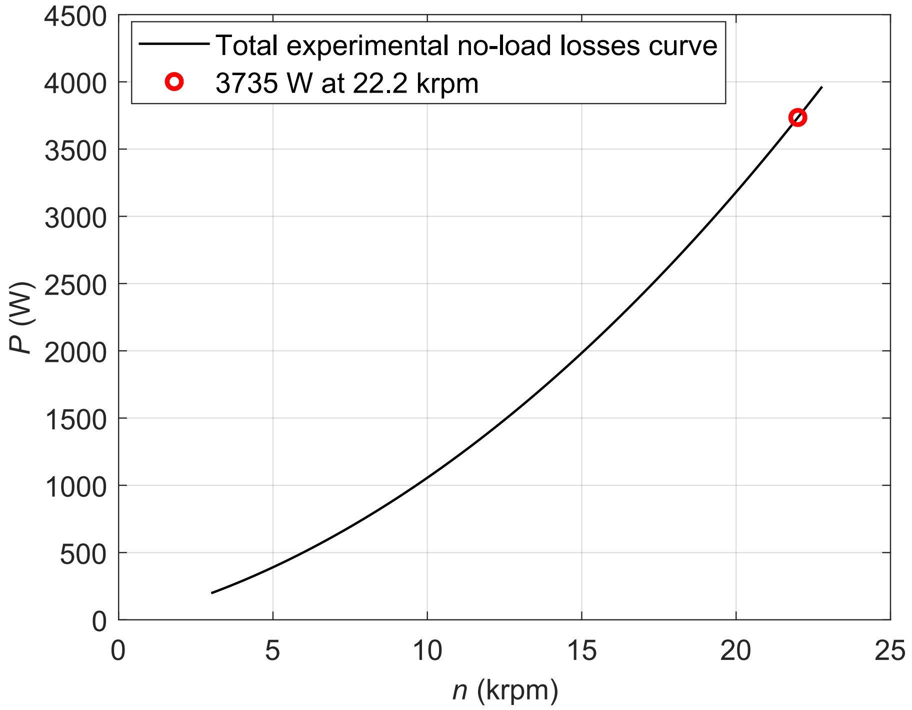

Fig. 6.12: Total experimental no-load losses

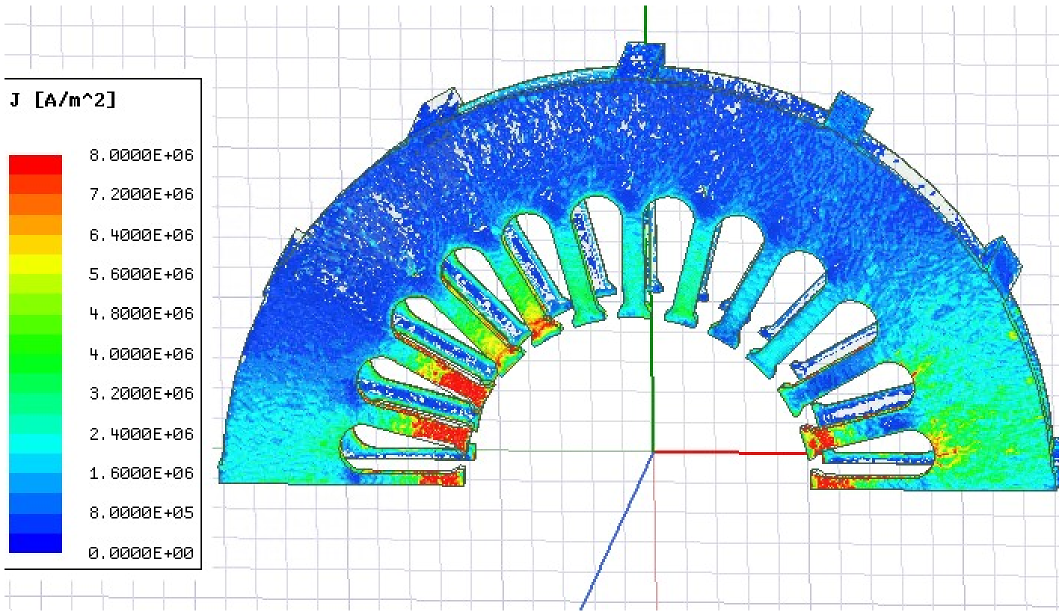

Fig. 6.13: Eddy current losses in the end plates

6.2.3 Determination of efficiency by calorimetric method

The purposes of this experiment are as follows:

(1) measuring the input current, voltage, and power to verify the magnetic field 2-D FEM model;

(2) measuring the total losses under load by calorimetric method to determine the efficiency of the motor;

(3) collecting the temperature of the windings to verify the thermal network model.

6.2.3.1 Electrical input power

When the motor was thermally stabilized, the input power P_{in} of the motor measured by the power analyzer was 84 kW at 22.2 krpm. The waveforms of terminal voltage and current recorded by the oscilloscope are shown in Fig. 6.14.

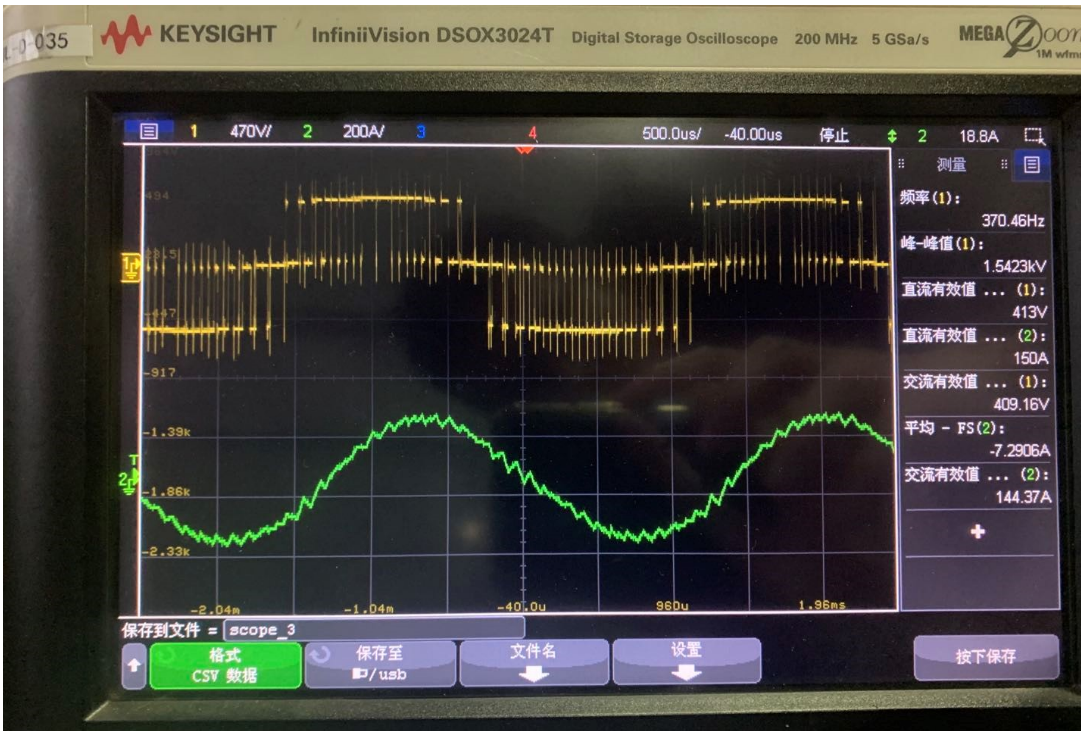

Fig. 6.14: Experimental waveforms of terminal voltage and current

6.2.3.2 Total losses measured by calorimetric method

According to IEC 60034-2-2 [93], losses are determined from the heat dissipated to the surrounding media plus the product of the amount of coolant and its temperature rise. As the temperature of the blower's volute was only 0.7 K lower than that of the saturated vapor inside the vessel, the heat dissipated from the blower can be ignored.

A. Heat dissipated from the surface

The surface area of the cuboid vessel in Chapter 5 is 1.44 m^2, and the thermal resistance of surface heat dissipation R_2 =0.159 K/W has been determined in Section 5.5.3.1. The surface area of the prototype motor is about 1.27 m^2 (the front surface of the motor is not included because it is covered by the volute), so the thermal resistance can be estimated to be 0.18 K/W. When the saturated vapor temperature inside the vessel is 60.0°C and the ambient temperature is 11.6°C, the surface heat dissipation power can be estimated to be 269 W.

B. Heat dissipated from water and air

According to the test records in Table 6.10, the heat dissipated from water and air is 2,747 W and 2,442 W, respectively.

Table 6.10: Test records of cooling water and cooling air

	Flow rate	Inlet temperature	Outlet temperature	Exchange power
Water	4.3 L/min	20.5°C	29.7°C	2,747 W
Air	2,000 L/min	16.8°C	73.5°C	2,442 W

6.2.3.3 Determination of efficiency

The total measured losses under load $P_{\text{loss}} = 5,458$ W can be obtained by adding the heat dissipated from surface, water and air. The measured efficiency of the motor results as:

$$\eta = \frac{P_{\text{in}} - P_{\text{loss}}}{P_{\text{in}}} = 93.5\% \tag{6.9}$$

Details on losses under load are listed in Table 6.11. The total calculated losses under load are 94.8 W lower than the measured value. The relative difference is -2%.

Table 6.11: Composition of load losses (Meas.: Measured, Calc.: Calculated)

P_{cu}	P_{fe}	P_{f}	$P_{\text{edd,r}}$	$P_{\text{bearing,r}}$	$P_{\text{bearing,s}}$	$P_{\text{edd,ep}}$	P_{loss}
Calc. 934.3 W	Calc. 1803 W	Calc. 772.4 W	Calc. 470.5 W	Meas. 573 W	Meas. 30 W	Calc. 780 W	Calc. 5,363.2 W

6.3 Summary

An immersion evaporative cooled high-speed prototype has been designed, manufactured, and load tested. The main contributions are as follows:

(1) The immersion evaporative cooling method can significantly increase the thermal loading capability of high-speed motors and expand their power limits. The test results

of the temperature rise show that the stator thermal network model's accuracy can fulfill the requirements of engineering applications. The thermal loading limit of this cooling method has been deduced.

(2) Calorimetry results have proved the accuracy and effectiveness of the loss models presented in this dissertation. The calorimetric method is a simple and practical method for efficiency determination of high-speed motors compare to the traditional method using an expensive high-speed torque transducer.

(3) Permanent magnets longer than the stator core show a noticeable axial magnetic convergence effect, increasing the equivalent air gap flux density of the SPM high-speed machines.

(4) Contrast test results show that finned tubes can effectively enhance the heat transfer capacity of the condensation side compared with smooth tubes. The results also indicate that the enhanced ratio formula is overestimated for high-finned tubes.

(5) The welded stator core with ventilation ducts and end plates used in the prototype introduces too much additional iron losses and should be avoided for high-speed motors. A bonded core is recommended.

7 Conclusion and Future Work

7.1 Conclusion

The main conclusions and contributions are as follows:

(1) A new iron loss model has been proposed in [41], which can cover a wide range of frequencies without using piecewise functions. Two types of punched edges are defined. The additional iron losses are tested, compared, and modeled so that the punching and burrs' connection effects on iron losses can be considered more accurate.

(2) The iron losses of a high-speed PM motor, including the punching and burrs' connection effects, have been calculated by the proposed new model. The iron losses of a bonded stator core with three different magnetized rotors have been measured to verify the calculation method. Among the three magnetization directions, the radial magnetization with a reduced magnet pitch of 0.85 is the best choice for the high-speed surface-mounted PMSM from the point of view of iron losses and output power capacity. The retardation method and a non-magnetized rotor are used to separate losses and determine the stator iron losses. Based on this method, the additional iron losses caused by welding and radial pressure have been measured. The experimental results show that the calculation error will be huge if the manufacturing factors are ignored. Also, the temperature influence on iron losses was evaluated.

(3) The air friction losses have been calculated and verified. A new test method has been proposed to compensate for the systematic errors caused by temperature rise and effectively improve the accuracy of air friction losses separation. Experiments show that the roughness coefficient k_f is substantially independent of the air gap length while k_2 in (3.11) will increase with the decrease of air gap length.

(4) The AC to DC resistance ratio of random-wound windings has been studied by an analytical method and verified by experiment. A series connection of windings has been proposed to minimize the influence of iron losses on AC resistance. Copper losses including proximity effect have been calculated.

(5) A thermal network model for stator with immersion evaporative cooling method has been established and verified by an immersion evaporative cooling test vessel. Leakage air rises to the upper part of the vessel. When air covers the condenser tubes, condensation is significantly reduced. Heat flux density and pressure have little influence on the total thermal resistance of the windings. The fixation bandage of end windings should be wound discontinuously for better evaporation.

(6) Finally, a high-speed PM motor prototype with immersion evaporative cooling was designed, built, and tested under load. The test results show that the immersion evaporative cooling method can significantly enhance the thermal loading and expand the power limit. The accuracy of the thermal network model is satisfactory. The permanent magnets longer than the stator core can increase the equivalent air gap flux density and thus expand the power limit. The experimental results show that finned tubes can significantly enhance the condensation heat transfer. The welded stator core with ventilation ducts and end plates used in the prototype introduces too much additional iron losses and should be avoided for high-speed motors. Calorimetry was used to determine the efficiency of the high-speed motor, and the results prove the accuracy and effectiveness of the loss models presented in this thesis.

7.2 Potential future work

More work is required on the stator stack layout to reduce the additional iron losses due to the manufacturing process.

An optimization of the magnet pitch and the axial magnet extension with respects to cost is necessary.

The enhancement ratio of high-finned tubes needs to be confirmed by further experiment.

Appendix

A1 Main structural parameters of the motors

Table A1: Main structural parameters

	Air-water	Evap		Air-water	Evap
Stator outer diameter	260 mm	same	Stator inner diameter	112 mm	same
Stator stack length	165 mm	70	Air gap length	3.5 mm	same
Number of slots	24	same	Number of poles	2	same
Winding layers	2	same	Coil pitch	10	same
Number of parallel	2	same	Conductors per slot	6	10
Number of strands	60	36	Wire diameter	0.7 mm	same
PM thickness	8 mm	same	Retaining sleeve thickness	4 mm	same

* "Air-water" refers to the existing air-water cooled high-speed PM motor used in Chapter 2 and 3.
* "Evap" refers to the high-speed PM motor prototype with immersion evaporative cooling.

A2 Material properties

Table A2: Magnetic properties of Sm_2Co_{17} at 20°C

B_r	H_c	H_{cj}	$\alpha\,(B_r)$
1.06 T	780 kA/m	1,433 kA/m	-0.03%/K

Table A3: Main material properties

Part	Material	Thermal conductivity $W/(m \cdot K)$	Conductivity (S/m)	Relative permeability
Retaining sleeve	Titanium alloy	21	588,000	1
Magnet	Sm_2Co_{17}	10	1,111,111	1.04
Interpole block	SAE 304	16.3	1,100,000	1
Shaft	4340 steel	42	5,260,000	500

A3 Cross-section drawings

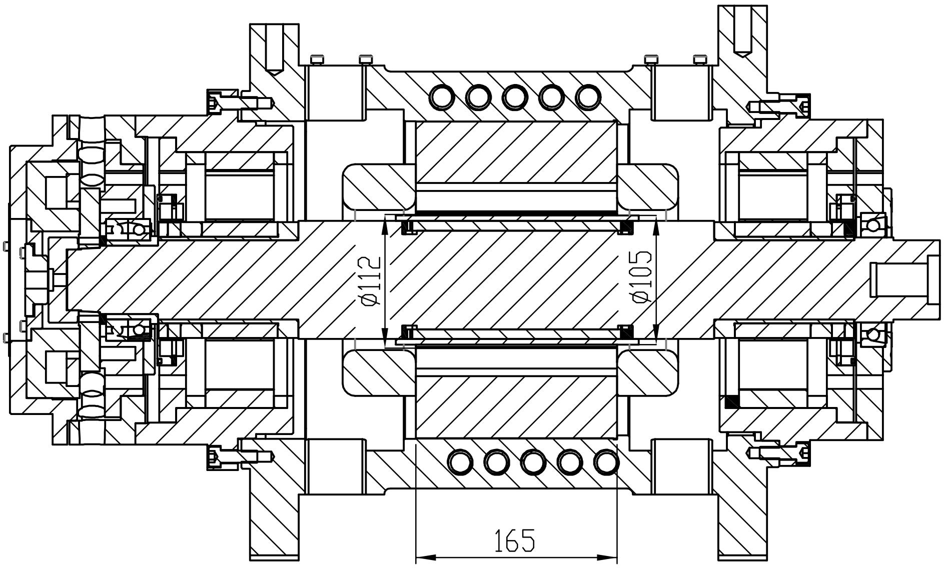

Fig. A1: Cross-section view of the air-water cooled high-speed PM motor

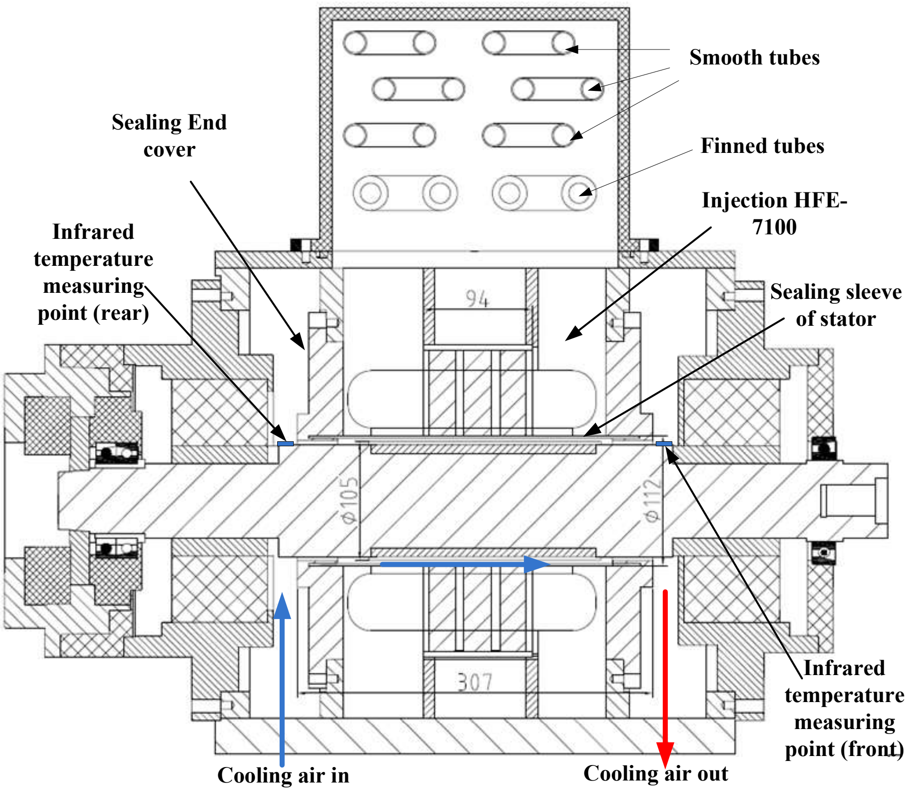

Fig. A2: Cross-section view of the immersion evaporative cooling prototype

A4 Finned tubes

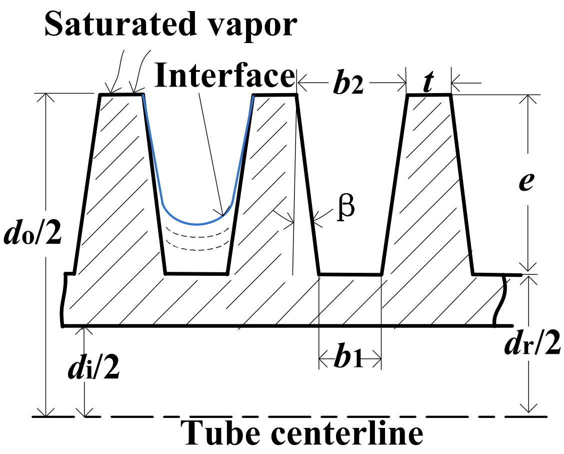

Fig. A3: Film condensation on trapezoidal finned tube [73]

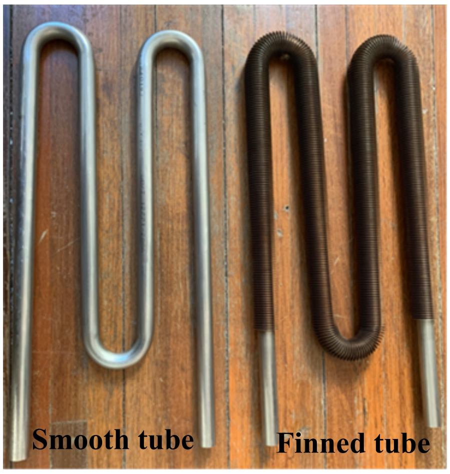

Fig. A4: Photo of smooth tube and finned tube

Table A4: Specifications of finned tubes

e	d_r	d_i	β	b_1	b_2	t
5 mm	20 mm	17.6 mm	0°	2.8 mm	2.8 mm	0.5 mm

* Symbols have defined in Fig. A3

When the outside diameter of the smooth tubes is equal to the root diameter of the finned tubes, the enhancement ratio k_fin for low-finned tubes is defined as the heat transfer coefficient ratio between the finned tubes and smooth tubes [91]:

$$\begin{aligned}
k_\mathrm{fin} &= \frac{\psi_1 + \psi_2 + \psi_3}{0.728 \cdot (b_2 + t)} \\
\psi_1 &= \left(\frac{d_\mathrm{o}}{d_\mathrm{r}}\right)^{3/4} \cdot t \cdot \left[0.281 + \frac{D_2 \cdot \sigma \cdot d_\mathrm{o}}{t^3 \cdot g \cdot (\rho_\mathrm{L} - \rho_\mathrm{s})}\right]^{1/4} \\
\psi_2 &= \frac{\phi_\mathrm{f}}{\pi} \cdot \frac{1 - f_\mathrm{f}}{\cos\beta} \cdot \frac{d_\mathrm{o}^2 - d_\mathrm{r}^2}{2 \cdot e_\mathrm{v}^{1/4} \cdot d_\mathrm{r}^{3/4}} \cdot \left[0.791 + \frac{D_2 \cdot \sigma \cdot e_\mathrm{v}}{e^3 \cdot g \cdot (\rho_\mathrm{L} - \rho_\mathrm{s})}\right]^{1/4} \\
\psi_3 &= \frac{\phi_\mathrm{f}}{\pi} \cdot D_3 \cdot (1 - f_\mathrm{r}) \cdot b_1 \cdot \left\{[\xi(\phi_\mathrm{f})]^3 + \frac{D_2 \cdot \sigma \cdot d_\mathrm{r}}{b_1^3 \cdot g \cdot (\rho_\mathrm{L} - \rho_\mathrm{s})}\right\}^{1/4}
\end{aligned} \tag{A1}$$

where

$$\phi_\mathrm{f} = \cos^{-1}\left(\frac{4 \cdot \sigma \cdot \cos\beta}{\rho_L \cdot g \cdot b_2 \cdot d_\mathrm{o}} - 1\right) \qquad \text{for } e > 2 \cdot b_2 \cdot (1 - \sin\beta)/\cos\beta \tag{A2}$$

$$\begin{aligned}
\xi(\phi_\mathrm{f}) =& 0.874 + 0.1991 \cdot 10^{-2} \cdot \phi_\mathrm{f} - 0.2642 \cdot 10^{-1} \cdot \phi_\mathrm{f}^2 + 0.5530 \cdot 10^{-2} \cdot \phi_\mathrm{f}^3 \\
&- 0.1363 \cdot 10^{-2} \cdot \phi_\mathrm{f}^4
\end{aligned} \tag{A3}$$

$$f_\mathrm{f} = \frac{1-\tan(\beta/2)}{1+\tan(\beta/2)} \cdot \frac{2\cdot\sigma\cdot\cos\beta}{\rho_\mathrm{L}\cdot g\cdot d_\mathrm{r}\cdot e} \cdot \frac{\tan\left(\phi_\mathrm{f}/2\right)}{\phi_\mathrm{f}} \tag{A4}$$

$$f_r = \frac{1-\tan(\beta/2)}{1+\tan(\beta/2)} \cdot \frac{4\cdot\sigma}{b_1\cdot\rho_\mathrm{L}\cdot g\cdot d_\mathrm{r}} \cdot \frac{\tan\left(\phi_\mathrm{f}/2\right)}{\phi_\mathrm{f}} \tag{A5}$$

$$e_\mathrm{v} = \frac{\phi_\mathrm{f}}{\sin\phi_\mathrm{f}}\cdot e \quad \text{for } \phi_\mathrm{f} \le \frac{\pi}{2} \tag{A6}$$

$$e_\mathrm{v} = \frac{\phi_\mathrm{f}}{2-\sin\phi_\mathrm{f}}\cdot e \quad \text{for } \frac{\pi}{2} \le \phi_\mathrm{f} \le \pi \tag{A7}$$

$D_2 = 0.143$ and $D_3 = 2.96$ are constants obtained by fitting the experimental data in [91].

A5 Specifications of instruments

Table A5: Specifications of instruments used in Chapter 2

Instrument	Range	Accuracy	Function
Pt100 data logger	-50–300°C	±0.15°C	Temperature measurement
Scales	0–100 kg	±2 g	Mass of the rotor parts
Oscilloscope	0–1000 V BW: 100 MHz	±5 V	Back EMF waveform recording

Table A6: Instruments used in Chapter 3

Instrument	Range	Accuracy	Function
Relative pressure gauge	-100–0 kPa	±0.4 kPa	Relative vacuum inside the vessel
Relative pressure gauge	0–1000 kPa	±4 kPa	Relative pressure
Air flow meter	0.2–20 m/s	±0.3 m/s	Air flow velocity
Pt100 data logger	-50–300°C	±0.15°C	Temperature measurement
Oscilloscope	0–1000 V BW: 100 MHz	±5 V	Back EMF waveform recording
Power analyzer	1.5–1000 V 0–100 A	±2 V ±0.3 A	Input power measurement

Table A7: Instruments used in Chapter 4

Instrument	Range	Accuracy	Function
DC resistance meter	200 mΩ/20 Ω	±0.2 mΩ/±0.02 Ω	DC resistance measurement
LCR Meter	10 Hz–200 kHz		LCR measurement
Power analyzer	1.5–1000 V, 0.5 A/1 A/2 A/5 A	±2 V 0.1%	Input power measurement
Adjustable AC power source	0–150 V, 8.4 A; 0–300 V, 4.2 A; 45.0–500.0 Hz	Voltage THD <0.5%	

Table A8: Instruments used in Chapter 5

Instrument	Range	Accuracy	Function
Pressure gauge	-100–100 kPa	±0.8 kPa	Relative pressure
Thermo-barometer	-10–60°C 30–120 kPa	±0.4°C ±0.3 kPa	Ambient temperature atmospheric pressure
Water flow meter	0–20 L/min	±0.1 L/min	Water flow rate
Infrared thermometer	-18–275°C	±2°C	Surface temperature
Pt100 data logger	-50–300°C	±0.15°C	Temperature measurement
Power analyzer	1.5–1000 V 0–500 A	±2 V ±0.5 A	Input power measurement
Digital clamp meter	0–600 VDC 0–40 A	±6 V ± 0.64 A	DC input power measurement
Three-phase voltage regulator	Voltage: 0–430 VAC Max current: 10 A		Adjust input power
DC power supply	43–55 V, 500 W, 4 sets; 48 V, 1000 W, 1 set		Adjust input power
Heater	220 VAC, 1200 W, 3 sets		Auxiliary heating

Table A9: Specifications of instruments in Chapter 6

Instrument	Range	Accuracy	Function
Relative pressure transducer	-100–10 kPa	0.25%	Relative pressure inside the vessel
Infrared temperature sensor	-50°C–600°C	±1 °C	Rotor temperature
Oscilloscope	0–1000 V 0–500 A	Voltage: ± 0.5% Current: ± 0.5%	Voltage and current waveform

A6 Test records

Table A10: Test results of the bottom row with different air content

No.	P_{all} (W)	P_1 (W)	V (mL)	H (mm)	T_{s} (°C)	p_{s} (kPa)	T_{water} (°C)	T_{ambient} (°C)
1	3,920	3,110	0	0	68.1	123.3	41.3	21.0
2	3,748	2,938	3,000	15.5	67.8	123.4	41.4	19.4
3	3,657	2,863	6,000	31	67.8	123.4	41.5	21.7
4	3,841	3,046	9,000	46.5	67.5	122.8	40.9	22.2
5	3,608	2,875	12,000	62	68.0	123.9	41.2	25.0
6	2,887	2,127	15,000	85	67.7	123.2	41.5	26.7
7	2,399	1,649	16,500	94	67.7	123.4	41.2	29.2
8	1,717	957	18,000	102	67.7	123.0	40.8	28.8
9	953	179	19,500	110	67.6	124.0	40.8	26.2
10	721	-29	20,100	113	67.2	123.7	40.8	28.4

* The actual air volume in the vessel is $V_1 = V \cdot (101.3 \text{ kPa})/p_{\text{s}}$, where V is the cumulative volume of air injected at 101.3 kPa; P_{all} is the measured total input power; P_1 is the calculated value by (5.23).

Table A11: Test results of the top row with different air content

No.	P_{all} (W)	P_1 (W)	V (mL)	H (mm)	T_{s} (°C)	p_{s} (kPa)	T_{water} (°C)	T_{ambient} (°C)
1	3,072	2,272	6,000	31	67.8	123.6	41.2	21.7
2	1,029	270	12,000	62	68.0	124.0	41.3	28.7
3	788	44	15,000	85	67.5	122.8	41.3	29.1

Table A12: Temperature records at different copper losses (°C)

Location	No.	1,736 W	1,000 W	900 W	800 W	700 W	610 W	500 W
Passive end winding	1	83.3	76.2	75.3	74.1	73.0	71.9	70.8
	2	100.2	86.4	84.4	82.2	80.2	78.1	76.0
	3	94.3	83.3	81.6	79.7	77.9	76.2	74.1
	4	87.3	77.9	76.8	76.6	74.8	73.1	69.6
End winding on supply side	17	116.1	97.0	93.5	89.2	86.1	83.1	81.5
	18	122.8	100.4	97.0	92.4	89.1	85.8	83.8
	19	114.5	95.2	92.2	88.9	85.8	82.4	79.1
	20	103.8	88.8	86.4	83.7	81.2	78.6	75.9
Windings in slots	8	98.0	85.0	83.0	80.7	78.6	76.4	74.1
	9	91.8	82.0	80.3	78.5	76.8	75.0	73.2
	10	95.3	84.3	82.3	80.3	78.4	76.1	74.2
	14	82.3	74.7	74.7	73.6	72.6	71.5	70.3
	15	105.1	89.1	86.8	84.2	81.7	79.4	76.6
	16	107.7	92.4	89.7	86.0	83.5	81.0	79.7

Table A13: Temperature records at different pressure (°C)

Location	No.	113 kPa (1,736 W)	123 kPa (1,725 W)	132 kPa (1,714 W)	143 kPa (1,704 W)	152 kPa (1,698 W)
Passive end winding	1	83.3	85.8	88.4	90.5	92.0
	2	100.2	102.4	104.4	106.0	107.0
	3	94.3	96.7	98.8	101.0	102.0
	4	87.3	89.5	90.9	92.6	96.2
End winding on supply side	17	116.1	118.9	120.8	123.0	125.0
	18	122.8	125.7	127.2	129.0	130.0
	19	114.5	116.8	118.7	120.0	122.0
	20	103.8	106.1	108.0	110.0	112.0
Windings in slots	8	98.0	99.5	102.0	104.0	106.0
	9	91.8	94.2	96.1	98.1	100.0
	10	95.3	97.7	99.8	102.0	104.0
	14	82.3	84.8	86.8	89.0	89.6
	15	105.1	107.2	109.0	111.0	112.0
	16	107.7	110.8	113.0	116.0	115.0
Liquid	21	65.1	67.7	70.1	72.4	74.6
	22	60.9	63.1	66.3	68.5	71.8
	27	70.5	73.6	75.9	78.5	79.9
	28	64.8	67.5	69.8	72.1	74.3

Table A14: Records of comparison experiment of the smooth tubes and finned tubes

	Water flow rate	Inlet water Temperature	Outlet water Temperature	Vapor Temperature
Three layers smooth tubes	8.27 L/min	30.6°C	35.8°C	54°C
Single layer finned tubes	8.24 L/min	27.3°C	32.4°C	56°C

Abbreviations

CFD	Computational fluid dynamics
CHF	Critical Heat Flux
DNB	Departure from Nucleate Boiling
EMF	Electromotive Force
FEM	Finite Element Method
IEECAS	Institute of Electrical Engineering in Chinese Academy of Sciences
IM	Induction machines
IPM	Interior Permanent Magnet
ONB	Onset of Nucleate Boiling
PM	Permanent Magnet
PMSM	Permanent Magnet Synchronous Motor
PWM	Pulse Width Modulation
RMS	Root mean square
SPM	Surface-Mounted Permanent Magnet
THD	Total Harmonic Distortion

Symbols

Greek and Other Symbols

α	Arc-angle of an arc segment, rad; magnet pitch; exponent in (2.9)
α_1, α_2	Fitting exponents of simulated eddy current losses for the target surface and the sample surface, respectively
β	Half-angle at the fin tip, rad
γ	Phase angle between the currents of the upper and lower layer in the slot, deg
δ	Air gap length, m
δ_{ef}	Effective air gap length, whose value is the sum of air gap length and retaining sleeve thickness, m
δ_{i}	Thickness of material i, m
δ_{liner}	Equivalent thickness of the slot liner, m
δ_{s}	Skin depth, m
δ_{sl}	Thickness of the sleeve, mm
ΔB_{jr}	Flux reversal, T
ΔP_{t}	Total loss difference, W
ΔP_{f}	Total air friction loss difference, W
Δp	Pressure difference, kPa
ΔT_{sat}	Wall overtemperature, K
Δx	Distance in x direction, m
η	Efficiency
θ	Inclination angle, deg

θ_{k}	Phase of k-th order harmonic, rad
θ_{kr}, $\theta_{\mathrm{k}\theta}$	Phase of k-th order harmonic in the r-axis and θ-axis directions, respectively, rad
λ_{a}	Thermal conductivity in the axial direction, $\mathrm{W/(m \cdot K)}$
λ_{av}	Average thermal conductivity in the xy plane, $\mathrm{W/(m \cdot K)}$
λ_{c}	Thermal conductivity in circumferential direction, $\mathrm{W/(m \cdot K)}$
λ_{cu}	Thermal conductivity of copper, $\mathrm{W/(m \cdot K)}$
λ_{f}	Fluid thermal conductivity, $\mathrm{W/(m \cdot K)}$
λ_{i}	Thermal conductivity of material i, $\mathrm{W/(m \cdot K)}$
λ_{L}	Thermal conductivity of the liquid, $\mathrm{W/(m \cdot K)}$
λ_{liner}	Equivalent thermal conductivity of the slot liner, $\mathrm{W/(m \cdot K)}$
λ_{r}	Thermal conductivity in radial direction, $\mathrm{W/(m \cdot K)}$
λ_{w}	Thermal conductivity of the tube wall, $\mathrm{W/(m \cdot K)}$
λ_{x}, λ_{y}	Thermal conductivity in the x and y directions, respectively, $\mathrm{W/(m \cdot K)}$
λ_1	Thermal conductivity of the silicon steel, $\mathrm{W/(m \cdot K)}$
λ_2	Thermal conductivity of static air, $\mathrm{W/(m \cdot K)}$
μ	Dynamic viscosity, Pa·s; magnetic permeability, H/m
μ_{L}	Dynamic viscosity of the liquid, Pa·s
μ_0	Reference dynamic viscosity of the air, Pa·s
ν	Fluid kinematic viscosity, $\mathrm{m^2/s}$
ρ	Density, $\mathrm{kg/m^3}$
ρ_{L}	Liquid density, $\mathrm{kg/m^3}$
ρ_{s}	Density of the saturated vapor, $\mathrm{kg/m^3}$
ρ_0	Reference density of the air, $\mathrm{kg/m^3}$
σ	Surface tension of the liquid, N/m; electrical conductivity, S/m

τ	Pole pitch of the rotor, m
Ψ_{AB}	Flux passing through the line segment AB in Fig. 6.3(a), Wb
Ψ_{b}	Flux passing through the line segment AB in Fig. 6.3(b), Wb
Ψ_{side}	Flux passing through the side segment in Fig. 6.3(a), Wb
$\omega(t)$	Angular rotational speed of the rotor, rad/s

Latin

A	Area of the evaporation surface, m^2
A_{s}	Specific electric loading, A/m
B'	Flux density extracted from the 2-D model, T
B_δ	RMS value of the air gap flux density, T
B_r	Remanence, T
$\vec{B}(t)$	Rotational flux density vector, T
B_{krm}, $B_{\mathrm{k}\theta\mathrm{m}}$	Amplitude of k-th order harmonic in the r-axis and θ-axis directions, respectively, T
B_{rm}	Amplitude of $B_{\mathrm{r}}(t)$, T
$B_{\mathrm{r}}(t)$, $B_\theta(t)$	Components of flux density in the r-axis and θ-axis directions, respectively, T
B_{side}	Actual flux density in the side segment of the stator core, T
b_1	Spacing between fins at the root, m
b_2	Spacing between fins at the tip, m
C_{f}	Air friction coefficient
C_1	A constant coefficient in (3.4.2)
c_{f}	Fluid specific heat capacity at constant pressure, $\mathrm{J/(kg \cdot K)}$
D	Exponent in (3.4.2)
D_{si}	Stator inner diameter, m
D_1	A constant with a value of 1.4472
d_{i}	Inner diameter of the tube, m
d_{o}	Outer diameter of the tube, m

d_{r}	Diameter of the tooth root of the finned tube, m
E_{d}	Dielectric strength, kV/m
E_0	RMS value of the fundamental component of line voltage of back EMF, V
$E(t)$	Rotor kinetic energy, J
e	Fin height, m
f	Frequency of a sinusoidal wave, Hz
f_{s}	Switching frequency, Hz
g	Gravitational acceleration, $\mathrm{m/s^2}$
H	Height of the air in the vessel, as defined in Fig. 5.28, mm
H_{c}	Coercivity, kA/m
H_{fg}	Latent heat of the liquid, J/kg
h_{c}	Average condensation heat transfer coefficient of one smooth tube, $\mathrm{W/(m^2 \cdot K)}$
h_{cN}	Average condensation heat transfer coefficient of horizontal tube bundle, $\mathrm{W/(m^2 \cdot K)}$
h_{evp}	Nucleate pool boiling heat transfer coefficient, $\mathrm{W/\left(m^2 \cdot K\right)}$
h_{f}	Convection heat transfer coefficient in the tube, $\mathrm{W/(m^2 \cdot K)}$
h_{m}	Permanent magnet thickness, m
I_{N}	RMS value of the phase current, A
I_{Nd}, I_{Nq}	d axis and q axis components of the phase current respectively, A
I_{k}	RMS of k-th order harmonic, A
i_{d}, i_{q}	d axis and q axis currents respectively, A
i_{d}^*, i_{q}^*	Reference d axis and q axis currents respectively, A
J	Moment of inertia, $\mathrm{kg \cdot m^2}$
k	Harmonic order

k_{ACL}	AC inductance ratio
k_{ACR}	Total AC to DC resistance ratio
k_{ACR1}	AC to DC resistance ratio due to skin effect
k_{ACR2}	Average AC to DC resistance ratio due to proximity effect in slots
$k_{\mathrm{ACR2,ABC}}$	k_{ACR2} in series connection
$k_{\mathrm{ACR2,Y}}$	k_{ACR2} in Y connection
k_{ACR3}	AC to DC resistance ratio of the ending windings
k_{c}	Coefficient in (2.9), $\mathrm{W}/\left(\mathrm{kg}\cdot\mathrm{T}^2\cdot\mathrm{Hz}^{\alpha}\right)$
k_{c1}, k_{c2},	Fitting coefficients of simulated eddy current losses for the target surface and the sample surface, respectively, $\mathrm{W}/\left(\mathrm{kg}\cdot\mathrm{T}^2\cdot\mathrm{Hz}^{\alpha}\right)$
k_{e}	Gibbs coefficient
k_{Fe}	Stacking factor of the laminated core
k_{f}	Roughness coefficient
k_{h}	A hysteresis loss related coefficient depending on properties of silicon steel sheet
k_{IIb}	Simulated specific eddy-current loss ratio
k_{m}	Ratio of Ψ_{AB} to Ψ_{b}
k_{s}	Ratio of winding length in slots to the average half turn length
$k_{\mathrm{total,I}}$	Correction factor of harmonic distortion for $B_{\mathrm{r}}(t)$ of point A
$k_{\mathrm{total,r}}$	Correction factor of harmonic distortion for $B_{\mathrm{r}}(t)$
k_{w}	Winding factor
k_2	A coefficient defined in (3.11)
L_{ABC}	AC inductance of three-phase windings in series connection, H
$L_{\mathrm{AC}}(f)$	AC inductance at frequency f, H
L_{choke}	Choke inductance, H
L_{end}	End-winding leakage inductance, H

L_{phase}	Average inductance of three-phase windings, H
L_{se}	Excessive part of the slot leakage inductance, H
$L_{10\,\text{Hz}}$	AC inductance at 10 Hz, H
l	Length of a cylinder, m
l_{a}	Axial length of an arc segment, m; length of line segment a, m
l_{av}	Average half turn length, m
l_{Fe}, l_{ef}	Physical and effective stator core length respectively, m
l_{m}	Total axial length of the permanent magnet, m
l_{side}	Length of the side segment, m
l_{t}	Total length of the prototype stator core, m
l_{tu}	Tube length, m
M	Mass of the cylinder, kg
M_{r}	Relative molar mass, dimensionless
m	Number of strand layers in the slot
N	Number of reversals in the positive half cycle as shown in Fig. 2.1
N_{r}	Number of rows in the vertical direction
Nu	Nusselt number
N_{v}	Number of the ventilation ducts
n	Rotational speed, revolutions per second
P	Internal heat generation of an arc segment, W
P_{all}	Total losses, W
P_{axial}	Additional air friction losses caused by axial throughflow, W
$P_{\text{bearing,r}}$	Iron losses in the rotor of the magnetic bearings, W
P_{cu}	Copper losses, W
$P_{\text{edd,ep}}$	Eddy current losses produced in the end plates, W
$P_{\text{edd,r}}$	Eddy current losses in the rotor, W

P_{fe}	Stator iron losses, W
P'_{fe}	Total basic iron losses corresponding to 347.5 V, W
$P_{\mathrm{fe,adp}}$	Additional iron losses due to punching and burrs' connection, W
$P_{\mathrm{fe,adw}}$	Additional iron losses due to welding and radial pressure, W
P_{feb}	$P_{\mathrm{fe}}+P_{\mathrm{bearing,r}}$, W
$P_{\mathrm{fe,b}}$	Basic iron losses, W
P_{f}	Air friction losses, W
P_{f0}	Air friction losses without axial flow, W
$P_{\mathrm{f}}\left(p\right)$	Air friction losses at absolute pressure p, W
$P'_{\mathrm{f}}\left(p\right)$	Calculated air friction losses with $k_{\mathrm{f}}=1$ at absolute pressure p, W
P_{heater}	Heater losses, W
P_{in}	Measured input power of the motor, W
P_{I}	Additional iron losses corresponding to punching edge type I, W
P_{IIb}	Additional iron losses caused by burrs' connection for punching edge type II, W
P_{IId}	Additional iron losses due to deterioration for punching edge type II, W
P_{loss}	Losses under load, W
Pr	Prandtl number
Pr_{w}	Prandtl number at the wall temperature
$P_{\mathrm{t}}\left(p\right)$	Total no-load losses at absolute pressure p, W
P_1	Condensation heat transfer power, W
P_2	Surface heat dissipation, W
P_3	Power flow through R_3, W
p	Mumber of pole pairs; absolute pressure of the gas, Pa
p_{crit}	Critical pressure, Pa

$p_{\mathrm{c,r}}$	Specific total eddy current losses for $B_{\mathrm{r}}(t)$, W/kg
$p_{\mathrm{c,sin}}\left(T, kf, B_{\mathrm{krm}}\right)$	Specific eddy current losses of k-th order harmonic in the radial direction at temperature T, W/kg
$p_{\mathrm{fe,r}}$, $p_{\mathrm{fe},\theta}$	Specific iron losses for $B_{\mathrm{r}}(t)$ and $B_{\theta}(t)$, respectively, W/kg
$p_{\mathrm{fe,rot}}$	Total specific iron losses for a rotational flux density, W/kg
$p_{\mathrm{h,r}}$	Specific total hysteresis losses for $B_{\mathrm{r}}(t)$, W/kg
$p_{\mathrm{h,sin}}\left(f, B_{\mathrm{rm}}\right)$	Specific hysteresis losses for sinusoidal flux density with amplitude of B_{rm} at frequency f, W/kg
$p_{\mathrm{I,h}}$, $p_{\mathrm{I,c}}$	Additional hysteresis losses and eddy current losses per unit punching area, respectively, W/m^2
p_{IIb}	Surface-related specific additional iron losses caused by burrs' connection for punching edge type II, W/m^2
p_{IId}	Surface-related specific additional iron losses due to the performance deterioration for punching edge type II, W/m^2
$p_{\mathrm{I,c,sin}}\left(kf, B_{\mathrm{krm}}, T\right)$	Additional eddy current losses per punching area of k-th order harmonic of $B_{\mathrm{r}}(t)$ at temperature T, W/m^2
$p_{\mathrm{I,h,sin}}\left(f, B_{\mathrm{rm}}\right)$	Additional hysteresis losses per unit punching area for sinusoidal magnetic flux density with amplitude of B_{rm} at frequency f, W/m^2
p_{r}	Reduced pressure
p_{s}	Saturated vapor pressure, Pa
p_0	Reference absolute pressure of the air, Pa
Q	Water flow rate, L/min
q	Heat flux, W/m^2
q_{DNB}	Critical Heat Flux, W/m^2
q_{ONB}	Heat flux of ONB, W/m^2
R	Half distance between the centers of the adjacent magnet wires defined in Fig. 5.10(a), m
R_{a1}, R_{a2}, R_{a3}	Thermal resistances of axial heat flow, K/W

R_{Aa}, R_{Bb}, R_{Cc}	Resistance of winding A, winding B , winding C, Ω
R_{ABC}	Resistance of three-phase windings in series connection, Ω
$R_{\mathrm{AC}}(f)$	AC resistance at frequency f, Ω
R_{c}	Condensation thermal resistance between the vapor and the outer wall of the smooth tubes, K/W
R_{c1}, R_{c2}, R_{c3}	Thermal resistances of circumferential heat flow, K/W
$R_{\mathrm{c-total}}$	Thermal resistance between saturated vapor and water, K/W
R_{cu}	Thermal resistances from the winding to liquid, K/W
$R_{\mathrm{cu-fe}}$	Thermal resistance between the winding and core, K/W
R_{DC}	DC resistance, Ω
Re	Reynolds number
Re_{r}	Reynolds number for rotating flow
Re_{δ}	Reynolds number for Taylor Couette flow
R_{evp}	Evaporation thermal resistance, K/W
R_{f}	Convection thermal resistance of water in the tubes, K/W
R_{fe}	Thermal resistances from the core to liquid, K/W; iron-resistance, Ω
R_{p}	Mean surface roughness, μm
R_{phase}	Average value of R_{Aa}, R_{Bb} and R_{Cc}, Ω
$R_{\mathrm{phase,AC}}$	AC phase resistance, Ω
R_{r1}, R_{r2}, R_{r3}	Thermal resistances of radial heat flow, K/W
R_{w}	Thermal resistances of the tubes wall, K/W
R_{w1}	Thermal resistances of one tube wall, K/W
R_2	Thermal resistance of surface heat dissipation, K/W
R_3	Defined in Fig. 5.5 , K/W
r	Radius of copper of the magnet wire, or radius of the cylinder, m

r_1, r_2	Inner radius and outer radius respectively, m
S	Apparent power, VA; Sutherland constant, K
S_{f}	Fill factor
S_{fmax}	The maximum fill factor
s	Axial clearance of a rotating disc from a stationary wall, m
T	Average temperature of an arc segment, °C; static temperature of the gas, K
Ta	Taylor number
Ta_{c}	Critical Taylor number with a value of 41.3
T_{ambient}	Ambient temperature, °C
T_{s}	Saturated vapor temperature, K or °C
T_{sc1}	Calculated saturated vapor temperature ignoring the R_3 branch, K or °C
T_{sc2}	Calculated saturated vapor temperature considering the R_3 branch, K or °C
T_{water}	Average water temperature, K or °C
T_{wo}	Tube outer wall temperature, K or °C
T_{δ}	Air gap temperature, °C
T_0	Reference temperature of the air, K
T_1, T_2	Temperatures of the left and right boundaries, respectively, K
t	Fin tip thickness, m
u	Velocity of the fluid, m/s
u_{c}	Circumferential fluid velocity, m/s
u_{DC}	DC bus voltage, V
u_1	Circumferential speed of the rotor, m/s
v_{a}	Average axial fluid velocity, m/s

Bibliography

[1] A. Arkkio, T. Jokinen, and E. Lantto, "Induction and permanent-magnet synchronous machines for high-speed applications," in *2005 International Conference on Electrical Machines and Systems*, vol. 2, pp. 871–876, 2005.

[2] R. Abebe, M. Di Nardo, D. Gerada, G. L. Calzo, L. Papini, and C. Gerada, "High speed drives review: Machines, converters and applications," in *IECON 2016 - 42nd Annual Conference of the IEEE Industrial Electronics Society*, pp. 1675–1679, 2016.

[3] D. Gerada, A. Mebarki, N. L. Brown, C. Gerada, A. Cavagnino, and A. Boglietti, "High-speed electrical machines: Technologies, trends, and developments," *IEEE Transactions on Industrial Electronics*, vol. 61, no. 6, pp. 2946–2959, 2014.

[4] M. D. Bui, *Maximum torque control of a high speed switched reluctance starter/generator used in more/all electric aircraft*. PhD thesis, TU-Berlin, 2014.

[5] J. F. Gieras and J. Saari, "Performance calculation for a high-speed solid-rotor induction motor," *IEEE Transactions on Industrial Electronics*, vol. 59, no. 6, pp. 2689–2700, 2012.

[6] "Advancing the next generation in subsea compression technology." `https://corporate.man-es.com/press-media/news-overview/details/2016/10/11/advancing-the-next-generation-in-subsea-compression-technology`. 11 Oct. 2016.

[7] A. Binder, T. Schneider, and M. Klohr, "Fixation of buried and surface-mounted magnets in high-speed permanent-magnet synchronous machines," *IEEE Transactions on Industry Applications*, vol. 42, no. 4, pp. 1031–1037, 2006.

[8] `http://esurging.com/blower/10/266.html`. 20 Sept. 2020.

[9] "Atlas copco launches its most energy-efficient oil-free compressor ever: the zh 350 +." `https://www.prweb.com/releases/2011/4/prweb8280839.htm`. 7 April 2011.

[10] `https://www.tamturbo.com/`. 20 Aug. 2020.

[11] "The world's leader in oil-free compressor technology." `https://www.danfoss.com/en/products/compressors/dcs/turbocor/`. 20 Sept. 2020.

[12] "A distributed generation case study of capstone turbine corporation," Sept. 2014.

[13] F. Luise, A. Tessarolo, F. Agnolet, S. Pieri, M. Scalabrin, and P. Raffin, "A high-performance 640-kW 10.000-rpm halbach-array PM slotless motor with active magnetic bearings. Part I: Preliminary and detailed design," in *2014 International Symposium on Power Electronics, Electrical Drives, Automation and Motion*, pp. 1237–1244, 2014.

[14] F. Luise, A. Tessarolo, F. Agnolet, S. Pieri, M. Scalabrin, and P. Raffin, "A high-performance 640-kW 10.000-rpm halbach-array PM slotless motor with active magnetic bearings. Part II: Manufacturing and testing," in *2014 International Symposium on Power Electronics, Electrical Drives, Automation and Motion*, pp. 1245–1250, 2014.

[15] "Brochure of direct drive system," 2009.

[16] Z. Kolondzovski, A. Arkkio, J. Larjola, and P. Sallinen, "Power limits of high-speed permanent-magnet electrical machines for compressor applications," *IEEE Transactions on Energy Conversion*, vol. 26, no. 1, pp. 73–82, 2011.

[17] R. Lin, *Insulation and Heat Transfer of Horizontal Evaporative Cooling Motor Stator (in Chinese)*. Beijing: Science Press, 2009.

[18] G. Wang and X. Li, *Design, Manufacture and Operation of Large Turbine Generator (in Chinese)*. Shanghai: Shanghai Scientific and Technical Publishers, 2012.

[19] F. Crescimbini, A. Lidozzi, G. Lo Calzo, and L. Solero, "High-speed electric drive for exhaust gas energy recovery applications," *IEEE Transactions on Industrial Electronics*, vol. 61, no. 6, pp. 2998–3011, 2014.

[20] Z. Huang, J. Fang, X. Liu, and B. Han, "Loss calculation and thermal analysis of rotors supported by active magnetic bearings for high-speed permanent-magnet electrical machines," *IEEE Transactions on Industrial Electronics*, vol. 63, no. 4, pp. 2027–2035, 2016.

[21] F. Zhang, G. Du, T. Wang, W. Cao, and J. L. Kirtley, "Electromagnetic design and loss calculations of a 1.12 MW high-speed permanent-magnet motor for compressor applications," *IEEE Transactions on Energy Conversion*, vol. 31, no. 1, pp. 132–140, 2016.

[22] Z. Zhu, S. Xue, W. Chu, J. Feng, S. Guo, Z. Chen, and J. Peng, "Evaluation of iron loss models in electrical machines," *IEEE Transactions on Industry Applications*, vol. 55, no. 2, pp. 1461–1472, 2019.

[23] H. Zhao, D. Zhang, Y. Wang, Y. Zhan, and G. Xu, "Piecewise variable parameter loss model of laminated steel and its application in fine analysis of iron loss of inverter-fed induction motors," *IEEE Transactions on Industry Applications*, vol. 54, no. 1, pp. 832–840, 2018.

[24] S. Xue, J. Feng, S. Guo, Z. Chen, J. Peng, W. Q. Chu, P. L. Xu, and Z. Zhu, "Iron loss model for electrical machine fed by low switching frequency inverter," *IEEE Transactions on Magnetics*, vol. 53, no. 11, pp. 1–4, 2017.

[25] R. D. Findlay, N. Stranges, and D. K. MacKay, “Losses due to rotational flux in three phase induction motors,” *IEEE Transactions on Energy Conversion*, vol. 9, no. 3, pp. 543–549, 1994.

[26] Y. Huang, J. Dong, J. Zhu, and Y. Guo, “Core loss modeling for permanent-magnet motor based on flux variation locus and finite-element method,” *IEEE Transactions on Magnetics*, vol. 48, no. 2, pp. 1023–1026, 2012.

[27] J. Lavers, P. Biringer, and H. Hollitscher, “A simple method of estimating the minor loop hysteresis loss in thin laminations,” *IEEE Transactions on Magnetics*, vol. 14, no. 5, pp. 386–388, 1978.

[28] S. Xue, J. Feng, S. Guo, J. Peng, W. Q. Chu, and Z. Zhu, “A new iron loss model for temperature dependencies of hysteresis and eddy current losses in electrical machines,” *IEEE Transactions on Magnetics*, vol. 54, no. 1, pp. 1–10, 2018.

[29] B. Bilgin, J. Liang, M. V. Terzic, J. Dong, R. Rodriguez, E. Trickett, and A. Emadi, “Modeling and analysis of electric motors: State-of-the-art review,” *IEEE Transactions on Transportation Electrification*, vol. 5, no. 3, pp. 602–617, 2019.

[30] N. Takahashi, H. Morimoto, Y. Yunoki, and D. Miyagi, “Effect of shrink fitting and cutting on iron loss of permanent magnet motor,” *Journal of Magnetism and Magnetic Materials*, vol. 320, no. 20, pp. e925–e928, 2008.

[31] H. Domeki, Y. Ishihara, C. Kaido, Y. Kawase, S. Kitamura, T. Shimomura, N. Takahashi, T. Yamada, and K. Yamazaki, “Investigation of benchmark model for estimating iron loss in rotating machine,” *IEEE Transactions on Magnetics*, vol. 40, no. 2, pp. 794–797, 2004.

[32] A. Schoppa, J. Schneider, C. D. Wuppermann, and T. Bakon, “Influence of welding and sticking of laminations on the magnetic properties of non-oriented electrical steels,” *Journal of Magnetism and Magnetic Materials*, vol. 254, no. none, pp. 367–369, 2003.

[33] Z. Gmyrek and A. Cavagnino, “Influence of punching, welding, and clamping on magnetic cores of fractional kilowatt motors,” *IEEE Transactions on Industry Applications*, vol. 54, no. 5, pp. 4123–4132, 2018.

[34] R. Bojoi, A. Cavagnino, Z. Gmyrek, and M. Lefik, “Experimental assessment of the annealing effects on magnetic core of fractional power synchronous reluctance motors,” in *2016 XXII International Conference on Electrical Machines (ICEM)*, pp. 1692–1699, 2016.

[35] M. Centner and U. Schafer, “Optimized design of high-speed induction motors in respect of the electrical steel grade,” *IEEE Transactions on Industrial Electronics*, vol. 57, no. 1, pp. 288–295, 2009.

[36] A. Schoppa, J. Schneider, and J. O. Roth, “Influence of the cutting process on the magnetic properties of non-oriented electrical steels,” *Journal of Magnetism and Magnetic Materials*, vol. 215, pp. 100–102, 2000.

[37] J. Fang, X. Liu, B. Han, and K. Wang, "Analysis of circulating current loss for high-speed permanent magnet motor," *IEEE Transactions on Magnetics*, vol. 51, no. 1, pp. 1–13, 2015.

[38] G. Bertotti, A. Boglietti, M. Chiampi, D. Chiarabaglio, F. Fiorillo, and M. Lazzari, "An improved estimation of iron losses in rotating electrical machines," *IEEE Transactions on Magnetics*, vol. 27, no. 6, pp. 5007–5009, 1991.

[39] D. M. Saban, C. Bailey, D. Gonzalez-Lopez, and L. Luca, "Experimental evaluation of a high-speed permanent-magnet machine," in *Petroleum and Chemical Industry Technical Conference*, 2008.

[40] C. Zwyssig, S. D. Round, and J. W. Kolar, "Analytical and experimental investigation of a low torque, ultra-high speed drive system," in *Industry Applications Conference*, 2006.

[41] L. Bi, U. Schafer, and Y. Hu, "A new high-frequency iron loss model including additional iron losses due to punching and burrs' connection," *IEEE Transactions on Magnetics*, vol. 56, no. 10, pp. 1–9, 2020.

[42] R. Schifer and T. A. Lipo, "Core loss in buried magnet permanent magnet synchronous motors," *IEEE Transactions on Energy Conversion*, vol. 4, no. 2, pp. 279–284, 1989.

[43] D. M. Saban, D. A. Gonzalez-Lopez, and C. Bailey, "Beyond IEEE Std 115 and API 546: Test procedures for high-speed multimegawatt permanent-magnet synchronous machines," *IEEE Transactions on Industry Applications*, vol. 46, no. 5, pp. 1769–1777, 2010.

[44] T. Nakata, M. Nakano, and K. Kawahara, "Effects of stress due to cutting on magnetic characteristics of silicon steel," *IEEE Translation Journal on Magnetics in Japan*, vol. 7, no. 6, pp. 453–457, 1992.

[45] J. Saari, *Thermal analysis of high-speed induction machines*. PhD thesis, Helsinki University of Technollogy, 1998.

[46] E. Bilgen and R. Boulos, "Functional dependence of torque coefficient of coaxial cylinders on gap width and Reynolds numbers," *Journal of Fluids Engineering*, vol. 95, no. 1, p. 122, 1973.

[47] W. Sutherland, "The viscosity of gases and molecular force," *Philosophical Magazine*, vol. 36, no. 223, pp. 507–531, 1893.

[48] W. Tao, *Heat Transfer - 5th edition (in Chinese)*. Beijing: Higher Education Press, 2019.

[49] P. N. Childs, *Rotating Flow*. Oxford: Elsevier, 2011.

[50] T. Theodorsen and A. Regier, "Experiments on drag of revolving disks, cylinders and streamline rods at high speeds," Advance Confidential Report L4F16, NACA, 1944.

[51] J. W. .Polkowski, "Turbulent flow between coaxial cylinders with the inner cylinder rotating," *Journal of Engineering for Gas Turbines and Power*, vol. 106, no. 1, pp. 128–135, 1984.

[52] J. W. Daily and R. E. Nece, "Chamber dimension effects on induced flow and frictional resistance of enclosed rotating disks," *Journal of Basic Engineering*, vol. 82, no. 1, p. 217, 1960.

[53] J. Fang and S. Xu, "Effects of eddy current in electrical connection surface of laminated cores on high-speed PM motor supported by active magnetic bearings," *IEEE Transactions on Magnetics*, vol. 51, no. 11, pp. 1–4, 2015.

[54] M. van der Geest, H. Polinder, J. A. Ferreira, and D. Zeilstra, "Current sharing analysis of parallel strands in low-voltage high-speed machines," *IEEE Transactions on Industrial Electronics*, vol. 61, no. 6, pp. 3064–3070, 2014.

[55] P. L. Dowell, "Effects of eddy currents in transformer windings," *Proceedings of the Institution of Electrical Engineers*, vol. 113, no. 8, pp. 1387–1394, 1966.

[56] D. C. Hanselman and W. H. Peake, "Eddy-current effects in slot-bound conductors," *IEE Proceedings - Electric Power Applications*, vol. 142, no. 2, pp. 131–136, 1995.

[57] F. Tourkhani and P. Viarouge, "Accurate analytical model of winding losses in round litz wire windings," *IEEE Transactions on Magnetics*, vol. 37, no. 1, pp. 538–543, 2001.

[58] J. A. Ferreira, "Analytical computation of AC resistance of round and rectangular litz wire windings," *IEE Proceedings B - Electric Power Applications*, vol. 139, no. 1, pp. 21–25, 1992.

[59] M. Popescu and D. G. Dorrell, "Skin effect and proximity losses in high speed brushless permanent magnet motors," in *2013 IEEE Energy Conversion Congress and Exposition*, pp. 3520–3527, 2013.

[60] S. D. Sudhoff, *Power Magnetic Devices: A Multi-Objective Design Approach*. Wiley, 2014.

[61] R. Wrobel, A. Mlot, and P. H. Mellor, "Contribution of end-winding proximity losses to temperature variation in electromagnetic devices," *IEEE Transactions on Industrial Electronics*, vol. 59, no. 2, pp. 848–857, 2012.

[62] C. Huynh, L. Zheng, and D. Acharya, "Losses in high-speed permanent magnet machines used in microturbine applications," *Journal of Engineering for Gas Turbines and Power*, vol. 131, no. 2, pp. 697–703, 2009.

[63] H. Hamalainen, J. Pyrhonen, J. Nerg, and J. Talvitie, "AC resistance factor of litz-wire windings used in low-voltage high-power generators," *IEEE Transactions on Industrial Electronics*, vol. 61, no. 2, pp. 693–700, 2013.

[64] "Danfoss turbocor tt series installation manual - revision N." `https://www.manualslib.com/manual/1535962/Danfoss-Turbocor-Tt-Series.html?page=21#manual`.

[65] F. Liu, L. Ruan, and G. Gu, "The effect of the coolant on the evaporative cooling system of the hydro-generator," in *2011 International Conference on Electrical Machines and Systems*, pp. 1–4, 2011.

[66] "3M Novec 7100 engineered fluid product information." https://multimedia.3m.com/mws/media/199818O/3m-novec-7100-engineered-fluid.pdf, Sept. 2009.

[67] "Immersion cooling for data centres." https://www.3mcanada.ca/3M/en_CA/novec-ca/immersion-cooling-for-data-centres/#temps. 20 Sept. 2020.

[68] M. H. Rausch, L. Kretschmer, S. Will, A. Leipertz, and A. P. Froba, "Density, surface tension, and kinematic viscosity of hydrofluoroethers HFE-7000, HFE-7100, HFE-7200, HFE-7300, and HFE-7500," *Journal of Chemical and Engineering Data*, vol. 60, no. 12, pp. 3759–3765, 2015.

[69] S. Bi, J. Cui, L. Ma, G. Zhao, and J. Wu, "Thermophysical properties of HFE-7100 and HFE-7500 (in Chinese)," *Chinese journal of chemical engineering*, vol. 5, no. 5, pp. 1680–1686, 2016.

[70] "3M Novec engineered fluid product information." https://max.book118.com/html/2017/0626/118159685.shtm. June 2011.

[71] V. Gnielinski, "New equations for heat and mass transfer in turbulent pipe and channel flow," *International Chemical Engineering*, vol. 16, no. 2, pp. 359–368, 1976.

[72] M. Shi, Y. Gan, and F. Ma, *Boiling and Condensation Heat Transfer (in Chinese)*. Beijing: Higher Education Press, 1995.

[73] A. Bejan and A. D. Kraus, *Heat Transfer Handbook*. Hoboken: Wiley, 2003.

[74] N. Simpson, R. Wrobel, and P. Mellor, "A general arc-segment element for three-dimensional thermal modeling," *IEEE Transactions on Magnetics*, vol. 50, no. 2, pp. 265–268, 2014.

[75] J. Shi, D. Wei, and X. Mu, "Three-dimensional temperature field analysis and calculation for automobile alternators (in Chinese)," *Micromotor*, vol. 48, no. 5, pp. 41–46, 2015.

[76] L. Tadrist, H. Combeau, M. Zamoum, and M. Kessal, "Experimental study of heat transfer at the transition regime between the natural convection and nucleate boiling: Influence of the heated wall tilt angle on the onset of nucleate boiling (ONB) and natural convection (ONC)," *International Journal of Heat and Mass Transfer*, vol. 151, p. 119388, 2020.

[77] M. S. Elgenk and H. Bostanci, "Saturation boiling of HFE-7100 from a copper surface, simulating a microelectronic chip," *International Journal of Heat and Mass Transfer*, vol. 46, no. 10, pp. 1841–1854, 2003.

[78] J. H. Lienhard and V. K. Dhir, "Extended extended hydrodynamic theory of the peak and minimum pool boiling heat fluxes," CR-2270, NASA, 1973.

[79] W. M. Rohsenow, "A method of correlating heat transfer data for surface boiling of liquids," *ASME Transaction*, vol. 74, pp. 969–976, 1952.

[80] M. G. Cooper, "Heat flow rates in saturated nucleate pool boiling – a wide-ranging examination using reduced properties," *Advances in heat transfer*, vol. 16, pp. 157–239, 1984.

[81] J. P. Mchale and S. V. Garimella, "Bubble nucleation characteristics in pool boiling of a wetting liquid on smooth and rough surfaces," *International Journal of Multiphase Flow*, vol. 36, no. 4, pp. 249–260, 2010.

[82] G. Tang, Z. Zhuang, and J. Wang, "Film condensation heating the transfer of the non-condensable gas (in Chinese)," *Journal of Xi'an Jiaotong University*, vol. 34, no. 11, pp. 31–35, 2000.

[83] Q. Gu and H. Gao, "The fringing effect in PM electric machines," *Electric Machines and Power Systems*, vol. 11, no. 2, pp. 159–169, 1986.

[84] Q. Gu and H. Gao, "Effect of slotting in PM electric machines," *Electric Machines and Power Systems*, vol. 10, no. 4, pp. 273–284, 1985.

[85] P. L. Alger, "The calculation of the armature reactance of synchronous machines," *Transactions of the American Institute of Electrical Engineers*, vol. 47, no. 2, pp. 493–512, 1928.

[86] Z. Zhu, K. Ng, N. Schofield, and D. Howe, "Analytical prediction of rotor eddy current loss in brushless machines equipped with surface-mounted permanent magnets. I. Magnetostatic field model," in *ICEMS'2001. Proceedings of the Fifth International Conference on Electrical Machines and Systems (IEEE Cat. No.01EX501)*, vol. 2, pp. 806–809 vol.2, 2001.

[87] Z. Zhu, K. Ng, N. Schofield, and D. Howe, "Analytical prediction of rotor eddy current loss in brushless machines equipped with surface-mounted permanent magnets. II. Accounting for eddy current reaction field," in *ICEMS'2001. Proceedings of the Fifth International Conference on Electrical Machines and Systems (IEEE Cat. No.01EX501)*, vol. 2, pp. 810–813 vol.2, 2001.

[88] M. Merdzan, S. Jumayev, A. Borisavljevic, K. O. Boynov, J. J. H. Paulides, and E. A. Lomonova, "Electrical and magnetic model coupling of permanent magnet machines based on the harmonic analysis," *IEEE Transactions on Magnetics*, vol. 51, no. 11, pp. 1–4, 2015.

[89] S. Jumayev, M. Merdzan, K. O. Boynov, J. J. H. Paulides, J. Pyrhonen, and E. A. Lomonova, "The effect of PWM on rotor eddy-current losses in high-speed permanent magnet machines," *IEEE Transactions on Magnetics*, vol. 51, no. 11, pp. 1–4, 2015.

[90] W. Gibbs, "Theory and design of eddy current slip couplings," *BEAMA Journal*, vol. 53, pp. 123–128, 1946.

[91] J. W. Rose, "An approximate equation for the vapour-side heat-transfer coefficient for condensation on low-finned tubes," *International Journal of Heat and Mass Transfer*, vol. 37, no. 5, pp. 865–875, 1994.

[92] "Fundamental technical specifications for evaporative cooling horizontal electrical machinery (in Chinese)," DL/T 1110–2009.

[93] "Rotating electrical machines – Part 2-2: Specific methods for determining separate losses of large machines from tests – Supplement to IEC 60034-2-1," 2010.